Sager, W.W., Winterer, E.L., Firth, J.V., et al., 1993
Proceedings of the Ocean Drilling Program, Initial Reports, Vol. 143

9. SITE 869[1]

Shipboard Scientific Party[2]

HOLE 869A

Date occupied: 3 May 1992

Date departed: 4 May 1992

Time on hole: 1 day 17 hr

Position: 11°0.091′N, 164°44.969′E

Bottom felt (rig floor, m; drill-pipe measurement): 4837.8

Distance between rig floor and sea level (m): 11.1

Water depth (drill-pipe measurement from sea level, m): 4826.7

Total depth (rig floor, m): 5004.3

Penetration (m): 166.5

Number of cores (including cores with no recovery): 18

Total length of cored section (m): 166.5

Total core recovered (m): 129.27

Core recovery (%): 77

Oldest sediment cored:
Depth (mbsf): 166.5
Nature: Chert
Age: Eocene
Measured velocity(km/s): 1.4–1.8

HOLE 869B

Date occupied: 4 May 1992

Date departed: 15 May 1992

Time on hole: 10 days 20 hr

Position: 11°0.093′N, 164°45.019′E

Bottom felt (rig floor, m; drill-pipe measurement): 4837.8

Distance between rig floor and sea level (m): 11.1

Water depth (drill-pipe measurement from sea level, m): 4826.7

Total depth (rig floor, m): 5634.0

Penetration (m): 796.2

Number of cores (including cores with no recovery): 69

Total length of cored section (m): 796.2

Total core recovered (m): 252.04

Core recovery (%): 31

Oldest sediment cored:
Depth (mbsf): 796.2
Nature: Volcanic sandstone
Age: Cenomanian
Measured velocity (km/s): 3.0–4.0

[1] Sager, W.W., Winterer, E.L., Firth, J.V., et al., 1993. *Proc. ODP, Init. Repts.,* 143: College Station, TX (Ocean Drilling Program).
[2] Shipboard Scientific Party is as given in list of participants preceding the contents.

Principal results: Site 869 (proposed Site Syl-3) is situated 45 nmi (83 km) southwest of the atoll-guyot pair, Pikinni Atoll (formerly Bikini) and Wodejebato Guyot (formerly Sylvania). Drilling at this location was planned to provide a basinal reference section for comparison to Leg 144 drill holes on the summit of Wodejebato and prior drilling on Pikinni. Site-survey data suggested that a thick, layered succession of sediments exists at the site that consists mainly of turbidites. Volcanic basement is not obvious in the site-survey seismic lines, so drilling was not expected to encounter basement basalt. Approximately 850 m of penetration was planned, and the expectation was to bottom in Cretaceous volcaniclastics produced by constructional volcanism on either or both Wodejebato and Pikinni.

The location of Site 869, at 11°00.09′N, 164°45.02′E, was chosen on the seafloor adjacent to both Pikinni and Wodejebato, close enough to receive sediments shed mainly by these edifices, but far enough away so that both would contribute. It was assumed that sedimentation at an adjacent basinal hole would parallel and complement that on the atoll-guyot pair. For example, erosional hiatuses on the summit might be expected to produce sediments on the archipelagic apron, thus filling "missing chapters" in the geologic history provided by summit holes. Drilling at Site 869 was undertaken to address the following primary goals:

1. Determining the history of volcanism on Pikinni/Wodejebato;
2. Developing a model of Cretaceous, mid-ocean guyot/atoll carbonate platform formation and evolution for the Marshall Islands;
3. Comparison of the timing and effects of fluctuations in relative sea level among Pacific guyots and relation to worldwide sea-level curves; and
4. Deciphering the cause(s) for the drowning(s) of some Marshall Islands guyots (such as Wodejebato) vs. the existence of Cenozoic reefs on nearby atolls (such as Pikinni).

Two holes were drilled at Site 869, an APC/XCB hole (Hole 869A), and an RCB hole (Hole 869B), the latter located about 93 m north of the former. The operational plan was to use the APC/XCB combination to obtain relatively undisturbed cores from the upper 300 to 400 m of the sedimentary column. In analogy to Site 462, hard chert layers were expected to frustrate drilling at about 300 to 400 mbsf, and a round-trip was planned to change to an RCB bit and begin a second hole. Chert and porcellanite were encountered at much shallower depths than expected, and Hole 869A was terminated at a depth of only 166.5 mbsf. Hole 869B was washed to 140.0 mbsf and cored continuously to a total depth of 796.2 mbsf.

Core recovery in Hole 869A, drilled with the APC/XCB combination, was mostly excellent, with the average being over 100% for the APC cores and 77.6% overall. In Hole 869B, recovery was variable (see "Operations" section, this chapter). In cherty sections, recovery was generally low, and we obtained only a few pebbles of chert in some cores. In contrast, recovery in Cretaceous volcaniclastic turbidites was typically in excess of 60%. In general, recovery increased downhole in Hole 869B, averaging about 20% from 200 to 500 mbsf and increasing to 70% at the bottom of the hole.

Using combined microfossil and macrofossil biostratigraphy, visual core descriptions augmented with smear-slide and thin-section data, physical properties data, and downhole logs, three principal stratigraphic units were recognized (see "Lithostratigraphy" section, this chapter). In stratigraphic order, from bottom to top, the lithologic divisions are described as follows:

1. Unit III (796.2–207.7 mbsf). Middle–upper Cenomanian to upper Campanian–lower Maastrichtian volcaniclastics interlayered with nannofossil and radiolarian claystone. This unit is characterized by numerous gray to green volcaniclastic sandstones and breccias intercalated with lighter-colored claystones. Seven lithologic subunits can be recognized on the basis of changes in the mix, grain sizes of, or depositional style of the dominant components. Subunits IIIF (780.7–653.3 mbsf), IIIE (653.3–536.1 mbsf), and IIIC (487.8–458.8 mbsf), and IIIA (381.5–207.7 mbsf) consist mostly of volcaniclastic sandstone interbedded with claystone. These similar subunits are punctuated by Subunits IIIG (796.2–780.7 mbsf), a volcanic siltstone with calcareous claystone, Subunits IIID (536.1–487.8 mbsf), a volcanic breccia, and IIIB (458.8–381.5 mbsf), which consists mainly of radiolarian-rich claystone.

The volcaniclastic layers consist mainly of sand-size grains, deposited as turbidites. Basaltic clasts are common, in places forming breccias, but also occurring within a fine-grained matrix and implying transportation by grain flow. Most clasts are subangular to subrounded, suggesting a moderate transport distance. The largest clasts are up to 80 mm in diameter, and most have been affected by light to moderate alteration. The volcaniclastic layers contain clinopyroxene, palagonite, feldspar, zeolite, epidote, and chlorite grains, attesting to a basaltic parentage. Zeolites are a common cement.

Claystones occur abundantly in some parts of the section (e.g., Subunit IIIB), but rarely in others (e.g., Subunit IIIF). They are locally calcareous, siliceous, and/or zeolitic. Radiolarian and nannofossil concentrations are variable; in some layers, these fossils are dispersed through the matrix and in others they are concentrated in millimeter-scale beds. Within the Cenomanian section, unequivocal shallow-water debris are absent. Shallow-water biogenic fragments occur only rarely in the Turonian to Maastrichtian beds above, mainly in Subunits IIIA, IIIB, and IIIC. Bivalve shell, gastropod, echinoid, red-algal, and recrystallized skeletal fragments were found as were orbitoid foraminifers, micritic ooids, peloids, and glauconite. Coalified woody fragments were found in Core 143-869B-51R, at a depth of 618 mbsf.

2. Unit II (166.5–88.2 mbsf, Hole 869A; 207.7–140.0 mbsf, Hole 869B). Lower Paleocene to upper Eocene radiolarian-nannofossil ooze and nannofossil-radiolarian ooze with porcellanites and chert. Recovery of this unit was low, but it appears to consist of alternating layers of hard chert and soft ooze. Porcellanites and cherts make up a significant fraction of the recovered lithology in the bottom of the unit and decrease in abundance upward. Layers of nannofossil limestone and chalk occur in places through the section.

3. Unit I (88.2–0.0 mbsf, Hole 869A). Upper Eocene to lower Miocene clayey nannofossil ooze and radiolarian-nannofossil ooze. Major components of the oozes are nannofossils, radiolarians, sponge spicules, and clay. Color and compositional changes show cycles, on various scales, as the mix of principal components varies. The unit is divided into two subunits by a stratigraphic gap between the upper Oligocene and lower Miocene.

Nannofossils provided most of the datable biomarkers for constructing an age framework for Holes 869A and 869B. Abundance increases uphole, from few to absent in the volcaniclastic turbidites to abundant in the ooze section. Preservation is generally moderate to poor. Foraminifers are few to rare and also generally increase in abundance uphole in the upper Cretaceous section; however, they are missing from all but the Oligocene of Hole 869A. Their preservation is typically poor. Radiolarians are common, but no specialist was on board this ship to study them, so these did not contribute to the shipboard biostratigraphy.

The lower portion of Hole 869B consists of about 320 m of intercalated turbidites and claystones of late Cenomanian age. Extremely rapid sedimentation rates are indicated, as virtually the entire Cenomanian sequence is within the upper two Cenomanian nannofossil biozones, CC10 and CC9. Foraminifers suggest a potentially greater time span, with most of the Cenomanian strata being within the upper Cenomanian, except the deepest cores, which may be from the middle Cenomanian.

Above the Cenomanian strata (up to 207.7 mbsf), more volcaniclastic turbidites and intercalated claystones range in age from Turonian to late Campanian/early Maastrichtian. This interval contains an expanded Campanian section, from approximately 400 to 225 mbsf. Poor recovery prevents the dating of the interval from 225 to 207 mbsf, but this interval resembles the Cretaceous volcaniclastic section in downhole logs. Into the Cenozoic, lithology changes to cherts and radiolarian-nannofossil oozes. The uppermost cored interval of Hole 869B is early Paleocene to early Eocene in age. Hole 869A yielded entirely Cenozoic sediments that range in age from middle Eocene to early Miocene. The stratigraphic progression at Site 869 is punctuated by five recognized hiatuses. The missing strata are (1) the upper Coniacian to lower Santonian; (2) upper Maastrichtian to lower Paleocene; (3) part of the upper Paleocene; (4) a section including the Oligocene/Miocene boundary; and (5) post-early Miocene age sediments missing at the seafloor. Of these, the most prominent is the upper Maastrichtian-lower Paleocene hiatus, which spans up to 10 m.y. and includes the Cretaceous/Tertiary boundary.

Paleomagnetic measurements of the sediments cored in Hole 869A were ruined by pervasive rust contamination of the APC/XCB cores. Measurements of discrete samples and archive-half samples from the Cretaceous section of Hole 869B showed normal polarity down to Core 143-869B-21R, reversed polarity from Cores 143-869B-21R to -26R, and normal polarity below. This reversed zone has been interpreted as Chron 33R, the first reversed polarity epoch after the Cretaceous Quiet Period (Cretaceous Long Normal Superchron, K-N). Paleolatitudes from Hole 869B samples are in low southern latitudes, 10°-20°S.

Because shipboard magnetic stratigraphy interpretations were hampered by rust contamination in Hole 869A and by the few reversals in the Cretaceous sections drilled in Hole 869B, calculated sedimentation rates were based solely on biostratigraphy. Sediments accumulated in the Cenomanian section, from the bottom of the hole up to about 470 mbsf, at the rapid rate of 60 m/m.y. or greater. In the Cretaceous section above, up to a depth of about 207 mbsf, the overall rate was about 15 m/m.y. A hiatus of 10 m.y. duration may separate the Cenozoic and Mesozoic parts of the sedimentation curve. The average sedimentation rate in the Cenozoic was about 4.5 m/m.y.

Marked downhole concentration trends of cations reflect diagenetic changes within the volcanogenic sediments: Ca and Sr are released by feldspars, whereas Mg, K, Na, and Rb are decreased by incorporation into alteration products. High silica concentrations in Hole 869A result from high biogenic silica concentrations. $CaCO_3$ percentage varied with the mix of sedimentary components, from high values of greater than 97% to low values of less than 1% in some cherts, claystones, and volcaniclastic layers. In Hole 869A, $CaCO_3$ increases with depth from about 50% in lithologic Subunit IA, is nearly constant above 90% in Subunit IB, and then decreases with depth to about 20% at the bottom of Unit II. In Hole 869B, $CaCO_3$ concentration is highly variable, but generally low, typically less than 10%. Peaks of $CaCO_3$, commonly greater than 20%, occur commonly within chalk and claystone layers intercalated between volcanogenic layers. TOC in both Holes 869A and 869B is low to very low, with the greatest values less than 0.8%.

Overall, physical-property trends at Site 869 are what one would expect for basinal sediments: bulk density and sonic velocity increase slightly downhole (from about 1.5 to 2.1 g/cm^3 and 1.5 to 2.6 km/s), whereas porosity and water content decrease (from 70% to 35% and 60% to 20%, respectively). Superimposed upon these trends are fluctuations caused by variations in the composition and layering of turbidites and volcanic breccias. The radiolarian and nannofossil-rich oozes of Hole 869A show remarkable variations in bulk density, apparently owing to variable carbonate content; nevertheless, the sonic velocity remains nearly constant throughout, except for the intercalated chert layers. Physical properties are more variable in cores from Hole 869B than in those from Hole 869A because the former have highly variable compositions that consist mostly of volcaniclastic turbidites and breccias interlayered with marly, nannofossil- and radiolarian-rich claystones. Sonic velocities as high as 4 to 5 km/s and anisotropies of more than 15% were measured from samples of cores from the lower 300 m of Hole 869B.

Four logging runs were conducted in Hole 869B. The first, using the quad-tool (gamma-ray, sonic-velocity, neutron-porosity, resistivity, and temperature), extended from 777 mbsf to the drill pipe at 112 mbsf. For the second and third runs (the formation microscanner [FMS] and Japanese magnetometer), hole-penetration problems dictated lowering the pipe to 235 mbsf, below the Cenozoic chert layers. The FMS and magnetometer were then lowered to 775 and 724 mbsf, respectively, and run up to the base of the pipe. The final run, with the geochemical tool string, was abbreviated because of time constraints, but it recorded data from 560 to 360 mbsf.

The quad-tool produced good data that showed excellent correlation of resistivity, density, and gamma-ray reflectance with lithology and the seismic reflection record. In particular, several prominent volcaniclastic turbidite-breccia layers show up as fining-upward sequences. The Japanese magnetometer showed prominent anomalies that also correspond to some of these units. Interpretation of the FMS and geochemical tool data await processing, but the preliminary FMS data, in particular, promise a good record of the structure of the borehole wall.

Combining downhole sonic velocity logs with lithologic and physical properties data, changes in acoustic impedance can be determined that correlate with most seismic reflectors. In general, the Cenozoic layers show hummocky forms that suggest turbidite channels, and strong reflectors appear to be caused by silicified layers of porcellanite or chert. The upper Mesozoic layers appear more flat-lying, and reflectors come in packets that probably were caused by volcaniclastic turbidites. The strongest and most continuous reflector, at a two-way traveltime of 0.44 s, appears to correlate with the sharp base of a unit of coarse volcanic breccia and turbidites cored from 509 to 543 mbsf. Reflectors beneath this depth become increasingly intermittent and indicate more relief, corresponding to massive volcaniclastic turbidites and breccias of the rapidly deposited Cenomanian section. Drilling at Site 869 terminated at a depth of 796.2 mbsf, short of at least two additional reflectors at two-way traveltimes of 0.89 and 1.05 s, with extrapolated depths of 1000 and 1230 mbsf. Nothing in the seismic records indicates true basaltic basement, which suggests that the sedimentary section at Site 869 may be thick.

Site 869 shows rapid deposition of Cretaceous sediments, mainly volcaniclastic sandstones, siltstones, and breccias, against a background of pelagic sedimentation. A thick section of Cenomanian volcaniclastics, over 300 m in thickness, was cored from the bottom of Hole 869B, and no bottom was reached. This suggests that volcanism on nearby seamounts (probably Wodejebato or Pikinni) contributed a large volume of material to the adjacent basin. Interestingly, dredges from nearby Wodejebato Guyot yielded Albian shallow-water carbonates, implying that the underlying seamount formed during or prior to the Albian, a chapter of the depositional history not sampled at Site 869.

The Cenomanian section is nearly devoid of shallow-water material, suggesting that the massive influx of volcaniclastics overwhelmed any influx of such material. Conversely, higher in the section, shallow-water debris becomes more abundant, although it is still rare. Volcaniclastic material waxed and waned through the rest of the Cretaceous, with a significant influx during the early to late Campanian, perhaps signaling another phase of volcanism on a nearby seamount. Campanian-Maastrichtian shallow-water fossils have been dredged from the summit of Wodejebato Guyot (see "Background and Objectives" section, this chapter), implying that it had built up into shallow water at that time. Grain sizes and distributions vary greatly in the volcaniclastic layers. Coarse-grained breccias (with clasts up to 80 mm in diameter), sand and silt-grade turbidites, and grain-flow deposits having large clasts surrounded by fine-grained matrix can be seen. These imply energetic, probably channelized, transport by turbidite, grain, and mass flows from relatively nearby sources.

At the end of the Cretaceous, the volcaniclastic sedimentation waned and pelagic sedimentation prevailed, beginning with nannofossil and radiolarian-rich oozes, some of which were silicified into chert and porcellanite layers. Sedimentation was episodic, with numerous hiatuses and low sedimentation rates during the Cenozoic. Many of the Cenozoic sedimentary layers are turbidites, probably shed from the nearby Wodejebato-Pikinni edifice. Sediments younger than early Miocene are not present at Site 869, and the seafloor morphology in 3.5-kHz records suggests that they have been removed, probably by bottom currents.

BACKGROUND AND SCIENTIFIC OBJECTIVES

Site 869 (proposed site Syl-3), located at 11°00.09′N, 164°45.02′E in water 4827 m deep, was drilled in the basin approximately 40 nmi (74 km) southwest of the dumbbell-shaped volcanic edifice consisting of Wodejebato Guyot (formerly Sylvania) and Pikinni Atoll (formerly Bikini) in the northern Marshall Islands (Fig. 1). Although they have foundations on the same volcanic edifice, Pikinni is a modern, living atoll, whereas Wodejebato has drowned. Drilling at Pikinni documented that a shallow-water carbonate platform has existed there since Miocene time (Cole, 1954; Schlanger, 1963) and by analogy to Anewetak, perhaps since Eocene time (Schlanger, 1963). Presumably, Pikinni and Wodejebato share a similar early history, but it is a mystery why the Pikinni platform grew, when Wodejebato drowned.

The purpose of the site was to sample the distal part of the archipelagic apron shed into the basin from the nearby atoll and guyot. This site is complementary to proposed Leg 144 sites on the summit of Wodejebato Guyot, as Site 463 was to the summit holes (866-868) drilled on Resolution Guyot. Not only will the core material help to define the history of volcanic and carbonate-platform growth events, but the patterns of redeposition possibly carry a signal from sea-level fluctuations. Site 869 data also provide a comparison with results from two other nearby basinal sites near guyots: Site 462 in the Nauru Basin (Larson and Schlanger, 1981) and Site 585 in the East Mariana Basin (Moberly, Schlanger, et al., 1986).

Seismic reflection data collected during site surveys (see "Site Geophysics" section, this chapter) show multiple reflections within about 1.055 two-way traveltime of the seafloor. Although the ages of the reflectors were not known, it was assumed that they represented most of the history of the nearby guyot and atoll: possible Early Cretaceous volcanism and carbonate platform initiation, middle to Late Cretaceous volcanism, and Neogene (and Paleocene?) carbonate platform sediments from Pikinni (Cole, 1954; Schlanger, 1963). The depth to volcanic basement was also uncertain because there was no clear, strong seismic reflector that could be interpreted as the bottom of the sediment pile. Consequently, drilling at Site 869 was not intended to reach oceanic basement. Instead, a hole 850 to 1000 m deep bottoming in volcaniclastics formed during the initial volcanism of the guyot pair was envisaged.

Site Selection

Site 869 was chosen at a spot some distance from Wodejebato/Pikinni so that the most continuous and complete record of the edifice evolution could be cored. A site closer to the feature would possibly obtain larger sedimentary grains, but at the risk of having some sediments bypass the site. The older sedimentary layers may onlap the flank of the volcanic pedestal and may not be present close to the feature. Furthermore, seafloor topography and seismic reflection records suggest that turbidite channels have criss-crossed the territory between the site and the edifice; thus, closer sites might miss portions of the sedimentary record because some turbidites might be deflected.

Seismic lines over Site 869 and in the vicinity show that the layers are relatively flat-lying, with only a very slight slope (0.3°) upward toward the Wodejebato/Pikinni edifice. Consequently, the exact position of the site was not critical. Pre-drilling seismic profiles showed no surprises, so a positioning beacon was dropped as close to the proposed site location as possible (see "Operations" section, this chapter). The proposed location was 11°00.00′N, 164°45.00′E and the actual position was 11°00.09′N, 164°45.02′E.

Geologic Background

Site 869 is within the Marshall Islands province, a group of atolls, guyots, and seamounts in the western central Pacific Ocean situated between the Mid-Pacific Mountains and the Ontong-Java Plateau. The seamounts stand on abyssal seafloor, 5500 to 5000 m deep,

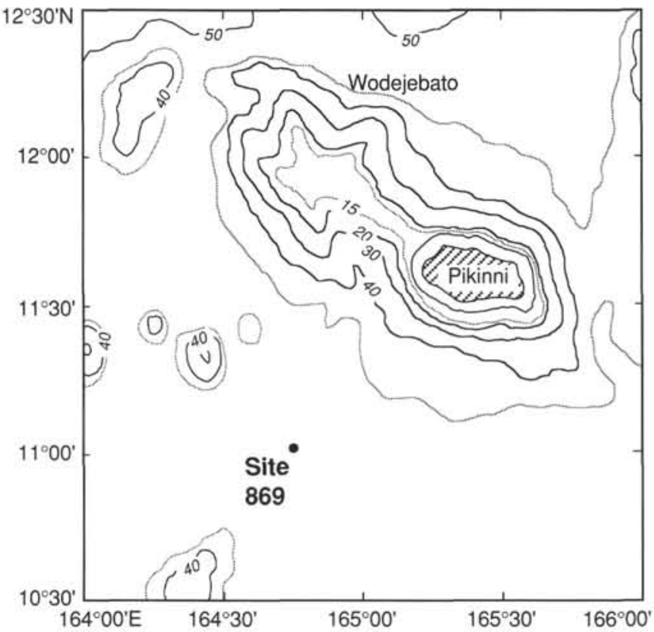

Figure 1. Location map for Site 869. Bathymetric contours (in hundreds of meters) at 1000-m intervals are shown as dark lines; auxiliary 500-m contours shown in gray.

between the Central Pacific Basin to the east and the East Mariana Basin to the west. They partially enclose another small basin to the south, the Nauru Basin (see "Introduction and Scientific Objectives" chapter, this volume, Fig. 4).

The Marshall Islands contain several linear, subparallel volcanic chains. The east side of the group is formed by the Marshall-Gilbert Ridge, a prominent, linear chain, trending approximately N20°W, and stretching from the northern boundary of the Fiji plateau, across the equator, to about 12°N. Limalok ("Harrie") Guyot, which was drilled during Leg 144, is a member of this chain. Two smaller, subparallel chains, the Ratak and Ralik ridges, are located near the north end of the Marshall-Gilbert Ridge. Another Leg 144 target, Wodejebato Guyot and its twin, Pikinni Atoll, are in the Ralik chain, upslope toward the northeast from Site 869. Most of the larger edifices, typically surmounted by modern atolls, are located in the Marshall-Gilbert, Ratak, and Ralik chains. In contrast, the northern part of the Marshall group contains fewer atolls and has many small seamounts and guyots.

No easily defined northern boundary is available for the Marshall Islands. The northern end intersects and blends into two diffuse seamount chains: the Marcus-Wake and Magellan seamount chains. These two chains branch off from the northern Marshall Islands and trend approximately N60°W westward to the Izu-Bonin and Mariana trenches. The Marcus-Wake chain intersects the Marshall Islands at about 20°N, in the vicinity of Wake Island, whereas the Magellan chain blends into the Ralik Ridge at about 10°N. The apparent continuity and difference in trends of these two chains and the Marshall chains has suggested to some that they are related. One hypothesis is that the Magellan and Marcus-Wake chains are older and that progressive volcanism, younging to the south and east, formed these volcanoes (Duncan and Clague, 1985). A corollary is that the "bend" between chains represents a change in the motion of the Pacific Plate that occurred in the middle to Late Cretaceous.

The Pacific Plate lithosphere beneath the Marshall Islands is Jurassic in age. Magnetic anomalies M21 through M29 (154–165 Ma; Kent and Gradstein, 1985), of the Phoenix lineation set, have been mapped in the Nauru Basin and surrounding the Ralik, Ratak, and Marshall-Gilbert Ridge (Larson, 1976; Nakanishi et al., 1992). The Ralik and Ratak chains are approximately perpendicular to the magnetic lineations and occur near lineation offsets, suggesting that they formed by volcanism along fracture zones (Larson, 1976). Site 869 is located to the northwest of these magnetic lineations, in a region known as the "Jurassic Quiet Zone" because of its subdued seafloor magnetic anomalies. The age trend of the magnetic lineations implies that the oceanic lithosphere beneath Site 869 is older than M29 (165 Ma).

Early geologic work in the Marshall Islands implied that they might be Tertiary in age. Drilling at Anewetak and Pikinni atolls in the 1940s and 1950s recovered shallow water limestones as old as early Miocene to possibly Oligocene at Pikinni and as old as Eocene at Anewetak (Emery et al., 1954; Cole, 1954; Schlanger, 1963). Volcanic basement was reached only at Anewetak, at depths of 1271 to 1388 m, and was dated at 51.4 to 61.4 Ma using conventional K-Ar radiometric techniques (Kulp, 1963). Recent work in the Marshall Islands, prior to drilling Legs 143 and 144, suggests that these results were misleading and that the volcanic pedestals of the Marshall Islands are much older and include two stages of volcanism and carbonate-platform growth (Lincoln et al., in press).

The first stage was probably submarine volcanism during Aptian to Albian time. Albian-age reefal material has been dredged from several Marshall Islands guyots, implying that their foundations are older. Furthermore, Site 462, in the Nauru Basin, cored Aptian-Albian plant debris, indicating the existence of wooded islands in the vicinity during those stages (Jenkyns and Schlanger, 1981). Only one Marshall Islands volcanic edifice, Look Seamount, located about 65 nmi (120 km) northeast of Pikinni Atoll, has yielded a radiometric date as old, 138.2 ± 0.2 Ma (approximately Valanginian-Berriasian; Lincoln et al., in press). However, a radiometric date of 111 ± 1 Ma (Pringle, 1992) from sills intruded into Albian sediments at Site 462, is consistent with Aptian-Albian volcanism and suggests a relation to the edifice formation.

Aptian-Albian volcanism built some of the Marshall Islands volcanoes up to sea level, where they became sites for carbonate platform formation. As the edifices sank, the carbonate platforms drowned, probably at about Cenomanian time (Lincoln et al., in press). Renewed volcanism during Santonian and Campanian time uplifted the volcanoes to sea level again. Evidence for this volcanic pulse is particularly abundant in the Marshall Islands: six guyots and atolls have ^{40}Ar-^{39}Ar radiometric ages between 75.9 and 86.7 Ma (Davis et al., 1989; Lincoln et al., in press), and volcaniclastic sediments of late Campanian to Maastrichtian age were recovered at Site 462 (Premoli Silva and Brusa, 1981). Some of the older platform sediments were probably eroded away, and Campanian-Maastrichtian reefs were formed (Lincoln et al., in press).

The two periods of Marshall Islands volcanism have analogs over much of the western Pacific. Indeed, one hypothesis is that two episodes of widespread, synchronous volcanism encompassed much of the Pacific Ocean north of the equator and west to the trenches during the periods between about 115 to 90 Ma and 83 to 65 Ma (Schlanger et al., 1981; Rea and Vallier, 1983). It has been suggested that volcanism in the Marshall Islands and other western Pacific Ocean seamount provinces resulted from the movement of the Pacific Plate over a cluster of hot spots, now located in the southeastern Pacific Ocean (Duncan and Clague, 1985; McNutt and Fisher, 1987). One explanation for these two periods of volcanism and uplift in the Marshall Islands is that the province transited two hot spot swells (Lincoln et al., in press). However, sparse dating of Marshall Islands edifices has prevented a conclusive test of either model, hot spot or volcanic pulse.

The last chapter in the history of Marshall Islands carbonate platforms took place in the early Tertiary. With subsidence after the Late Cretaceous volcanic episode, some platforms drowned. Others did not, and these evolved into modern atolls and built thick caps of Eocene and Neogene carbonate sediments (Schlanger, 1963; Lincoln et al., in press).

Drilling Objectives

The general goals of drilling at Site 869 were as follows:

1. To develop a history of Cretaceous mid-ocean carbonate platform growth and evolution by determining the lithologic, biostratigraphic, isotopic, and seismic stratigraphic succession within the sediment apron adjacent to a guyot/atoll pair for

A. Correlation of cores and seismic records with other guyots drilled during Legs 143 and 144; and

B. Comparisons of the timing and effects of changes in relative sea level among Pacific guyots and world-wide sea-level curves;

2. To decipher the volcanic history of the Wodejebato/Pikinni edifice;

3. To determine the cause(s) for the drowning(s) of the platform on Wodejebato and the reason for the existence of the Pikinni reefs during Cenozoic time.

Because Site 869 is located on deep seafloor, rather than the top of the guyot, scientific goals were not restricted to carbonate-platform objectives. Some specific Site 869 objectives are as follows:

4. To calculate paleolatitudes for constraining the tectonic history of the Marshall Islands and Pacific Plate;

5. To refine the magnetic polarity reversal time scale for the Early to Late Cretaceous;

6. To compare carbonate-platform biotic assemblages with others of similar age elsewhere as a clue to migration patterns;

7. To study the diagenetic history of deep-water sediments;

8. To gather pore-water samples as a means of inferring residence times and chemical evolution of interstitial waters;

9. To determine seismic wave velocities in Cretaceous to Tertiary deep-sea sediments for use in interpretation and correlation of seismic reflection and refraction data; and

10. To obtain a suite of downhole logs that would illuminate the structure, stratigraphy, and composition of deep-sea sediments in the vicinity of atolls and guyots.

Objectives Addressed and Accomplished

As outlined in the sections of this chapter, preliminary shipboard study of core samples and downhole logs collected at Site 869 suggest that the main scientific objectives can be met through further post-cruise study of the data and samples. Core recovery was mostly good to excellent, amounting to nearly 100% in the APC and XCB cores of Hole 869A, and typically 15% to 40% in the RCB cores of Hole 869B. Recovery decreased significantly, to less than 5%, when chert layers were encountered, but the downhole logs were particularly helpful for filling the gaps.

The first, stratigraphic set of objectives was addressed by detailed examination of lithology and fossil content of the cored sediments. Shipboard age data from microfossil studies are preliminary and must be adjusted for possible time lags caused by redeposition; nevertheless, they place strong constraints on the ages of the sediments and seismic reflectors as well as the timing of events. Additional age constraints will become available through post-cruise strontium-isotope measurements in core samples.

Determining the volcanic history of the Wodejebato/Pikinni edifice (Objective 2) will be addressed by obtaining dates for redeposited volcaniclastic sediments. Ages for the volcaniclastic grains come from direct ^{40}Ar-^{39}Ar radiometric dating. Furthermore, biostratigraphic and isotopic dates will help when constraining age. These dates will be used with magnetic polarity measurements to address Objective 5, refining the magnetic polarity reversal time scale.

Objective 3, determining the cause(s) of drowning for the carbonates atop Wodejebato, will be pursued by a study of the types, ages, and compositions of carbonate sediments shed by the edifice. These data will be compared with the results of drilling on the summit of the guyot by Leg 144 as well as data from other Leg 143 and 144 sites.

A paleolatitude history, Objective 4, will be the result of detailed shore-based studies of the paleomagnetism of core samples from Site 869. Because the sediments have ages spanning much of the history of the guyot/atoll pair, it should be possible to examine paleolatitude trends for implications of the tectonic drift history of the edifice and the Pacific Plate.

Carbonate-platform biotic assemblages (Objective 6) will be studied by microscopic and macroscopic examinations of carbonate debris contained within the redeposited sediments. The fossil content will be compared with the known ranges and ages of Cretaceous carbonate-platform biota.

The diagenesis of deep-sea sediments (Objective 7) will be addressed by detailed petrographic examination of thin sections, combined with petrologic and isotopic analyses of rock compositions. Downhole logs will be used for additional information about composition and stratigraphic framework. Other properties, such as paleomagnetism, may also yield information cogent to this problem.

Objective 8, pore-water geochemistry, was accomplished by analyzing interstitial waters squeezed from whole-round samples taken from softer sediments and from crushed sedimentary rock fragments.

Objective 9, the derivation of velocity and density vs. depth curves for seismic interpretation, was attacked from several directions. One tack was to obtain downhole logs of in-situ sonic wave velocity and density. Another was to perform complementary measurements for the recovered cores. In addition, a seismic refraction line was shot across Site 869 using an expendable sonobuoy (see "Operations" section, this chapter).

Once again, downhole logs (Objective 10) proved to be extremely valuable for reconstructing the stratigraphy of Site 869. Not only did these provide a framework for understanding partial core recovery, they contributed continuous downhole data sets of physical and chemical properties that were used to see general trends in the sediments. Geophysical (sonic velocity, spectral gamma-ray, bulk density, resistivity, and porosity) and geochemical strings were run to measure in-situ physical properties and compositional variations. Downhole magnetic field data were obtained with the Japanese magnetometer to record volcanic layers and their magnetic properties. In addition, the FMS was used to map resistivity variations in the borehole wall to provide a picture of structure and bedding.

OPERATIONS

Transit from Site 868

After completing the exit survey over Resolution Guyot upon leaving Site 868, the ship turned on a course toward proposed Site Syl-3, now Site 869, in the basin immediately west of Wodejebato (formerly Sylvania) Guyot and Pikinni (formerly Bikini) Atoll, in the central part of the Marshall Islands Chain. We made slight deviations in the ship's course to Site 869 to obtain seismic-reflection and magnetic data from several poorly surveyed guyots that lie close to the great circle route to Site 869. One of these guyots was Wodejebato Guyot, which was scheduled for drilling during Leg 144 (see "Underway Geophysics" chapter, this volume).

Approach to Site 869

After terminating the pass over Wodejebato Guyot, the ship resumed its normal speed of about 10.5 kt until arriving at a point about 10 nmi (19 km) northeast of Site 869, where the ship slowed to 6 kt to obtain good-quality seismic-reflection data and a sonobuoy refraction line over the proposed site. The first expendable sonobuoy was deployed, but failed after about half an hour. A backup sonobuoy was deployed, but because the ship was now only 2.5 nmi (4.5 km) from the site, the refraction line was extended. At about 6 nmi (11 km) past the site, the signal faded, but not before a good wide-angle refraction profile with several refractors was obtained (see "Underway Geophysics" chapter, this volume).

The geophysical gear was hauled aboard, and the ship turned to go back to the proposed site. The seismic reflectors at Site 869 are relatively flat-lying; thus, little was to be gained by adjusting the site location. Therefore, an acoustic beacon was dropped at 1935 UTC, 2 May, at the proposed Syl-3 location. This beacon gave an erratic signal, so after the ship was on location, this first beacon was released and recovered and another beacon dropped in its stead.

Coring Operations at Hole 869A

A bottom-hole assembly (BHA) was assembled for use with the APC/XCB coring system. The plan was to go as far as possible with this coring method in Hole 869A and then to trip out and run in Hole 869B with the RCB system, washing through most of the interval cored with the APC/XCB in the previous hole, and then coring ahead. The plan envisioned using a rotary bit all the way to acoustic basement (estimated to be at a depth of about 900 mbsf), and reentering the hole using a minicone should the first bit not last.

Hole 869A was spudded in at about 0230 UTC, 3 May 1992, and an APC core, Core 143-869A-1H, taken from 4837.8 to 4847.5 m below the rig floor. When retrieved, the core barrel was seen to be full, and the depth to the seafloor (from the derrick floor) was accepted as 4837.8 m. This compares with the 4842.4-m depth predicted from the PDR.

Coring proceeded (Table 1) with the APC system without difficulty and with complete recovery down to a depth of 85.7 mbsf (Fig. 2). Core 143-869B-10H returned empty and with the piston rod sheared. It appeared that the core barrel had hit a hard layer and stopped, but the pressure behind the APC broke the rod. Because the resistance of the sediments to coring was increasing, we elected to use the XCB system and because the interval of the core had not actually been drilled, the XCB was used to drill through the same interval. It returned with 2.7 m of core, including a hard chert layer more than 10 cm thick. We then cored ahead to 165.5 mbsf in Eocene pelagic sediments that contained a few small fragments of porcellanous chert (Fig. 2). Between 165.5 and 166.6 mbsf, while trying to

Table 1. Coring summary for Holes 869A and 869B.

Core no.	Date (May 1992)	Time (UTC)	Depth (mbsf)	Length cored (m)	Length recovered (m)	Recovery (%)
143-869A-						
1H	3	0330	0.0–9.7	9.7	9.69	99.9
2H	3	0445	9.7–19.2	9.5	9.84	103.0
3H	3	0540	19.2–28.7	9.5	9.83	103.0
4H	3	0630	28.7–38.2	9.5	9.76	103.0
5H	3	0725	38.2–47.7	9.5	9.92	104.0
6H	3	0820	47.7–57.2	9.5	9.94	104.0
7H	3	0920	57.2–66.7	9.5	10.17	107.0
8H	3	1020	66.7–76.2	9.5	10.12	106.5
9H	3	1120	76.2–85.7	9.5	10.01	105.3
10X	3	1405	85.7–95.5	9.8	2.72	27.7
11X	3	1455	95.5–105.5	10.0	7.15	71.5
12X	3	1555	105.5–115.5	10.0	7.34	73.4
13X	3	1800	115.5–125.5	10.0	6.38	63.8
14X	3	1900	125.5–135.5	10.0	7.75	77.5
15X	3	2030	135.5–145.5	10.0	8.38	83.8
16X	3	2230	145.5–155.5	10.0	0.22	2.2
17X	4	0000	155.5–165.5	10.0	0.05	0.5
18X	4	0200	165.5–166.5	1.0	0.00	0.0
Coring totals				166.5	129.27	77.6
143-869B-						
1W	4	2330	0.0–140.0	140.0	9.54	(wash core)
2R	5	0110	140.0–149.6	9.6	0.50	5.2
3R	5	0215	149.6–159.3	9.7	0.09	0.9
4R	5	0400	159.3–168.9	9.6	0.64	6.7
5R	5	0520	168.9–178.6	9.7	1.08	11.1
6R	5	0645	178.6–188.3	9.7	0.27	2.8
7R	5	0810	188.3–197.9	9.6	0.28	2.9
8R	5	0955	197.9–207.6	9.7	0.12	1.2
9R	5	1120	207.6–217.2	9.6	0.10	1.0
10R	5	1240	217.2–226.9	9.7	2.24	23.1
11R	5	1405	226.9–236.6	9.7	6.42	66.2
12R	5	1530	236.6–246.2	9.6	0.06	0.6
13R	5	1700	246.2–255.8	9.6	5.34	55.6
14R	5	1845	255.8–265.4	9.6	0.24	2.5
15R	5	2000	265.4–275.1	9.7	6.66	68.6
16R	5	2130	275.1–284.8	9.7	1.08	11.1
17R	5	2330	284.8–294.4	9.6	2.00	20.8
18R	6	0100	294.4–304.1	9.7	0.21	2.2
19R	6	0230	304.1–313.8	9.7	4.12	42.5
20R	6	0410	313.8–323.5	9.7	5.30	54.6
21R	6	0530	323.5–333.1	9.6	1.07	11.1
22R	6	0940	333.1–342.8	9.7	3.34	34.4
23R	6	1205	342.8–352.5	9.7	3.17	32.7
24R	6	1400	352.5–362.2	9.7	0.01	0.1
25R	6	1800	362.2–371.8	9.6	4.00	41.6
26R	6	2030	371.8–381.5	9.7	1.65	17.0
27R	7	0000	381.5–391.1	9.6	0.70	7.3
28R	7	0200	391.1–400.8	9.7	0.16	1.7
29R	7	0350	400.8–410.4	9.6	0.19	2.0
30R	7	0600	410.4–420.1	9.7	0.26	2.7
31R	7	0905	420.1–429.8	9.7	2.16	22.2
32R	7	1130	429.8–439.4	9.6	3.32	34.6
33R	7	1400	439.4–449.1	9.7	1.68	17.3
34R	7	1620	449.1–458.8	9.7	3.53	36.4
35R	7	1915	458.8–468.4	9.6	0.98	10.2
36R	7	2130	468.4–478.1	9.7	5.38	55.4
37R	7	2320	478.1–487.7	9.6	0.29	3.0
38R	8	0245	487.7–497.4	9.7	3.79	39.1
39R	8	0550	497.4–507.1	9.7	2.99	30.8
40R	8	0945	507.1–516.8	9.7	3.68	37.9
41R	8	1340	516.8–526.4	9.6	6.52	67.9
42R	8	1645	526.4–536.1	9.7	5.18	53.4
43R	8	2130	536.1–545.6	9.5	2.51	26.4
44R	9	0145	545.6–555.3	9.7	7.24	74.6
45R	9	0530	555.3–564.6	9.3	6.80	73.1
46R	9	0825	564.6–574.3	9.7	0.80	8.3
47R	9	1035	574.3–583.9	9.6	0.04	0.4
48R	9	1420	583.9–593.5	9.6	0.81	8.4
49R	9	1715	593.5–603.2	9.7	0.27	2.8
50R	9	2245	603.2–612.7	9.5	8.99	94.6
51R	10	0145	612.7–622.4	9.7	8.41	86.7
52R	10	0400	622.4–632.0	9.6	8.09	84.3
53R	10	0720	632.0–641.8	9.8	5.55	56.6
54R	10	1340	641.8–651.5	9.7	8.56	88.2
55R	10	1700	651.5–661.2	9.7	6.82	70.3
56R	10	2000	661.2–670.7	9.5	4.69	49.3
57R	10	2315	670.7–680.4	9.7	6.40	66.0
58R	11	0230	680.4–690.0	9.6	7.95	82.8
59R	11	0530	690.0–699.7	9.7	8.33	85.9
60R	11	0840	699.7–709.4	9.7	9.89	102.0
61R	11	1110	709.4–719.1	9.7	4.91	50.6
62R	11	1345	719.1–728.7	9.6	0.13	1.4
63R	11	2030	728.7–738.4	9.7	9.83	101.0
64R	11	2300	738.4–747.9	9.5	8.92	93.9
65R	12	0200	747.9–757.6	9.7	5.20	53.6
66R	12	0520	757.6–767.3	9.7	3.84	39.6
67R	12	0750	767.3–776.9	9.6	8.41	87.6
68R	12	1050	776.9–786.6	9.7	6.19	63.8
69R	12	1410	786.6–796.2	9.6	2.12	22.1
Coring totals				656.2	242.50	37.0
Washing totals				140.0	9.54	
Combined totals				796.2	252.04	

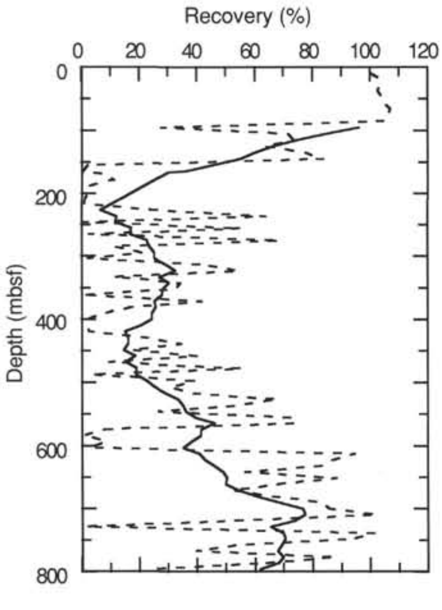

Figure 2. Core recovery rates at Site 869 plotted vs. core depth. The dashed line shows rates for each core, and the solid line represents a 10-point moving average.

cut Core 143-869A-18X, the bit advanced only 1 m in 1 hr and the core barrel returned empty. We concluded that the rocks were too hard for the XCB system and began to pull the drill pipe out of Hole 869A to change bits. The bit was on deck at 1030 UTC, 4 May, ending operations at Hole 869A.

Coring Operations in Hole 869B

Hole 869B was spudded in at 2045 UTC, 4 May 1992, at the same depth and about 30 m east of Hole 869A. The rotary bit was washed down to a depth of 140 mbsf with a core barrel latched in place (Core 143-869B-1W). Normal rotary coring then began in cherty Eocene, Paleocene, and Campanian/Maastrichtian strata, from which core recovery was poor, averaging only about 4% (Table 1). Beginning at about 217.2 mbsf (Core 143-869B-10R), the lithology changed to graded layers of volcaniclastic sandstone and claystone interbedded with marly pelagic limestone, and recovery rates began to improve markedly (Fig. 2). Coring rates gradually, but irregularly, decreased through the turbidites and debris flows of the Campanian-Turonian, and slowed still further in the highest 100 m of the upper Cenomanian, in coarse volcaniclastic debris flows. Below these coarse debris flows, coring rates again improved, but then increased gradually toward the total depth of Hole 869B at 796.2 mbsf (Figs. 3 and 4). The final core (Core 143-869B-69R) was retrieved at 1410 UTC, 12 May, and preparations begun for logging Hole 869B.

Logging Operations at Site 869

Following conditioning of Hole 869B, the bit was dropped and the pipe raised until the bottom of the BHA was at a depth of 90 mbsf. The heave compensator was used during all logging runs; it was turned on at 177 mbsf for the first logging run and at 344 mbsf for all subsequent runs.

Logging Run 1: Beginning at 0100 UTC, 13 May, a string of logging tools comprising (in order from top to bottom) the gamma-ray, sonic, neutron-porosity, density, resistivity, and the Lamont temperature tools and measuring about 32 m in length, was assembled, and at 0300 UTC, the string was lowered into the hole to a depth of 778 mbsf. During the upward run, a highly useful set of logs was obtained; the tools were back on deck at 0930 UTC.

Logging Run 2: The next logging run was with the FMS tool string. This was lowered in the hole until we discovered that the cable had gone slack and about 680 m of log cable was kinked because the tool string had met an obstruction. The tool string was raised to the surface and about 750 m was cut off the logging cable. The drill string was lowered until the bottom of the BHA was at a depth of 148 mbsf, and the FMS tool string was then lowered until it became blocked at about 166 mbsf. The tool string was raised again to the rig floor, and the drill pipe lowered until the bottom of the BHA was at a depth of about 235 mbsf, about 28 m below the contact between the Cenozoic cherty pelagic sediments and the underlying Upper Cretaceous volcaniclastic sediments, where the caliper log from the first logging run suggested that less rugose hole conditions might prevail. Finally, the FMS tool string passed down the hole to a depth of 774 mbsf and a successful log was made, up to 235 mbsf. The tool string was back on deck at 0930 UTC, 14 May.

Logging Run 3 was with the Japanese magnetometer, which was successfully run, beginning at 1000 UTC, 14 May, from a depth of 724 mbsf up to the bottom of the BHA (235 mbsf). This tool was back on deck at 1630 UTC.

During a logging run with the geochemical tool string, which obtained successful logs from a depth of 560 up to 360 mbsf, the tool string had to be raised to the surface because time had expired for scheduled downhole operations at Site 869. This run began at 1730 UTC, and the tool was back on deck at 2300 UTC, 14 May 1992.

A summary of well-log data from Hole 869B is given in Table 2.

After completion of logging operations, the drill string was retrieved, the thrusters raised, the acoustic beacon recovered, and the ship made ready for departure. The vessel was under way for Anewetak Atoll, the locale of Site 870, at 0830 UTC, 15 May 1992.

SITE GEOPHYSICS

Site 869 (proposed Site Syl-3), at 11°00.09′N, 164°45.02′E, is situated on deep seafloor approximately 45 nmi (83 km) southwest of the guyot-atoll pair, Wodejebato and Pikinni (Fig. 5). Its location was chosen to core redeposited sediments shed by the volcanic edifices and their carbonate caps, thus providing data complementary to those acquired by Leg 144 drilling on the summit of Wodejebato and by prior drilling on Pikinni (Cole, 1954; Emery et al., 1954).

Wodejebato Guyot has received scrutiny by numerous oceanographic expeditions, beginning in the 1950s (Emery et al., 1954; Hamilton and Rex, 1959). Recent surveys and dredging were conducted on DSDP and ODP site-survey cruises in 1981 (Cruise KK81062604; Peterson et al., 1986) 1988, and 1990 (Cruises MW8805 and MW9009; Lincoln et al., in press) by the University of Hawaii. Data collected to date indicate that Wodejebato has had at least two stages each of volcanism and carbonate-platform formation. The volcanic pedestal formed prior to the end of the Albian and was topped by an Albian carbonate platform, drowned, was uplifted by a volcanic episode during the Santonian, and was again capped by carbonates of Campanian to Maastrichtian age (Lincoln et al., in press).

In contrast to nearby Wodejebato and Pikinni, the geology and geophysics of the adjacent basin to the west is not as well known, owing to sparse geophysical track-line coverage. Site 869 is located in the Jurassic Quiet Zone about 150 nmi (278 km) north of M29 (Nakanishi et al., 1992); thus, the age of the oceanic lithosphere can be estimated only by extrapolation. Using the Kent and Gradstein (1985) geomagnetic polarity-reversal time scale, the age of the lithosphere at Site 869 is approximately 165 Ma. An unknown thickness of sediment rests upon this oceanic crust. Perhaps the best analog to Site 869 is Site 462, located 195 nmi (361 km) to the south in the Nauru Basin. At this site, approximately 440 m of Tertiary sediments, ranging from Paleocene to Pleistocene in age, overlies a Cretaceous section consisting mainly of volcaniclastics and intruded by a Cretaceous sill complex (Larson and Schlanger, 1981). An important component in the sediments was redeposited reef and plant fragments from nearby seamounts showing that islands and carbonate platforms

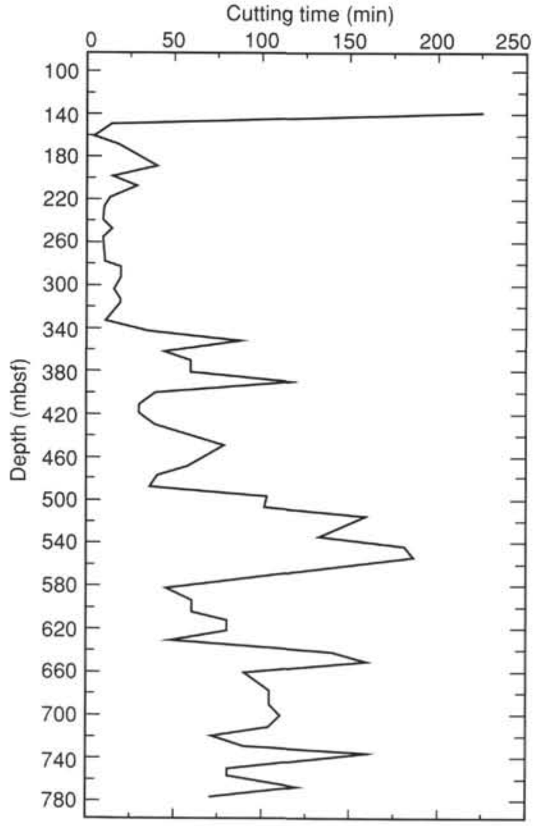

Figure 3. Cutting time for cores in Hole 869B, plotted vs. core depth.

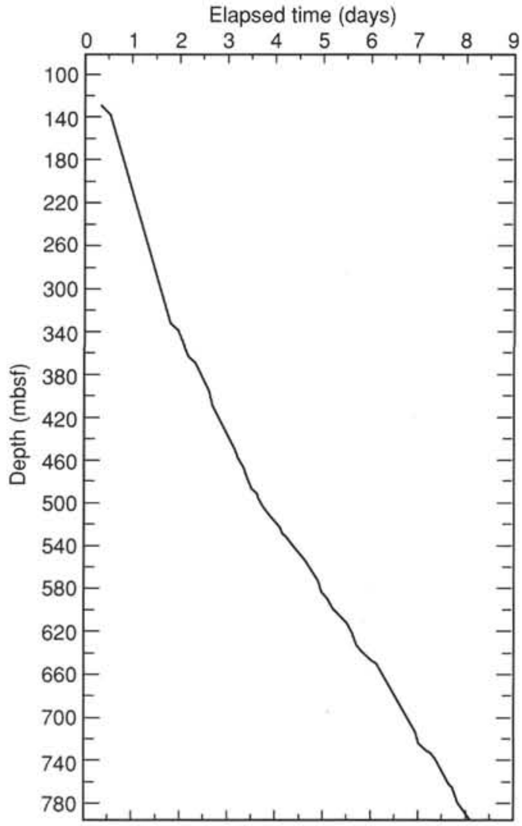

Figure 4. Elapsed time for coring operations at Hole 869B plotted vs. depth. The plot begins at spud-in and ends with retrieval of the final core.

existed in the region during the Early Cretaceous (Larson and Schlanger, 1981). Similar results were expected at Site 869.

Site Survey Data (Cruises MW8805 and TUNE08WT)

Proposed Site Syl-3 was chosen along one of the MW8805 site-survey lines trending approximately perpendicular to the trend of the Pikinni-Wodejebato edifice (Fig. 5). The 80-in.^{3} water-gun reflection record shows (1) the seafloor at a two-way traveltime (twtt) of 6.47 s and (2) a series of reflectors that gradually fade with depth. These reflectors dip slightly (about 0.3°) away from the volcanic edifices, implying that the sediments at this location are from the archipelagic apron of the atoll-guyot pair. A faint, discontinuous reflector at 0.85 s twtt beneath the seafloor at the site was selected as the deepest visible horizon. Several seismic reflectors just above this horizon appear to onlap it, thus, the reflector was tentatively identified as a "basement" of basalt or volcaniclastics.

Another geophysical line across the site, nearly parallel to the edifice pair, was obtained in January 1992 during cruise TUNE08WT of the *Thomas Washington.* A seismic reflection record of excellent quality was obtained with an 80-in.^{3} water gun (Fig. 6). The record shows a series of reflector packets, each of which contains multiple reflections, interlayered with intervals containing few or weak reflectors (see "Seismic Stratigraphy" section, this chapter). In the middle, at 0.35 to 0.43 s twtt below the seafloor, is a prominent, continuous, and relatively flat series of reflectors that prior to drilling were thought to be Eocene to Late Cretaceous cherts, in analogy with similar layers at the same depth at Site 462. The deepest coherent reflector was traced at about 0.85 to 0.90 s twtt below the seafloor, corresponding to the "basement" reflector in the MW8805 profile. Extrapolating the velocity-depth profile from Site 462, the depth of this horizon was estimated as approximately 900 mbsf.

Pre-drilling Survey, *JOIDES Resolution*

Transiting through the Marshall Islands en route to Site 869, the *JOIDES Resolution* crossed Wodejebato Guyot from northeast to southwest so that a 3.5-kHz echo-sounder and 200-in.^{3} water-gun seismic reflection profile could be obtained over its summit (Fig. 7; see also "Underway Geophysics" chapter, this volume).

After leaving Wodejebato Guyot, the ship resumed its cruising speed of 10.5 kt until reaching a point about 10 nmi (19 km) north of the proposed site. The ship slowed to 6.5 kt to acquire a good-quality seismic reflection profile over the site with the 200-in.^{3} water gun. At the same time, an expendable sonobuoy was launched to obtain wide-angle seismic refraction data (see "Underway Geophysics" chapter, this volume). The first buoy failed part-way along the line, so another was launched, and the seismic profile was extended 6 nmi (11 km) past the proposed site (Fig. 8).

Because of the larger seismic source used, the *JOIDES Resolution* seismic profile has an appearance that is slightly different from the 80-in.^{3} profiles obtained during the site surveys. The reflectors near the surface are not as prominent as in the site-survey profiles, but three packets of deeper reflectors stand out at 0.20, 0.35, 0.54, and 0.83 s twtt beneath the seafloor (Fig. 9). The latter reflector is apparently the one identified as "basement" in the site survey lines; however, additional reflections can be seen up to about 1.05 s twtt subseafloor. Assuming typical deep-ocean-sediment seismic velocities, this observation implies that the top of the oceanic crust is more than 1 km in depth at Site 869.

Another notable feature of the site-survey and pre-drilling seismic profiles over Site 869 is the roughness of the seafloor and seismic reflectors. Unlike most deep-sea sediment layers, which appear nearly horizontal in seismic reflection profiles, considerable relief is seen in the layers in the vicinity of Site 869 (Figs. 6 and 9). This relief is

Table 2. Well-log data from Hole 869B.

Log type	Depth[a] (mbsf)
Resistivity	89.5–777.2
Bulk density	89.5–774.5
Neutron porosity	89.5–773.0
Sonic velocity	89.5–772.5
[b]Gamma ray	0–771.3
U-Th-K	360.0–555.8
Aluminum	360.0–558.0
Geochemistry	360.0–560.2
Caliper	89.5–774.5
Formation microscanner	234.8–774.9
[c]Lamont temperature	0–778.5

[a] Assumes seafloor at 4837.8 m, with all logs correlated and depth shifted to the gamma-ray log from the geophysical tool string.
[b] This log was recorded in drill pipe from 89.5 to 0 mbsf.
[c] This log was recorded in drill pipe from 89.5 to 0 mbsf during the first run, and from 235.0 to 0 mbsf during the runs with the FMS and geochemical tool strings.

typically a few hundredths of seconds (twtt), but in places, variability of 0.05 s can be noted over a few miles of horizontal distance. Most seismic horizons in the area also are laterally discontinuous, with only a few displaying continuity across the entire profile (Fig. 6). Furthermore, in places, the reflectors have been interrupted and only diffracted energy can be seen, suggesting filled channels within the sedimentary sequence. The 3.5-kHz profile indicates that the seafloor is rough, with hyperbolas, discontinuous reflectors, and depth variations of as much as about 10 m over short distances (Fig. 10).

Taken together, these observations imply that sedimentation in the area of Site 869 has been energetic with erosion and patchy sedimentation. This agrees with the scenarios that sedimentation occurs at this location primarily through turbidity currents and that thermohaline bottom currents were strong at times during the Neogene. The structure of the seismic layering suggests that sedimentation occurs in archipelagic fan lobes with channels that frequently shift locations. Furthermore, the relief of the seafloor and discontinuities imply seafloor erosion, perhaps caused by turbidites or rapid bottom-water currents.

LITHOSTRATIGRAPHY

Lithologic units have been defined by characteristics such as color, carbonate and clay content, fossil and particle constituents, lithification, sedimentary structures, stratigraphy, and log signature. The sequence was divided into three major lithologic units: (1) cyclically bedded very pale brown to yellow-brown to dark reddish-brown nannofossil ooze, radiolarian nannofossil ooze, and clayey nannofossil ooze; (2) cyclically bedded white to very pale brown to dark yellowish-brown clayey nannofossil ooze to nannofossil radiolarian ooze to radiolarian ooze containing porcellanite and chert; (3) a series of gray to green breccias and similarly colored, typically graded and parallel-laminated volcaniclastic sandstones interbedded with calcareous claystones.

Lithologic Units

Unit I

Core 143-869A-1H to Section 143-869A-10X-2, 97 cm
Depth: 0–88.20 mbsf
Age: early Miocene to late Eocene

The dominant sedimentary theme of Unit I (Fig. 11) is one of cycles, on various scales, which are characterized by regular changes in color and composition (Fig. 12). The principal sedimentary components are nannofossils, radiolarians, sponge spicules, and clay.

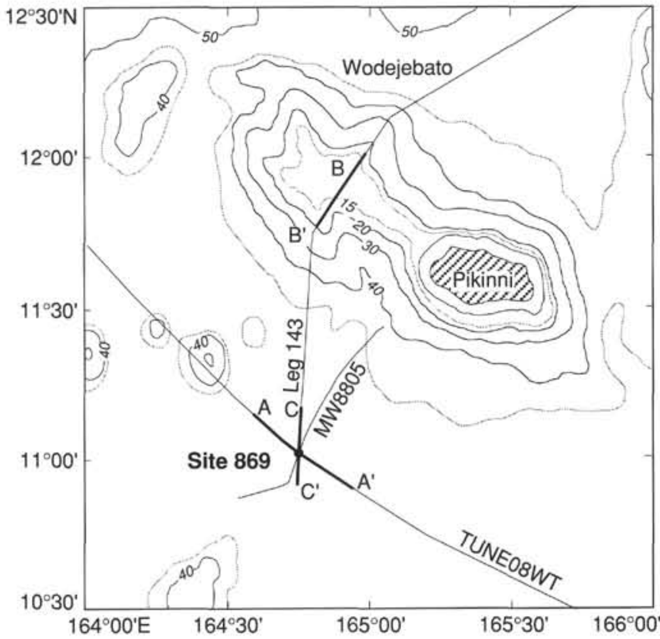

Figure 5. Location map for Site 869. Bathymetric contours (in hundreds of meters) at 1000-m intervals are shown as dark lines; auxiliary 500-m contours shown in gray. Site-survey ships' tracks across the site, from Cruises MW8805 and TUNE08WT, are shown as thin lines, as is track of the *JOIDES Resolution.* Solid lines denote portions of seismic lines shown in Figures 6 (A-A′), 7 (B-B′), and 9 (C-C′).

Colors vary from pale brown to yellow-brown to dark reddish brown, and compositions range from nannofossil ooze through radiolarian nannofossil ooze to clayey nannofossil ooze. Thicknesses of the different lithologies are on the scale of tens of centimeters, although some bands are thinner. Subunit IA is separated from Subunit IB by a stratigraphic gap.

Subunit IA

Core 143-869A-1H to Interval 143-869A-4H-3, 79 cm
Depth: 0–32.5 mbsf
Age: early Miocene

A striking feature of the upper three cores is the presence of nonhorizontal contacts between different lithologies, locally attaining slopes of 30°. Core 143-869A-1H is dominated by clays containing variable amounts of nannofossils and radiolarians; Cores 143-869A-2H and -3H and Sections 143-869A-4H-1 and -2 by radiolarian-nannofossil ooze and nannofossil-radiolarian ooze. These cores are heavily bioturbated.

Subunit IB

Intervals 143-869A-4H-3, 79 cm, to -10X-2, 97 cm
Depth: 32.5–88.20 mbsf
Age: late Oligocene to late Eocene

In Interval 143-869A-4H-3, 79–82 cm, can be seen a white sand-grade layer, intercalated between brown clayey nannofossil ooze, that contains a mixture of planktonic and large and small benthic foraminifers, echinoderm spines and plates, red algae, bryozoans, rare ostracods and bivalves, and nannofossils with phosphate and glauconite (see "Biostratigraphy" section, this chapter). The age of the fossil assemblage within the redeposited material is earliest Oligocene, which makes it older than the upper Oligocene sediment immediately below. The top of this layer, which corresponds to a stratigraphic gap between

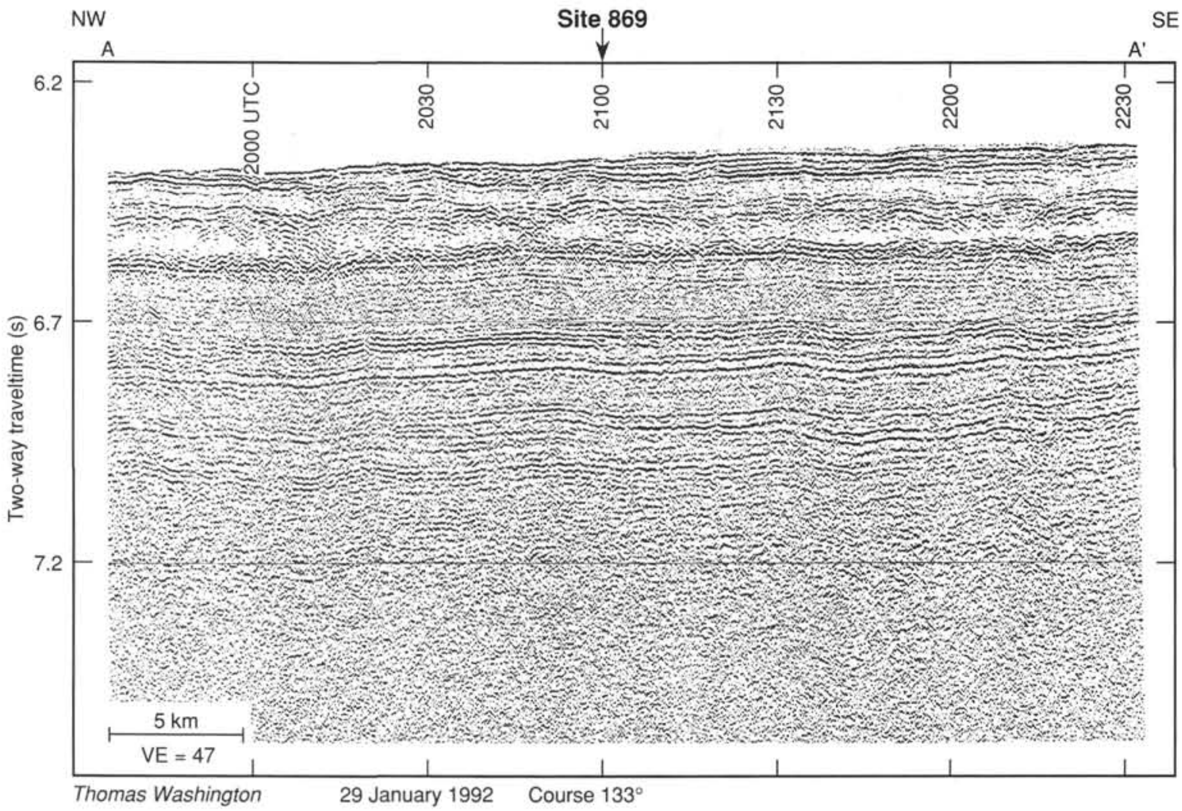

Figure 6. Seismic reflection profile across Site 869, shot with an 80-in.^{3} water-gun source. Time is shown on the horizontal axis; two-way traveltime on the vertical axis. Data were acquired by the *Thomas Washington* of Scripps Institution of Oceanography during Cruise TUNE08WT. Location shown in Figure 5.

the uppermost Oligocene and lowermost Miocene, is taken to define the boundary between the two subunits.

Nannofossil ooze is the dominant lithology throughout Section 143-869A-4H-3 to Core 143-869A-9H. The discordant bedding that is so characteristic of the upper three cores is also manifest in Sections 143-869A-5H-3, -7H-2, and -6H-6 and is particularly striking in Section 143-869A-8H-2, where sedimentary dips reach 90° and the strata show appreciable soft-sediment deformation.

Unit II

Interval 143-869A-10X-2, 97 cm, to Core 143-869A-18X
Depth: 88.2–166.5 mbsf
Age: late Eocene to middle Eocene

Core 143-869B-2R to Interval 143-869B-9R-1, 10 cm
Depth: 140.0–207.7 mbsf
Age: early Eocene to late Campanian–early Maastrichtian

As in Unit I, the dominant sedimentary theme of Unit II is one of cycles on various scales characterized by regular changes in color and composition. In Core 143-869A-10X, the first porcellanite appears; this is associated with clayey nannofossil ooze. Porcellanites and cherts appear intermittently at first, but increase in percentage downhole until they constitute the dominant recovered lithology. Also included in this section are Cores 143-869B-2R to -9R, whose recovered lithology is dominated by porcellanite and chert, colored various shades of brown, locally containing radiolarians, and accompanied in some places by nannofossil limestone.

Well-preserved trace fossils are a feature of Section 143-869A-12X-2: recognizable forms include *Chondrites*, *Planolites*, *Teichichnus*, and *Zoophycos* (Figs. 13 and 14; cf. Warme et al., 1973), and the burrow systems are superimposed upon and interpenetrate one another. Very similar tiering of trace-fossil assemblages has been described from modern deep-sea environments by Wetzel (1991). This section also contains several millimeter- to centimeter-thick levels of graded radiolarian sand that exhibit sharp contacts with the enveloping clayey radiolarian ooze. Radiolarian ooze, colored in various shades of yellowish-brown, becomes a progressively more important sediment type in Cores 143-869A-12X through -15X, where it contains subsidiary and variable amounts of clay and nannofossils. Those levels containing abundant nannofossils in Core 143-869A-15X are chalky in texture. In Cores 143-869A-16X and -17X, only very dark gray or brown chert, showing conchoidal fracture and vitreous luster, was recovered.

Unit III

Interval 143-869B-9R-1, 10 cm, to Core 143-869B-69R
Depth: 207.7–796.2 mbsf
Age: early Maastrichtian/late Campanian to late–middle Cenomanian

Unit III is characterized by the presence of repeated sequences of gray to green volcaniclastic sandstones and breccias intercalated between lighter-colored nannofossil and radiolarian claystones. In Subunit IIIA, the intercalated claystones are generally grayish-green and zeolitic; in Subunit IIIB, they are grayish brown to dark reddish brown, radiolarian-rich and the redeposited component is less significant; in Subunit IIIC, sedimentary colors return to greenish gray and olive gray. Subunit IIID is characterized by thick (meter-scale) beds of green volcaniclastic breccia containing clasts of basalt interbedded with thinner (tens of centimeters-scale) volcaniclastic sandstone. Subunit IIIE is characterized by the presence of volcaniclastic sandstones and interbedded reddish radiolarian claystone and nannofossil

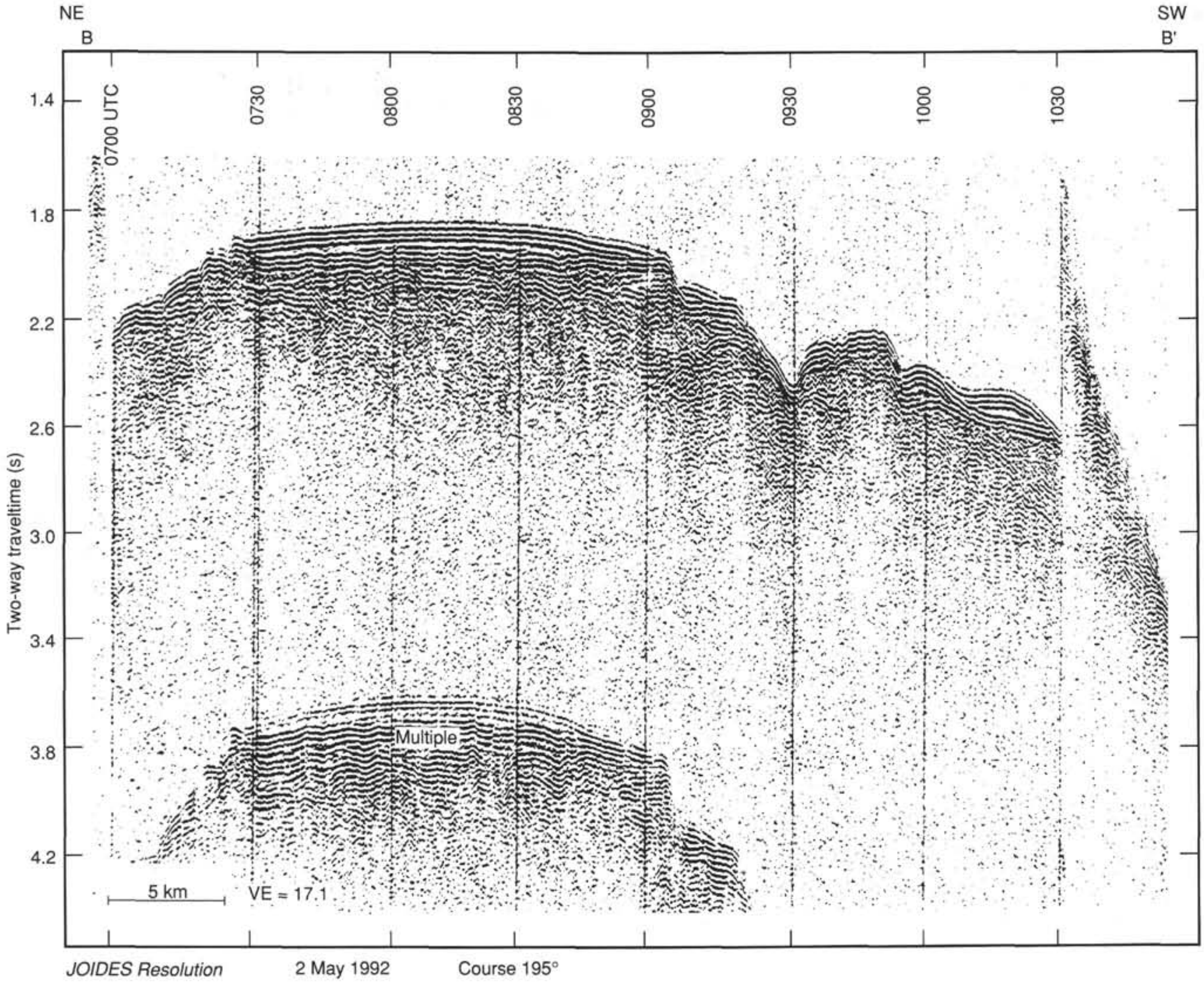

Figure 7. Seismic reflection profile over Wodejebato Guyot, shot with a 200-in.^{3} water gun. Time is shown on the horizontal axis; two-way traveltime on the vertical axis. Data were acquired by the *JOIDES Resolution* on approach to Site 869. Location shown in Figure 5.

chalk with minor intervals of breccia. Subunit IIIE is separated from Subunit IIIF at the contact by one such level of breccia with an underlying volcaniclastic siltstone. Subunit IIIF essentially consists of dark greenish gray volcaniclastic sandstones to siltstones, varying in structure from massive to graded and parallel laminated, and interbedded with calcareous claystones. Subunit IIIG contains thin-bedded volcaniclastic sandstone, siltstone and claystone interbedded with nannofossil limestone and radiolarian siltstone. The base of this subunit was not reached. A summary of the lithology is given in Figure 15.

Subunit IIIA

Interval 143-869B-9R-1, 10 cm, to Core 143-869B-26R
Depth: 207.7–381.5 mbsf
Age: early Maastrichtian/late Campanian to early Campanian

Subunit IIIA comprises a series of volcaniclastic sediments intercalated between claystones of brownish gray to light brown color (typical of Cores 143-869B-10R to -19R) and gray to greenish gray color (typical of Cores 143-869B-20R to -26R) that are variably rich in nannofossils. In one particularly calcareous level in Interval 143-869B-11R-3, 22–24 cm, a well-preserved specimen of *Inoceramus* is present. This bivalve is a not uncommon constituent of Upper Cretaceous deep-sea drilling cores from all major ocean basins. The claystones are locally burrowed, and in Section 143-869B-20R-1, contain burrows attributed to *Planolites* and vertical traces similar to *Skolithos*; in other levels, they reveal a faint millimeter lamination. Claystones in Cores 143-869B-10R through -19R are more calcareous than those in Cores 143-869A-20R to -26R.

The volcaniclastic sandstones are typically colored gray through dark gray through greenish-black to black. Typically, they have a sharp base, are locally scoured and graded and show a variety of sedimentary structures, such as massive units, pervasive parallel lamination and minor cross-lamination (Fig. 16). Most of the grains are sand grade; some basal units extend up to granule size. The organization and bedding patterns of these redeposited units are illustrated and discussed in more detail below.

In terms of composition the basaltic parentage of the grains is obvious: they comprise zeolites, clinopyroxene, opaque oxides, palagonite, feldspars, epidote, chlorite, and opaques. A significant feature is the presence of associated shallow-water material in the cores of this subunit, typically being concentrated in the coarser basal layers of the graded units. Such material is particularly noticeable in Sections 143-869B-11R-1 and -2, of early Maastrichtian–late Campanian age, where it includes bivalve, echinoid, and red-algal fragments, "orbitoid

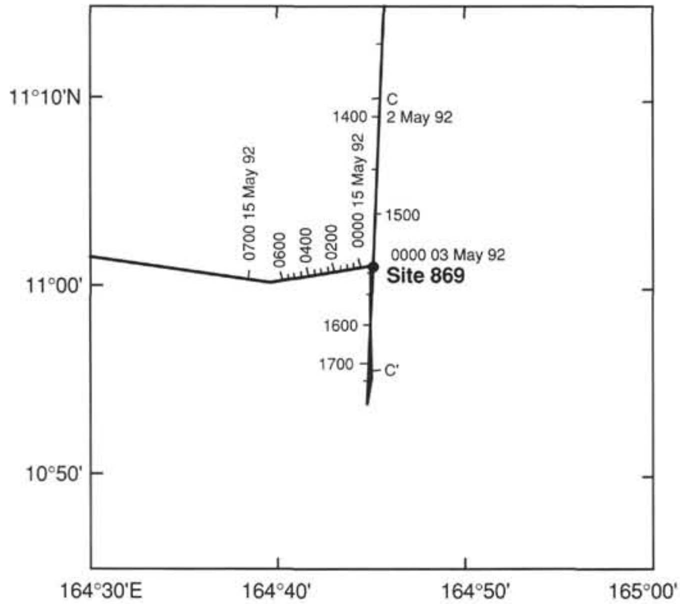

Figure 8. *JOIDES Resolution* track chart for the vicinity of Site 869. C-C′ denotes the ends of seismic reflection profile in Figure 9.

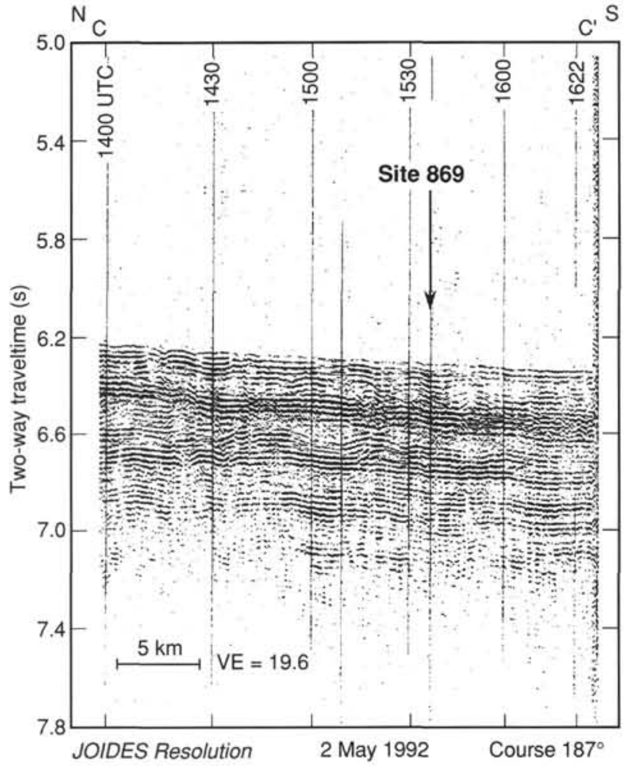

Figure 9. Seismic reflection profile over Site 869, shot with a 200-in.^{3} water gun. Time is shown on the horizontal axis; two-way traveltime on the vertical axis. Data were acquired by the *JOIDES Resolution* on approach to Site 869. Location shown in Figures 5 and 8.

foraminifers," "micritic ooids," and glauconite. Other specific examples include Interval 143-869B-22R-3, 26–27 cm, which contains much recrystallized skeletal calcite and angular fragments of pelletal grainstone, and Interval 143-869B-25R-1, 40–50 cm, the basal fraction of a graded layer of early Campanian age, which yields benthic foraminifers, possible recrystallized red algae, bivalve fragments, and concentrically laminated micritic ooids. Scattered benthic foraminifers and fragments of macrofossil skeletal calcite also occur within more finer-grained volcaniclastic siltstones, as in Interval 143-869B-26R-1, 34–36 cm.

Subunit IIIB

Cores 143-869B-27R to -34R
Depth: 381.5–458.8 mbsf
Age: early Campanian to middle/late Turonian

This subunit is dominantly composed of radiolarian claystone to siltstone, grayish-brown to dark reddish-brown in color, locally calcareous and zeolitic. The dominant zeolite is clinoptilolite, according to shipboard XRD data. Redeposited volcaniclastic material occurs only in millimeter-thick laminae in Cores 143-869B-27R through -30R. In Cores 143-869B-31R through -33R and the upper part of Core 143-869B-34R, the graded greenish-black volcaniclastic sandstones characteristic of Subunit IIIA have been intercalated between the radiolarian-rich strata. Convolute bedding can be seen in Interval 143-869B-34R-1, 132–135 cm, in the upper part of a graded volcaniclastic layer (Fig. 17). Radiolarian concentration is variable; the microfossils may be distributed throughout the groundmass or concentrated in millimeter-scale beds. Laminations occur in this pelagic facies where it has been intercalated between redeposited beds; elsewhere, it may be bioturbated. Shallow-water material, such as micritic ooids and peloids, is present in the redeposited units. Chert occurs in radiolarian siltstone in Core 143-869B-30R. The contact with the underlying subunit is gradational.

Subunit IIIC

Core 143-869B-35R to Interval 143-869B-38R-1, 6 cm
Depth: 458.8–487.8 mbsf
Age: middle/late Turonian to late Cenomanian

Subunit IIIC is essentially similar to Subunit IIIA in that it consists of graded gray to greenish-gray volcaniclastic sandstones to siltstones interbedded with finer-grained calcareous levels, zeolitic (clinoptilolite), and locally contains radiolarians. Some chert and minor silicified claystone is seen. Grain-types recognized include feldspar, clinopyroxene, chlorite, opaques, and zeolites. Shallow-water grains accompany these igneous components in some of the graded beds: in Interval 143-869B-34R-1, 142–144 cm, a wealth of bioclastic detritus with micritic ooids was observed; Interval 143-869B-35R-1, 44–46 cm, contains abundant micritic ooids and large benthic foraminifers; Section 143-869B-36R-1 yielded large foraminifers (orbitolinids), echinoids, gastropods, and ooids. An interesting feature of this subunit can be observed in the gamma-ray log, namely a positive excursion at the level of Core 143-869B-37R, close to the Cenomanian/Turonian boundary. On the other hand, the geochemical log shows that this interval has been enriched in potassium, but not in uranium. This suggests ashy, rather than organic-rich, beds.

Subunit IIID

Interval 143-869B-38R-1, 6 cm, to Section 143-869B-42R-CC
Depth: 487.8–536.1 mbsf
Age: late Cenomanian

Subunit IIID is characterized by the presence of green volcaniclastic breccias, the clasts of which may be rodlike to equant in shape, angular to subrounded, and range in size up to 80 mm. Most of the large clasts are subrounded (e.g., clasts in Intervals 143-869B-41R-4, 69–76 cm, and -42R-2, 87–92 cm), and the elongated fragments tend to be horizontal in orientation. Another interesting feature of these clasts is that their lower side is characteristically rimmed (~0.1–1 mm) with white zeolite. Zeolites also fill a few thin (0.1–2 mm) fractures that cut the volcaniclastic breccia in some places

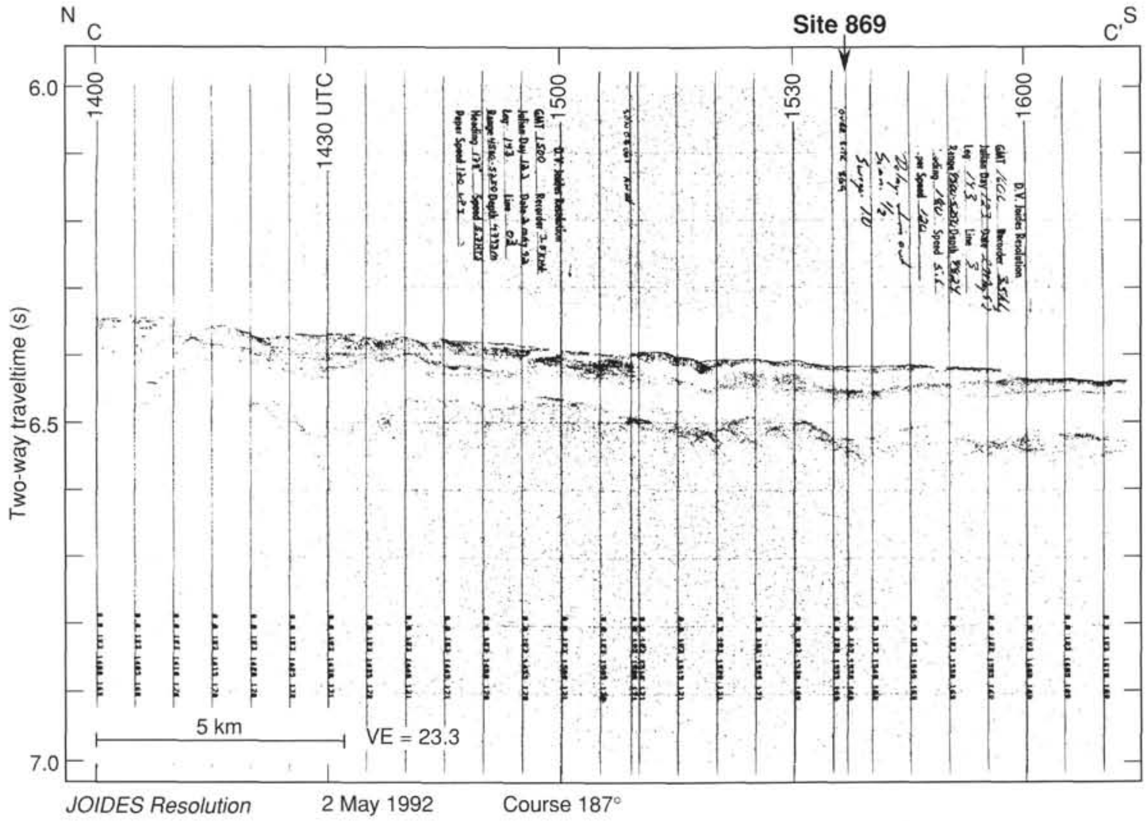

Figure 10. 3.5-kHz echo-sounder profile over Site 869. Time is shown on the horizontal axis; two-way traveltime on the vertical axis. Data were acquired by the *JOIDES Resolution* on approach to Site 869. Location shown in Figures 5 and 8.

(Fig. 18). The dominant zeolite-group mineral (identified by XRD) is analcite, which is accompanied locally by trace quantities of phillipsite and thomsonite.

The clasts are generally polymictic, although almost all the large (>1 cm) ones are basaltic. The dominant type is bluish-gray, aphyric to sparsely phyric, slightly to moderately altered pyroxene or plagioclase-pyroxene-olivine basalt. Generally, the phenocrysts are no more than 2 mm in size and are set in a groundmass of quenched plagioclase, dust of opaque oxides, and interstitial glass, with the latter altered to calcite and clay minerals, including chlorite. Plagioclase phenocrysts occur as anhedral to subhedral stubby laths that range from fresh to moderately altered; pyroxene phenocrysts are anhedral to subhedral grains that are slightly to moderately altered. Olivine occurs as anhedral to euhedral prisms that are completely pseudomorphed by clays with minor calcite; a trace of pyrite (<0.1 mm) was also observed in some olivine pseudomorphs in Core 143-869B-43R. This type of basalt is generally nonvesicular; if vesicles are present, they are not abundant (<2%), are generally small (<1 mm), subrounded, and filled with whitish zeolite, brown smectitic clay minerals, and traces of calcite.

A few of the basalt clasts are reddish in color. This type is generally vesicular, with vesicles locally constituting up to 30% of the rock (e.g., clast in Interval 143-869B-41R-5, 66–72 cm) and containing whitish zeolite and minor calcite. Texturally, the second type is more phyric than the first, although it ranges from aphyric to moderately phyric pyroxene or plagioclase-pyroxene basalt; it is generally more altered than the first type.

The smaller clasts (~1 cm and smaller) include (1) fragments of igneous rocks of varied textures in shades of gray and brown, (2) palagonitized glass shards that locally have concentric layers and/or are vesicular and generally contain tiny (<0.1 mm), fresh plagioclase inclusions, and (3) anhedral, broken portions or subhedral, complete prisms of pyroxene megacrysts. Not surprisingly, these clasts are more altered and more angular than the large clasts. They are randomly distributed throughout the matrix, although a few pockets seem to have more glass shards than others.

Subunit IIIE

Core 143-869B-43R to Interval 143-869B-55R-2, 26 cm
Depth: 536.1–653.3 mbsf
Age: middle to late Cenomanian

Subunit IIIE comprises dark green volcaniclastic sandstone with interbedded reddish-brown radiolarian claystone, locally silicified, and clayey nannofossil chalk. The claystones are generally laminated but bioturbated levels do occur. The sandstones consist of altered glass and basaltic fragments, are locally graded, commonly parallel-laminated, more rarely cross-laminated. Water-escape structures are present in Core 143-869B-51R (Fig. 19). In Sections 143-869B-45R-3 and -4, inverse grading occurs and the sandstones contain millimeter-scale clasts; bedding contacts lie between 10° and 45° to the horizontal. A significant feature of Interval 143-869B-44R-4, 91–93 cm, found in thin section, is the presence of a concentrically laminated micritic ooid having a trace of radial structure in its outer cortex that may be part of a derived limestone clast. Section 143-869B-45R-4 contains very sparse carbonate grains, including one recognizable echinoderm fragment in Interval 143-869B-45R-4, 103 cm. Interval 143-869B-49R-1, 28–30 cm, within volcaniclastic sandstone, yielded a gastropod and an orbitolinid foraminifer (see "Biostratigraphy" section, this chapter). A piece of bivalve shell is present in Interval 143-869B-54R-3, 25 cm. Inclined contacts between lithologies are found in Interval 143-869B-50R-1, 107–111 cm (35°), and -52R-4, 142–145 cm (27°).

Other features of note include imbrication of larger mudstone clasts within the sandstone (Fig. 20); and coalified woody fragments in Interval 143-869B-51R-4, 25–40 cm. Also present in this subunit

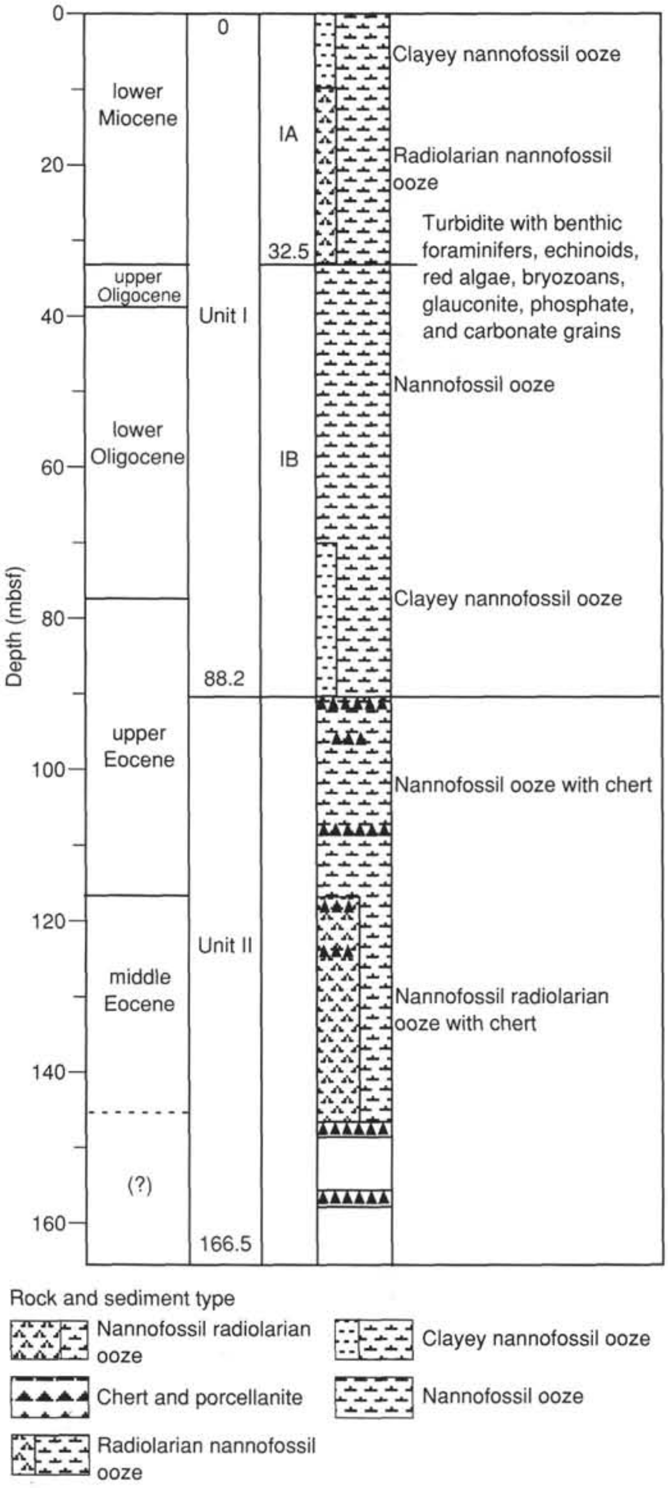

Figure 11. Stratigraphic column for Hole 869A.

are a number of intercalations of volcanic breccia, the most important of which is a thick dark greenish gray to greenish black level that occurs from Section 143-869B-54R-1 to Interval 143-869B-55R-2 at 26 cm, and the base of which is taken to define the lower boundary of the subunit. The clasts in this unit are subrounded to subangular, graded, and of centimeter scale; locally, they carry zeolite rims and in some places, the precipitate becomes a major pore-filling cement (Fig. 21). The zeolites have been identified as analcite and chabazite by XRD. The fabric of the rock varies from clast- to matrix-supported. Other breccias are finer-grained, being dominantly composed of granule- to fine pebble-sized clasts.

Subunit IIIF

Intervals 143-869B-55R-2, 26 cm, to -68R-3, 79 cm
Depth: 653.3–780.7 mbsf
Age: middle to late Cenomanian

Subunit IIIF is composed primarily of dark greenish-gray to greenish black volcaniclastic sandstones and siltstones with scattered discrete levels of lighter-colored nannofossil-rich siltstone to limestone and some radiolarian-rich layers. The igneous grains are largely constituted by yellowish volcanic glass, variably palagonitized with pronounced brown rims where alteration has been maximized, together with fresh clinopyroxene, aphyric to moderately phyric basaltic clasts, and rare plagioclase. The glasses range from aphyric to vitriphyric with subhedral to euhedral, slightly altered clinopyroxene as the dominant phenocrystic phase; alteration to smectite is commonplace.

A wide range of sedimentary structures, such as grading, wavy, cross- and parallel-lamination is present, but significant intervals of both the sandstones and siltstones are essentially structureless. In terms of thickness, the stratigraphically lowest beds are only a few centimeters thick, whereas the higher graded units are typically on a scale of meters or a little less, and some of them have erosional bases. A number of divisions of the Bouma Sequence are clearly identifiable throughout the subunit; and a sole mark is recognizable in Interval 143-869B-64R-3, 86 cm. Soft-sediment deformation is present in Interval 143-869B-63R-3, 17–34 cm. Evidence for bioturbation, including escape burrows, can be found, but is uncommon.

Radiolarians occur intermittently throughout the subunit (locally filled by zeolites or green smectite), but also are concentrated in interturbidite siltstones, commonly as millimeter-thick layers, as for example in Intervals 143-869B-67R-1, 91 cm; -67R-5, 91 cm; -67R-5, 99 cm; and -67R-6, 61 cm.

Subunit IIIG

Interval 143-869B-68R-3, 80 cm, to Core 143-869B-69R
Depth: 780.7–796.2 mbsf
Age: middle–late Cenomanian

This subunit mainly consists of greenish-gray, fine-grained volcaniclastic sandstones and siltstones showing parallel-and cross-lamination and alternating with zeolitic claystones on a scale of tens of centimeters. Interval 143-869B-68R-4, 25–76 cm, contains faintly laminated, light greenish-gray clayey nannofossil limestone, brownish-gray claystone, and chert. The interval has been disturbed by drilling, so that the interrelation of these lithologies could not be established. Interval 143-869B-68R-5, 58–67 cm, is radiolarian-rich limestone displaying millimeter-thick parallel laminations (Fig. 22). Oblique bedding, soft-sediment deformation, and locally brecciated siltstone layers are common in Sections 143-869B-68R-4 and -5. The base of this subunit was not reached.

Interpretation of Sedimentary Environments

Deposition of Unit III began, in mid- to late Cenomanian time, with deposition of dark-colored volcaniclastic sandstones to siltstones set against a background pelagic sedimentation of nannofossils and radiolarians (Subunits IIIF and IIIG). The sedimentary structures in the volcaniclastics indicate deposition by turbidity currents. No evidence was found of any contribution of shallow-water material to the sediment, which is in contrast to the situation higher in the sequence.

Subunit IIIE was characterized by the deposition of volcaniclastic sandstones and breccias, which interrupted the background sedimentation of clay, radiolarians, and nannofossil ooze. Repeated influxes

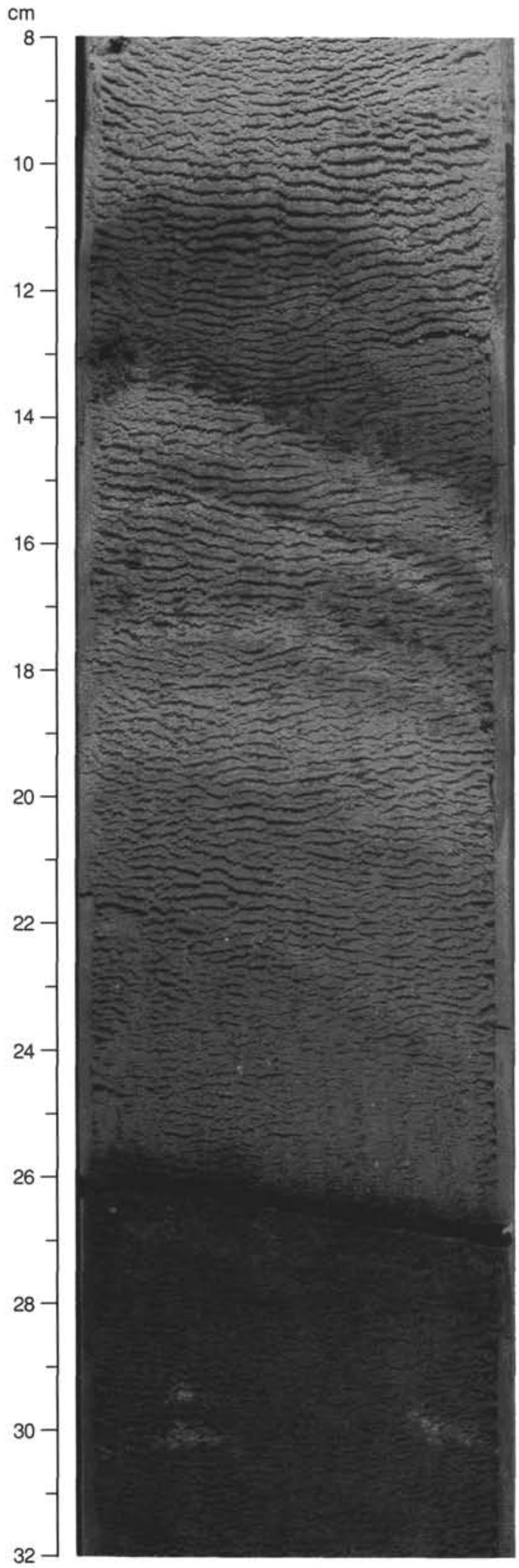

Figure 12. Centimeter-scale color banding caused by varying ratios of nannofossils vs. radiolarians. Radiolarian-rich ooze is darker. Note inclination of layers toward the right of photograph (Interval 143-869A-3H-6, 8–32 cm; age, early Miocene).

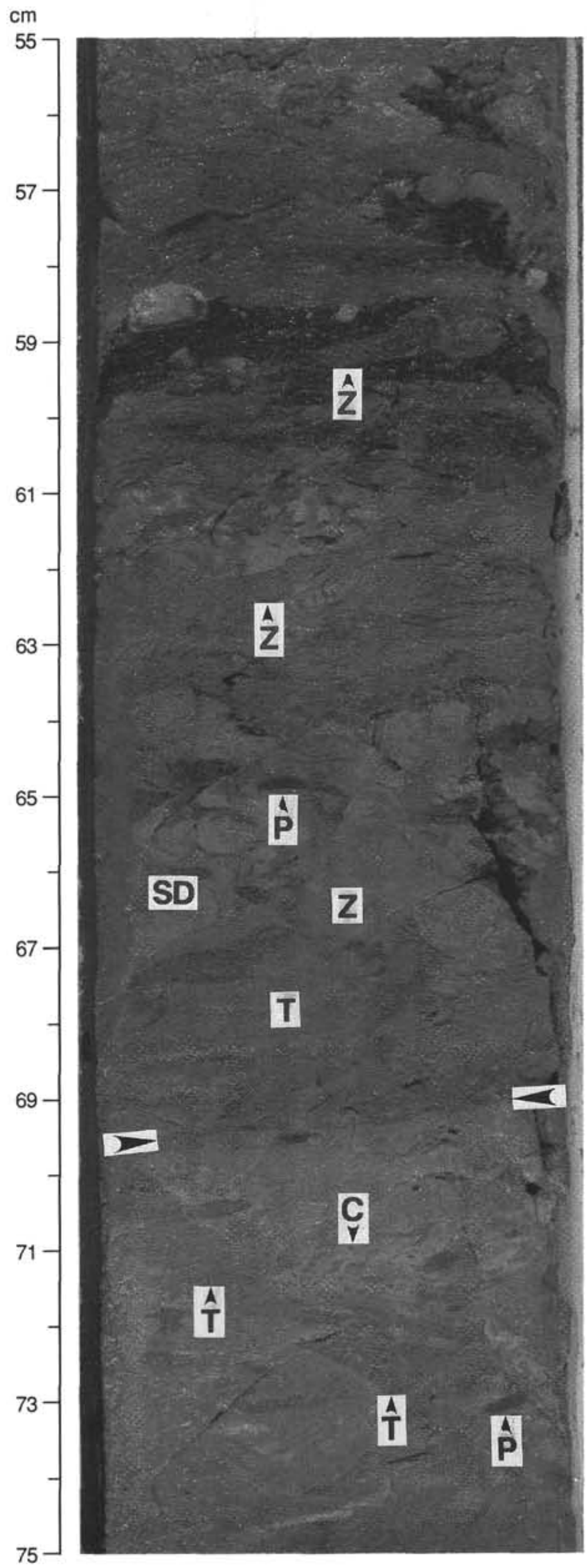

Figure 13. Mixing of lighter radiolarian-nannofossil and darker nannofossil-radiolarian oozes resulting from intense bioturbation. Recognizable trace fossils include *Teichichnus* (T), *Zoophycos* (Z), *Planolites* (P), and *Chondrites* (C). Some synsedimentary soft-sediment deformation occurs locally (SD). A sharp contact (arrows) between muddy sediment below and sandy sediment above indicates the base of a graded radiolarian layer (Interval 143-869A-12X-2, 55–75 cm; age, late Eocene).

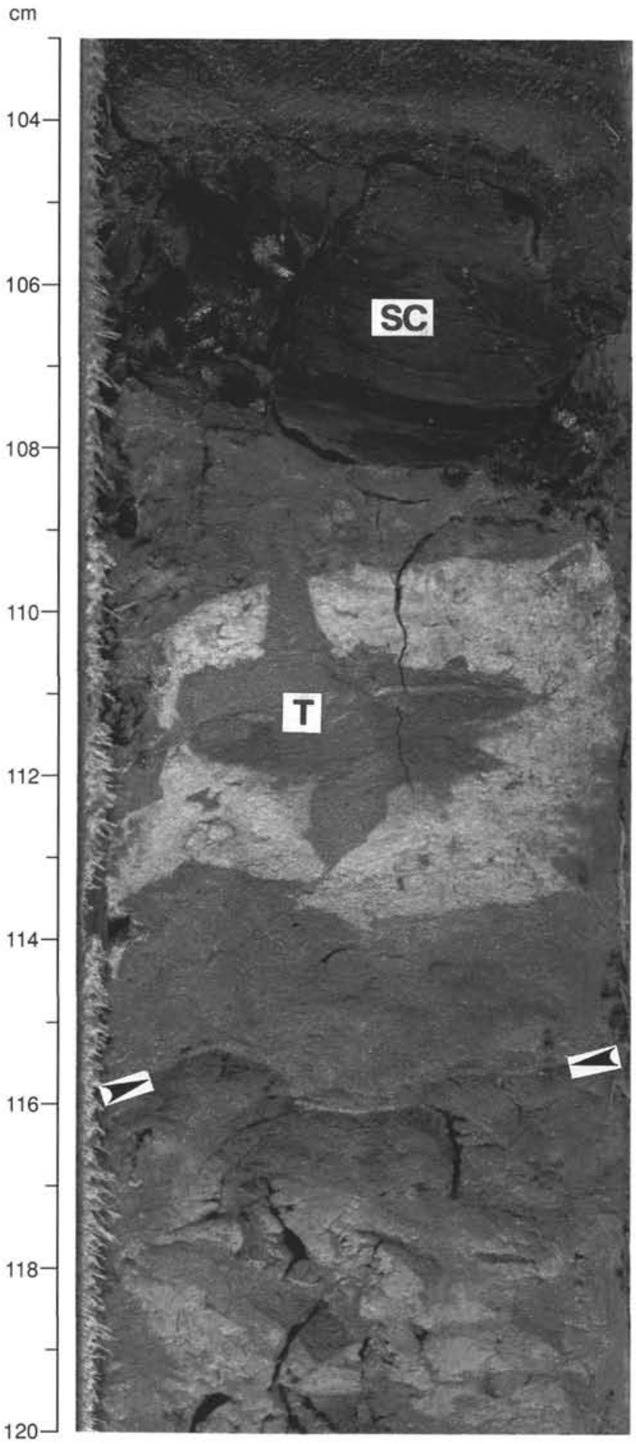

Figure 14. Large *Teichichnus* burrow (T) cutting through white nannofossil ooze. A sharp contact (arrows) between darker, muddy sediment below and lighter, sandy sediment above identifies the base of a graded radiolarian interval. Silicified claystone (SC) forms a hard layer. Deformation is caused mostly by drilling disturbance, but may also be partly from burrowing and synsedimentary differential compaction (Interval 143-869A-12X-2, 103–120 cm; age, late Eocene).

of turbidity currents carried basaltic sand to the site. Large clasts were probably transported by debris flows, but the absence of a clay matrix in many deposits suggests frequent transport by grain flow. The inclined sedimentary contacts in Cores 143-869B-50R and -52R suggest soft-sediment deformation on a sloping seafloor. Some shallow-water material, such as orbitolinid foraminifers, derived ooids, or oolitic limestone and, more specifically, the coalified woody fragments, indicate the presence of one or several emergent volcanic islands that acted as a sediment source.

Subsequently, during late Cenomanian time, came the deposition of coarse, poorly sorted basaltic breccias comprising multiple units of amalgamated graded beds (Subunit IIID). Deposition as debris and grain flows is suggested by these and other sedimentary features, such as locally observed inverse grading. Most of the large clasts were probably derived from nearby lavas that were erupted/intruded at considerable water depth because these are generally fine-grained and aphyric. Sheet lava flows or thin intrusive sills or dikes, which generally cool rapidly, are the most likely source. Certainly the dominance of abundant glass shards implies that some of the basalt was erupted underwater. The phenocryst assemblage suggests that these are most probably only mildly alkalic or intraplate tholeiitic in composition and are not highly alkalic. The smaller clasts, deriving perhaps from more distant regions, are more varied in texture and composition, and the presence of free-floating pyroxene crystals suggests a source of highly pyroxene-rich megaphyric basalt. The bivalve fragment in Interval 143-869B-54R-3, 26 cm, and the very sparse carbonate grains in Section 143-869B-45R-4, including a recognizable echinoderm fragment, could suggest, albeit equivocally, that distal modest-depth environments may have existed in the region. Generally, however, such material was not supplied or was overwhelmingly diluted by volcaniclastic detritus.

The subrounded form of the basaltic clasts indicates transport paths of considerable distance. Diagenesis of this material involved devitrification of glass shards and their replacement by zeolite as well as precipitation of zeolitic cement in available pore space; shelter pores under the larger clasts were an important site for such cement.

A change in the pattern of sedimentation followed, with the deposition of Subunit IIIC occurring around the time marked by the Cenomanian/Turonian boundary. Coarse centimeter-scale debris was no longer deposited at the site, and the pattern of sedimentation switched to that typical of turbidites with the emplacement of sand- and silt-grade material (Fig. 15). This change from proximal to distal facies can be interpreted in terms of the Cenomanian-Turonian rise in sea level commonly viewed as eustatic (e.g., Hancock and Kauffman, 1979; Schlanger, 1986), which partially flooded the source terrain. Alternatively, volcanism may have waned or ceased in the region supplying detritus. Sources for the igneous material presumably lay in shallow water, given the presence of shallow-water carbonate debris in the graded volcaniclastics. The shallow-water material indicates a normal-marine source area and may have derived from an off-bank environment; it is notable, for example, that the ooids are concentrically laminated and micritic and resemble the pelagic "ooids" described from a number of "deeper-water" environments in the Tethyan-Atlantic and Pacific Mesozoic (Jenkyns, 1972; Schlager, 1980; Haggerty and Premoli Silva, 1986). Nannofossils, planktonic foraminifers, and radiolarians were being supplied as a background sediment during this period and were diagenetically altered to produce calcareous siltstones and chert.

During the deposition of Subunit IIIB, the background sedimentation consisted of brown and reddish-brown radiolarian claystone and siltstone. Initially, the supply of volcaniclastic material was maintained, while later, the influx of material waned or was directed elsewhere, with a consequent increase in the proportion of the pelagic component deposited. However, with the deposition of Subunit IIIA, deposition of sand-grade volcaniclastics recommenced with the development of typical turbidites.

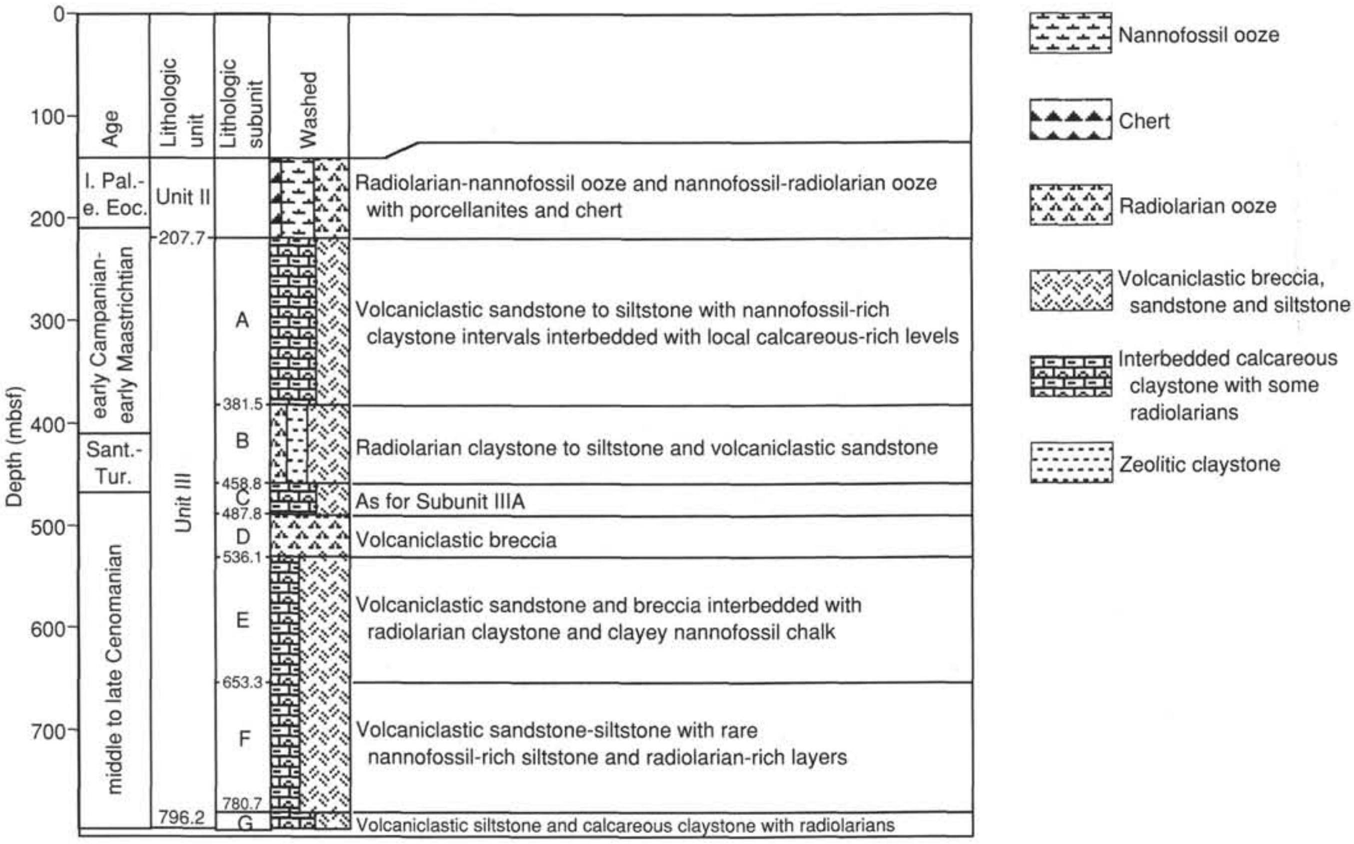

Figure 15. Stratigraphic column for Hole 869B.

The sedimentary evolution of Unit III can be explained in terms of the classical models proposed for siliciclastic submarine fan systems (e.g., Normark, 1970; Mutti and Ricci Lucchi, 1972; see also Pickering et al., 1989). Figure 23 shows the observed turbidite sequences and grain debris-flow deposits in Unit III. Figure 24 is a compilation of features, such as predominance of turbidite intervals, according to the Bouma classification, maximum thicknesses of mass flows, maximum organic carbon contents, and influx of shallow-water carbonate grains. In this figure, we also attempt an interpretation of the depositional environments.

Subunit IIIG displays thin, fine-grained turbidites that are dominated by the Td interval and that also contain Tc-Td couplets. This suggests a depositional environment on the outer fan. Local scouring and deposition of Ta intervals, as well as soft-sediment deformation and inclined bedding, indicate that at times fan lobes prograded rapidly toward the basin. Nannofossil limestone, radiolarian siltstone, and chert in Core 143-869B-68R represent distal facies that were deposited during a rise in relative sea level, or during a period of volcanic quiescence.

The change to Subunit IIIF is very abrupt (Figs. 23 and 24). Thick turbidite sequences with well-developed Ta intervals, which fine upward into Tc–Td couplets, suggest channel fills on the middle fan. Sediment supply was high and distances of transport fairly long, which resulted in relatively fine-grained and well-sorted textures. Local levels of larger clasts imply rip-up from channel floors.

Subunit IIIE shows an evolution toward more proximal conditions: grain flows transporting pebble-sized clasts prograded over the finer sandstones and siltstones of Subunit IIIF (Fig. 25). Again, fining-upward sequences are well developed (Fig. 26), pointing to channel fills in an inner-fan depositional setting. The top of this subunit, however, indicates a shift to more distal conditions (Fig. 24).

The thick, meter-scale beds of volcaniclastic breccias and sandstones of Subunit IIID again indicate a proximal setting, at a canyon outlet or in deep channels on the inner fan, if a point source was present, or over large distances at the base of the slope, if sediment aprons predominated. The general absence of a muddy matrix and the observed shelter pores under large clasts suggest transport by grain flow, whereby the sand-sized grains acted as a transporting agent for the larger fragments. In coarse material, packing was locally very loose, and pore space was rapidly filled by zeolitic cements (Fig. 21).

A very rapid change from deposition of proximal to distal facies occurred during the late Cenomanian: this is registered as a pronounced facies change in the top of Core 143-869B-38R, at the boundary between Subunits IIIC and IIID (Fig. 24). The relative abundance of couplets of thin, fine-grained Bouma divisions Tc and Td suggests deposition on the outer fan, whereas the return to slightly coarser facies in Core 143-869B-35R implies a minor progradation of the fan system. It is important to note that chert occurs in Cores 143-869B-37R and -35R, and that in Core 143-869B-35R the turbidites have been silicified.

The lower part of Subunit IIIB contains thin Tc and Td divisions of volcaniclastic sediment (Fig. 27), which suggests an outer-fan setting. The upper part of this subunit is dominated by pelagic material, such as red clay and radiolarians, which were found to have been reworked in a few of the thin turbidites. Volcaniclastic sediment has been confined to very thin turbiditic layers, suggesting deposition on the basin plain.

Passing up through Core 143-869B-26R, which shows an outer-fan facies association, the turbidites rapidly become coarser and thicker (Subunit IIIA). Complete Ta-Te turbidites occur commonly (Figs. 16 and 23). This subunit generally exhibits meter-scale sequences, beginning with densely stacked, fine-grained Tc-Td divi-

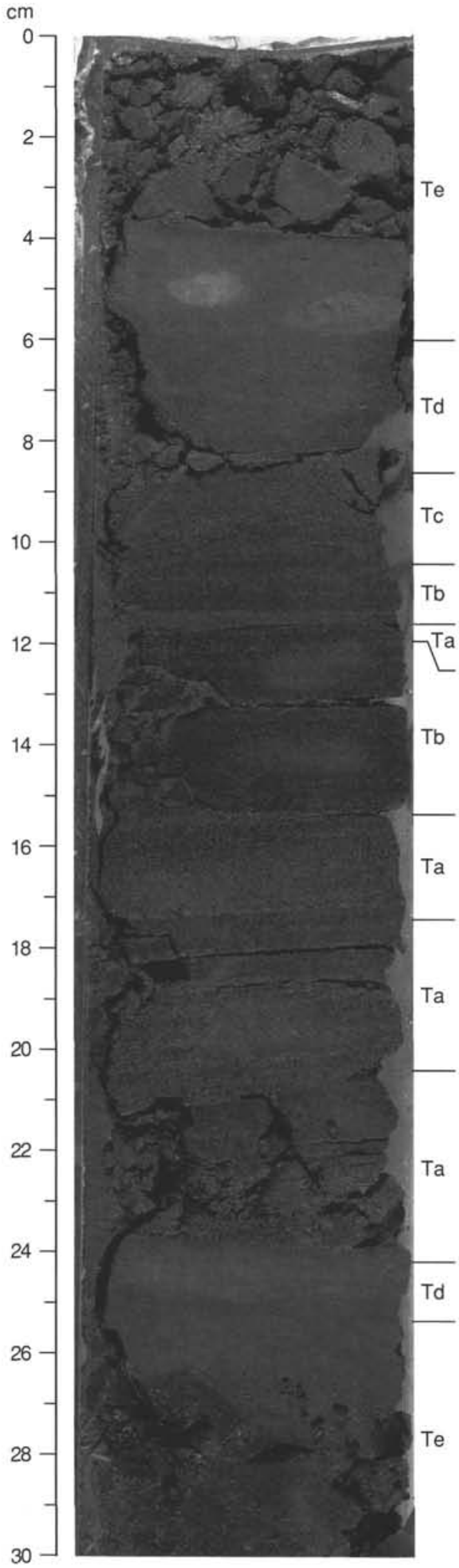

Figure 16. Complete Ta-Te intervals of turbidite in Subunit IIIA on top of amalgamated Ta and Ta-Tb successions. Note bioturbation in Te and partly in Td level (Interval 143-869B-23R-2, 0–30 cm).

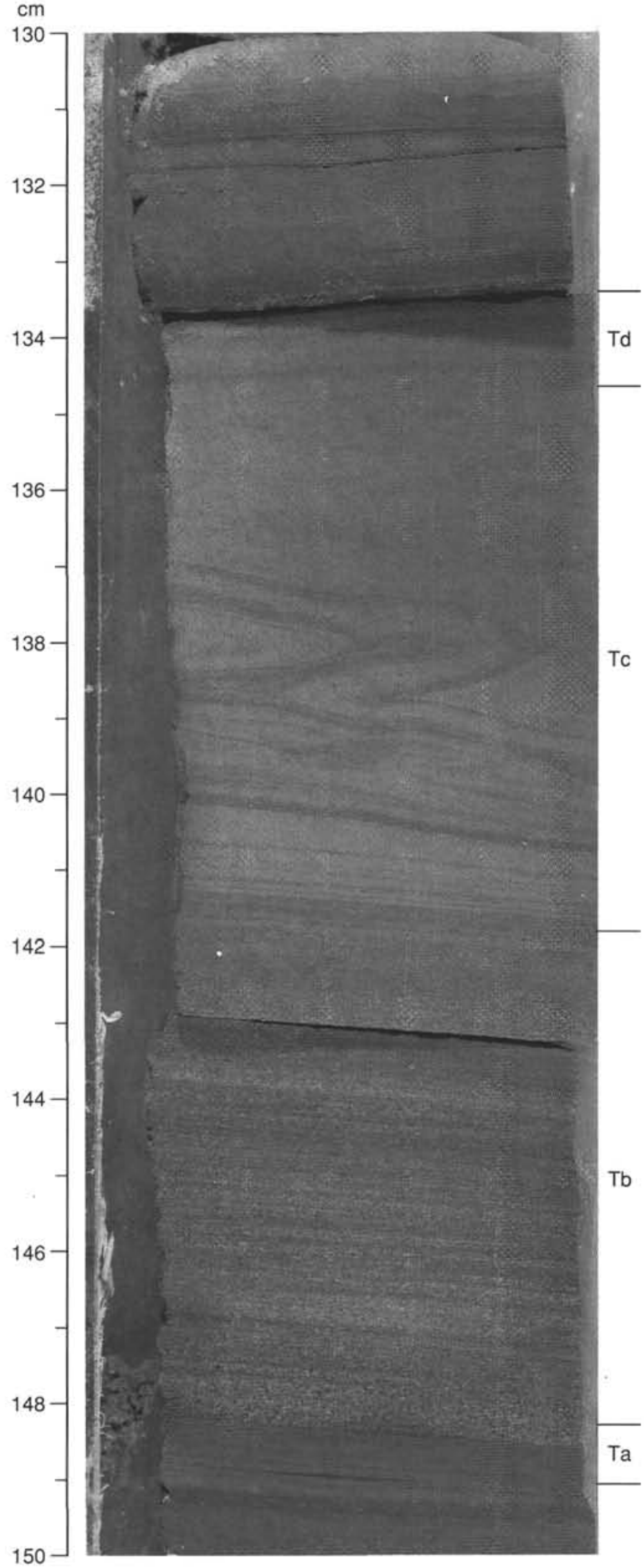

Figure 17. Turbidite in Subunit IIIB, showing well-developed convolute bedding (Interval 143-869B-34R-1, 130–150 cm).

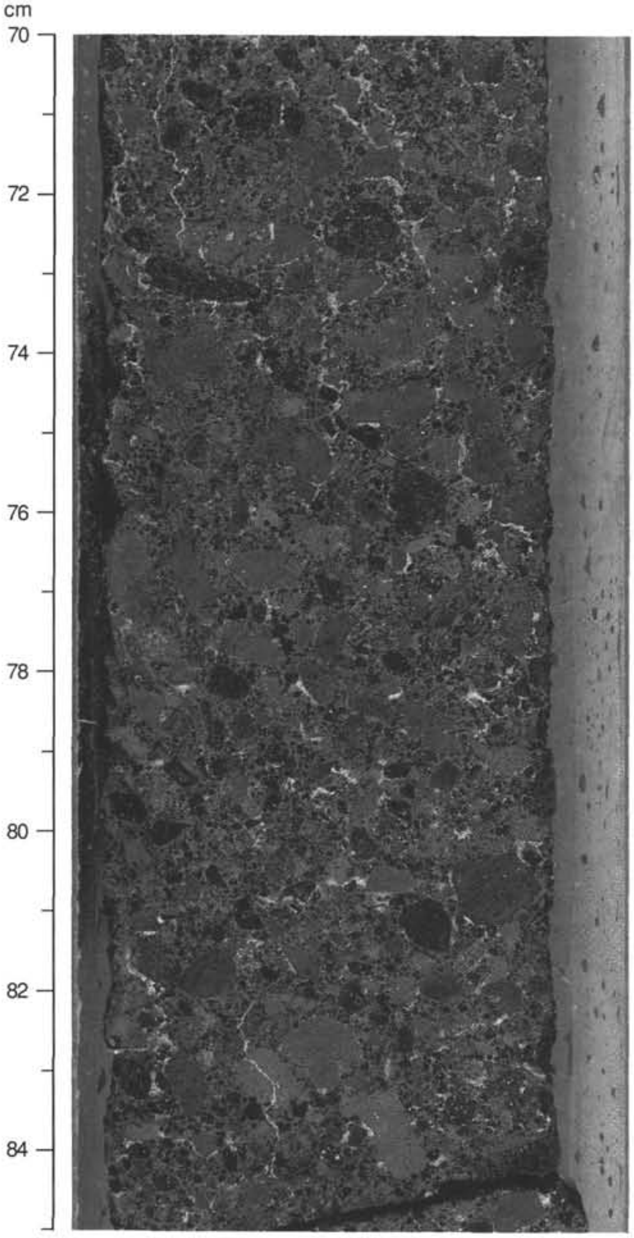

Figure 18. Volcaniclastic breccia (grain to debris-flow deposit) with fine, zeolite-filled fractures showing white on photograph (Interval 143-869B-54R-2, 70–85 cm).

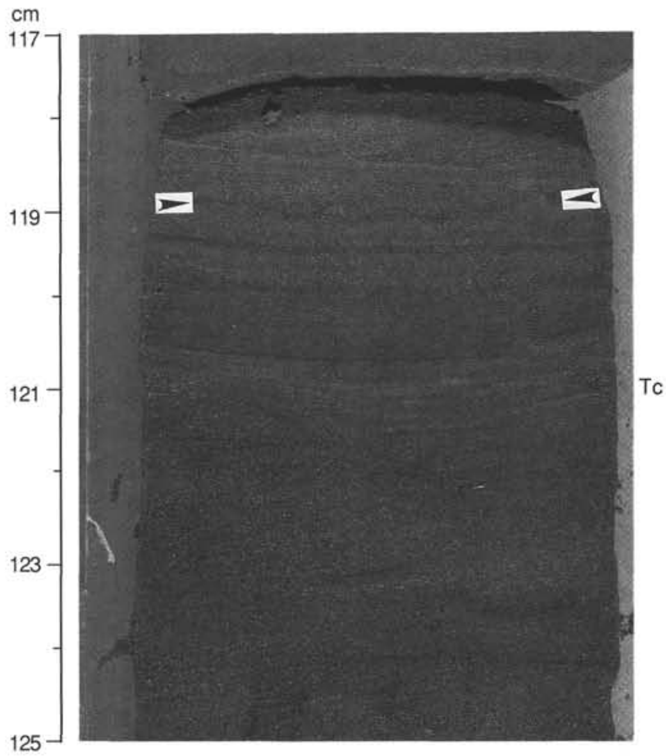

Figure 19. Water-escape structures (dish structures, arrows) in Tc interval of a turbidite in Subunit IIIE (Interval 143-869B-51R-2, 117–125 cm).

sions, which are abruptly overlain by a fining and thinning-upward turbidite succession. Bioturbated Te divisions become more important toward the top of these sequences (Fig. 28). Commonly, the bioturbation has mixed sediment from the Td and Te divisions (Fig. 29). The fine-grained basal part may correspond to overbank deposits, whereas the fining-upward succession can be interpreted as a channel fill (Mutti and Ricci Lucchi, 1972). These small-scale sequences are stacked in larger sequences, which show a thickening- and coarsening-upward trend (Figs. 23 and 24). Such a facies association is characteristic for the middle-fan depositional environment, where channelled lobes prograde because sediment was supplied at fairly rapid rates. Slumps occur locally and suggest the development of inner-fan complexes. Avulsion and channel switching are common in these settings. From the present information, one can not conclude whether the variations from more proximal to more distal facies observed in Subunit IIIA (Fig. 24) were the result of such autocyclic processes, of sea-level fluctuations, or of variations in sediment supply. The general trend, however, was from a more proximal to a more distal middle-fan environment.

The early Campanian–early Maastrichtian interval also saw a change in color of the accompanying claystones from the reddish-brown of Subunit IIIB to the greenish-gray of Subunit IIIA, which may reflect the increased volume of fine-grained igneous material therein, as well as indicate more rapid burial rates, preventing seafloor oxidation of iron compounds. Redeposition of shallow-water material from reef-fringed volcanic islands during Campanian–Maastrichtian time is a regional phenomenon across much of the central Pacific Ocean that affect the Line Islands and the Nauru Basin west of the Marshall Islands (Schlanger and Premoli Silva, 1981; Schlanger et al., 1981) and seems to have resulted from a final phase of volcanism in the area.

In many cases, the turbidites in Unit III containing redeposited shallow-water material occur in rather distal facies of the middle to outer fan (Fig. 24). This might suggest that either the shallow-water material was strongly diluted by rapid volcaniclastic sedimentation in a proximal setting, or that transport of carbonate particles from a shallow ramp or bank was only possible when relative sea level was high. The contents of total organic matter are generally very low in Unit III (see "Organic Geochemistry," this chapter). However, higher-than-average values seem to correlate with relatively distal facies, where sedimentation rates were low (Fig. 24).

Supply of volcaniclastic sediments to Site 869 ceased rather abruptly and, at the onset of Unit II time (early Eocene), deposition of radiolarian oozes became dominant. The sedimentary record of the early Eocene interval is largely represented by diagenetic equivalents of these oozes, namely porcellanites and cherts. Mid-Eocene sediments are dominated by remarkably pure radiolarian oozes. Their bioturbated intervals indicate periods of good oxygenation of the bottom waters and relatively high sedimentation rates (Wetzel, 1991).

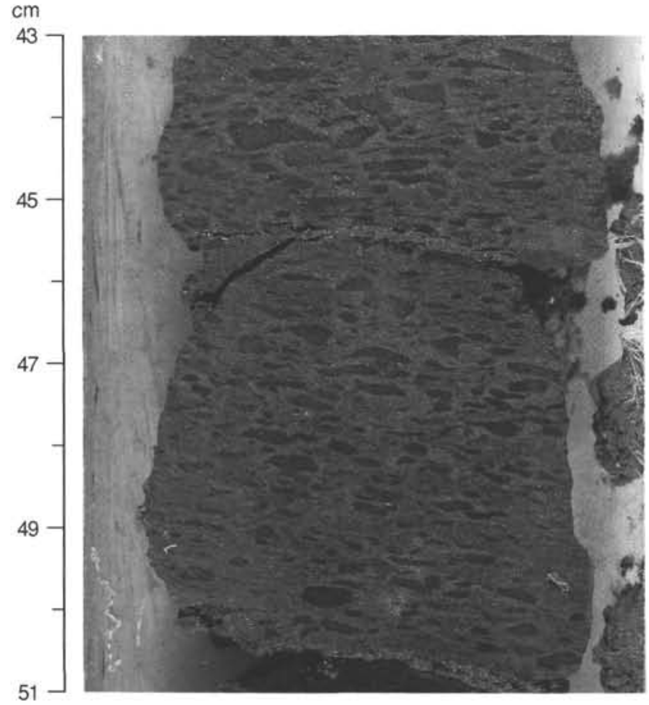

Figure 20. Flattened and slightly imbricated mud clasts in grain to debris-flow deposit of Subunit IIIE (Interval 143-869B-52R-4, 43–51 cm).

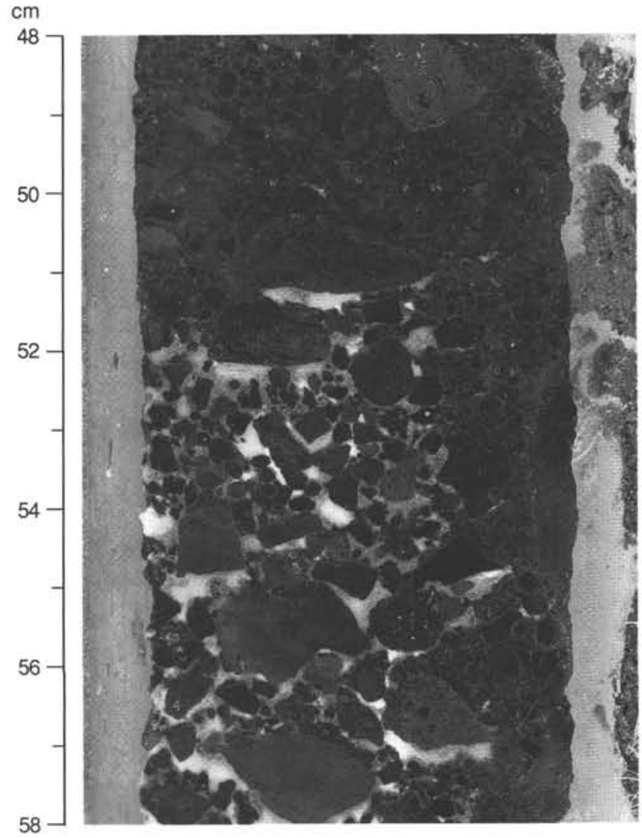

Figure 21. White zeolite cement fills large pores in loosely packed volcaniclastic breccia. Note shelter effect beneath larger clasts (Interval 143-869B-54R-4, 48–58 cm).

The overall change upsection from sediment dominated by radiolarians (Unit II) to that increasingly dominated by nannofossils (Unit I) can be interpreted in terms of changes in fertility of near-surface waters or in the level of the calcite compensation depth (CCD), or a combination of the two. The present-day equatorial Pacific Ocean is a zone of relatively high productivity, and radiolarian-rich sediments predominate in depths close to or below the CCD level (Lisitzin, 1971). It is likely that Site 869 lay under the equator during mid- to late Eocene time and received such sediments until northward passage of the Pacific Plate moved it into less fertile waters dominated by nannofossils (e.g., Berger and Winterer, 1974). Alternatively, the facies change may be viewed simply as a response to an early Oligocene decrease in the CCD from a mid- to late Eocene high: such changes are documented from a number of Pacific Ocean sites (van Andel, 1975). Superimposed on this general trend was a high-frequency variation in the nature of the sediment imposed by changes in the proportionality of nannofossils, radiolarians, and clay. Cycles of one type or another are known from virtually all pelagic sediments and are now conventionally attributed to orbitally induced climatic variation that controlled such factors as biogenic productivity, influx of eolian clay, deep-sea dissolution of carbonate, either singly or in combination (e.g., Fischer, 1986).

The presence of graded radiolarian oozes in Section 143-869A-12X-2 implies local downslope transport by turbidity currents, and evidence for redeposition of material from distal shallow-water sites is provided by the carbonate sand layer in Interval 143-869A-4H-3, 79–82 cm, which contains an array of redeposited shallow-water material. Although of early Oligocene age, these grains were transported during late Oligocene time, and their emplacement likely reflects the regional erosional event affecting mid-Pacific atolls (e.g., Anewetak), correlative with a decrease in glacio-eustatic sea level (Schlanger and Premoli Silva, 1986). The unconformity within the pelagic section (uppermost Oligocene–lowermost Miocene) immediately above the redeposited layer is slightly younger than the erosional/solutional gap calibrated from the shallow-water sequence of Anewetak Atoll, and the two phenomena apparently are not related. Indications of bottom slopes are provided by the considerable dip of the strata in the upper cores, which may have been imposed by soft-sediment slippage; the vertical strata in Core 143-869A-8H suggest the local presence of slump folds. That conditions on the seafloor were generally conducive to life is indicated by the abundant traces of bioturbation and the relatively diverse trace-fossil assemblages throughout many levels in the cores.

BIOSTRATIGRAPHY

Calcareous Nannofossils

Hole 869A

Calcareous nannofossil biostratigraphy of Hole 869A indicates a lower Miocene sequence unconformably overlying a relatively expanded Oligocene-Eocene section. Excellent APC/XCB core recovery renders this a sequence of biostratigraphic utility, although nannofossil preservation is moderate to poor throughout. The following summary is based largely on the investigation of core-catcher samples, although more detailed toothpick sampling was conducted in stratigraphically important intervals.

The uppermost sediments recovered in Hole 869A belong to early Miocene age nannofossil Zone NN2 of Martini (1971) (Fig. 30). Samples 143-869A-1H-1, 30 cm, to -4H-3, 78 cm, contain a combination of the following species: *Discoaster druggii*, *Sphenolithus dissimilis*, *Triquetrorhabdulus carinatus*, *Cyclicargolithus floridanus*, *Discoaster variabilis*, *Discoaster deflandrei*, and *Dictyococcites scrippsae*. Interestingly, *Sphenolithus belemnos*, which normally occurs in this zone, is absent. A thin, white, graded sand recovered between Samples 143-869A-4H-3, 79 and 82 cm, contains an Oligocene assemblage consisting of *Dictyococcites bisectus*, *Ericsonia formosa*, *Reticulofenestra umbilica*, *Sphenolithus predistentus*, and *S. ra-*

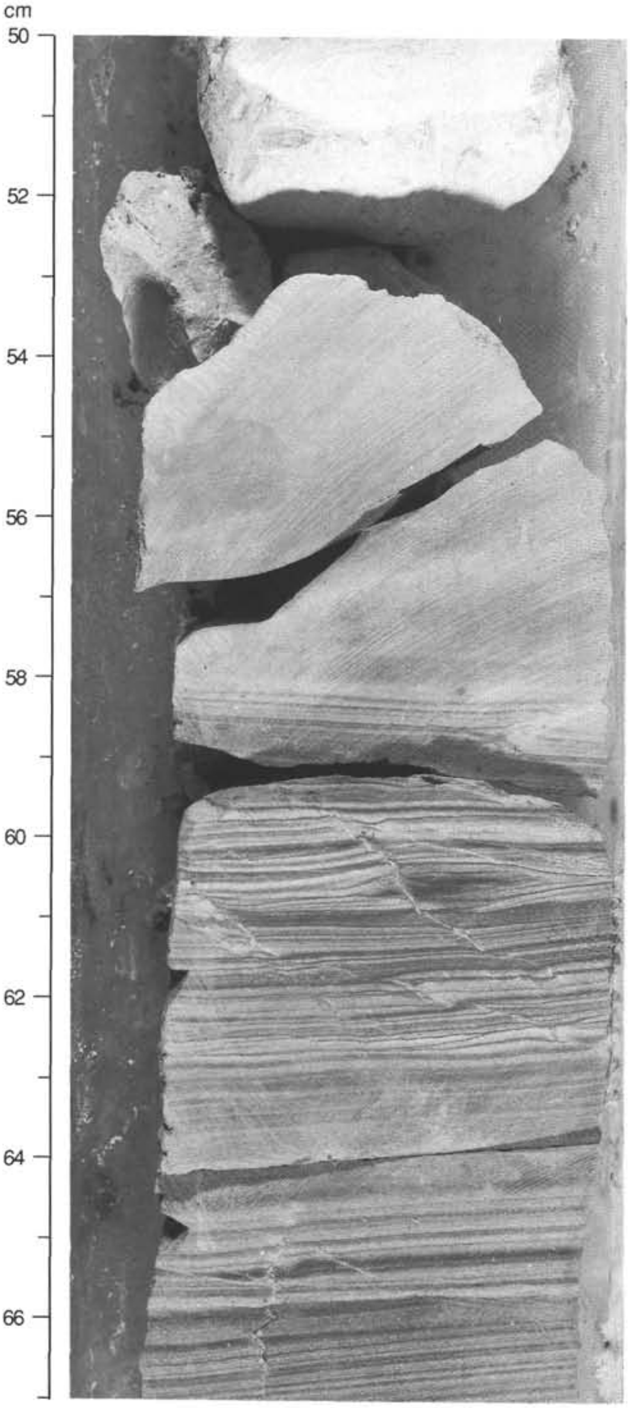

Figure 22. Thinly laminated radiolarian siltstones in Subunit IIIG (Interval 143-869B-68R-5, 50–67 cm).

dians which belong to Oligocene Zone NP21. Sediments below this sand layer, for example, in Sample 143-869A-4H-3, 85 cm, contain *Sphenolithus ciperoensis*, *Sphenolithus distentus*, and *S. predistentus*, the combination of which indicates an assignment to Oligocene Zone NP24. Considered in their sedimentological context, these biostratigraphic data suggest that the graded layer was redeposited from the erosion of older sediment upslope during the late Oligocene. The absence of Zones NP25 and NN1 suggests a brief interval of erosion and/or nondeposition during the latest Oligocene and earliest Miocene.

The Oligocene of Hole 869A has been subdivided as follows: Oligocene Zone NP24 extends from Sample 143-869A-4H-3, 85 cm, to -4H-CC; Cores 143-869A-5H and -6H belong to Oligocene Zone NP23, based on the occurrence of *Sphenolithus predistentus* and absence of *S. ciperoensis* and *Reticulofenestra umbilica*. Oligocene Zone NP21 extends from Sample 143-869A-7H-2, 47 cm, to -9H-4, 20 cm, based on the occurrence of *Ericsonia formosa*, *Ericsonia subdisticha* and *Reticulofenestra umbilica* and the absence of *Discoaster barbadiensis* and *Discoaster saipanensis*. A detailed analysis was conducted of the transition between Zones NP20 and NP21, often taken to identify the Eocene/Oligocene boundary. This boundary, which can be defined by the last occurrence of *D. saipanensis* and, alternatively, by the last occurrence of *D. barbadiensis*, lies between Samples 143-869A-9H-4, 20 cm, and 50 cm. This interval, which corresponds to an interval of brown clayey nannofossil ooze, is marked both by a dramatic decrease in the abundance and scattered occurrence of both boundary markers.

Similar problems were experienced in the zonal division of the upper Eocene sequence of Hole 869A, as happened with previous Leg 143 sites. Owing to the absence of the marker species, we had to rely on secondary markers. The interval from Samples 143-869A-9H-4, 50 cm, to -10X-1, 0 cm, was placed in Zone NP20, based on the occurrences of *D. barbadiensis*, *D. saipanensis*, and *E. subdisticha*. Samples 143-869A-11X-3, 113 cm, and -11X-5, 22 cm, probably belong to upper Eocene Zones NP18 and NP19, as suggested by the absence of both *E. subdisticha* and *Chiasmolithus grandis*. The interval from Samples 143-869A-11X-CC to -12X-CC contains an assemblage that includes *Sphenolithus furcatolithoides*, *Chiasmolithus grandis*, *Chiasmolithus solitus*, and *R. umbilica*. These occurrences and the absence of *Chiasmolithus gigas* indicate that this interval lies in middle Eocene Zones NP16 and NP17. Middle Eocene Zone NP15 extends from Samples 143-869A-13X-5, 15 cm, to -14X-6, 40 cm, based on the occurrence of *Sphenolithus furcatolithoides* and *C. gigas* and the absence of *R. umbilica*. We tentatively assign the lowermost fossiliferous sediments in Hole 869A, in Samples 143-869A-14X-CC and -15X-CC to lower and middle Eocene Zones NP13 and NP14, based on the occurrences of *Discoaster lodoensis* and *Reticulofenestra dictyoda* and absence of *Sphenolithus editus*, *Sphenolithus conspicuus* and species of *Toweius*.

Hole 869B

Hole 869B was washed to a depth of 140 mbsf. Calcareous nannofossil biostratigraphy of the cored interval of Hole 869B indicates about 40 m of Eocene to lower Paleocene sediments overlying approximately 600 m of predominantly clastic sediments of Late Cretaceous age. The hole was abandoned in hemipelagic sediments of Cenomanian age at a depth of 796.2 mbsf. In addition to core-catcher samples, numerous additional samples were examined in critical stratigraphic intervals, or where nannofossiliferous horizons alternated with barren intervals. A total of 119 samples were studied. The preservation is moderate in the uppermost cores (Cores 143-869B-4R to -15R) and deteriorates considerably downward. In general, the assemblages from the turbidite sequence (Cores 143-869B-15R to- 28R) and those of the volcaniclastic sequence (Cores 143-869B-36R to -69R) show poor preservation. Thus, in several intervals, preservational factors lower the attainable biostratigraphic resolution. In many intervals of the Paleogene and Cretaceous, we have relied upon secondary marker taxa to date sediments because of the absence of zonal markers. In these places, we have used the ranges compiled for these species by Perch-Nielsen (1985).

Uppermost Core 143-869B-1W, which covers the interval from 0 to 140 mbsf, contains radiolarian nannofossil ooze overlying siliceous mudstone. Two samples were examined from Section 143-869B-1W-7. A sample from the ooze contains *S. predistentus* and *R. dictyoda*, but lacks *S. ciperoensis* and *R. umbilica*, and therefore has been assigned to Oligocene Zone NP23. A sample from the mudstone

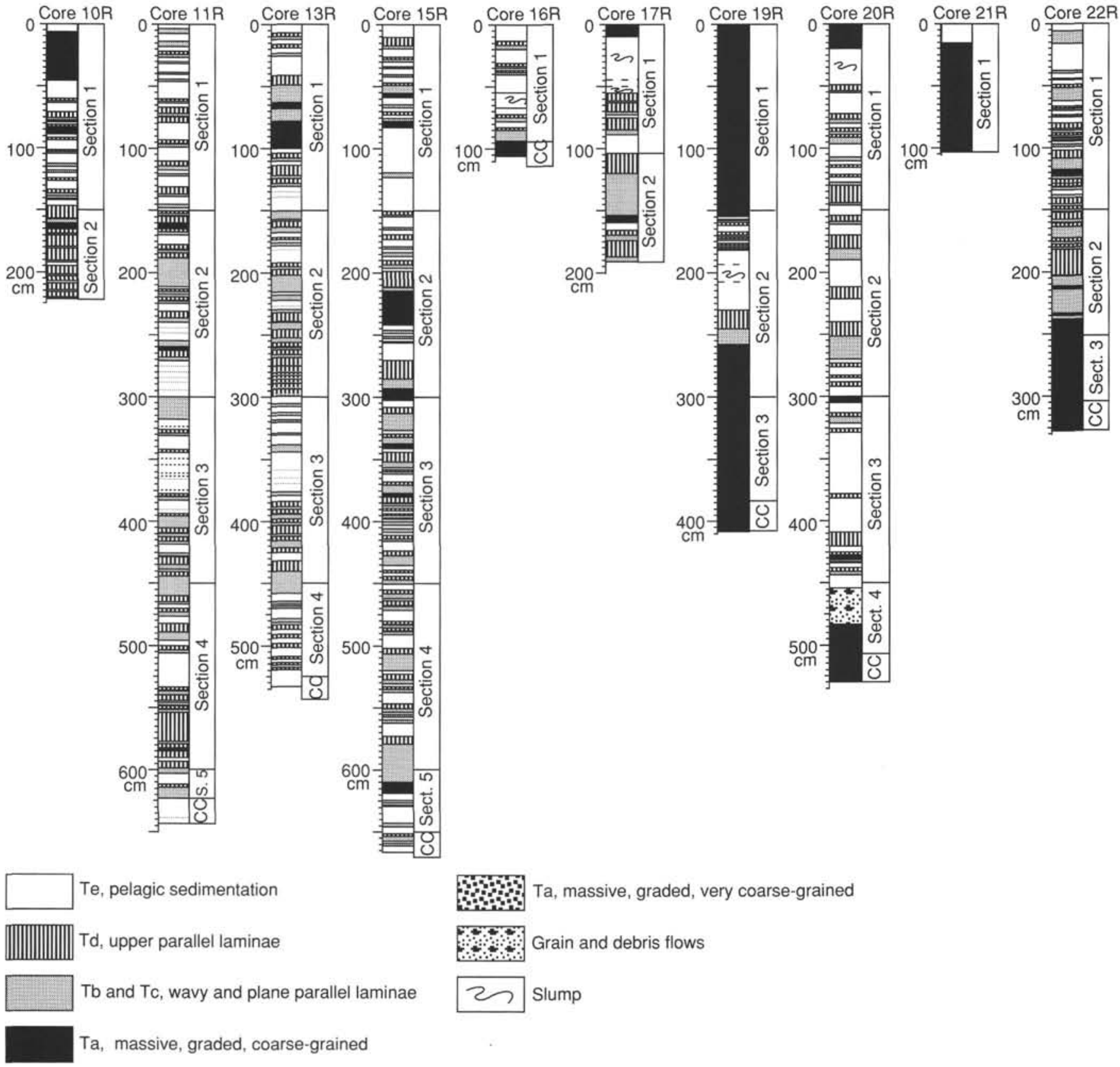

Figure 23. Graphic logs of Bouma sequences and intervals of grain flows and debris flows in Unit III.

contains *D. barbadiensis*, *D. saipanensis*, *R. umbilica*, and *C. grandis*, indicating a probable correlation to middle Eocene Zone NP17. Chert fragments recovered in Cores 143-869B-2R and -3R were undatable, however those in Cores 143-869B-4R to -8R possess stringers of fossiliferous chalk. Assemblages from Samples 143-869B-4R-1, 40 cm, to -5R-1, 94 cm, contain *Discoaster multiradiatus* and *D. barbadiensis*, indicating that this interval belongs to the lower Eocene Zone NP10 of Martini (1971) (Fig. 31). This interval also is constrained by the presence of minute specimens of *Zygrhablithus bijugatus* and the absence of *Fasciculithus tympaniformis* in Sample 143-869B-5R-1, 94 cm. A major unconformity, which includes upper Paleocene Zones NP9 to NP5, lies in the lower part of Core 143-869B-5R. The next dated sample, from Section 143-869B-6R-1, belongs to the middle Paleocene Zone NP4. This assignment is based on the occurrences of early species of *Fasciculithus*, including *Fasciculithus pileatus* and *Fasciculithus stonehengi*, and the absence of *F. tympaniformis*, the first occurrence of which marks the base of Zone NP5. Sample 143-869B-7R-1, 20 cm, contains *Cruciplacolithus tenuis*, *Cruciplacolithus primus*, and *Toweius pertusus* and is also tentatively correlated to Zone NP4. The lowermost Paleocene Zones NP1 to NP3 were not observed.

The interval between the recovered portions of Cores 143-869B-7R and -8R is marked by a second major unconformity that includes the Cretaceous/Tertiary boundary. This correlates to the interval between lower Paleocene Zone NP4 and lower Maastrichtian Zone CC23 of Sissingh (1977). Precise zonal assignment is difficult in the Upper Cretaceous sequence as a number of the Sissingh (1977) markers, including *Reinhardtites anthophorus*, *Reinhardtites levis*, *Calculites obscurus*, *Lucianorhabdus cayeuxii*, *Lucianorhabdus maleformis*, and *Microrhabdulus decoratus*, are missing or very rare. In the following

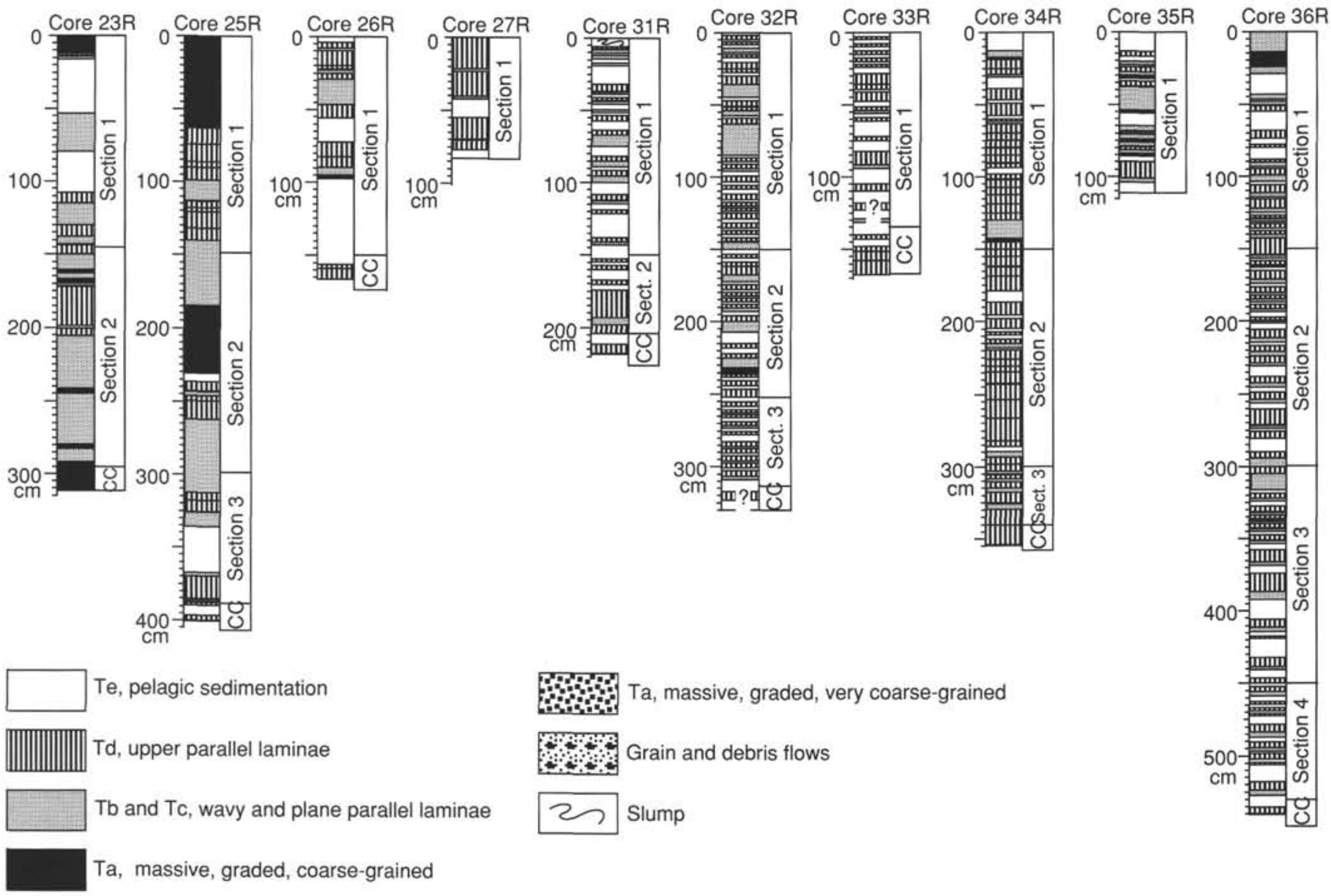

Figure 23 (continued).

discussion, we therefore rely on the ranges of a number of secondary markers. Samples 143-869B-8R-CC through -10R-CC have been assigned to uppermost Campanian to lower Maastrichtian Zones CC22 to CC23, based on the occurrence of primary marker *Quadrum trifidum* and secondary markers *Quadrum gothicum* and *Quadrum sissinghi*. The subsequent interval between Samples 143-869B-11R-CC and -16R-CC lies in upper Campanian Zone CC21, as suggested by the occurrence of secondary markers *Q. sissinghi* and *Q. gothicum*, *Ceratolithoides aculeus*, and *Ceratolithoides verbeekii* and the absence of primary marker *Q. trifidum*. Based on the presence of secondary markers *C. aculeus* and *C. verbeekii*, and the absence of secondary markers *Q. sissinghi* and *Q. gothicum*, the interval between Samples 143-869B-17R-1, 100 cm, and -19-CC has been assigned to upper Campanian Zone CC20.

It is difficult to date the interval between Samples 143-869B-20R-1, 70 cm, and -21R-CC owing to poor preservation. All of the traditional marker species are absent, extremely rare, or very overgrown. Based on the absence of primary marker *Q. sissinghi*, this interval has been tentatively assigned to lower Campanian Zones CC18 to CC19. Samples 143-869B-22R-1, 46 cm, to -25R-CC belong to Subzones CC18b and CC19a, based on the occurrence of primary marker *Bukryaster hayi*, *Q. gothicum*, and rare *C. verbeekii*. Sections 143-869B-16R-1 through -28R-CC are in the lowermost Campanian Zone CC18, based on the occurrence of rare primary marker *Broinsonia parca* ssp. *parca*, *Q. gothicum*, *Lithraphidites grillii*, and the absence of primary marker *Marthasterites furcatus*. Samples 143-869B-29R-CC and -30R-CC contain *M. furcatus* and secondary markers *Micula decussata*, *Quadrum gartneri*, and *Lithastrinus grillii*. The co-occurrence of these species, and the absence of *B. parca* ssp. *parca*, suggests an earliest Campanian to Santonian age within Zones CC16 or CC17. An unconformity, which includes the upper Coniacian to Santonian Zones CC14 to CC15, lies in between Sections 143-869B-30R-CC and -31R-1.

Coniacian Zone CC13 correlates to Sections 143-869B-31R-1 to -32R-3, based on the combined occurrence of primary marker *M. furcatus* and *Q. gartneri* and the absence of primary marker *M. decussata*. Sections 143-869B-33R-1 to -35R-CC lie in Turonian to lower Coniacian Zones CC11 to CC12, as indicated by the presence of *Eiffellithus eximius* and the absence of *M. furcatus* and *M. decussata*.

The remainder of the sequence from Core 143-869B-36R through -69R is of middle to late Cenomanian age and correlates to Zones CC9 to CC10. Distinction between these zones is not possible because the marker *Microrhabdulus decoratus* has not been observed in this interval. This age is based on the occurrence of *Corollithion kennedyi* throughout the sequence and of *Lithraphidites acutus* in the interval between Samples 143-869B-46R-1, 35 cm, and -66R-3, 14 cm. Whereas *L. acutus* is limited to the upper Cenomanian Zone CC10, the range of *C. kennedyi* extends down through the Cenomanian. *Eiffellithus turriseiffelii*, which has its first occurrence in the latest Albian, is common throughout the sequence. Other species that last occur in the Cenomanian, including *Rhagodiscus asper*, *Microstauus chiastius*, and *Axopodorhabdus albianus*, have been found in numerous samples. In the volcaniclastic sediments, nannofossils are most commonly found in interbedded claystones and are rare or absent in coarser lithologies.

The source of nannofossils in these sediments is open to question. It is likely in most of the Cretaceous sequence that nannofossils are of pelagic origin because there is no likely hemipelagic source upslope.

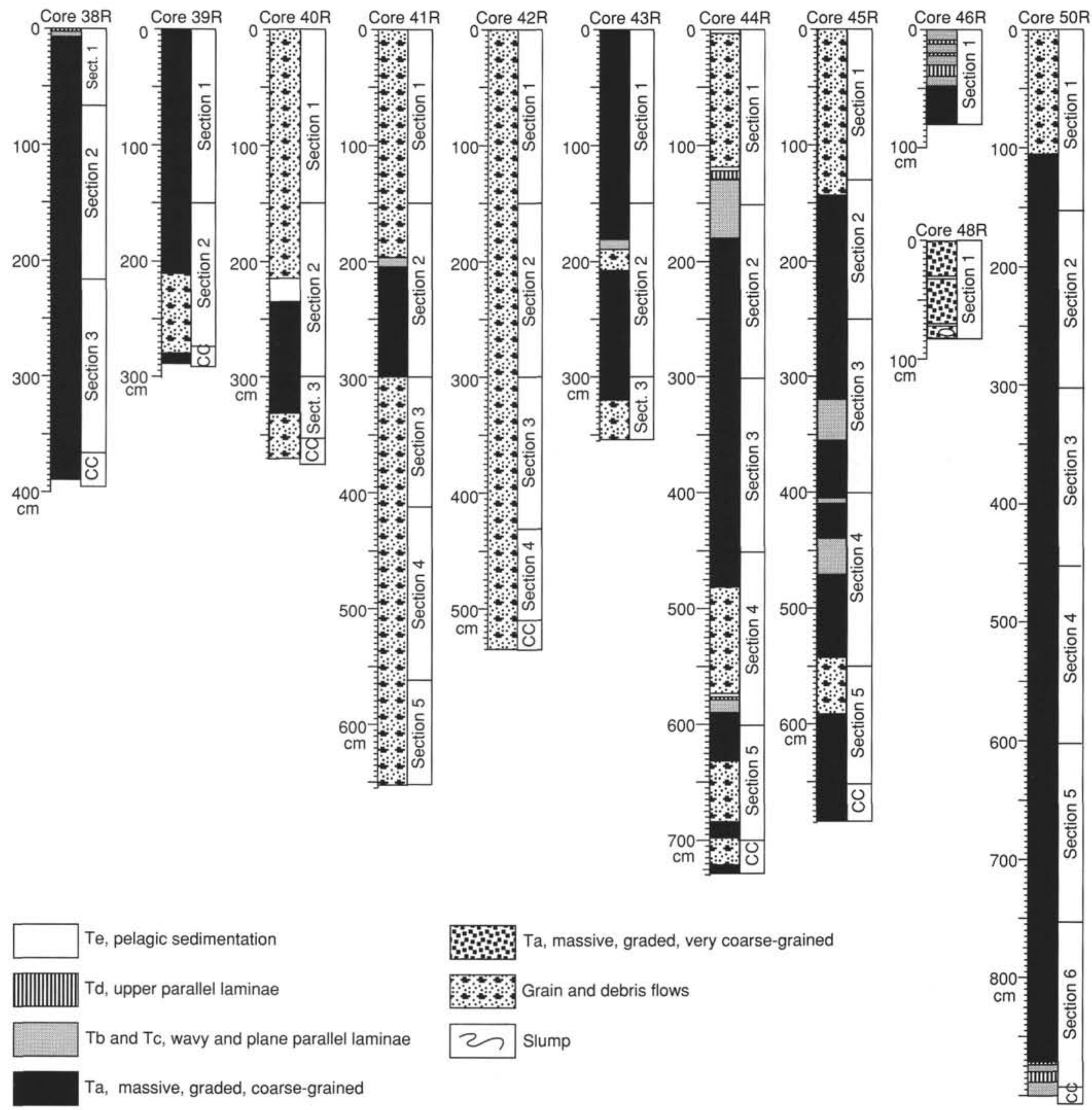

Figure 23 (continued).

However, in Cenozoic sediments, it is possible that nannofossils were redeposited in the distal parts of turbidite fans. This would explain their preservation at paleodepths below the CCD and the absence of foraminifers in many intervals as a result of sorting.

Palynomorphs

Samples 143-869A-1H-CC and -869B-34R-CC, 9–10 cm, were processed for palynology and found to be barren. Other samples were not processed for palynology after visual inspection and organic geochemical analyses of the cores indicated little reason to expect any recoverable palynomorphs.

Foraminifers

Hole 869A

Planktonic foraminifers from Hole 869A are limited to the lower Oligocene in Cores 143-869B-4H to -8H. Assemblages consist of rare-to-abundant, poorly to moderately well-preserved specimens. Washed residues from Cores 143-869A-1H to -3H and -9H to -15H are devoid of foraminifers and instead contain poorly preserved radiolarians, with the addition of sponge spicules in the lower cores.

The Oligocene sequence ranges from Zones P20/21 down to Zone P18, in apparent stratigraphic continuity, with the exception of a rede-

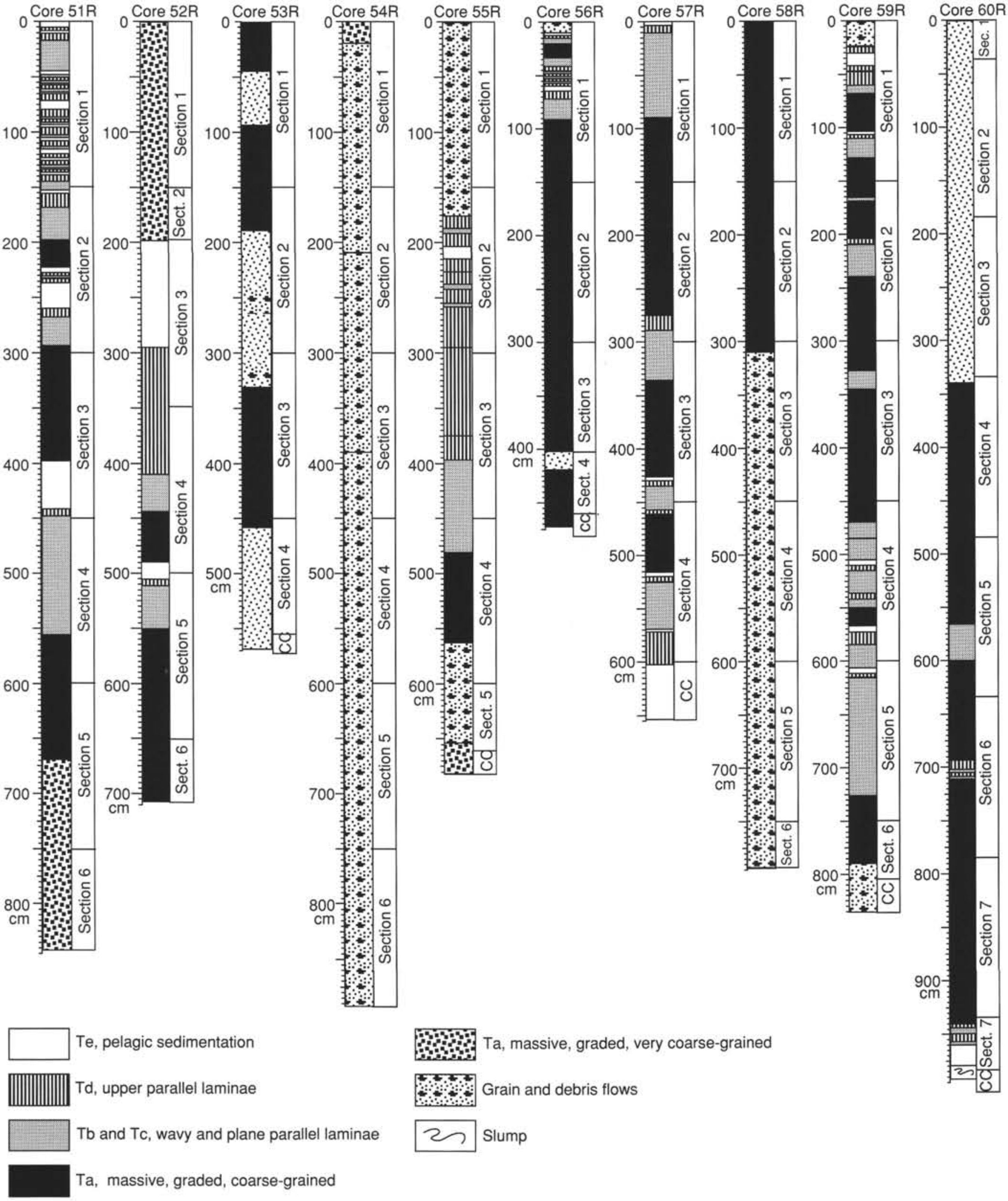

Figure 23 (continued).

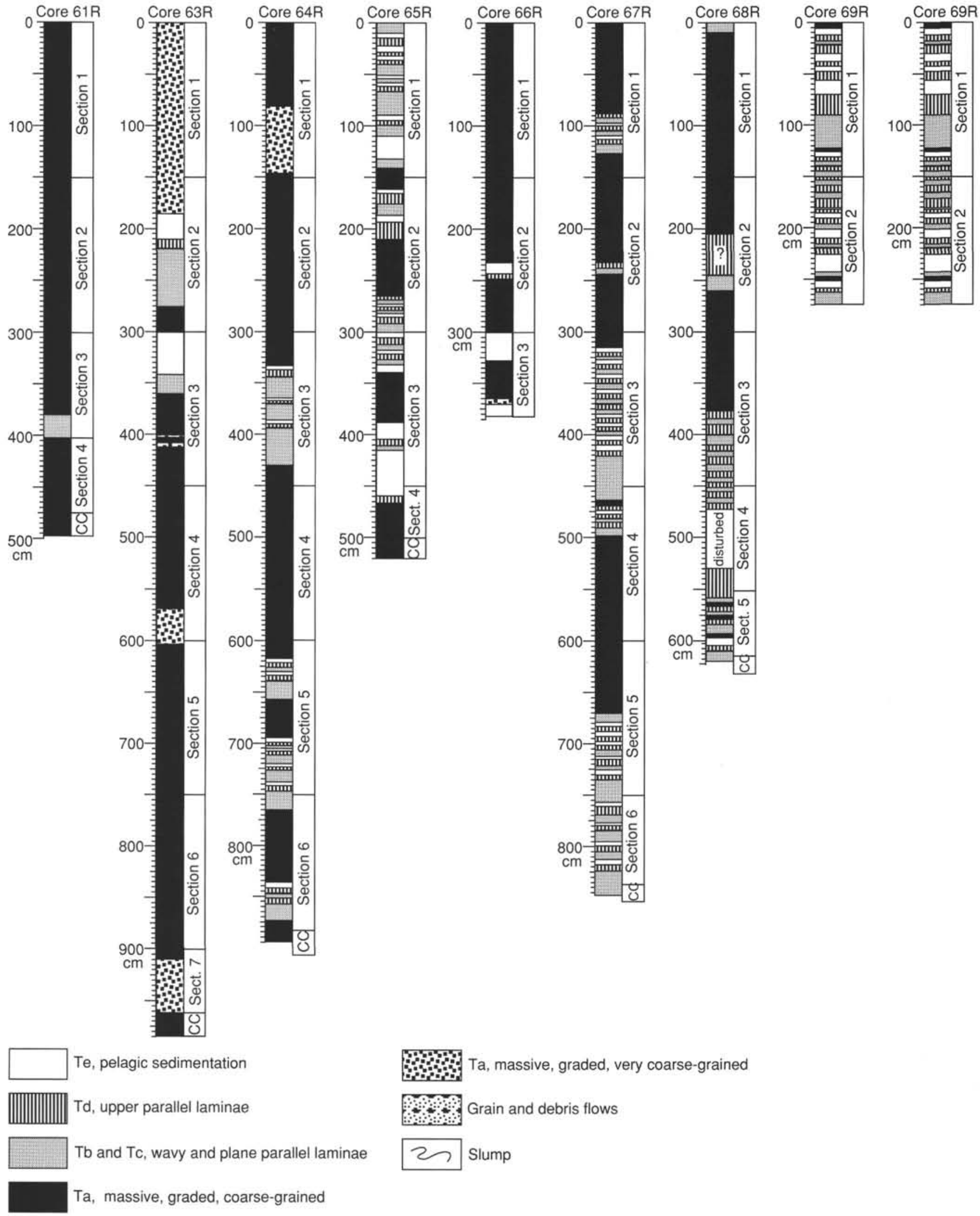

Figure 23 (continued).

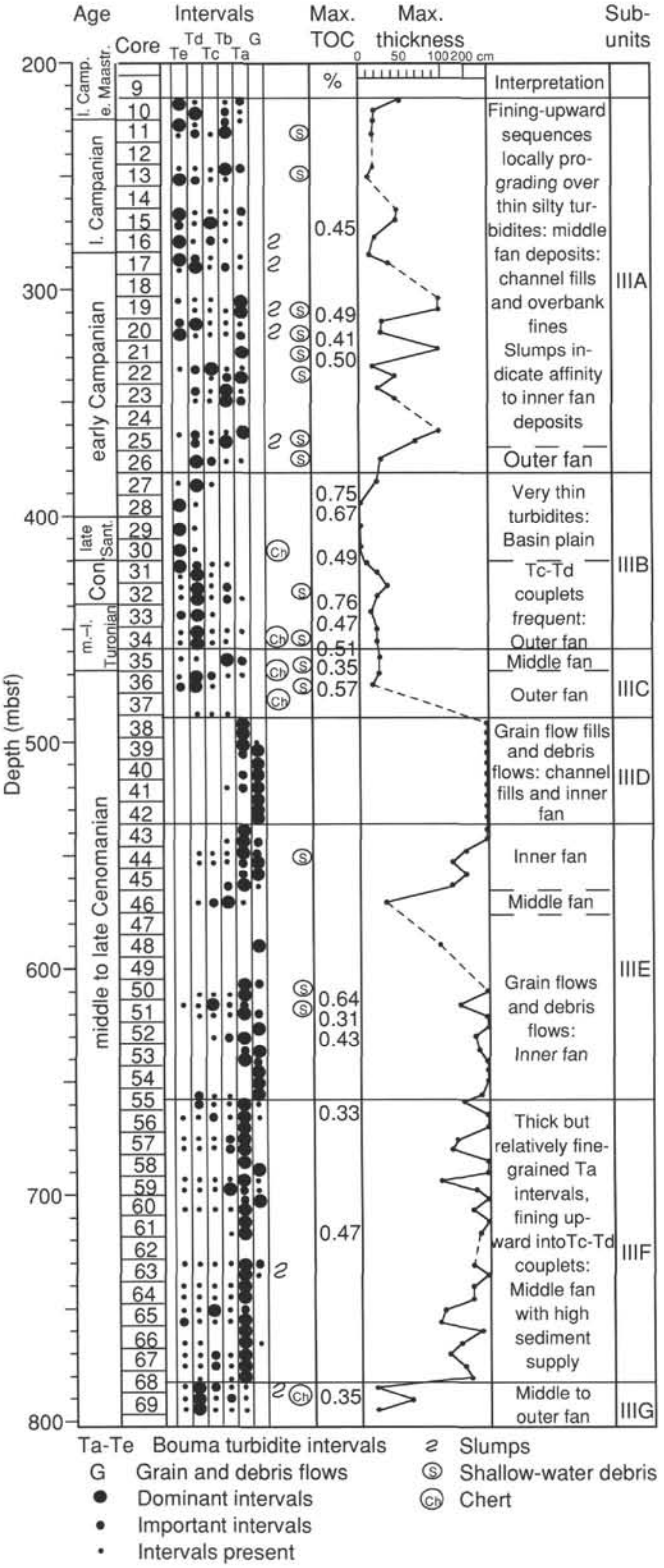

Figure 24. Summary diagram of the observed sedimentary features in Unit III and interpretation of the corresponding depositional environments. Relative abundance of mass-flow intervals and maximum thicknesses have been plotted for the upper and lower halves of recovered material in each core; where only one section was recovered, only one plot was made. Cores having less than 50 cm of recovered material were not considered. Note the change of scale at 100 cm in the maximum-thickness column. Thicknesses of grain and debris flows may reach several meters. The values of total organic carbon (TOC) have been plotted only where they significantly exceed a background value of 0.2% to 0.3%.

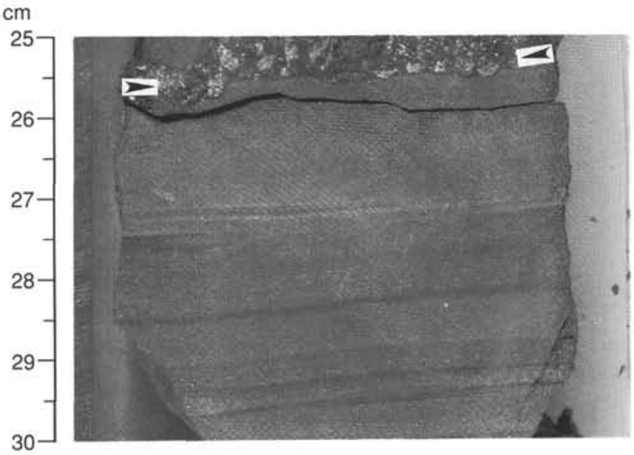

Figure 25. Contact between Subunits IIIE and IIIF, where a coarse volcaniclastic mass flow overlies fine-grained Td intervals. Note traction carpet at base of grain-flow unit (arrows) (Interval 143-869B-55R-2, 25–30 cm).

posited older assemblage in Sample 143-869A-4H-3, 80–82 cm. The latter assemblage from a turbidite layer consists of *"Turborotalia" ampliapertura, Subbotina gortanii, "Globigerina" tapuriensis*, and *Pseudohastigerina micra,* which characterize Zone P18. The sample also contains redeposited bryozoan fragments, larger benthic foraminifers, small calcareous benthic foraminifers, ostracodes, echinoid spines, bivalve fragments, and radio- larians, in addition to in-situ agglutinated abyssal foraminifers and fish debris. Sample 143-869A-4H-CC is younger and was assigned to Zones P20/21 by the presence of *Paragloborotalia opima, "Globigerina" ciperoensis, G. venezuelana, Globigerina tripartita,* and *Catapsydrax dissimilis*. This assemblage continues downhole to Sample 143-869A-5H-CC.

The occurrence of *"Turborotalia" ampliapertura, Turborotalia pseudoampliapertura*, and *Subbotina angiporoides* in Sample 143-869A-6H-CC indicates Zones P19/20. This is followed by the overlap of *Globigerina sellii, Pseudohastigerina* sp., and *Cassigerinella chipolensis* in Sample 143-869A-7H-CC that defines a stratigraphic position within Zones P18 and P19. Finally, Sample 143-869A-8H-CC has been preliminarily referred to Zone P18 by the presence of very poorly preserved *"Turborotalia" ampliapertura, Subbotina praeturritilina*, and *Paragloborotalia opima nana*, among others.

Biogenic constituents in the Oligocene sequence, with the exception of the sample from the turbidite layer in Core 143-869A-4H, are characterized by agglutinated foraminifers, fish debris, and radiolarians, consistent with deposition at abyssal water depths. Preservation of the lower Oligocene planktonic foraminifers at these depths and the absence of foraminifers in the radiolarian-dominated older and younger Cenozoic sediments may be related to passage of the site beneath the equatorial zone of high productivity caused by plate motion, perhaps augmented by the decrease in CCD near the Eocene/Oligocene boundary (Berger et al., 1981).

Hole 869B

Because of poor recovery owing to the presence of porcellanite and chert, Cenozoic planktonic foraminifers from Hole 869B have been limited in Cores 143-869B-1R to -10R to Eocene assemblages identified in thin section from limestone in Core 143-869B-4R. The sparse and poorly preserved fauna consists of *Morozovella aequa, Morozorella formosa, Morozorella marginodentata, Muricoglobigerina soldadoensis, Pseudohastigerina*, and *Planorotalites* sp. cf. *P. chapmani* that yield an early Eocene age (Zones P6c–P7). Elements of this assemblage occur in Samples 143-869B-4R-1, 48–51 cm, 82–84 cm, along with rare calcareous benthic foraminifers and volcanogenic debris.

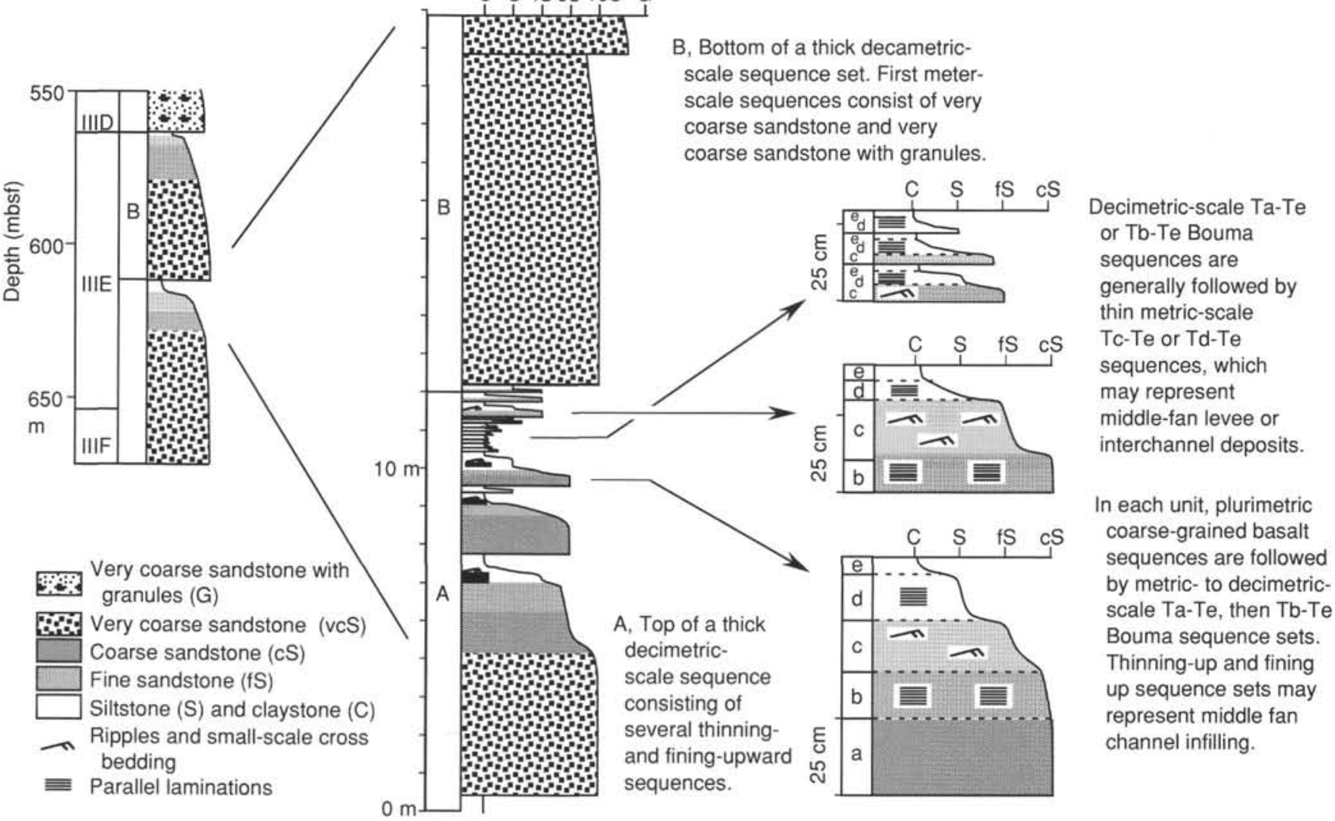

Figure 26. Schematic representation of mass-flow sequences typical of Subunit IIIE, based on observations from Sections 143-869B-50R-1 to -52R-2.

Cretaceous planktonic foraminifers, identified in both washed samples and thin section, were found in Cores 143-869B-10R to -52R and range from Maastrichtian to late Cenomanian in age. Specimens are mostly rare to few in abundance and characteristically poor in preservation owing to calcite dissolution. Maastrichtian planktonic foraminifers were found in Samples 143-869B-10R-CC and -11R-1, 4–6 cm, and consist of *Globotruncanita stuarti, Globotruncanita stuartiformis, Globotruncanita elevata, Globotruncana linneiana*, questionable *Globotruncana aegyptiaca*, and *Contusotruncana fornicata*, among others. Both samples contain larger benthic foraminifers (e.g., orbitoidids), whereas the latter sample also contains ooids, bivalve fragments, and echinoid debris.

Planktonic foraminifers of Campanian age were found in Samples 143-869B-11R-CC to -28R-CC and include *Globotruncana arca, Globotruncana bulloides, Globotruncana mariei, Globotruncana subspinosa, Globotruncana orientalis, Globotruncana ventricosa, Globotruncanita stuartiformis, Contusotruncana fornicata*, and *Contusotruncana patelliformis*, among others. The presence of *Globotruncana ventricosa* in Core 143-869B-28R, adjacent to older planktonic foraminifers in Core 143-869B-30R, suggests the presence of an unconformity that involves much of the early Campanian age *Globotruncanita elevata* Zone. Other biogenic material in the Campanian samples includes redeposited neritic and bathyal smaller calcareous benthic foraminifers, bryozoans, bivalve and echinoid fragments, sponge spicules, and radiolarians, as well as in-situ fish debris and agglutinated abyssal foraminifers. Redeposited ooids are restricted to Samples 143-869B-19R-CC, -20R-CC, and -25R-1, 43–45 cm.

Older planktonic foraminifers appear in the siltstone of Core 143-869B-30R. The assemblage of very small, size-sorted specimens includes *Heterohelix moremani, Heterohelix reussi, Hedbergella planispira*, and *Globigerinelloides* sp. and supports an age no younger than Santonian. This assemblage is associated with poorly preserved radiolarians and sponge spicules. A more abundant and diverse assemblage of early Coniacian age (*Dicarinella primitiva* Zone) appears in Sample 143-869B-31R-1, 72–74 cm. Present are *Marginotruncana sigali, Marginotruncana schneegansi, Marginotruncana pseudolinneiana, Dicarinella primitiva, Dicarinella imbricata, Whiteinella baltica, Whiteinella aprica*, and *Praeglobotruncana gibba*, among others. Associated with these species are reworked middle to upper Cenomanian forms, such as *Rotalipora cushmani* and *Rotalipora greenhornensis*. Redeposited material includes ooids, gastropods, echinoid spines, *Inoceramus* prisms, ostracodes, sponge spicules, and small calcareous benthic foraminifers.

Lower to middle Turonian planktonic foraminifers (*Helvetoglobotruncana helvetica* Zone) occur in Samples 143-869B-34R-1, 142–144 cm, and -35R-1, 44–46 cm. In addition to the nominate species, the assemblage includes *Dicarinella algeriana, D. imbricata, Dicarinella canaliculata, Dicarinella hagni, Praeglobotruncana gibba*, and *Marginotruncana sigali*, among others. Associated redeposited material includes ooids and coated grains, bivalve and echinoid fragments, sponge spicules, and both calcareous and agglutinated benthic foraminifers.

Upper Cenomanian planktonic foraminifers first appear in Sample 143-869B-36R-3, 13–14 cm, and continue downhole to Sample 143-869B-52R-5, 12–15 cm. The fauna is representative of the *Dicarinella algeriana* Subzone of the middle to late Cenomanian age *Rotalipora cushmani* Zone and includes both nominate species, plus *Rotalipora deeckei, Rotalipora greenhornensis, Praeglobotruncana delrioensis, Praeglobotruncana stephani, Whiteinella aprica*, and *Heterohelix moremani*. Redeposited material includes rare ooids, gastropods, echinoid spines, larger and smaller calcareous benthic foraminifers, and radiolarians mixed with in-situ abyssal benthic foraminifers.

Planktonic foraminifers and redeposited calcareous material become increasingly sparse downhole in the coarse grain and debris

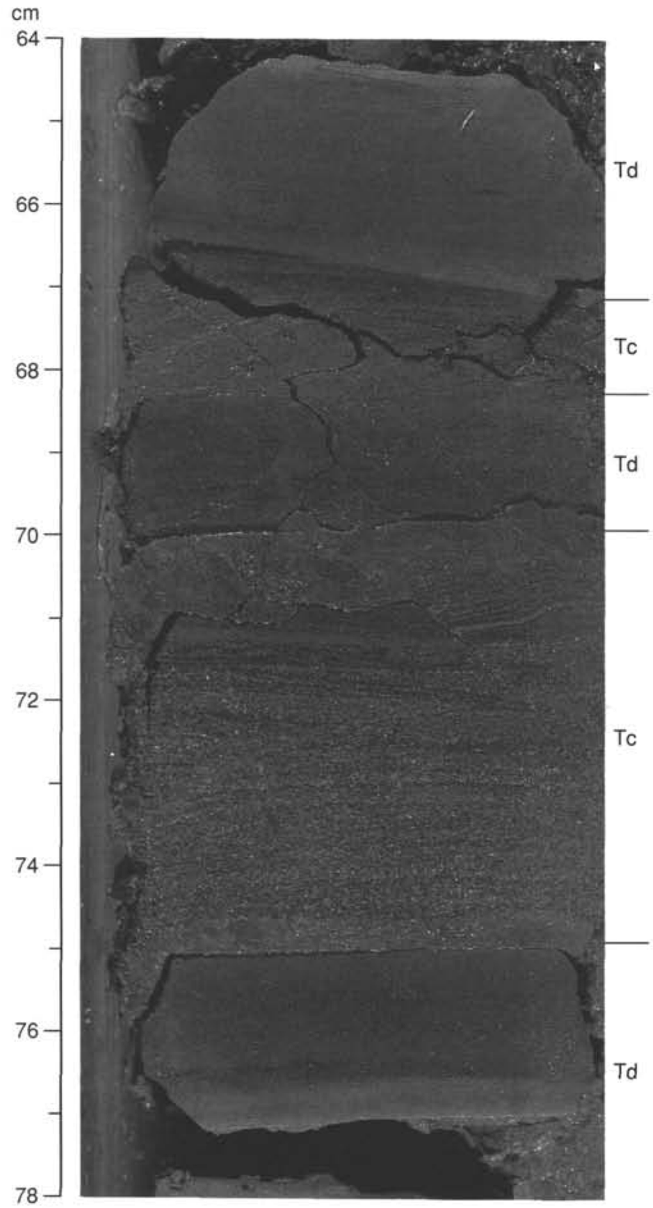

Figure 27. Two Tc-Td couplets typical of the lower part of Subunit IIIB. Note soft-sediment deformation in the lower Tc interval and current ripple in the upper one (Interval 143-869B-31R-1, 64–78 cm).

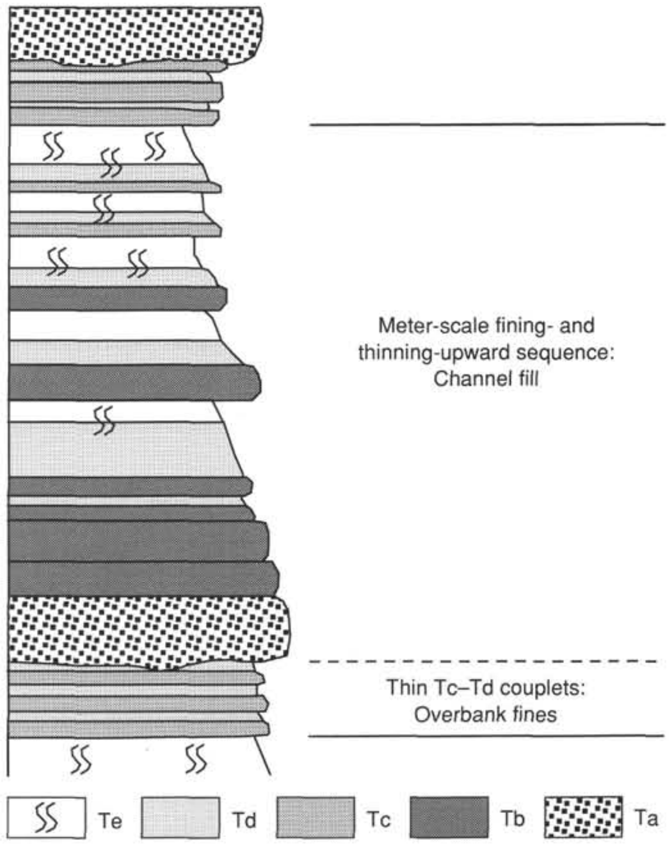

Figure 28. Schematic sequences typical of Subunit IIIA. For discussion refer to text.

flows of Cores 143-869B-38R to -57R and are then succeeded by radiolarians to the bottom of the hole. The lowest occurrence of planktonic foraminifers is in Sample 143-869B-57R-2, 122–125 cm, and consists of extremely small, thin-walled hedbergellids associated with radiolarians in volcaniclastic siltstone. That these dissolution susceptible specimens are preserved with radiolarians suggests that dissolution below the CCD was not the sole reason for the lack of planktonic and calcareous benthic foraminifers. The presence of radiolarians in graded layers and thin laminae associated with size-sorted volcaniclastic material throughout the Cenomanian sequence, and especially noticeable in Cores 143-869B-68R and -69R, attests to the redeposited nature of these deposits. Presumably, the absence of shallow-water material and neritic benthic foraminifers reflects a volcanic source at deeper water depths. Following this argument, the absence of bathyal benthic foraminifers is evidence of rapid and continued sedimentation that overwhelmed the deeper-water benthic communities. The exclusion of planktonic foraminifers, in contrast to the radiolarians and calcareous nannofossils, if not related to differential dissolution, then is perhaps primary and related to changes in the upper-water column caused by the continued volcanism that modified the pelagic habitats.

PALEOMAGNETISM

APC Cores

The archive halves of Cores 143-869A-1H through -9H were measured with the pass-through cryogenic magnetometer at a spacing of 5 cm. After measuring natural remanent magnetization (NRM), we subjected the cores to alternating-field (AF) magnetic "cleaning" at 15 mT. Whole-core magnetic-susceptibility measurements were performed using the MST.

NRM intensities varied on the order of 0.1 to 1000 mA/m, and intensity peaks tended to occur within the top 40% to 50% of each core, with a pattern similar to that which was typical of the APC cores from Site 865. The upper-core intensity peak varies in magnitude from 10 to 1000 times the intensity values in the lower sections, and magnetic directions are erratic. Three possible causes of this observed disturbance are (1) rust contamination, (2) drill-string overprint, and (3) physical disturbance resulting from the coring process. The lower densities at the core breaks seen in the GRAPE data (see "Physical Properties" section, this chapter) may indicate some possible physical disturbance at the top of the core that resulted during coring.

In the report for Site 865, we suggested that rust contamination (Sager, 1986, 1988; Tarduno et al., 1991) could be a possible cause of the abnormally high intensities observed in the upper sections of the cores. At this site, we observed large (>1 mm) rust flakes between the sediment and the core liner in the top sections of highly magnetic cores. We also detected smaller rust flakes in smear slides of the

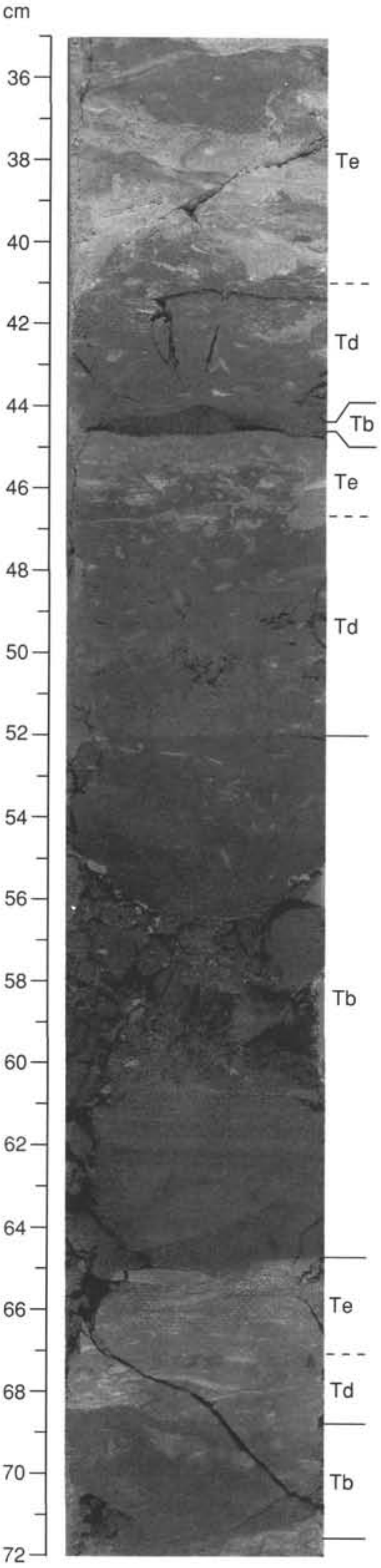

Figure 29. Stacked Tb-Td-Te intervals in the upper part of a fining-upward channel-fill sequence. Td intervals are dark-colored by clays. Bioturbation partly mixed the fine turbiditic and the light-colored pelagic sediment (Interval 143-869B-13R-2, 35–72 cm).

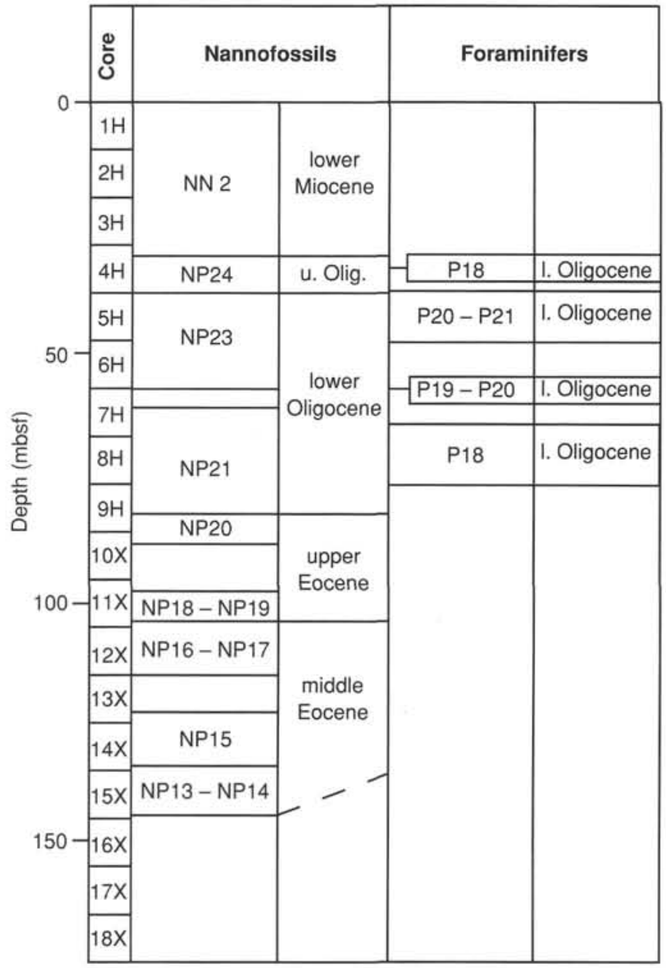

Figure 30. Cenozoic nannofossil and planktonic foraminiferal biostratigraphy of Hole 869A. Martini's zones (1971) are illustrated for the hole as well as corresponding epochs. Abbreviations: u. = upper; l. = lower.

sediments taken near the core liner, even in the few cores that seemed less affected.

Magnetic Polarity Stratigraphy

As a result of drilling disturbance, we were unable to resolve a reliable magnetostratigraphy from the whole-core measurements of the archive halves of the APC cores. Because the rust seems to be confined to the outside of the core between the core liner and the core itself, it may be possible to extract reliable magnetostratigraphic data using a discrete-sampling program.

Magnetic Susceptibility

The range of magnetic susceptibility readings is on the order of 0 to 1000 μcgs, with the highest susceptibilities at the top of each core (Fig. 32). These peaks correspond to the peaks in magnetic intensity mentioned earlier. The low values of susceptibility between 35 and 75 mbsf correspond to a section having high percentages of calcium carbonate (see "Organic Geochemistry" section, this chapter), which suggests dilution of this section by calcium carbonate.

RCB Cores

RCB coring at Hole 869B resulted in the recovery of long, continuous core segments, beginning with Core 143-869B-19R, that

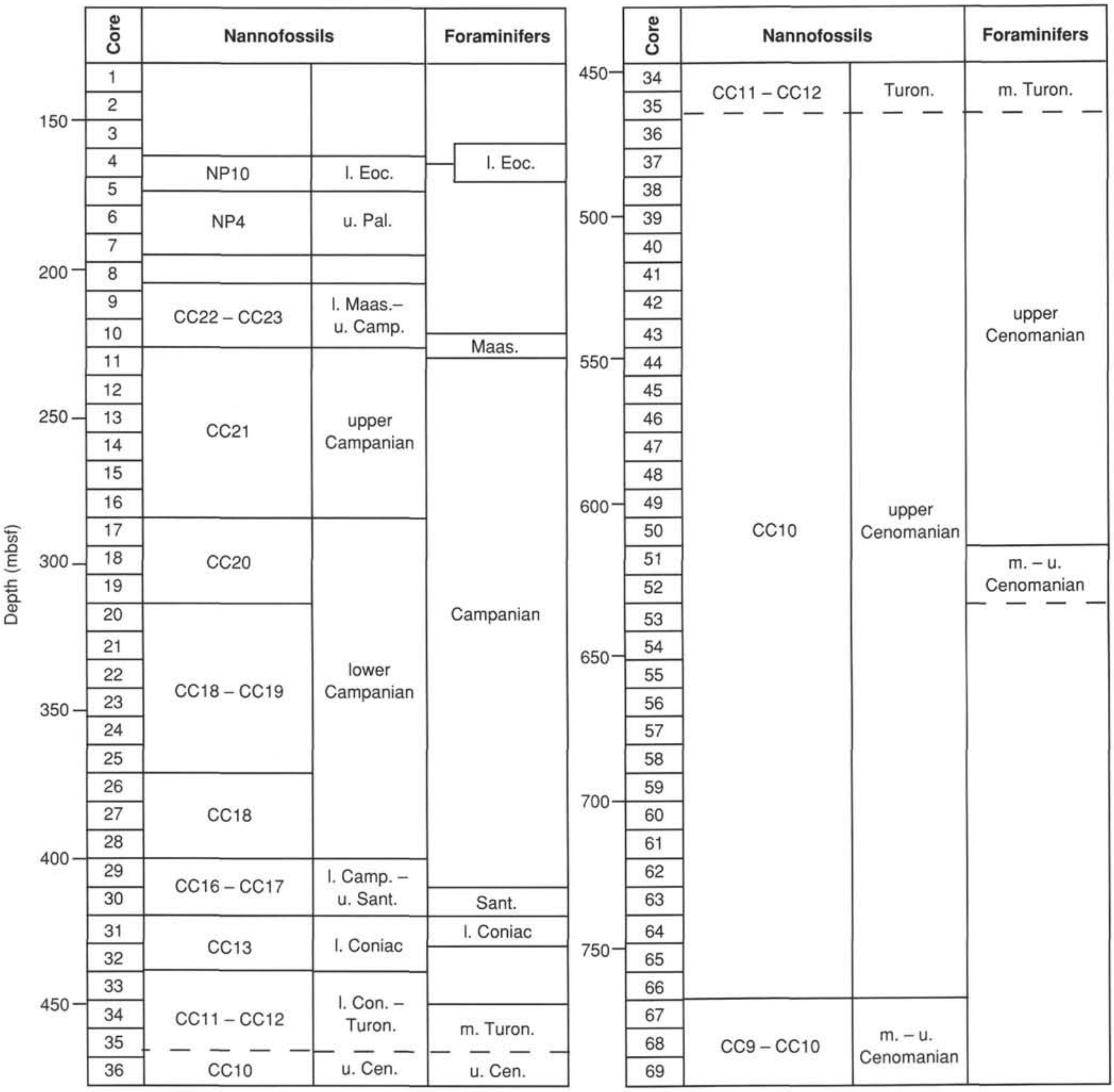

Figure 31. Cenozoic and Cretaceous nannofossil and planktonic foraminiferal biostratigraphy of Hole 869B. Abbreviations: u. = upper; l. = lower.

were suitable for measuring with the pass-through cryogenic magnetometer. Measurements were taken at a 5-cm interval of the NRM and remanence after demagnetization at 15 mT. The raw data obtained by these pass-through measurements contain numerous edge effects, which are created when two separate core pieces, having different azimuthal orientations and hence declinations, are measured. Accounting for these spurious values, the pass-through measurements can be used to divide the column into the following magnetic units:

1. Unit 1 (Cores 143-869B-19R to -20R). This unit is characterized by small changes in direction with AF demagnetization. The most continuous pieces (i.e., in Core 143-869B-19R) have inclinations after 15 mT demagnetization of between –10° and –30°.

2. Unit 2 (Cores 143-869B-21R to -26R). This unit is characterized by large changes in direction with demagnetization. After demagnetization at 15 mT, the most continuous pieces have inclinations that are positive, but scattered and typically range from +10° to +40°.

3. Unit 3 (Cores 143-869B-34R to -69R). This unit is characterized by small changes in direction with demagnetization. The most continuous pieces have inclinations of between –30° and –40° after demagnetization at 15 mT.

In Cores 143-869B-27R to -33R, recovery was not sufficient for meaningful pass-through measurements; thus, this interval has been omitted from the classification.

The demagnetization behavior exhibited by paleomagnetic Unit 2 is similar to that observed in paleomagnetic studies of pelagic sediments from other Pacific Ocean sites (e.g., Site 167, Magellan Rise, see Tarduno et al., 1989). Specifically, the data most closely resemble the situation when a present-day overprint (having a positive inclination)

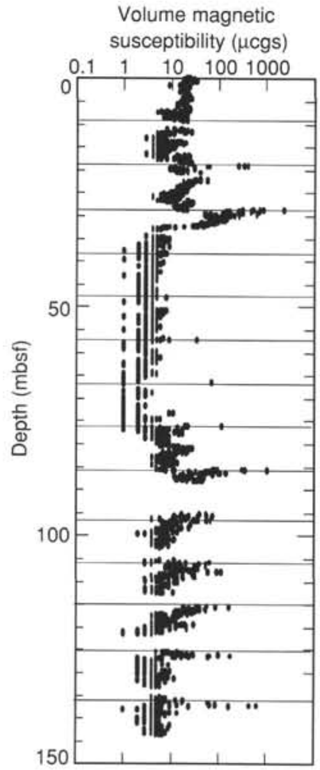

Figure 32. Volume-magnetic susceptibility plotted with depth for Hole 869A. Horizontal lines indicate core breaks.

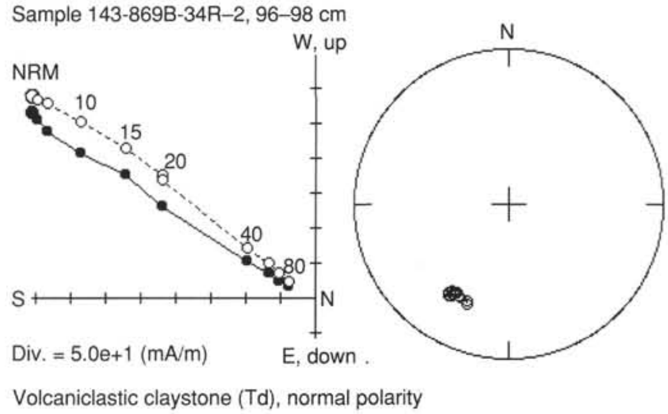

Figure 33. Orthogonal vector plot (left) of progressive AF demagnetization of volcaniclastic claystone (Sample 143-869B-34R-2, 96–98 cm). Open circles = inclination; closed circles = declination (unoriented); large circles = natural remanent magnetization (NRM); small circles = vector end points after demagnetization (labeled in mT). Demagnetization steps shown (mT): 0, 2.5, 5.0, 10.0, 15.0, 20.0, 30.0, 40.0, 50.0, 60.0, 80.0. Stereonet plot (right) of vector end points after progressive AF demagnetization.

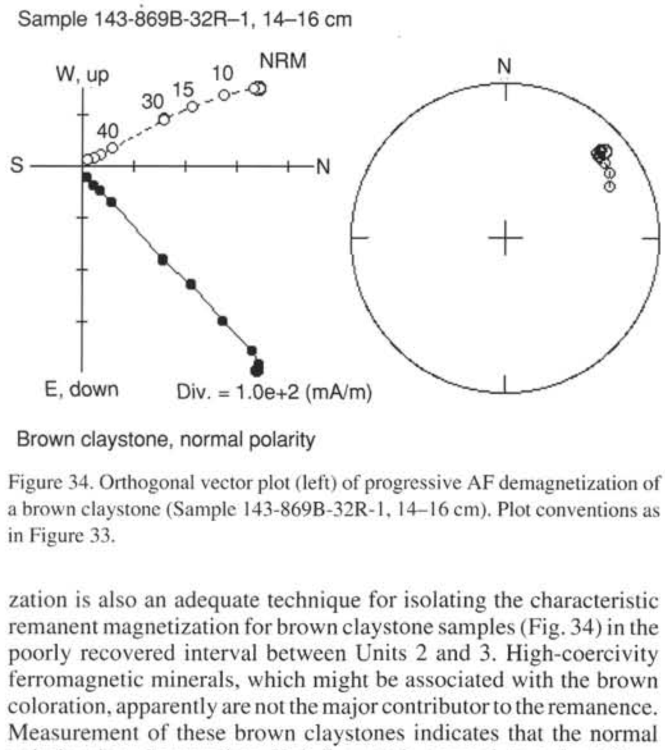

Figure 34. Orthogonal vector plot (left) of progressive AF demagnetization of a brown claystone (Sample 143-869B-32R-1, 14–16 cm). Plot conventions as in Figure 33.

is removed from samples having a primary reversed-polarity magnetization (having a negative inclination) acquired in the Southern Hemisphere. The differences in both inclination and declination between the present-day-field overprint and the primary direction are reflected by large changes in direction with AF demagnetization.

Paleontological age assignments (see "Biostratigraphy" section, this chapter) place paleomagnetic Unit 1 in the early Campanian (nannofossils), Unit 2 in the early Campanian (nannofossils) and Unit 3 in the Turonian to Cenomanian (nannofossils and foraminifers). Based on analogy with the demagnetization behavior observed in previous studies (Tarduno et al., 1989) and the standard biostratigraphic correlation of geologic stage with polarity chron (Kent and Gradstein, 1985), the simplest magnetostratigraphic assignment of the paleomagnetic units is as follows: Unit 1 records the lower portion of C33N; Unit 2 represents C33R, and Unit 3 represents the upper to middle portion of the Cretaceous normal polarity superchron (K-N).

To test whether the pass-through measurements accurately record the primary geomagnetic polarity, discrete samples were collected from paleomagnetic Units 2 and 3 and subjected to step-wise demagnetization. Discrete samples were also collected from the poorly recovered interval between Units 2 and 3. The discrete samples were demagnetized up to 20 mT using the pass-through AF demagnetization system; higher AF demagnetization steps were applied with the Schonstedt AF demagnetizer. In many samples, the intensities after application of 20 mT (with the pass-through demagnetizer) are essentially identical to those after demagnetization of 30 mT (with the Schonstedt system), which suggests a calibration problem with one (or both) system(s). The vector end point directions are also essentially identical, indicating that this calibration discrepancy does not affect the accuracy of the directional data significantly.

Demagnetization of volcaniclastic sediments from paleomagnetic Unit 3 reveals a single component of magnetization, which trends to the origin of orthogonal vector plots after the removal of a minor, low-inclination component (Fig. 33). Interestingly, AF demagnetization is also an adequate technique for isolating the characteristic remanent magnetization for brown claystone samples (Fig. 34) in the poorly recovered interval between Units 2 and 3. High-coercivity ferromagnetic minerals, which might be associated with the brown coloration, apparently are not the major contributor to the remanence. Measurement of these brown claystones indicates that the normal polarity that characterizes Unit 3 extends upward to at least Core 143-869B-32R.

Some samples from paleomagnetic Unit 2 have a demagnetization behavior that differs greatly from that displayed by the samples from paleomagnetic Unit 3. Such samples show a large angular difference between the NRM and vector end point after demagnetization at relatively high peak AFs (60–80 mT) (Fig. 35). This behavior is similar to that observed at other Pacific Ocean sites, where a present-day overprint has been removed from a sample having a primary reversed-polarity component, as discussed above. A great circle path is defined by the vector end points (Fig. 35) and marks the vector track of a normal-polarity overprint-declination value to a reversed-polarity primary-declination value. The angular difference between the NRM and primary direction differs from 180° by only the small rotation of

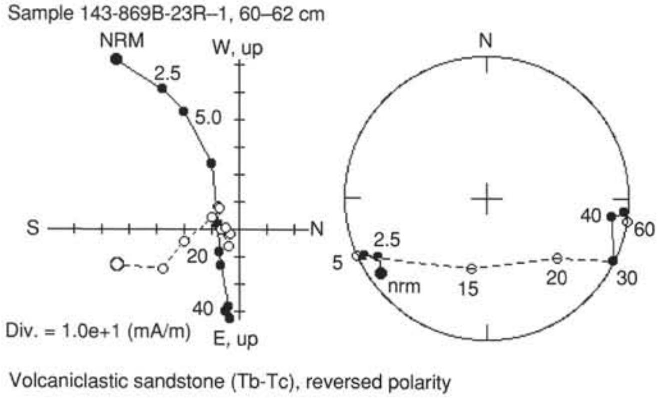

Figure 35. Orthogonal vector plot (left) of progressive AF demagnetization of volcaniclastic Sample 143-869B-23R-1, 60–62 cm. Demagnetization steps shown (mT): 0, 2.5, 10.0, 15.0, 20.0, 30.0, 40.0, 50.0, 60.0. Other plot conventions as in Figure 33.

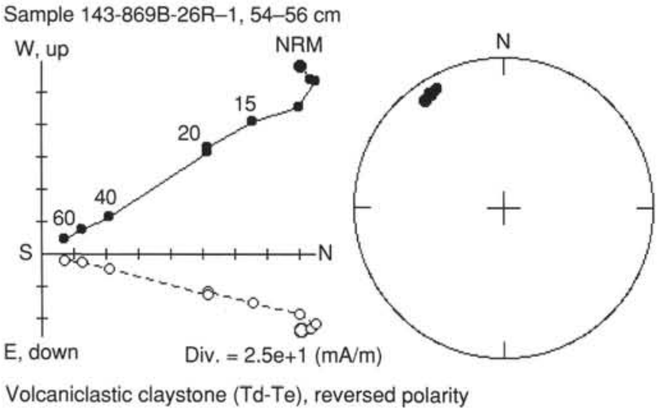

Figure 36. Orthogonal vector plot (left) of progressive AF demagnetization of volcaniclastic claystone Sample 143-869B-26R-1, 54–56 cm. Demagnetization steps shown (mT): 0, 2.5, 10.0, 15.0, 20.0, 30.0, 40.0, 50.0, 60.0. Other plot conventions as in Figure 33.

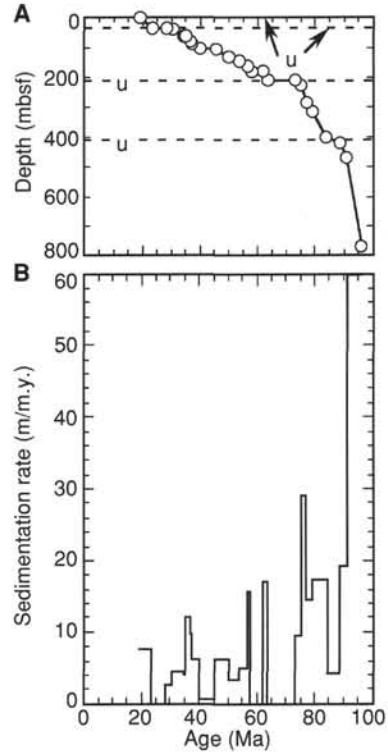

Figure 37. **A.** Age vs. depth plot for Site 869. **B.** Sedimentation rate vs. age for Site 869. Unconformities denoted by "u" (see text for details).

the Pacific Plate since the Late Cretaceous and by inadequacies in the AF cleaning (see Tarduno et al., 1989 for discussion). Other samples from paleomagnetic Unit 2 display a simpler demagnetization behavior, similar to that displayed by the discrete samples from paleomagnetic Unit 3, but having an inclination of opposite sign (Fig. 36).

In summary, data from the discrete samples indicate that the pass-through measurements are an accurate measure of polarity and confirm the correlation of magnetic units with polarity chrons. Differential overprinting of the present-day field, as observed in the discrete samples, most likely explains the scattered inclination values observed in the pass-through measurements of paleomagnetic Unit 2. This differential overprinting is probably related to lithology. For example, a volcaniclastic claystone (Te) shows only a minor overprint component (Fig. 36), while a coarser- grained volcaniclastic sample (Tb–Tc) displays a large overprint component (Fig. 35). The available data suggest that the coarser-grain lithologies may record a more substantial overprint, perhaps reflecting a greater range of magnetic grain sizes. Further shore based studies will be needed to test this suggestion.

The relatively simple magnetic behavior exhibited by the discrete samples from paleomagnetic Unit 3, the high sedimentation rates implied by the biostratigraphic data (see "Biostratigraphy" section, this chapter), and the continuity of the recovered turbidite cores permits a near-continuous evaluation of magnetic polarity for most of the upper Cenomanian and part of the middle Cenomanian, based on the pass-through cryogenic magnetometer measurements. In no interval was any evidence for reversed polarity observed. This shipboard survey lends further support to the suggestion that previously reported intervals of brief reversed polarity in Cenomanian sediments from the Ruhr area of Germany (Hambach and Krumsiek, 1989) result instead to overprinting in a Matuyama (or late Tertiary) field (Tarduno et al., 1992).

SEDIMENTATION RATES

Figure 37 shows the depth-vs.-age plot and sedimentation rates for the Cenozoic and Cretaceous section recovered in Holes 869A and 869B. The ages used in calculations are based on nannofossil zonal boundaries taken from the Berggren et al. (1985) time scale for the Cenozoic and from the Kent and Gradstein (1985) time scale for the Cretaceous. In Figure 37A, sub-bottom depth has been plotted vs. age. This plot shows the position of four postulated unconformities. These include (1) the top of Hole 869A, where we spudded into lower Miocene sediments, (2) across the Oligocene/Miocene boundary, (3) the upper Paleocene; and (4) the Cretaceous/Tertiary boundary. The latter unconformity includes part of the lower Paleocene and much of the Maastrichtian. Kent and Gradstein's time scale (1985) does not give ages for several of Sissingh's zonal markers (1977), which we used to date the section. Thus, this plot shows less detail than is apparent from our preliminary biostratigraphic investigations. Missing also from the section is much of the Santonian and part of the Coniacian at an unconformity at the base of Core 143-869B-30R.

Figure 37B shows a plot of age vs. sedimentation rate for Holes 869A and 869B. This illustrates somewhat variable rates of deposition in the lower Miocene and Paleogene part of the section, between 0.7 and 17 m/m.y. Some of this variation may be derived from the nondetailed sampling that forms the basis of this analysis or from our assumption that certain zones are complete in these holes, whereas they may be only partly represented. Note that average Cenozoic sedimentation rates are higher than in the contemporaneous part of

Site 865, on the summit of Allison Guyot. This may result from the large flux of radiolarians at this site or from the possible downslope redeposition of part of the sediment fraction, including nannofossils.

Figure 37B differentiates the sedimentary environments that led to the deposition of the Cretaceous section in Hole 869B. Campanian turbiditic sediments were deposited at rates between 15 and 30 m/m.y., whereas rates between 4 and 9 m/m.y. characterized hemipelagic deposition. The sedimentation rate of 60 m/m.y. calculated for the middle and upper Cenomanian volcaniclastic deposits is a minimum estimate that assumes: (1) a Cenomanian/Turonian boundary age of 91 Ma, (2) that we actually identified the first occurrence of *Lithraphidites acutus* in Core 143-869B-66R, and (3) that the age given for this datum by Kent and Gradstein (1985) is accurate. In fact, recent age estimates for the Cenomanian/Turonian boundary lie close to 93 Ma (J.D. Obradovich, pers. comm., 1992). In addition, because *L. acutus* has a patchy occurrence in this hole, it is possible that its range extends down to the base of the section. Finally, the age of this datum given by Kent and Gradstein (1985) is probably a little old. Therefore, it is not unreasonable to suppose that the entire Cenomanian section was deposited in 1 m.y. or less at rates close to 300 m/m.y.

INORGANIC GEOCHEMISTRY

Interstitial Waters

Interstitial waters were taken from 15 core samples in Holes 869A and 869B and analyzed according to the methods outlined in the "Explanatory Notes" chapter (this volume). Five of these samples came from Miocene to Eocene nannofossil and radiolarian oozes in Hole 869A, and 10 samples from the volcaniclastic-dominated strata of Campanian age in Hole 869B (Table 3).

Salinity and Chlorinity

Pore-water salinities in Holes 869A and 869B range from 35 to 41‰. Samples from the upper 420 mbsf have salinities that are similar to seawater, whereas samples from 691.5 mbsf and below have salinities of 39 to 41‰ (Fig. 38). Chlorinity values are similar to those of seawater throughout both holes (547–591 mM Cl^-; Fig. 38). A minimum chlorinity value of 547 mM Cl^- was measured in the sample from Section 143-869B-20R-2 with a maximum value of 591 mM in the sample from Section 143-869B-59R-1.

Alkalinity and pH

The alkalinity and pH measurements have mean values of 3.15 ± 0.3 and 7.68 ± 0.07 in Hole 869A and 0.68 ± 0.3 and 7.77 ± 0.45 in Hole 869B, respectively. The major trend in the alkalinity and pH values throughout both holes indicates that alkalinity decreases dramatically with depth and pH increases slightly. This change in pore-water chemistry is associated with the lithologic change between the nannofossil and radiolarian oozes in Hole 869A and the volcaniclastic-dominated facies in Hole 869B. The large decrease in alkalinity is related to the decrease in cations in the pore waters within the volcaniclastic sediments (Table 3). Superimposed on the major alkalinity change (between Holes 869A and 869B), is a subtle trend toward increasing alkalinities within Hole 869A, which may be related to organic carbon degradation.

Calcium, Magnesium, Sodium, Potassium, Strontium, and Rubidium

Concentrations of the cations that were measured in Holes 869A and 869B all show significant downhole changes. Calcium concentrations are near that of seawater in Hole 869A (10.7 ± 0.4 mM), but increase to a maximum of 190.6 mM in Sample 143-869B-31R-1 (Table 3; Fig. 38). Magnesium concentrations are near that of seawater in Hole 869A (53.3 ± 0.48), but decrease through Hole 869B to a minimum of 4.4 mM in Sample 143-869B-31R-1 (Table 3; Fig. 38). The average change between Holes 869A and 869B is 1017% or a 98.1 mM increase for calcium and 77% or a 41.3 mM decrease for magnesium.

The sodium concentrations in Hole 869A are near seawater values (473 ± 28 mM), but decrease by 24% or 112 mM to a mean of 361 ± 97 mM in Hole 869B. Similar trends occur in the potassium concentrations: pore-water potassium concentrations are similar to those of seawater in Hole 869A (10.4 ± 0.5), but decrease to a minimum of 0.5 mM in Hole 869B. This decrease in potassium is, on average, 8.8 mM or 85% between Holes 869A and 869B. Strontium concentrations increase from 75 µM in the uppermost sample of Hole 869A to a minimum of 291 µM in Hole 869B. A sharp increase occurs at the break between Holes 869A and 869B. Rubidium concentrations decrease from 1.84 µM in the uppermost sample of Hole 869A to 0.17 µM in the deepest measurement from Hole 869B.

Table 3. Interstitial-water data from Holes 869A and 869B.

Core, section interval (cm)	Depth (mbsf)	Water (mL)	pH	Alkal.	Salin. (‰)	K^+ (mM)	Na^+ (mM)	Rb^+ (µM)	Sr^{2+} (µM)	Cl^- (mM)	PO_4 (µM)	NH_4 (µM)	Si^{4+} (µM)	SO_4 (mM)	Ca^{2+} (mM)	Mg^{2+} (mM)
Hole 869A																
1H-5, 145–150	7.5	72.0	7.75	2.87	36.0	10.93	466.	1.84	75.	556.	1.60	8.	442.	27.41	10.6	53.0
4H-5, 145–150	36.2	40.0	7.60	3.07	36.0	10.44	469.	1.83	75.	564.	1.97	13.	569.	27.00	10.4	53.9
7H-5, 145–150	63.3	26.0	7.60	3.09	36.0	10.27	469.	1.77	76.	568.	2.35	22.	726.	26.76	10.7	53.5
10X-1, 145–150	87.2	72.0	7.63	3.25	36.0	10.74	477.	1.78	76.	564.	4.60	0.	1297.	27.52	10.8	53.5
13X-3, 145–150	120.0	60.0	7.75	3.45	36.0	9.48	437.	1.73	82.	568.	4.60	0.	1176.	25.56	11.3	53.1
Hole 869B																
10R-1, 145–150	218.7	16.0	7.58	0.70	35.5	2.96	409.	0.24	228.	558.	0.84	17.	371.	20.79	63.3	20.3
11R-2, 145–150	229.9	28.0	7.89	0.34	36.0	2.39	426.	0.35	291.	565.	1.20	31.	247.	21.36	63.5	18.3
13R-1, 145–150	247.7	33.0	6.96	0.79	35.5	1.80	386.	0.27	276.	563.	1.60	28.	202.	19.15	62.8	17.5
17R-2, 0–5	285.8	4.0			35.0	2.24	430.		273.	560.		70.		20.84		
20R-2, 145–150	316.8	25.0	8.19	0.58	36.5	1.71	431.	0.24	285.	547.	1.20	42.	143.	21.34	72.3	14.3
23R-1, 145–150	344.3	26.0	8.22	0.99	36.5	1.81	447.	0.23	272.	567.	1.20	38.	158.	23.63	70.4	15.3
31R-1, 145–150	421.6	5.5			36.5	1.86	414.	0.17	291.	570.	1.97	60.	659.	20.23	95.1	6.1
59R-1, 146–150	691.5	4.0			41.0	0.65	222.		120.	591.	0.69	48.	167.	12.55	190.6	4.4
65R-2, 145–150	750.9	15.0			39.0	0.50	208.		244.	561.	0.69	45.	257.	17.03	186.9	4.6
69R-1, 27–32	788.0	7.5			39.0	0.51	246.		251.	571.	0.69	24.	228.	17.54	173.9	7.2

Alkal. = alkalinity; Salin. = salinity. Core designations include the core, drill type (H = hydraulic pistion corer, X = extended core barrel, R = rotary) and section number; water = water yield in the analyzed samples.

The changes in pore-water concentration in the measured cations have been interpreted as reflecting diagenetic changes within the volcaniclastic sediments. Calcium and strontium are released from feldspars of the volcaniclastics, whereas magnesium, potassium, sodium, and rubidium are incorporated in the alteration products of the volcaniclastic sediments and, thus, are reduced in the pore water. The increase in salinity that was observed in the three lowest samples results from an increase in calcium that more than compensates for decreases in the concentration of other cations (Table 3; Fig. 38).

Silica

Silica concentrations range between 143 and 1297 μM (Table 3). The silica content of the pore water in general, and especially in Section 143-869B-13X-3, reflects the high biogenic silica concentrations in the radiolarian oozes of Hole 869A.

Ammonium, Sulfate, and Phosphate

The ammonium content varies between 0 and 70 μM, but all of the samples in Hole 869A contained little (≤22 μM) or no ammonium, whereas the samples from Hole 869B indicate a slight trend toward increasing concentration with depth (Fig. 39). The sulfate values decrease with depth (from 27.4 mM at the top of Hole 869A to 12.55 mM in Section 143-869B-59R-1, Fig. 39), indicating a progressive increase in the amount of sulfate reduction. The increases in ammonium and decreases in sulfate concentrations in Holes 869A and 869B presumably are associated with organic-matter decomposition.

Phosphate values are near the detection limit (~1 μM) of the analytical method (see "Explanatory Notes" chapter, this volume), with a maximum concentration of 4.6 μM in Sections 143-869A-10X-1 and -13X-3. No increases in phosphate concentrations were observed in the volcaniclastic sediments.

ORGANIC GEOCHEMISTRY

At Site 869, in addition to safety monitoring for hydrocarbon gases, 234 samples were used to determine carbonate content with the Coulometrics carbon dioxide coulometer. Total nitrogen, sulfur, and carbon contents were measured by means of an NA 1500 Carlo Erba NCS analyzer. The procedures used for these analyses are outlined in the "Explanatory Notes" chapter (this volume).

Volatile Hydrocarbons

As part of the shipboard safety and pollution monitoring program, the hydrocarbon gases were measured in the sediments at Site 869, using the headspace technique and the Carle gas chromatograph to determine C_1–C_3 concentrations. The results of 39 headspace analyses are reported in Table 4. Only very low levels of volatile hydrocarbon were detected. Methane concentrations range from 2 to 5 ppm, whereas traces of ethane are noted, but are below the concentration threshold of the integrator. Compared with a laboratory background of 2 ppm, the concentrations in the sediment are minor. The low overall content of methane in the sediments suggests that either the biogenic methane usually produced during microbial degradation of organic matter migrated out of the sedimentary column, or that conditions were not favorable enough to sustain methanogenesis.

Inorganic Carbon

In Hole 869A, 71 samples were analyzed for inorganic carbon (IC). The calcium carbonate content is variable in relation to the primary nature of the lithologic facies (Table 5). According to the calcium carbonate record, the sedimentary sequence in Hole 869A can be divided into three parts (Fig. 40) that correspond well to lithologic Subunits IA and IB and Unit II (see "Lithostratigraphy" section, this chapter). The upper 32.5 mbsf is characterized by high-amplitude variations that range from 23.6% to 93.4% $CaCO_3$, with a general upward decrease. The brown radiolarian ooze shows low-to-moderate carbonate content (between 23.6% and 53.7%), whereas light-beige nannofossil ooze indicates higher values. The transition between beige and brown ooze is well documented. For example, a progressive upward decrease of carbonate content from light-beige ooze to overlying beige and brown radiolarian ooze was established from the data of Core 143-869A-2H (Table 5). The redeposited white level occurring in Interval 143-869A-4H-3, 77–78 cm (see "Lithostratigraphy" section, this chapter) defines the base of the first part. The second part (Sections 143-869A-4H-3 to -9H-2), corresponding to Subunit IB, shows relatively constant, high calcium carbonate contents, with values everywhere exceeding 91%. The third part (Section 143-869A-9H-4 to Core 143-869A-15X) is characterized by an upward increase of calcium carbonate, with short-term high-amplitude variations. The $CaCO_3$ contents fluctuate between 6.7% and 73.2%, which corresponds to the chert and claystone alternations of lithologic Unit II.

In Hole 869B, 163 samples were analyzed for IC (Table 6). The brown cherts occurring in Cores 143-869B-2R to -9R, and corresponding to lithologic Unit II have very low calcium carbonate content (<1%), except for a white siliceous chalk (Sample 143-869B-4R-1, 46–47 cm) that contains 76.6% $CaCO_3$ (Fig. 41). Between 207.7 and 458.8 mbsf (lithologic Subunits IIIA and IIIB), the carbonate record shows high-amplitude variations from 0.2% to 83.3%. The volcaniclastic sandstones and radiolarian claystones present lower values, whereas nannofossil-rich claystone and mudstone levels show high values. The thin Subunit IIIC is characterized by a sharp decrease of calcium carbonate content to values below 16.2%. The redeposited volcaniclastic facies forming lithologic Subunits IIID to IIIF contain little calcium carbonate (<5%), except for a few horizons that occur in Cores 143-869B-48R, -50R, -51R, and -55R, where fine sandy facies contain between 13% and 60% $CaCO_3$. It seems that within the turbidite beds the coarser layers indicate lower calcium carbonate contents than the interlayers of fine sandstone and claystone beds. Subunit IIIG, where calcareous claystone with radiolarians and pale green mudstone are present again, shows a slight increase of carbonate (Fig. 41).

Organic Carbon Contents

Total organic carbon (TOC) values were calculated by difference between total carbon, determined with the NCS analyzer, and IC. The results of 234 analyses from Holes 869A and 869B are reported in Tables 5 and 6, respectively. Total nitrogen and sulfur concentrations commonly are below the detection threshold of the NCS analyzer (Table 5). Thus, TOC/N and TOC/S ratios tend thus to be highly variable; the highest ratios are generally recorded in samples that are low in both nitrogen and sulfur.

In Hole 869A, the total organic carbon contents are very low. TOC fluctuates from 0% to 0.67%, with a mean value of 0.15% (Fig. 42).

In Hole 869B, the organic contents measured are low throughout the sampled interval. TOC fluctuates from 0% to 0.76% (Fig. 43). The lowest TOC contents can be found in the chert facies of lithologic Unit II and in the coarse volcaniclastic facies of lithologic Subunits IIID to IIIF. These values are somewhat higher in fine siltstone and claystone levels of Unit III, but still remain below 0.7% TOC. Surprisingly, some beige claystones and volcaniclastic sandstones contain about 0.5% TOC. It is not yet clear if these values are geochemically significant or if they are at least partly the result of a systematic error in the analytical procedure (e.g., by acid-resistant carbonate which could yield too high a difference between total carbon and IC).

Twelve samples were analyzed using the Geofina hydrocarbon meter (Table 7). Only four samples show values that can be interpreted. In accordance with their low organic carbon content, their

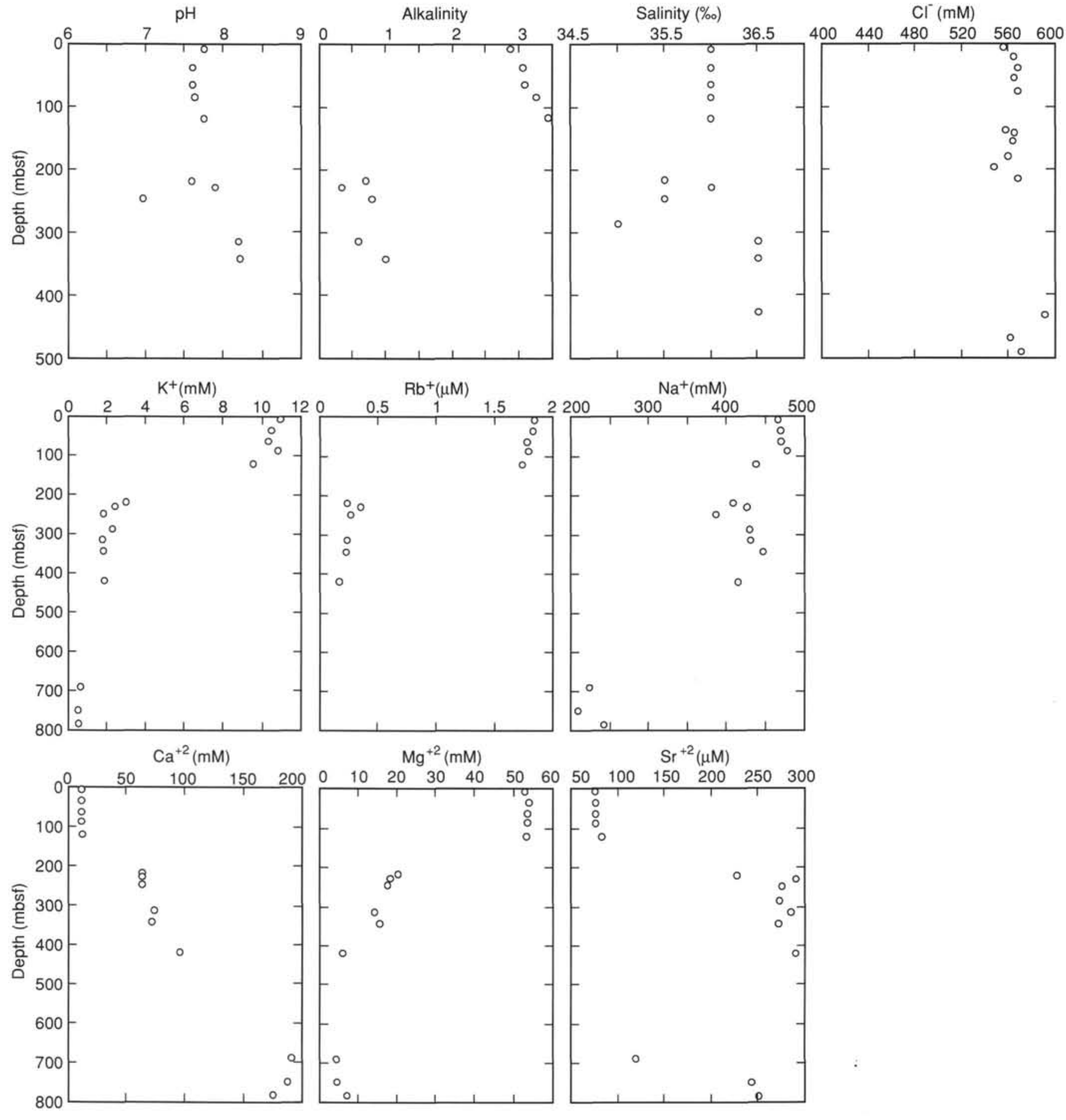

Figure 38. The pH, alkalinity, salinity, and concentrations of chloride, potassium, rubidium, sodium, calcium, magnesium, and strontium as a function of depth in Holes 869A and 869B.

hydrocarbon potential is very low. S_1 signals are extremely low, and S_2 values remain below 0.24 mg hydrocarbon/g dry sediment. Furthermore, T_{max} parameters were difficult to calculate on the basis of very flat S_2 peaks. T_{max} values (ranging from 345 to 454) indicate that no clear maximum is discernible. The approximate HI values are very low (<58 mg hydrocarbons/g TOC) and indicate that the organic matter may consist of so-called "dead carbon" or type IV organic matter (i.e., organic matter that has been completely oxidized and deprived of its hydrogen content).

PHYSICAL PROPERTIES

Introduction

Site 869 objectives were to drill the deep-apron location Syl-3 to recover sediments having a possible provenance from Wodejebato Guyot and Pikinni Atoll. The objectives of the physical-property measurement program were (1) to measure the standard shipboard physical properties, to analyze *P*-wave velocities in unlithified to fully lithified

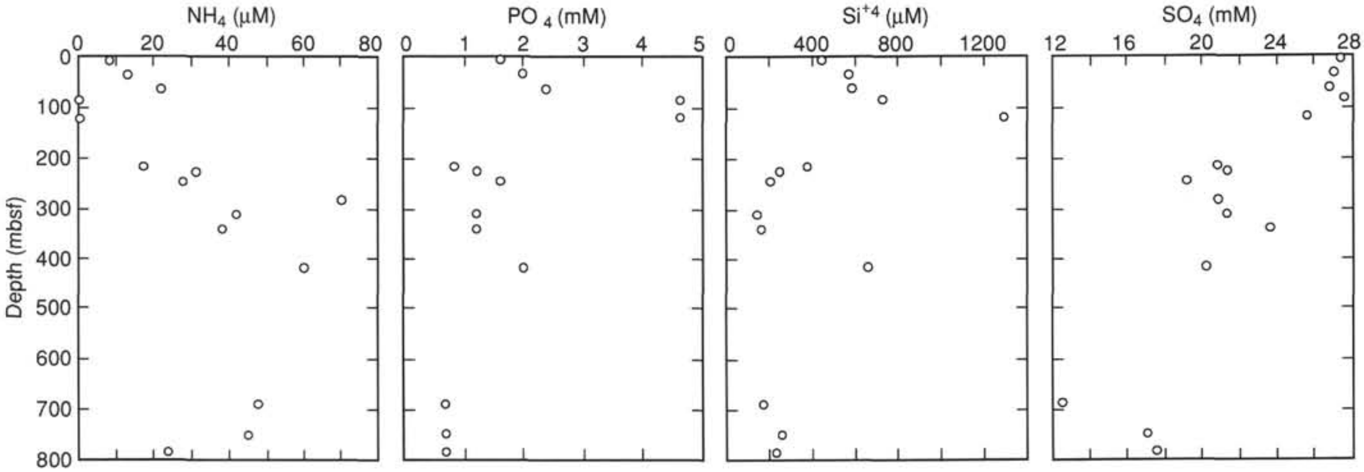

Figure 39. Concentrations of ammonium, phosphate, silica, and sulfate as a function of depth in Holes 869A and 869B.

sediments, to measure thermal conductivity, and to collect GRAPE-density and *P*-wave velocity data from the multisensor track (MST); and (2) to identify physical-property units for correlation with downhole logs (sonic velocity, gamma-ray, and density), lithology, and with discrete measurements of *P*-wave velocity and index properties.

Sediments recovered at Site 869 comprise unlithified to semilithified nannofossil and radiolarian ooze (0–207.7 mbsf) and volcanic claystone, sandstone, and breccia, alternating with intervals of nannofossil to radiolarian-rich claystone and chalk (207.7–796.2 mbsf).

The unlithified to semilithified sediments, drilled with the APC and XCB, showed variable indications of coring disturbance. Nevertheless, they were run through the MST for GRAPE density and *P*-wave velocity and measured for thermal conductivity. In addition, measurements for *P*-wave velocity were performed using the digital sound velocimeter (DSV) down to a depth of 226.9 mbsf in Hole 869B and then cored with the RCB. At this depth, sediments were too dense and too physically disturbed to use the DSV longer, so discrete samples were collected from deeper intervals for *P*-wave velocity measurements in both longitudinal and transverse directions with the Hamilton Frame apparatus. For each pair of horizontal and vertical velocity measurements, the anisotropy was calculated. Discrete measurements of index properties in Hole 869A: bulk density, porosity, water content (expressed as percentage of dry weight), and grain density seemed to be in good agreement with the GRAPE-density logs. In Hole 869B, index properties were measured using the cubes collected for *P*-wave velocity measurements. No correction for salt content was made (see "Physical Properties" section, "Site 866" chapter, this volume).

In general, recovery was good and permitted correlations among the various tools measuring density (GRAPE-density and density from discrete measurements of beaker samples and cubes) and *P*-wave velocity (*P*-wave logger, DSV, and discrete measurements). Furthermore, correlations could be made among lithology, physical-property units, and well logs.

Data for Holes 869A and 869B are presented in Tables 8, 9, 10, and 11, giving the index properties, discrete sonic velocity measurements, velocity measurements performed with the DSV and thermal conductivity readings, respectively, as a function of depth. Figure 44 presents the depth distribution of index properties, GRAPE density, and sonic velocity from discrete measurements for both Holes 869A and 869B. Figure 45 shows the depth distribution of *P*-wave velocity from the MST (*P*-wave logger) and velocity measured by the DSV, discrete bulk-density measurements, and GRAPE density for Hole 869A. Figure 46 shows the depth distribution of sonic velocity and anisotropy of sonic velocity from discrete measurements and velocity from the DSV, bulk density (discrete measurements), and percentage of recovery. Bulk density and sonic velocities from physical-properties sediments have been compared with log measurements and lithologic units in Figure 47.

Physical Property Units

Five major physical-property units were defined for Site 869 on the bases of significant downhole trends in index properties, *P*-wave measurements, and in one instance, anisotropy of sonic velocity. Only a few boundaries have been associated with lithologic features. Depending on recovery and sample-spacing, most boundaries for physical property (PP) units have been arbitrarily placed midway between discrete samples (see Fig. 46). In the following section, unless mentioned otherwise, data presented for sonic velocity are those measured in the vertical direction from cubes. Similarly, data about index properties were those measured from cubes.

Physical Property Unit 1 (Hole 869A: 0–166.5 mbsf; Hole 869B: 149.6–210 mbsf)

This unit consists of unlithified to semilithified clayey nannofossil to radiolarian ooze with, near the bottom, chert intervals. In the upper part, between 0 and 80 mbsf, recovery was near 100%. From about 80 to 145 mbsf, recovery was approximately 60%, but between 145 and 210 mbsf, recovery was only about 5%. Along with trends in physical properties, percentage of recovery was used to identify the boundaries of the PP units. Sonic velocity shows a gradual downhole increase to about 145 mbsf. Between 145 and 210 mbsf, recovery decreases abruptly, and high-velocity lithologies were recovered. Bulk density increases gradually down to about 75 mbsf, decreases downhole between 75 and 100 mbsf, and remains steady down to about 150 mbsf. Between 150 and 225 mbsf, preferentially high-density lithologies were recovered.

Physical Property Subunit 1a (Hole 869A: 0–80 mbsf)

The lower boundary of this subunit, consisting of unlithified clayey nannofossil to radiolarian ooze, has been defined by the abrupt changes in recovery and bulk density (measured from discrete samples) at 80 mbsf. However, sonic velocity shows a gradual increase over this range (both from discrete samples as well as from the DSV) from 1.45 to 1.55 km/s. Overall, bulk density increases downcore from 1.2 to 1.8 g/cm^3, porosity shows scattered values in the first 50 mbsf, followed by steady values of 55% to 60%, and water content (% dry weight) decreases from 60% to 40%.

Table 4. Hydrocarbon gas data for Site 869.

Core, section, interval (cm)	Depth (mbsf)	Sample type[a]	C_1 (ppm)
Hole 869A			
1H-5, 142–143	7.42	HS	3
3H-4, 0–3	23.70	HS	3
4H-6, 0–3	36.20	HS	4
5H-6, 0–3	45.70	HS	3
6H-6, 0–3	55.20	HS	3
7H-6, 0–3	63.32	HS	3
8H-4, 0–3	69.75	HS	2
9H-2, 0–3	77.70	HS	3
10X-2, 0–3	87.20	HS	2
11X-3, 0–3	98.50	HS	3
12X-3, 0–3	108.50	HS	4
13X-3, 142–145	119.92	HS	3
14X-4, 147–150	131.47	HS	3
15X-6, 69–71	143.69	HS	2
Hole 869B			
11R-2, 142–145	229.82	HS	2
13R-1, 142–145	247.62	HS	3
15R-4, 147–150	271.37	HS	3
16R-1, 0–3	275.10	HS	3
17R-2, 2–5	285.85	HS	3
18R-CC, 0–3	294.40	HS	3
19R-3, 84–85	307.94	HS	3
20R-2, 142–145	316.72	HS	3
21R-1, 106–107	324.56	HS	3
22R-1, 147–150	334.57	HS	3
23R-1, 142–145	344.22	HS	3
25R-3, 88–89	366.08	HS	3
26R-1, 149–150	373.29	HS	3
27R-1, 40–41	381.90	HS	3
28R-CC, 18–19	391.28	HS	3
29R-CC, 8–9	400.88	HS	3
32R-1, 0–3	429.80	HS	3
35R-1, 37–38	459.17	HS	3
36R-1, 144–145	469.84	HS	4
37R-CC, 0–3	478.10	HS	4
38R-3, 140–142	491.24	HS	3
39R-CC, 10–11	500.22	HS	3
49R-CC, 0–3	593.50	HS	5
57R-4, 0–3	675.20	HS	4
65R-2, 144–145	750.84	HS	3

[a] HS = headspace vial.

Physical Property Subunit 1b (Hole 869A: 80–145 mbsf)

Subunit 1b mainly consists of nannofossil ooze and, downcore, has relatively constant index properties and sonic velocity. The upper boundary was defined on the bases of an abrupt shift in bulk density (discrete samples), from 1.70 to 1.55 g/cm^3 (downcore), and recovery, from 100% to 30%. The lower boundary was selected where recovery decreased to about 5% to 10% and the chert intervals were first cored. On average, bulk density has values that range from 1.23 to 2.15 g/cm^3, water content ranges from 1.85% to 222.5% (dry weight), and porosity ranges from 3.91% to 90.3%. Sonic velocity, measured by the DSV, is relatively constant and varies between 1.50 and 1.55 km/s. One core (Section 143-869A-10X-CC) contained a chert pebble with a sonic velocity (measured on the Hamilton Frame) of 3.95 km/s. Overall, physical properties in this unit were constant, and it had lower densities and velocities than the overlying PP Subunit 1a.

Physical Property Subunit 1c (Hole 869A: 145–166.5 mbsf; Hole 869B: 149.6–210 mbsf)

Physical property measurements in Subunit 1c were limited to well-indurated chert intervals, as the softer clayey nannofossil to radiolarian oozes were washed out. Recovery was on average lower than 5%. Discrete measurements of index properties and sonic velocity thus are not representative for in-situ values. Bulk density ranges from 1.43 to 2.54 g/cm^3, water content (% dry weight) ranges from 0.94% to 110.05%, and porosity varies between 2.28% and 74.96%. Sonic velocity from cubes ranges from 2.07 to 4.91 km/s. The upper and lower boundaries of this subunit were selected at the first and last occurrences of high velocities caused by the presence of chert intervals.

Physical Property Unit 2 (Hole 869B: 210–377 mbsf)

Physical property Unit 2 had variable recovery, with values ranging between 5% and 50%, that reflect the alternation of semi-indurated nannofossil claystone and calcareous layers and volcaniclastic sand- to siltstone. Consequently, physical properties are variable. Bulk density values range from 1.47 to 2.58 g/cm^3, with a mean of 1.98 g/cm^3. Water content ranges from 7.46% to 89.36%, with a mean of 42.26%, and porosity varies between 17.94% and 71.81%, with an average of 50.09%. *P*-wave velocity ranges from 1.05 to 2.67 km/s, with an average of 1.95 km/s. The slightly lower values of bulk density and velocity correspond to the less-indurated and more-porous nannofossil claystone and calcareous layers. The lower boundary of PP Unit 2 corresponds with an abrupt downcore increase of sonic velocity at approximately 377 mbsf.

Physical Property Unit 3 (Hole 869B: 377–534 mbsf)

Physical properties in Unit 3 show a decrease downcore in bulk density and sonic velocity in the interval from 377 to 425 mbsf (Subunit 3a), followed by a gradual increase downcore in the lower interval from 425 down to 534 mbsf (Subunit 3b). Sediments consist of radiolarian clay- to siltstone and, near the base of Subunit 3b, volcaniclastic breccias. An overall increase in recovery occurs downcore from about 5% to 50%, corresponding to the gradual increase downcore in volume of volcaniclastics.

Physical Property Subunit 3a (Hole 869B: 377–425 mbsf)

Sediments in this PP subunit are predominantly radiolarian claystone and thin layers of volcaniclastic silt to sand. Physical properties, bulk density, and sonic velocity near the top of the unit are higher and more constant than in the overlying PP Unit 2. Bulk density ranges from 1.87 to 2.14 g/cm^3, with an average of 2.02 g/cm^3, water content ranges from 12.31% to 32.47%, with a mean value of 19.61%, and porosity ranges from 22.80% to 47.00%, with a mean value of 32.09%. Sonic velocity shows a gradual decrease downcore from about 3 to 2 km/s near the lower boundary of this unit. This boundary with underlying PP Subunit 3b marks a sharp break in density and sonic velocity.

Physical Property Subunit 3b (Hole 869B: 425–534 mbsf)

The upper part of PP Subunit 3b consists of radiolarian claystone and siltstone, as in overlying Subunit 3a, and has moderately low values of bulk density and sonic velocity that range from about 1.8 to 1.9 g/cm^3 and from 2 to 2.5 km/s, respectively. The lower part of Subunit 3b consists of a thick interval of volcaniclastic breccia (lithologic Unit IIID) and shows an increase downcore in density and velocity up to 2.1 g/cm^3 and about 4 km/s, respectively. The lower boundary of PP Subunit 3b is sharp and corresponds to a rapid decrease in sonic velocity in underlying Unit 4. In addition, this boundary correlates with the change from lithologic Subunits IIID to IIIE. In general, values of bulk density range from 1.81 to 2.28 g/cm^3, with an average of 2.04 g/cm^3, water content ranges from 9.39% to 34.85%, with a mean of 22.17%, and porosity varies between 19.60% and 48.01%, with an average of 35.89%. *P*-wave velocity ranges from 1.88 to 4.02 km/s, with a mean of 2.74 km/s. The gradual increase downcore of sonic velocity and, in part, bulk density (in the lower part of Subunit 3b) about 380 down to 534 mbsf, corresponds to a

Table 5. Concentrations of total, inorganic, and organic carbon and of total nitrogen and sulfur in sediments from Hole 869A.

Core, section, interval (cm)	Depth (mbsf)	Sample type[a]	TC (%)	IC (%)	TOC (%)	$CaCO_3$ (%)	N (%)	S (%)	TOC/N	TOC/S	Lithology
143-869A-											
1H-1, 81–82	0.81	CARB	8.72	8.61	0.11	71.7	0.01	0.23	11.0	0.5	Light-brown ooze
1H-5, 77–78	6.77	CARB	2.94	2.83	0.11	23.6	0.01	0.00	11.0		Brown ooze
1H-5, 145–150	7.45	IWSC	11.14	11.10	0.04	92.5	0.05	0.00	0.8		Light-brown ooze
2H-1, 39–40	10.09	CARB	7.78	7.75	0.03	64.6	0.01	0.00	3.0		Light-brown ooze
2H-1, 60–61	10.30	CARB	6.63	6.41	0.22	53.4	0.00	0.06		3.6	Light-brown ooze
2H-1, 80–81	10.50	CARB	4.06	3.86	0.20	32.2	0.02	0.22	10.0	0.9	Brown ooze
2H-1, 100–101	10.70	CARB	7.51	7.36	0.15	61.3	0.01	0.10	15.0	1.5	Light-brown siliceous ooze
2H-2, 30–31	11.50	CARB	9.24	9.23	0.01	76.9	0.01	0.10	1.0	0.1	Light-brown ooze
2H-2, 50–51	11.70	CARB	7.05	6.89	0.16	57.4	0.01	0.18	16.0	0.9	Light-brown ooze
2H-2, 60–61	11.80	CARB	8.83	8.41	0.42	70.1	0.08	0.12	5.2	3.5	Light-brown ooze
2H-2, 65–66	11.85	CARB	9.08	9.04	0.04	75.3	0.03	0.08	1.0	0.5	Light-brown ooze
2H-2, 70–71	11.90	CARB	11.04	10.92	0.12	91.0	0.00	0.00			White ooze
2H-2, 75–76	11.95	CARB	10.97	10.93	0.04	91.0	0.00	0.04		1.0	White ooze
2H-2, 85–86	12.05	CARB	11.02	11.00	0.02	91.6	0.01	0.00	2.0		White ooze
2H-2, 100–101	12.20	CARB	11.09	11.07	0.02	92.2	0.01	0.00	2.0		White ooze
2H-5, 1–2	15.71	CARB	11.09	10.86	0.23	90.5	0.01	0.00	23.0		Light-brown ooze
2H-5, 20–21	15.90	CARB	11.22	11.21	0.01	93.4	0.01	0.00	1.0		White ooze
2H-5, 40–41	16.10	CARB	10.88	10.87	0.01	90.5	0.00	0.00			Light-brown ooze
2H-5, 59–60	16.29	CARB	10.99	10.81	0.18	90.0	0.00	0.00			Light-brown ooze
2H-5, 79–80	16.49	CARB	10.95	10.90	0.05	90.8	0.00	0.00			White ooze
2H-5, 99–100	16.69	CARB	11.24	11.13	0.11	92.7	0.00	0.01		11.0	White ooze
3H-1, 69–70	19.89	CARB	10.34	10.01	0.33	83.4	0.07	0.00	4.7		Light-brown ooze
3H-3, 82–83	23.02	CARB	5.65	5.60	0.05	46.6	0.00	0.12		0.4	Brown ooze
3H-5, 73–74	25.93	CARB	10.22	9.96	0.26	83.0	0.00	0.00			White ooze
3H-7, 30–31	28.50	CARB	9.12	9.00	0.12	75.0	0.00	0.00			Light-brown ooze
4H-1, 76–77	29.46	CARB	9.82	9.74	0.08	81.1	0.01	0.01	8.0	8.0	Light-brown ooze
4H-3, 66–67	32.36	CARB	10.43	10.07	0.36	83.9	0.00	0.00			Light-brown ooze
4H-3, 71–72	32.41	CARB	8.13	8.01	0.12	66.7	0.00	0.05		2.4	Brown ooze
4H-3, 77–78	32.47	CARB	6.86	6.45	0.41	53.7	0.00	0.09		4.5	Brown ooze
4H-3, 81–82	32.51	CARB	11.53	11.34	0.19	94.5	0.01	0.00	19.0		White turbiditic layer
4H-3, 85–86	32.55	CARB	11.52	11.40	0.12	95.0	0.00	0.00			White ooze
4H-3, 92–93	32.62	CARB	11.46	11.33	0.13	94.4	0.00	0.00			Light-brown ooze
4H-5, 145–150	36.15	IWSC	11.92	11.57	0.35	96.4	0.03	0.16	11.0	2.2	Light-brown ooze
4H-6, 59–60	36.79	CARB	11.29	11.18	0.11	93.1	0.00	0.00			Light-brown ooze
5H-1, 101–102	39.21	CARB	11.44	11.24	0.20	93.6	0.00	0.00			Light yellowish ooze
5H-3, 25–26	41.45	CARB	11.31	11.16	0.15	93.0	0.01	0.12	15.0	1.2	Light yellowish ooze
5H-4, 78–79	43.48	CARB	11.65	11.34	0.31	94.5	0.01	0.00	31.0		White ooze
5H-6, 80–81	46.50	CARB	10.96	10.95	0.01	91.2	0.03	0.00	0.3		White ooze
6H-2, 76–77	49.96	CARB	11.31	11.10	0.21	92.5	0.00	0.00			White ooze
6H-4, 75–76	52.95	CARB	11.43	11.25	0.18	93.7	0.02	0.00	9.0		White ooze
6H-6, 75–76	55.95	CARB	11.26	11.17	0.09	93.0	0.00	0.00			Light yellowish ooze
7H-2, 39–40	57.71	CARB	11.47	11.32	0.15	94.3	0.01	0.00	15.0		White ooze
7H-2, 75–76	58.07	CARB	11.34	11.26	0.08	93.8	0.00	0.00			White ooze
7H-5, 145–150	63.27	IWSC	11.80	11.58	0.22	96.5	0.05	0.13	4.4	1.7	White ooze
8H-3, 77–78	69.02	CARB	11.65	11.58	0.07	96.5	0.05	0.00	1.0		White ooze
8H-6, 86–87	73.61	CARB	11.43	11.20	0.23	93.3	0.08	0.00	2.9		White ooze
8H-8, 71–72	76.46	CARB	11.47	11.51		95.9	0.07	0.00			White ooze
9H-2, 78–80	78.48	CARB	12.11	11.70	0.41	97.5	0.07	0.00	5.8		White ooze
9H-4, 79–81	81.49	CARB	7.98	8.00	0.00	66.6	0.07	0.24	0.0	0.0	Light-beige ooze
9H-6, 77–79	84.47	CARB	8.68	8.61	0.07	71.7	0.09	0.25	0.8	0.3	Light-beige ooze
10X-1, 73–74	86.43	CARB	8.06	7.39	0.67	61.6	0.10	0.00	6.7		Beige ooze
10X-1, 145–150	87.15	IWSC	6.20	5.98	0.22	49.8	0.07	0.24	3.1	0.9	Brown ooze
10X-2, 69–70	87.89	CARB	8.23	8.20	0.03	68.3	0.09	0.23	0.3	0.1	Light-beige ooze
10X-CC, 5–6	88.34	CARB	2.59	2.41	0.18	20.1	0.09	0.00	2.0		Siliceous chalk
11X-2, 82–83	97.82	CARB	7.33	6.91	0.42	57.6	0.08	0.30	5.2	1.4	White ooze
11X-4, 36–37	100.36	CARB	5.92	5.45	0.47	45.4	0.07	0.00	6.7		White ooze
12X-1, 62–63	106.12	CARB	8.89	8.79	0.10	73.2	0.08	0.25	1.2	0.4	White ooze
12X-4, 66–67	110.66	CARB	0.84	0.80	0.04	6.7	0.08	0.33	0.5	0.1	White ooze
12X-5, 104–105	112.54	CARB	8.65	8.64	0.01	72.0	0.12	0.25	0.1	0.0	White ooze
12X-5, 116–117	112.66	CARB	1.19	1.04	0.15	8.7	0.10	0.31	1.5	0.5	Light-beige ooze
13X-2, 23–24	117.23	CARB	1.14	0.88	0.26	7.3	0.17	0.40	1.5	0.7	Light-beige ooze
13X-3, 145–150	119.95	IWSC	0.49	0.35	0.14	2.9	0.06	0.00	2.3		Light-brown ooze
13X-4, 50–51	120.50	CARB	0.13	0.03	0.10	0.2	0.09	0.00	1.1		Light-beige ooze
13X-CC, 4–5	121.66	CARB	8.80	8.59	0.21	71.6	0.08	0.25	2.6	0.8	Light-beige ooze
14X-1, 86–87	126.36	CARB	5.94	6.03		50.2	0.85	0.00			Light-beige ooze
14X-3, 38–39	128.88	CARB	2.00	1.98	0.02	16.5	0.20	1.04	0.1	0.0	Light-beige ooze
14X-5, 46–47	131.96	CARB	0.14	0.04	0.10	0.3	0.10	0.00	1.0		Beige ooze
15X-2, 69–70	137.69	CARB	0.12	0.04	0.08	0.3	0.08	0.31	1.0	0.3	Light-beige ooze
15X-2, 114–115	138.14	CARB	0.54	0.49	0.05	4.1	0.10	0.26	0.5	0.2	White ooze
15X-4, 10–11	140.10	CARB	2.47	2.51		20.9	0.06	0.23			White ooze
15X-6, 32–33	143.32	CARB	2.28	2.25	0.03	18.7	0.08	0.25	0.4	0.1	White ooze

[a] Sample type: CARB = carbonate; IWSC = interstitial-water squeeze cake.

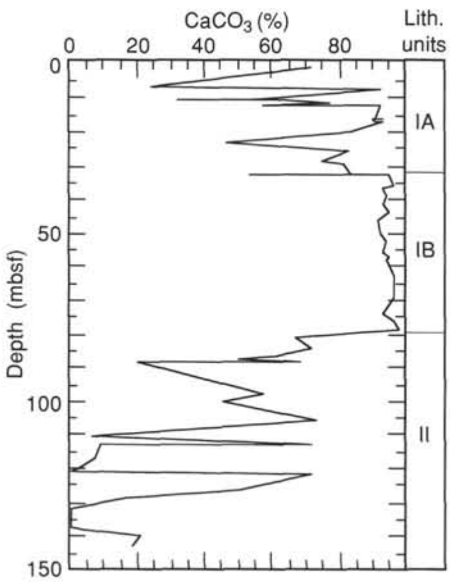

Figure 40. Depth distribution of calcium carbonate in Hole 869A.

change from more muddy, fine-grained volcaniclastics to predominantly coarse-grained, locally pebbly, cemented volcaniclastics (see "Lithostratigraphy" section, this chapter).

Physical Property Unit 4 (Hole 869B: 534–639 mbsf)

The top of PP Unit 4 is the well-defined lower boundary of a thick succession, about 55 m thick, that consists of coarse-grained volcaniclastic breccias then changes downcore into alternating radiolarian claystone, nannofossil chalk, and volcaniclastic siltstone and sandstone. Mass physical properties within Unit 4 are relatively constant downcore; bulk density varies between 1.96 and 2.45 g/cm^3, with an average of 2.12 g/cm^3, water content ranges from 5.49% to 28.45%, with an average of 19.67, and porosity ranges from 12.74% to 43.43%, with a mean value of 34.01%. Sonic velocity ranges from 2.14 and 4.73 km/s, with an average of 2.75 km/s. The lower boundary of PP Unit 4 shows a well-defined and abrupt downcore increase in the range of sonic velocity and correlates with the change from lithologic Subunit IIIE to the underlying lithologic Subunit IIIF (depth of boundaries are 639 and 653.3 mbsf, respectively). From about 600 mbsf downward, overall recovery increases dramatically from less than 5% to 70%. No apparent correlation is present between this change in recovery and physical properties and/or lithology.

Physical Property Unit 5 (Hole 869B: 639–796.2 mbsf)

On average, sonic velocity values in PP Unit 5 are slightly higher and more varied than those in the overlying PP Unit 4. The upper part of PP Unit 5, 639 to 720 mbsf (Subunit 5a), shows a high variance in sonic velocity, with values ranging from about 2.1 to more than 5 km/s. The lower part of PP Unit 5, 720 to 796.2 mbsf (Subunit 5b), has more constant values of sonic velocity. The sediments constituting PP Unit 5 are predominantly volcaniclastic sandstone and siltstone alternating with minor amounts of nannofossil- and radiolarian-rich layers.

Physical Property Subunit 5a (Hole 869B: 639–720 mbsf)

Although bulk density shows little downcore variation in Subunit 5a (ranging from 1.89 to 2.25 g/cm^3, with an average of 2.08 g/cm^3), sonic velocity is highly variable and ranges from 2.38 up to 5.50 km/s, with an average of 3.29 km/s. Water content ranges from 8.70% to 28.69%, with an average of 17.01%, and porosity varies between 16.04% and 42.79%, averaging 29.66%. Rapid fluctuations in sonic velocity are suggested to correlate with changes in sediment fabric and mineralogy within the volcaniclastics. The presence of a zeolite cement instead of clay in the volcaniclastics and of elevated carbonate percentages in the clayey nannofossil and radiolarian oozes tends to increase the relative sonic velocity. The lower boundary of PP Subunit 5a exhibits a gradual decrease in the variability of sonic velocity and, in addition, a subtle change in anisotropy of velocity. The general decrease downcore in anisotropy in Subunit 5a reverses into an increase downcore in Subunit 5b. This boundary has no correlative lithologic contact.

Physical Property Subunit 5b (Hole 869B: 720–796.2 mbsf)

Physical properties in PP Subunit 5b are relatively constant downcore: bulk density ranges from 1.90 to 2.36 g/cm^3, with an average of 2.60 g/cm^3, water content ranges from 3.58% to 30.69%, with an average of 20.68%, and porosity varies between 7.46% and 44.61%, with a mean of 34.14%. Sonic velocity has values that range from 2.44 to 4.36 km/s, with an average of 2.92 km/s. Sediments consist primarily of volcaniclastic siltstone to sandstone with nannofossil and radiolarian claystone and, near the bottom (from about 780 mbsf downward), an increase in carbonate content (see "Organic Geochemistry" section, this chapter).

Discussion

Recovery at Site 869 was high, nearly 100%, in the unlithified to semilithified upper part (0–145 mbsf), moderate, 5% to 45%, in the section containing well-layered volcaniclastics and chalks from about 145 to about 600 mbsf, and high again in the lower portion, on average more than 60%, from about 600 down to 796.2 mbsf, that contains predominantly massive volcaniclastic layers. Therefore, these data should reflect, with the exception of the poorly recovered section of PP Subunit 1c, the lithologic succession at Site 869. Physical properties (see Fig. 46) indicate a general subdivision into three major intervals: (1) an uppermost interval, 0 down to 210 mbsf, of unlithified to semilithified nannofossil to radiolarian ooze having low densities and low velocities, including a chert-rich interval having low recovery; (2) an intermediate interval, 210 to 377 mbsf, characterized by highly variable bulk density and, to a minor extent, sonic velocity consisting of alternating, thin-layered volcaniclastics and semi-indurated nannofossil claystone; and (3) a lowermost interval, 377 down to 796.2 mbsf, of well-layered to massive volcaniclastics with minor nannofossil to radiolarian chalk and claystone, characterized by well-defined trends in bulk density and sonic velocity.

Boundaries between PP units generally correspond to changes in lithology, as indicated by downhole logs where recovery was sparse, or to major changes in character of gravity deposits within these lithologic units (Fig. 47). Few boundaries have no correlation with lithologic units, (e.g., the lower boundary of PP Subunit 5a). This may also be related to a zone of low recovery. We postulate that higher frequency variations within the lower PP units (Units 3, 4, and 5) are related to the alternation of lithologies of different fabric and mineralogy. Within volcaniclastic successions, in general, muddy textures have lower velocity and bulk density than textures devoid of mud and cemented by zeolite. Similarly, higher carbonate concentrations in pelagic sediments tend to increase the sonic velocity and bulk density. Major changes in velocity and density are correlated with boundaries between lithologic subunits that consist of a base of coarse, gravelly, volcaniclastic debris flows with finer-grained volcaniclastics, alternating with pelagic sediments toward the top (see also "Lithostratigraphy" section, this chapter). The lithologic contacts at 536.1 and 653.3 mbsf (the boundaries between lithologic Subunits IIID/IIIE and IIIE/IIIF, respectively) have corresponding signatures in sonic velocity and, to a lesser extent, bulk density (the boundaries between PP

Subunit 3b/Unit 4 and Unit 4/Subunit 5a, respectively). However, the resulting change in physical properties, downcore decrease or increase, is not the same for both transitions, which may be related to degree of induration and/or fabric type. The slight change in anisotropy of velocity at about 720 mbsf has no direct correlation with a lithologic change or has been obscured because of low recovery. This may reflect a significant transition in clay mineralogy and therefore clay fabric, or a change in compaction history. Both the trends in anisotropy as well as the physical property features associated with the lithologic transitions over the boundaries between different volcaniclastic gravity flows need further study.

DOWNHOLE MEASUREMENTS

Introduction

Wireline measurements were conducted at Hole 869B, which penetrated 796.2 m of calcareous oozes, cherts, and volcaniclastic turbidite deposits at a basinal fan site southwest of Wodejebato Guyot and Pikinni Atoll. Four tool strings were run during the logging program at Hole 869A, including the sonic-porosity-density-resistivity-gamma-ray-temperature, the geochemical tool string, the Japanese downhole magnetometer, and the FMS temperature tool string. We positioned the bottom of the drill pipe at 89.0 mbsf, and good logs were obtained within the open borehole between 89.0 and 778.5 mbsf for the geophysical tool string. Bridges (i.e., formations causing reduced hole sizes that were impassible for logging tools) controlled the logging strategy thereafter. Following several failed attempts to break through an obstruction at about 166.0 mbsf, the pipe was lowered to 238.4 mbsf for the FMS. The magnetometer was run from 724.2 to 234.8 mbsf. Because of time constraints the geochemical tool was run only from 560.2 to 360.0 mbsf.

Reliability of Logs

Logging data from Hole 869A cover the interval from the bottom of the drill string (89.0 mbsf) to near the base of the hole at 778.5 mbsf, and all are of generally high quality. Hole size is the most important control on accuracy of the logs in Hole 869A. Two caliper logs were obtained on two separate runs: the lithodensity tool caliper, and the four-arm caliper of the FMS. The two give generally similar results, except that the FMS caliper has a maximum opening of 16 in. (40.64 cm), and the lithodensity caliper measures to a maximum of 18 in. (45.7 cm). Broad swings in the hole size from about 650 to 700 mbsf are probably related to changes in circulation patterns during drilling. Very large hole diameters (>17 in. or 43.16 cm) over the intervals at 90.0–165.2, 263.4–333.6, 473.2–499.2, and 558.7–598.2 mbsf account for questionable FMS and density/porosity data from these zones. Most other logs do not require pad contact and therefore are less insensitive to the changes in borehole size.

Some occurrence of both cycle skipping and noise interference can be seen in the sonic-velocity logging data. The noise problems are predominantly localized to specific depths, and we anticipate that many of the problems with noise can be overcome by close examination of sonic waveforms during post-cruise processing.

Each log was shifted in depth, by correlating the gamma-ray logs between runs, to correct for differences in the stretch of the logging cable. All logs were then corrected to depth as meters below sea floor by subtracting the depth from rig floor to sea floor (4837.8 m). These depths should be accurate to within ±2 m.

Depths for the temperature tool were determined using the pressure recorded in the instrument and a depth vs. pressure table derived from pressure readings at depths noted during logging.

The geochemical and spectral gamma-ray logs have been processed onshore and are discussed elsewhere (see "Onshore Geochemical Processing" chapter, this volume).

Log Relationships

Velocity and resistivity correlate well throughout the entire logged interval at Site 869 (Fig. 48). The extremely high variability in both resistivity and velocity indicates correspondingly high variability in porosity. Increases in velocity and density with depth do not follow a simple compaction profile, suggesting that diagenesis and grain-size fluctuation affect porosity much more than does mechanical compaction. The most notable feature is that zones exist where the resistivity, velocity and density decrease with increasing depth, contrary to the normal compaction profile (e.g., logging Unit 5, Figs. 48 and 49). Velocity and resistivity decrease gradually with depth from the top of logging Subunit 1b to the base of logging Unit 2. Below logging Unit 2, the base level of resistivity increases gradually, but superimposed on this base level are the highly resistive peaks of the sandstones and breccias (Fig. 48).

Furthermore, resistivity, velocity, and density correlate moderately well with the gamma-ray log (SGR in Fig. 49), in that the gamma-ray maxima correspond to velocity, resistivity, and density minima. Higher clay-mineral concentration is evident by higher gamma-ray counts and porosity (clay minerals substantially increase the porosity of uncompacted [<2 km overburden] sediments). The abundances of thorium and potassium seen in Figure 50 account for most of the SGR signal in the logged interval; the uranium signal increases near the end of the logged interval. The potassium log exhibits a variable style, with values in the range of 0% to 7% and with some peaks that correlate with low-resistivity and velocity anomalies, the most notable of which is at the base of logging Unit 4.

Figure 51 presents a strong correlation among the geochemical logs. Log values for potassium, aluminum, and silica (all abundant in the clay minerals illite and kaolinite) are positively correlated with each other. Iron values are somewhat correlated with values for these other elements, but in general, variations in iron values probably are related to the volcanic influx. Calcium values are uniformly zero for the entire logged portion of Hole 869B. The porosity log in Figure 49 only moderately correlates with resistivity and velocity logs.

Temperature

The data recorded on both logging runs were not useful because the pressure transducer in the tool malfunctioned.

Downhole Three-component Magnetometer Log

The magnetometer measured three components of the geomagnetic field within Hole 869B from 239 to 725 mbsf. Because the magnetometer takes a measurement every 3 s, at the speed of 500 m/hr, the sampling interval was about 0.4 m. The horizontal and vertical components of the magnetic field inside the hole were calculated from the observed three components of the magnetic field. The orientation of the tool with respect to the present geomagnetic field also was determined from the magnetic field measured by the two orthogonal horizontal axes of the magnetometer. The field and orientation variations are shown in Figure 52.

The horizontal magnetic component is degraded by sharp, very high-amplitude variations. These variations were caused by the sensitivity of the horizontal component to changes in tool orientation. Because the data are of such poor quality, they are not included in this analysis. The abrupt changes in the tool orientation also affected the vertical magnetic field variations, but the amplitude of the vertical magnetic field variations is much lower than that of the horizontal, about 500 nT.

Below the boundary between logging Units 4 and 5 (~490 mbsf), the vertical magnetic field gradually increases and then abruptly decreases at about 530 mbsf. The amplitude of this variation is almost

Table 6. Concentrations of total, inorganic, and organic carbon and of total nitrogen and sulfur in sediments from Hole 869B.

Core, section, interval (cm)	Depth (mbsf)	Sample type[a]	TC (%)	IC (%)	TOC (%)	$CaCO_3$ (%)	N (%)	S (%)	TOC/N	TOC/S	Lithology
143-869B-											
2R-1, 3–5	140.03	CARB	0.19	0.09	0.10	0.7	0.07	0.37	1.4	0.3	Brown chert
3R-CC, 10–12	149.70	CARB	0.23	0.11	0.12	0.9	0.06	0.45	2.0	0.3	Brown chert
4R-1, 15–16	159.45	CARB	0.14	0.04	0.10	0.3	0.12	0.34	0.8	0.3	Brown chert
4R-1, 46–47	159.76	CARB	9.37	9.20	0.17	76.6	0.65	0.00	0.3		White siliceous chalk
4R-1, 63–64	159.93	CARB	0.14	0.04	0.10	0.3	0.07	0.00	1.4		Beige chert
5R-1, 10–12	169.00	CARB	0.12	0.05	0.07	0.4	0.03	0.16	2.0	0.4	Yellow chert
6R-1, 7–8	178.67	CARB	0.23	0.08	0.15	0.7	0.11	0.28	1.3	0.5	Beige chert
9R-CC, 11–12	207.71	CARB	5.81	5.73	0.08	47.7	0.10	0.33	0.8	0.2	Yellow claystone
10R-1, 33–34	217.53	CARB	3.84	3.45	0.39	28.7	0.08	0.00	4.9		Tubiditic sand
10R-1, 145–150	218.65	IWSC	5.70	5.43	0.27	45.2	0.07	0.22	3.8	1.2	Light-brown claystone
10R-2, 45–46	219.15	CARB	7.89	7.56	0.33	63.0	0.09	0.00	3.6		Beige clayey mudstone
11R-1, 88–89	227.78	CARB	3.23	2.89	0.34	24.1	0.09	0.43	3.8	0.8	Brown claystone
11R-2, 145–150	229.85	IWSC	8.09	8.06	0.03	67.1	0.05	0.20	0.6	0.2	Light-gray clayey mudstone
11R-3, 62–63	230.52	CARB	4.88	4.87	0.01	40.6	0.10	0.25	0.1	0.0	Brown claystone
11R-4, 129–131	232.69	CARB	0.93	0.60	0.33	5.0	0.06	0.47	5.5	0.7	Gray claystone
13R-1, 94–95	247.14	CARB	0.50	0.37	0.13	3.1	0.08	0.34	1.6	0.4	Volcanic turbiditic sand
13R-1, 145–150	247.65	IWSC	7.27	7.26	0.01	60.5	0.06	0.00	0.1		Beige clayey mudstone
13R-2, 87–88	248.57	CARB	3.98	3.72	0.26	31.0	0.12	0.00	2.1		Gray claystone
13R-2, 144–146	249.14	CARB	1.36	1.19	0.17	9.9	0.07	0.37	2.4	0.5	Gray-greenish claystone
13R-3, 30–32	249.50	CARB	10.01	10.00	0.01	83.3	0.10	0.00	0.1		White mudstone
13R-4, 51–52	251.21	CARB	7.59	7.26	0.33	60.5	0.10	0.26	3.3	1.2	Beige clayey mudstone
15R-1, 125–126	266.65	CARB	5.03	4.99	0.04	41.6	0.06	0.28	0.6	0.1	Gray claystone
15R-2, 127–128	268.17	CARB	3.12	3.10	0.02	25.8	0.01	0.18	2.0	0.1	Gray claystone
15R-4, 146–147	271.36	CARB	0.37	0.36	0.01	3.0	0.05	0.30	0.2	0.0	Volcanic turbiditic sand
15R-CC, 15–16	272.03	CARB	7.11	6.66	0.45	55.5	0.07	0.23	6.4	1.9	Beige clayey mudstone
16R-1, 68–69	275.78	CARB	3.83	3.70	0.13	30.8	0.13	0.00	1.0		Beige claystone
16R-1, 89–90	275.99	CARB	0.37	0.30	0.07	2.5	0.08	0.29	0.9	0.2	Volcanic turbiditic sand
17R-2, 0–5	285.83	IWSC	0.21	0.10	0.11	0.8	0.10	0.32	1.1	0.3	Volcanic turbiditic sand
17R-2, 21–22	286.04	CARB	0.28	0.19	0.09	1.6	0.04	0.18	2.0	0.5	Volcanic turbiditic sand
17R-2, 75–76	286.58	CARB	5.45	5.44	0.01	45.3	0.07	0.00	0.1		Gray claystone
17R-CC, 7–9	286.78	CARB	0.13	0.11	0.02	0.9	0.03	0.18	0.6	0.1	Volcanic turbiditic sand
19R-1, 30–31	304.40	CARB	1.53	1.51	0.02	12.6	0.04	0.14	0.5	0.1	Volcanic turbiditic sand
19R-2, 10–11	305.70	CARB	2.83	2.34	0.49	19.5	0.11	0.31	4.4	1.6	Dark-gray claystone
20R-1, 12–13	313.92	CARB	1.00	0.77	0.23	6.4	0.05	0.00	4.6		Volcanic turbiditic sand
20R-2, 135–136	316.65	CARB	1.77	1.36	0.41	11.3	0.05	0.40	8.2	1.0	Gray claystone
20R-2, 145–150	316.75	IWSC	1.17	0.99	0.18	8.2	0.23	0.95	0.8	0.2	Dark-gray claystone
20R-3, 58–59	317.38	CARB	0.73	0.61	0.12	5.1	0.09	0.00	1.3		Dark-gray claystone
20R-CC, 12–13	318.98	CARB	1.67	1.65	0.02	13.7	0.05	0.00	0.4		Volcanic turbiditic sand
21R-1, 54–55	324.04	CARB	1.34	0.84	0.50	7.0	0.12	0.29	4.1	1.7	Volcanic turbiditic sand
22R-1, 102–103	334.12	CARB	0.78	0.50	0.28	4.2	0.19	0.82	1.5	0.3	Gray claystone
22R-2, 8–9	334.68	CARB	2.52	2.49	0.03	20.7	0.21	0.93	0.1	0.0	Dark-gray claystone
23R-1, 115–116	343.95	CARB	0.32	0.06	0.26	0.5	0.18	0.79	1.4	0.3	Green sandy claystone
23R-1, 142–145	344.22	HS	2.17	2.12	0.05	17.7	0.06	0.22	0.8	0.2	Green-grayish claystone
23R-1, 145–150	344.25	IWSC	0.46	0.42	0.04	3.5	0.22	0.88	0.2	0.1	Green-grayish claystone
23R-2, 104–105	345.34	CARB	0.90	0.70	0.20	5.8	0.17	0.72	1.2	0.3	Volcanic turbiditic sand
25R-2, 104–105	364.74	CARB	3.26	3.09	0.17	25.7	0.21	0.83	0.8	0.2	Green claystone
26R-1, 75–76	372.55	CARB	0.61	0.27	0.34	2.2	0.29	1.33	1.2	0.3	Gray greenish claystone
26R-1, 109–110	372.89	CARB	0.45	0.18	0.27	1.5	0.21	0.90	1.3	0.3	Dark-gray sandy claystone
27R-1, 6–7	381.56	CARB	0.40	0.03	0.37	0.2	0.28	1.12	1.3	0.3	Gray claystone
27R-1, 58–59	382.08	CARB	0.79	0.03	0.76	0.2	0.60	0.00	1.2		Beige claystone
27R-1, 72–73	382.22	CARB	3.73	2.99	0.74	24.9	0.76	0.00	1.0		Beige calcareous claystone
28R-CC, 14–15	391.24	CARB	0.69	0.02	0.67	0.2	0.56	2.20	1.2	0.3	Gray claystone
29R-CC, 20–21	401.00	CARB	3.07	2.68	0.39	22.3	0.54	2.14	0.7	0.2	Beige calcareous claystone
30R-1, 15–16	410.55	CARB	0.65	0.16	0.49	1.3	0.43	0.00	1.1		White sandy claystone
31R-1, 7–8	420.17	CARB	7.10	6.82	0.28	56.8	0.21	0.83	1.3	0.3	Calcareous sandstone
31R-1, 81–82	420.91	CARB	2.51	2.43	0.08	20.2	0.22	0.90	0.4	0.1	Volcanic turbiditic sandstone
31R-1, 99–100	421.09	CARB	0.35	0.08	0.27	0.7	0.21	0.87	1.3	0.3	Brown claystone
31R-1, 145–150	421.55	IWSC	3.32	3.10	0.22	25.8	0.03	0.00	7.3		Brown claystone
32R-1, 0–3	429.80	HS	0.34	0.03	0.31	0.2	0.25	1.02	1.2	0.3	Sandy claystone
32R-1, 67–68	430.47	CARB	1.12	0.42	0.70	3.5	0.20	0.84	3.5	0.8	Volcanic turbiditic sandstone
32R-1, 70–72	430.50	CARB	1.15	1.04	0.11	8.7	0.20	0.82	0.6	0.1	Volcanic turbiditic sandstone
32R-2, 90–91	432.20	CARB	0.43	0.05	0.38	0.4	0.27	0.00	1.4		Brown claystone
33R-1, 17–18	439.57	CARB	3.27	3.03	0.24	25.2	0.31	0.00	0.8		Light-beige mudstone
33R-1, 74–75	440.14	CARB	0.47	0.02	0.45	0.2	0.35	1.40	1.3	0.3	Beige claystone
33R-CC, 19–20	440.94	CARB	0.38	0.02	0.36	0.2	0.23	0.95	1.5	0.4	Gray claystone
34R-1, 51–52	449.61	CARB	0.54	0.03	0.51	0.2	0.38	0.00	1.3		Gray claystone
34R-1, 89–90	449.99	CARB	6.23	5.98	0.25	49.8	0.35	0.00	0.7		Light-gray mudstone
34R-2, 109–110	451.69	CARB	1.78	1.58	0.20	13.2	0.17	0.71	1.2	0.3	Gray claystone
34R-CC, 2–3	452.52	CARB	0.79	0.54	0.25	4.5	0.20	0.89	1.2	0.3	Gray claystone
35R-1, 7–8	458.87	CARB	0.04	0.04	0.00	0.3	0.03	0.00	0.0		Light-gray sandstone
35R-1, 41–43	459.21	CARB	1.95	1.94	0.01	16.2	0.02	0.00	0.5		Gray-greenish sandstone
35R-1, 78–80	459.58	CARB	0.04	0.02	0.02	0.2	0.08	0.00	0.2		Light-gray sandstone
36R-1, 25–26	468.65	CARB	0.69	0.12	0.57	1.0	0.05	0.00	11.0		Gray claystone
36R-1, 145–150	469.85	IWSC	1.25	1.03	0.22	8.6	0.03	0.00	7.3		Gray claystone
36R-2, 107–108	470.97	CARB	0.64	0.42	0.22	3.5	0.15	0.59	1.4	0.4	Gray claystone
36R-3, 5–7	471.45	CARB	0.45	0.30	0.15	2.5	0.16	0.67	0.9	0.2	Volcanic turbiditic sandstone
38R-1, 53–54	488.23	CARB	1.10	1.05	0.05	8.7	0.04	0.00	1.0		Volc. sandstone with calcite veins
38R-3, 36–37	490.20	CARB	0.13	0.10	0.03	0.8	0.03	0.00	1.0		Volcaniclastic sandstone
38R-CC, 4–5	491.30	CARB	0.14	0.09	0.05	0.7	0.03	0.00	1.0		Volcaniclastic sandstone
39R-1, 128–129	498.68	CARB	0.16	0.15	0.01	1.2	0.03	0.00	0.3		Volcaniclastic sandstone
39R-CC, 8–9	500.20	CARB	0.15	0.10	0.05	0.8	0.02	0.00	2.0		Volcaniclastic sandstone
40R-1, 102–103	508.12	CARB	0.15	0.10	0.05	0.8	0.02	0.00	2.0		Coarse volcaniclastic sandstone

Table 6 (continued).

Core, section, interval (cm)	Depth (mbsf)	Sample type[a]	TC (%)	IC (%)	TOC (%)	$CaCO_3$ (%)	N (%)	S (%)	TOC/N	TOC/S	Lithology
41R-2, 116–117	519.46	CARB	0.14	0.09	0.05	0.7	0.03	0.00	1.0		Volcaniclastic sandstone
41R-4, 4–5	520.96	CARB	0.11	0.06	0.05	0.5	0.03	0.00	1.0		Coarse volcaniclastic sandstone
42R-1, 64–65	527.04	CARB	0.16	0.09	0.07	0.7	0.03	0.00	2.0		Coarse volcaniclastic sandstone
42R-2, 67–68	528.52	CARB	0.12	0.09	0.03	0.7	0.03	0.00	1.0		Coarse volcaniclastic sandstone
42R-3, 30–31	529.65	CARB	0.11	0.08	0.03	0.7	0.04	0.00	0.7		Coarse volcaniclastic sandstone
42R-4, 33–34	530.99	CARB	0.10	0.07	0.03	0.6	0.03	0.00	1.0		Coarse volcaniclastic sandstone
43R-1, 85–86	536.95	CARB	0.17	0.12	0.05	1.0	0.02	0.00	2.0		Fine volcaniclastic sandstone
43R-2, 40–41	538.00	CARB	0.19	0.18	0.01	1.5	0.03	0.00	0.3		Fine volcaniclastic sandstone
44R-1, 94–95	546.54	CARB	0.25	0.06	0.19	0.5	0.04	0.55	4.7	0.3	Coarse volcaniclastic sandstone
44R-2, 32–33	547.42	CARB	0.31	0.12	0.19	1.0	0.05	0.30	3.8	0.6	Fine volcaniclastic sandstone
44R-CC, 26–27	552.81	CARB	0.41	0.38	0.03	3.2	0.01	0.92	3.0	0.0	Fine volcaniclastic sandstone
45R-1, 32–34	555.62	CARB	0.32	0.11	0.21	0.9	0.01	0.05	21.0	4.2	Coarse volcaniclastic sandstone
46R-1, 77–78	565.37	CARB	0.34	0.13	0.21	1.1	0.01	0.21	21.0	1.0	Fine volcaniclastic sandstone
48R-1, 32–33	584.22	CARB	1.24	1.09	0.15	9.1	0.03	0.30	5.0	0.5	Fine volcaniclastic sandstone
48R-CC, 15–16	584.67	CARB	6.60	6.53	0.07	54.4	0.03	0.13	2.0	0.5	Fine calcareous sandstone
49R-CC, 0–3	593.50	HS	0.95	0.81	0.14	6.7	0.03	0.17	4.6	0.8	Black argillaceous sandstone
49R-CC, 19–20	593.69	CARB	0.35	0.17	0.18	1.4	0.01	0.14	18.0	1.3	Fine volcaniclastic sandstone
50R-1, 1–2	603.21	CARB	0.43	0.15	0.28	1.2	0.01	0.19	28.0	1.5	Coarse volcaniclastic sandstone
50R-5, 1–3	609.21	CARB	0.60	0.23	0.37	1.9	0.01	0.61	37.0	0.6	Coarse volcaniclastic sandstone
50R-6, 134–135	612.04	CARB	2.30	1.66	0.64	13.8	0.05	0.25	13.0	2.5	Fine volcaniclastic sandstone
51R-1, 56–57	613.26	CARB	3.43	3.02	0.41	25.2	0.04	0.00	10.0		Dark-gray sandy claystone
51R-1, 72–73	613.42	CARB	7.19	7.14	0.04	59.5	0.01	0.10	4.0	0.4	Light-gray sandy mudstone
51R-3, 104–105	616.74	CARB	0.88	0.57	0.31	4.7	0.01	0.00	31.0		Brown sandy claystone
51R-4, 33–34	617.53	CARB	0.30	0.13	0.17	1.1	0.01	0.19	17.0	0.9	Dark-gray sandy claystone
52R-1, 146–148	623.86	CARB	0.23	0.08	0.15	0.7	0.01	0.11	15.0	1.3	Coarse volcaniclastic sandstone
52R-2, 113–115	625.03	CARB	1.40	0.97	0.43	8.1	0.04	0.03	11.0	14.0	Gray sandy claystone
52R-4, 2–4	626.92	CARB	0.77	0.52	0.25	4.3	0.01	0.09	25.0	2.8	Gray-greenish sandy claystone
53R-1, 53–54	632.53	CARB	0.44	0.16	0.28	1.3	0.01	1.03	28.0	0.3	Coarse volcaniclastic sandstone
54R-1, 88–91	642.68	CARB	0.20	0.12	0.08	1.0	0.01	0.09	8.0	0.9	Coarse volcaniclastic sandstone
54R-4, 63–65	646.60	CARB	0.19	0.09	0.10	0.7	0.01	0.02	10.0	5.0	Volc. sandstone with calcite veins
55R-2, 56–57	653.56	CARB	7.86	7.79	0.07	64.9	0.01	0.00	7.0		Light-gray sandy limestone
55R-3, 32–33	654.82	CARB	2.25	1.92	0.33	16.0	0.04	0.00	8.2		Green sandstone
56R-1, 55–56	661.75	CARB	0.43	0.27	0.16	2.2	0.01	0.07	16.0	2.3	Dark-gray sandstone
56R-1, 76–77	661.96	CARB	0.28	0.19	0.09	1.6	0.01	0.23	9.0	0.4	Green sandstone
56R-3, 63–64	664.83	CARB	0.23	0.05	0.18	0.4	0.01	0.09	18.0	2.0	Volcaniclastic sandstone
57R-1, 31–33	671.01	CARB	0.27	0.09	0.18	0.7	0.01	0.05	18.0	3.6	Green sandstone
57R-2, 131–132	673.51	CARB	0.34	0.29	0.05	2.4	0.03	0.00	1.0		Gray sandstone
57R-3, 56–57	674.26	CARB	0.22	0.08	0.14	0.7	0.03	0.00	4.6		Green sandstone
57R-CC, 26–27	676.88	CARB	1.62	1.56	0.06	13.0	0.00	0.00			Green sandstone
58R-1, 78–80	681.18	CARB	0.28	0.07	0.21	0.6	0.04	0.11	5.2	1.9	Coarse volcaniclastic sandstone
58R-5, 99–101	687.39	CARB	0.29	0.04	0.25	0.3	0.01	0.00	25.0		Coarse volcaniclastic sandstone
59R-1, 56–58	690.56	CARB	0.28	0.18	0.10	1.5	0.01	0.00	10.0		Green sandstone
59R-1, 146–150	691.46	IWSC	0.10	0.08	0.02	0.7	0.00	0.01		2.0	Volcaniclastic sandstone
59R-3, 8–9	693.08	CARB	0.28	0.12	0.16	1.0	0.01	0.00	16.0		Green sandy claystone
59R-4, 3–4	694.53	CARB	0.33	0.06	0.27	0.5	0.01	0.18	27.0	1.5	Green sandstone
59R-5, 9–10	696.09	CARB	0.29	0.20	0.09	1.7	0.02	0.00	4.0		Green sandstone
60R-2, 84–86	700.84	CARB	0.21	0.05	0.16	0.4	0.07	0.00	2.3		Coarse volcaniclastic sandstone
60R-5, 79–80	705.29	CARB	0.26	0.05	0.21	0.4	0.02	0.00	10.0		Fine volcaniclastic sandstone
60R-7, 121–122	708.71	CARB	0.20	0.05	0.15	0.4	0.05	0.00	3.0		Coarse volcaniclastic sandstone
60R-8, 19–20	709.19	CARB	0.53	0.47	0.06	3.9	0.02	0.01	3.0	6.0	Sandy claystone
61R-1, 46–47	709.86	CARB	0.53	0.06	0.47	0.5	0.19	0.00	2.5		Coarse volcaniclastic sandstone
61R-3, 51–54	712.91	CARB	0.17	0.05	0.12	0.4	0.01	0.01	12.0	12.0	Coarse volcaniclastic sandstone
62R-CC, 9–11	719.19	CARB	1.47	1.43	0.04	11.9	0.00	0.09		0.4	Gray calcareous sandstone
63R-2, 50–51	730.70	CARB	0.98	0.97	0.01	8.1	0.00	0.02		0.5	Fine green sandstone
63R-4, 80–81	734.00	CARB	0.10	0.07	0.03	0.6	0.00	0.02		1.0	Volcaniclastic sandstone
63R-6, 109–110	737.29	CARB	0.04	0.03	0.01	0.2	0.00	0.00			Volcaniclastic sandstone
63R-CC, 6–8	738.37	CARB	0.04	0.03	0.01	0.2	0.00	0.00			Volcaniclastic sandstone
64R-1, 115–116	739.55	CARB	0.08	0.04	0.04	0.3	0.01	0.08	4.0	0.5	Volcaniclastic sandstone
64R-2, 41–42	740.31	CARB	0.09	0.08	0.01	0.7	0.00	0.00			Green sandstone
64R-3, 49–50	741.89	CARB	0.04	0.04	0.00	0.3	0.00	0.00			Green sandstone
64R-5, 104–105	745.44	CARB	0.20	0.19	0.01	1.6	0.00	0.00			Green sandstone
65R-1, 17–18	748.07	CARB	1.36	1.33	0.03	11.1	0.00	0.00			Green sandstone
65R-2, 116–117	750.56	CARB	0.11	0.10	0.01	0.8	0.00	0.01		1.0	Green sandstone
65R-2, 125–126	750.65	CARB	0.27	0.27	0.00	2.2	0.00	0.00			Green sandstone
65R-2, 145–150	750.85	IWSC	0.38	0.37	0.01	3.1	0.00	0.00			Green sandstone
66R-1, 3–4	757.63	CARB	0.09	0.08	0.01	0.7	0.00	0.00			Green sandstone
66R-2, 2–3	759.12	CARB	0.07	0.05	0.02	0.4	0.00	0.01		2.0	Volcaniclastic sandstone
66R-3, 60–61	761.20	CARB	0.11	0.06	0.05	0.5	0.00	0.00			Volcaniclastic sandstone
67R-1, 76–77	768.06	CARB	0.08	0.08	0.00	0.7	0.00	0.08		0.0	Green sandstone
67R-2, 74–75	769.54	CARB	0.08	0.08	0.00	0.7	0.00	0.02		0.0	Green sandstone
67R-2, 98–99	769.78	CARB	0.14	0.13	0.01	1.1	0.00	0.00			Green sandstone
67R-4, 42–43	772.22	CARB	0.04	0.04	0.00	0.3	0.00	0.00			Green sandstone
67R-5, 93–94	774.23	CARB	0.12	0.11	0.01	0.9	0.00	0.00			Green sandstone
68R-2, 54–55	778.94	CARB	0.68	0.66	0.02	5.5	0.00	0.00			Green sandstone
68R-4, 48–49	781.88	CARB	0.03	0.02	0.01	0.2	0.00	0.00			Green sandy claystone
68R-4, 61–62	782.01	CARB	8.25	7.90	0.35	65.8	0.01	0.00	35.0		Pale-green mudstone
68R-4, 65–66	782.05	CARB	0.03	0.03	0.00	0.2	0.00	0.00			Greenish-red laminated claystone
68R-4, 68–69	782.08	CARB	0.03	0.02	0.01	0.2	0.00	0.00			Green claystone
69R-1, 55–56	787.15	CARB	1.40	1.31	0.09	10.9	0.00	0.08		1.0	Green calcareous sandstone
69R-2, 52–53	788.62	CARB	3.55	3.41	0.14	28.4	0.00	0.01		14.0	Green laminated mudstone
69R-2, 62–63	788.72	CARB	3.56	3.48	0.08	29.0	0.00	0.00			Green laminated mudstone

[a] Sample type: CARB = carbonate; HS = headspace; IWSC = interstitial-water squeeze cake.

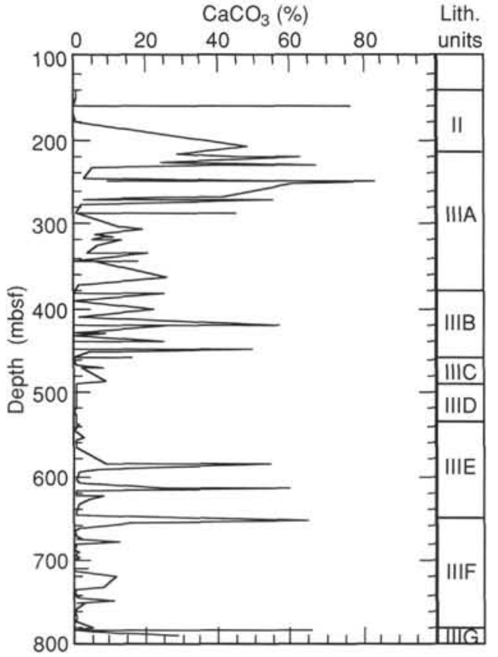

Figure 41. Depth distribution of calcium carbonate in Hole 869B.

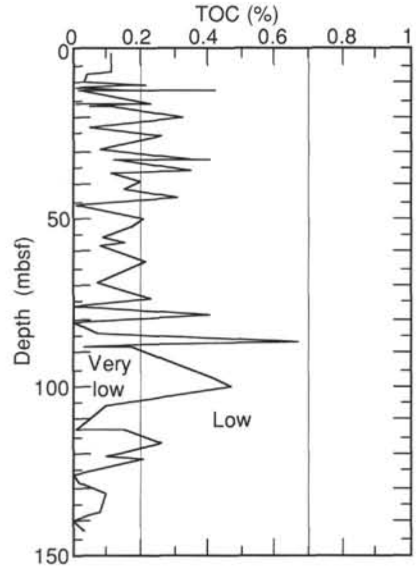

Figure 42. Depth distribution of total organic carbon (TOC) concentrations in Hole 869A.

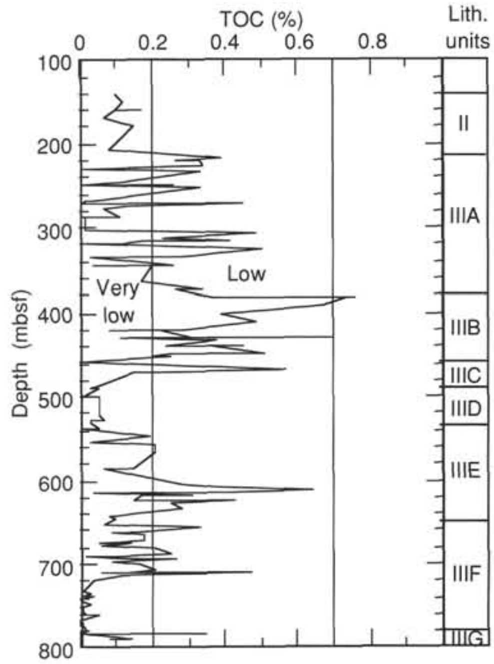

Figure 43. Depth distribution of total organic carbon (TOC) concentrations in Hole 869B.

1500 nT. This high-amplitude variation corresponds to lithological Subunit IIID (487.8–536.1 mbsf) and is caused by volcaniclastic breccias. This high-amplitude variation is also concordant with the high intensity of magnetization of volcaniclastic breccias (Cores 143-869B-40R through 143-869B-42R) determined from shipboard paleomagnetic studies. The increase of the vertical magnetic field component indicates that the volcaniclastic breccias have a negative inclination of magnetization.

The high-amplitude, sharp increase at about 650 mbsf marks the boundary between logging Unit 5 and Unit 6. The character of vertical magnetic field variations in logging Unit 6 is different from that of logging Unit 5. Vertical magnetic field variations in logging Unit 6 exhibit long wavelengths (about 10 m) and relatively higher amplitude (about 500 nT). Logging Unit 6 corresponds to lithological Subunit IIIF (653.3–780.7 mbsf), a series of massive sandstone and siltstone beds. These vertical magnetic field variations are probably caused by a succession of sandstone-siltstone sequences. Clear boundaries between logging Units 2, 3, and 4 are not observed from vertical magnetic field variations.

The arrows in Figure 52 indicate the normal-reverse polarity boundary inferred from vertical magnetic field variations and shipboard paleomagnetic results. The upper arrow shows the boundary between Chrons 33N and 33R and the lower one between Chron 33R and the Cretaceous normal superchron. The boundary between 33N and 33R lies at about 330 mbsf and that between 33R and the Cretaceous normal superchron is at about 410 mbsf. The character of the vertical magnetic variations indicated by the arrows in Figure 52 are different from those below and above the arrows. The vertical magnetic variations at the arrows show abrupt decreases and longer wavelengths (about 10 m) than those below and above the arrows, respectively. The average trend of the vertical magnetic field variations between the arrows seems to be lower than that above the upper arrow and below the lower arrow. Shipboard paleomagnetic results indicate that the boundary between 33N and 33R lies between Cores 143-869B-20R (313.8–323.5 mbsf) and 143-869B-21R (323.5–333.1 mbsf). Paleomagnetic results also show that the boundary between 33R and the Cretaceous normal superchron is probably located near Core 143-869B-32R (429.8–439.4 mbsf). These results suggest that the vertical magnetic field shown by the arrows indicates the boundaries between Chrons 33N, 33R, and the Cretaceous normal superchron.

Log-based Units

Six logging units were identified using the geophysical and geochemical logs. These units are defined primarily on the basis of the resistivity, velocity, density, and gamma-ray logs.

Logging Unit 1 (Base of Pipe, 89.0–224.2 mbsf)

Logging Unit 1 corresponds to lithologic Unit II, an interval of porcellanite associated with clayey nannofossil and radiolarian oozes.

Table 7. Results of the Geofina hydrocarbon meter analyses and concentrations of carbonate, total organic carbon, and nitrogen for selected samples from Hole 869B.

Core, section, interval (cm)	Depth (mbsf)	Sample type[a]	Lithology	$CaCO_3$ (%)	TOC (%)	T_{max} GHM	T_{max} RE	S_1	S2	HI	N (%)	TOC/N
143-869B-												
15R-CC, 15–16	272.03	CARB	Beige claystone	55.5	0.45						0.07	6.4
19R-2, 10–11	305.70	CARB	Dark gray claystone	19.5	0.49						0.11	4.5
20R-2, 135–136	316.65	CARB	Gray claystone	11.3	0.41	405	345	0.16	0.24	58	0.05	8.2
21R-1, 54–55	324.04	CARB	Volcaniclastic sandstone	7.0	0.50						0.12	4.2
27R-1, 6–7	381.56	CARB	Gray claystone	0.3	0.37	425	365	0.05	0.03	8	0.28	1.3
27R-1, 72–76	382.22	CARB	Beige calcareous claystone	24.9	0.74	514	454	0.02	0.20	26	0.76	1.0
28R-CC, 14–15	391.24	CARB	Gray claystone	0.2	0.67						0.56	1.2
30R-1, 15–16	410.55	CARB	White sandy claystone	1.3	0.49						0.43	1.1
33R-1, 74–75	440.14	CARB	Beige claystone	0.2	0.45						0.35	1.3
34R-2, 109–110	451.69	CARB	Gray claystone	13.2	0.20						0.17	1.2
36R-1, 25–26	468.65	CARB	Gray claystone	1.0	0.57	443	383	0.04	0.10	17	0.05	11.4
51R-1, 56–57	613.26	CARB	Dark gray sandy claystone	3.0	0.41						0.04	10.3

[a] Sample type: CARB = carbonate.

Note: S_1 = free hydrocarbons; S_2 = pyrolyzable hydrocarbons (both in mg hydrocarbons/g of rock). HI = hydrogen index (in mg hydrocarbons/g TOC), blank space indicates no clear data or below the detection threshold of GHM.

Logging Subunit 1a (Base of Pipe, 89.0–165.2 mbsf)

Based on log responses alone, the nannofossil oozes of logging Subunit 1a are homogeneous, with only minor intervals of porcellanite and chert to a depth of 139.2 mbsf. The first significant chert intervals occur from 139.2 to 142.6 mbsf; the lithologies above and below this interval appear similar based on log responses. The base of this subunit is clearly defined by all geophysical logs. Resistivity values within the oozes of Subunit 1a range from 0.4 to 0.5 ohm-m. Except for cherty intervals, density is less than 1.4 g/cm^3 for the entire interval to 165.2 mbsf. Gamma-ray counts are uniformly 0 to 5.0 API units.

Logging Subunit 1b (165.2–224.2 mbsf)

Logging Subunit 1b corresponds to the lower portion of lithologic Unit II. A stepwise increase in resistivity, from 0.4 to 1.6 ohm-m, and density, from 1.4 to 2.0 g/cm^3, defines the top of this subunit. Porcellanite is the dominant lithology of the uppermost portion; numerous porcellanite intervals of varying thickness alternate with the radiolarian oozes that are typical of the lower part of Subunit 1b. Total gamma rays (SGR in Fig. 50) increase downhole, whereas density and resistivity decrease, reflecting the increasing clay content of Subunit 1b sediments.

Logging Unit 2 (224.2–302.3 mbsf)

Logging Unit 2 corresponds to the upper portion of lithologic Subunit IIIA (207.7–381.5 mbsf), a series of intercalated claystones and volcaniclastic silts and fine sands. This unit is heavily bioturbated, hence the uniform appearance on the resistivity log. Resistivity decreases slightly downhole from 1.9 to 1.0 ohm-m; density decreases to very low values at the base of logging Unit 2.

Logging Unit 3 (302.3–402.2 mbsf)

Logging Unit 3 corresponds to the lower part of lithologic Subunit IIIA (207.7–381.5 mbsf) plus the upper 20 m of lithologic Subunit IIIB (381.5–458.8 mbsf). The top of this unit is defined by sharp increases in gamma, resistivity and density logs. Logging Unit 3 is a very heterogeneous interval having many thin, alternately resistive and conductive intercalations; resistivity values range from 1.0 to 4.9 ohm-m for most of the unit. Near the base of the unit is a thick (378.8–393.1 mbsf) interval displaying uniformly low gamma-ray counts, medium-high resistivity, high density, and very high silicon content (Fig. 51). Although recovery in this interval was poor, logging results indicate that it is probably a cherty interval. Similarly, the numerous minor excursions to high resistivity and density occurring throughout this unit probably result from the presence of thin chert layers or layerlike concentrations of nodules. Chert and porcellanite fragments were recovered in Cores 143-869B-22R and -24R. The situation in this zone appears to fit the case where a shallow resistivity response of greater amplitude, both higher and lower than the other two resistivity measurements, suggests the presence of thin layers. This effect is highlighted in Figure 53. The differences between the three resistivity log types are attributed here to the different depths of investigation, but the differences are accentuated by the large hole diameter.

Although the overall lithologies, dominantly claystone with minor intercalations of volcaniclastic sandstone, are similar to those of logging Unit 2, logging Unit 3 may represent a subtle change in depositional environment, from low energy, infrequent, distal turbidites that are heavily bioturbated in logging Unit 2, to high energy, more frequent influxes in logging Unit 3.

Logging Unit 4 (402.2–487.2 mbsf)

Logging Unit 4 corresponds to most of lithologic Subunit IIIB and all of Subunit IIIC. Recovered lithologies are similar for both of these subunits. The top and base of this coarsening-upward unit are defined by sharp changes in the gamma-ray log. The coarse fraction at the top of the unit is the volcaniclastic sand common in logging Units 2 and 3. The interval from 412.2 to 442.0 mbsf is heavily bioturbated and has a uniform resistivity response of about 1.1 ohm-m. The high-gamma-ray, conductive basal portion of logging Unit 4 is probably an ashy layer, judging from the broad peak in potassium abundance (Fig. 50).

Logging Unit 5 (487.3–654.4 mbsf)

Logging Unit 5 corresponds to lithologic Subunits IIID (487.8–536.1 mbsf) and IIIE (536.1–653.3 mbsf). Unit 5 is bounded at the top and bottom by large fining-upward sequences: the first from 487.2 to 534.0 mbsf (Cores 143-869B-38R through -42R) and the second from 625.8 to 654.2 (Cores 143-869B-52R through Section 143-869B-55R-2; Fig. 54). The lower contact of the coarse basal breccias of the second sequence with the underlying silty claystone is prominent in the photograph of Core 143-869B-55R (Fig. 55). In both sequences, the resistivity decreases in a stepwise fashion (Fig. 48); the lithologies corresponding to these stepped decreases in resistivity form sharp contacts that are also documented in the core material. Isolated, thin, conductive events in the coarse sandstones and breccias (Bouma "A" unit) probably correspond to concentrations of claystone and/or siltstone clasts. Isolated resistive events in the massive sandstones may be caused by local concentrations of zeolite cement, which in turn is caused by alteration of volcanic glass.

Table 8. Index property data for Holes 869A and 869B.

Core, section, interval (cm)	Depth (mbsf)	Water content (%)	Bulk density (g/cm^3)	Grain density (g/cm^3)	Porosity (%)
143-869A-					
1H-1, 77–79	0.77	174.40	1.34	2.63	83.40
1H-5, 74–76	6.74	360.70	1.24	2.02	95.00
2H-1, 77–79	10.47	219.80	1.28	2.45	85.60
2H-3, 76–78	13.46	62.00	1.67	2.72	62.40
3H-1, 106–107	20.26	83.10	1.55	2.66	68.60
3H-2, 99–101	21.69	126.90	1.42	2.60	77.40
4H-1, 75–77	29.45	55.90	1.56	2.62	54.40
4H-6, 60–62	36.80	105.80	1.66	2.67	83.40
5H-4, 75–77	43.45	56.90	1.71	2.72	60.60
6H-4, 74–76	52.94	54.20	1.72	2.69	58.90
7H-2, 39–41	57.71	57.90	1.70	2.69	60.90
7H-2, 75–77	58.07	65.30	1.67	2.71	64.30
7H-6, 74–76	64.06	46.60	1.86	2.71	57.70
8H-3, 78–80	69.03	49.40	1.77	2.69	57.20
8H-6, 87–89	73.62	54.30	1.76	2.69	60.30
8H-8, 72–74	76.47	49.10	1.79	2.69	57.50
9H-2, 78–80	78.48	57.00	1.72	2.72	61.10
9H-4, 79–81	81.49	107.20	1.46	2.54	74.00
9H-6, 77–79	84.47	112.70	1.53	2.26	78.90
10X-1, 71–73	86.41	112.40	1.50	2.53	77.30
10X-2, 69–71	87.89	90.40	1.43	2.65	66.40
10X-CC, 6–8	88.36	1.85	2.15	2.20	3.91
11X-2, 83–85	97.83	114.30	1.41	2.42	73.30
11X-4, 37–39	100.37	129.40	1.37	2.39	75.50
12X-1, 60–62	106.10	82.90	1.53	2.55	67.80
12X-4, 68–70	110.68	201.90	1.25	2.11	81.40
13X-2, 20–22	117.20	222.50	1.34	2.09	90.30
13X-4, 52–54	120.52	210.90	1.23	2.08	81.50
14X-3, 40–42	128.90	171.90	1.29	2.18	79.60
14X-5, 44–46	131.94	212.90	1.24	2.07	82.30
15X-2, 68–70	137.68	199.50	1.25	2.07	81.50
15X-6, 32–34	143.32	145.60	1.34	2.19	77.60
143-869B-					
2R-1, 3–6	140.07	6.89	2.15	2.33	13.86
3R-CC, 10–13	149.18	1.53	2.45	2.51	3.70
4R-1, 16–17	159.46	57.83	1.50	2.11	55.02
4R-1, 45–46	159.75	110.05	1.43	2.72	74.96
4R-1, 62–63	159.92	0.94	2.43	2.47	2.28
5R-1, 10–12	169.01	1.46	2.54	2.60	3.65
6R-1, 5–7	178.12	7.57	2.04	2.22	14.38
11R-4, 1–3	231.42	41.87	1.85	2.88	54.68
13R-4, 52–54	251.00	31.13	1.96	2.80	46.60
15R-1, 124–127	266.65	62.64	1.66	2.84	64.03
15R-4, 144–146	271.35	43.12	1.87	2.99	56.30
15R-CC, 13–16	272.00	32.01	1.95	2.80	47.24
16R-1, 66–68	275.77	31.65	2.01	2.96	48.40
16R-1, 90–92	276.01	89.36	1.52	2.85	71.81
17R-2, 76–78	285.57	7.46	2.58	2.93	17.94
17R-CC, 6–8	286.78	29.10	1.99	2.80	44.92
19R-1, 28–30	304.39	78.93	1.55	2.77	68.58
19R-2, 9–11	305.70	12.52	2.32	2.78	25.84
20R-1, 13–15	313.94	21.83	2.12	2.80	37.94
20R-2, 136–138	316.67	68.82	1.61	2.79	65.72
20R-3, 57–59	317.38	67.98	1.60	2.69	64.64
20R-CC, 12–14	318.43	29.10	1.96	2.71	44.10
21R-1, 19–21	323.70	28.01	2.00	2.79	43.87
22R-3, 22–24	335.83	27.06	2.00	2.74	42.56
23R-1, 114–116	343.95	88.10	1.47	2.52	68.96
23R-2, 103–105	345.34	23.64	2.07	2.78	39.68
25R-2, 4–6	363.75	31.59	1.93	2.73	46.32
25R-2, 104–106	364.75	40.39	1.83	2.75	52.61
25R-3, 75–77	365.96	20.77	2.08	2.68	35.79
26R-1, 33–35	372.14	32.28	1.92	2.73	46.81
26R-1, 73–75	372.54	74.79	1.56	2.70	66.86
27R-1, 7–9	381.58	21.21	1.97	2.48	34.50
27R-1, 55–57	382.06	13.23	2.02	2.34	23.65
27R-1, 70–72	382.22	13.34	2.05	2.38	24.09
28R-CC, 12–14	391.23	12.31	2.08	2.40	22.80
29R-CC, 21–23	401.03	13.84	2.14	2.53	25.97
30R-1, 12–14	410.53	15.89	2.08	2.50	28.46
31R-1, 5–7	420.16	25.03	2.01	2.68	40.17
31R-1, 82–84	420.93	32.47	1.92	2.73	47.00
31R-1, 97–99	421.08	29.14	1.87	2.51	42.21
32R-1, 65–67	430.46	34.85	1.86	2.65	48.01
32R-1, 86–88	430.67	26.27	1.95	2.61	40.66
32R-2, 87–89	432.18	34.16	1.81	2.50	46.10
33R-1, 16–18	439.57	26.06	1.93	2.55	39.93
33R-CC, 17–18	440.93	31.84	1.83	2.49	44.26
34R-1, 87–89	449.98	13.95	2.15	2.57	26.36
34R-2, 111–113	451.72	23.99	2.07	2.78	40.00
34R-3, 31–33	452.42	22.78	2.07	2.74	38.43
35R-1, 13–14	458.94	27.82	1.92	2.57	41.70
35R-1, 41–44	459.23	9.39	2.28	2.60	19.60
36R-1, 25–27	468.66	20.41	2.10	2.72	35.68
36R-2, 105–107	470.96	28.21	1.97	2.72	43.38
36R-3, 4–6	471.45	26.82	2.07	2.90	43.71
38R-1, 51–53	488.22	25.28	2.01	2.69	40.50
38R-3, 34–36	490.19	20.98	2.07	2.67	35.92
38R-CC, 2–4	491.29	19.33	2.11	2.69	34.18
39R-1, 126–128	498.67	26.54	2.01	2.75	42.23
39R-CC, 7–9	500.20	18.80	2.16	2.76	34.17
41R-2, 118–120	517.99	14.81	2.06	2.44	26.55
41R-4, 9–11	521.02	10.71	2.16	2.46	20.85
42R-1, 110–112	527.51	12.52	2.12	2.46	23.56
42R-4, 19–21	530.86	12.15	2.19	2.55	23.68
43R-1, 83–85	536.94	19.38	2.12	2.71	34.46
43R-2, 38–40	537.99	21.63	2.08	2.71	36.93
44R-1, 94–96	546.55	5.49	2.45	2.66	12.74
44R-2, 33–34	547.44	21.84	2.06	2.68	36.92
44R-CC, 26–28	551.87	19.56	2.10	2.68	34.43
45R-1, 32–34	555.63	7.93	2.38	2.67	17.45
45R-CC, 19–21	561.96	19.67	2.13	2.75	35.08
46R-1, 76–79	565.38	25.77	2.01	2.72	41.20
48R-1, 44–46	584.37	24.55	2.01	2.67	39.58
50R-1, 2–5	603.24	19.80	2.15	2.78	35.48
50R-5, 1–3	609.22	19.28	2.14	2.75	34.64
50R-6, 126–128	611.97	23.68	2.03	2.69	38.95
51R-1, 55–57	613.26	15.75	2.22	2.74	30.17
51R-3, 104–106	616.75	23.76	2.04	2.72	39.23
51R-4, 33–35	617.54	28.45	1.96	2.69	43.34
52R-1, 146–148	623.87	17.60	2.13	2.66	31.87
52R-2, 113–115	625.04	19.01	2.13	2.71	34.03
52R-4, 2–4	626.93	20.77	2.08	2.68	35.76
53R-2, 53–55	635.44	19.79	2.05	2.58	33.84
54R-1, 91–93	642.72	13.53	2.17	2.59	25.91
54R-4, 36–38	646.34	9.89	2.25	2.57	20.26
54R-6, 108–110	650.06	12.96	2.21	2.63	25.41
55R-2, 56–58	653.57	12.85	2.23	2.65	25.42
55R-3, 31–33	654.82	14.62	2.21	2.68	28.13
55R-3, 111–113	655.62	17.72	2.10	2.61	31.63
55R-5, 48–50	657.99	22.19	2.04	2.65	36.98
56R-1, 79–81	662.00	20.65	2.08	2.67	35.53
56R-2, 115–117	663.86	8.82	2.03	2.24	16.47
56R-3, 70–72	664.91	12.59	1.89	2.13	21.16
57R-1, 31–33	671.02	21.68	2.03	2.62	36.19
57R-2, 131–133	673.52	21.22	2.04	2.61	35.63
57R-3, 56–57	674.27	24.69	2.00	2.66	39.66
57R-CC, 16–17	675.37	12.56	2.23	2.64	24.89
58R-1, 78–80	681.19	15.42	2.03	2.41	27.12
58R-5, 99–101	687.40	8.70	2.00	2.20	16.04
59R-1, 56–58	690.57	26.20	1.94	2.58	40.30
59R-3, 7–9	693.08	22.55	2.03	2.65	37.43
59R-4, 2–4	694.53	21.58	2.05	2.66	36.44
59R-5, 8–10	696.09	19.42	2.04	2.55	33.15
60R-2, 84–86	700.85	12.73	2.09	2.43	23.63
60R-5, 81–83	705.32	16.42	2.15	2.65	30.32
60R-7, 122–124	708.73	17.37	2.12	2.63	31.37
60R-8, 20–22	709.21	28.69	1.92	2.61	42.79
61R-1, 44–46	709.85	25.04	1.99	2.65	39.86
61R-2, 48–50	709.47	10.27	2.09	2.36	19.52
63R-2, 48–50	730.69	18.40	2.10	2.63	32.57
63R-3, 74–76	732.45	25.68	1.95	2.58	39.82
63R-4, 78–80	733.99	20.66	2.04	2.61	35.00
63R-6, 109–111	737.30	3.90	2.09	2.19	7.86
63R-CC, 6–8	738.38	3.58	2.16	2.25	7.46
64R-1, 112–114	739.53	15.78	2.12	2.57	28.88

Table 8 (continued).

Core, section, interval (cm)	Depth (mbsf)	Water content (%)	Bulk density (g/cm^3)	Grain density (g/cm^3)	Porosity (%)
143-869B-					
64R-2, 38–40	740.29	23.49	1.99	2.59	37.87
64R-3, 46–48	741.87	24.96	1.96	2.57	39.05
64R-4, 78–80	743.69	22.61	2.04	2.67	37.62
64R-5, 105–107	745.46	27.25	1.92	2.56	41.12
64R-6, 125–127	747.16	22.29	2.00	2.58	36.50
65R-1, 14–17	748.05	24.32	1.99	2.62	38.91
65R-2, 115–117	750.56	22.18	2.04	2.65	37.00
65R-2, 123–125	750.64	25.30	1.96	2.60	39.64
65R-3, 14–16	751.05	23.41	2.04	2.69	38.62
65R-CC, 17–19	752.58	25.10	1.97	2.61	39.62
66R-1, 2–4	757.63	20.95	2.04	2.62	35.40
66R-2, 2–4	759.13	16.69	2.06	2.50	29.46
66R-3, 59–61	761.20	19.90	2.09	2.67	34.72
67R-1, 74–76	768.05	21.20	2.04	2.61	35.60

Core, section, interval (cm)	Depth (mbsf)	Water content (%)	Bulk density (g/cm^3)	Grain density (g/cm^3)	Porosity (%)
143-869B-					
67R-2, 72–74	769.53	12.49	2.20	2.59	24.47
67R-2, 96–98	769.77	30.69	1.90	2.62	44.61
67R-4, 40–42	772.21	24.2	2.02	2.68	39.36
67R-5, 91–93	774.22	28.70	1.93	2.63	42.99
67R-6, 50–52	775.31	26.27	1.96	2.63	40.87
68R-1, 58–60	777.49	27.52	1.95	2.63	42.03
68R-2, 48–50	778.89	22.47	2.03	2.63	37.17
68R-3, 67–69	780.58	22.34	2.02	2.62	36.91
68R-4, 57–59	781.98	9.67	2.36	2.71	20.79
68R-5, 58–60	783.49	19.19	2.06	2.58	33.15
69R-1, 7–9	786.68	9.02	2.35	2.68	19.46
69R-1, 144–146	788.05	22.11	2.04	2.64	36.88
69R-2, 21–23	787.94	20.27	2.09	2.68	35.23

The intervening portion of logging Unit 5 contains numerous fining- and coarsening-upward sequences at various scales. Bed thickness varies between 1 (the lower bound on resolution of the resistivity tool) to 12 m. Many of the large fining/coarsening-upward sequences are composed of smaller sequences. Some sequences terminate in a thin, conductive, high-gamma-ray level and probably correspond to the claystone, or "E" unit, of the Bouma sequence.

The sharp peak in gamma rays at 615.7 mbsf coincides with the depth at which recovery of coalified woody fragments was reported in Interval 143-869B-51R-4 at 25–40 cm.

Logging Unit 6 (654.4–770.0 mbsf)

Logging Unit 6 corresponds to lithologic Subunit IIIF (653.3–780.7 mbsf), a series of massive sandstone and siltstone beds. The resistivity log indicates that logging Unit 6 is a highly heterogeneous interval having numerous thin, conductive intercalations (massive siltstones) separating the highly resistive peaks of the compact, well-cemented sandstones. Many of the beds of this succession of sandstone-siltstone sequences exhibit sharp lower contacts; in many places, the erosive nature of these contacts is revealed in recovered core material as siltstone clasts contained in the bases of the overlying sandstone units. Upper contacts appear gradational in the resistivity and density logs. Bed thickness varies from about 1 to 9 m. Fairly good correlation between logs and core can be made through the FMS in laminated intervals with parallel boundaries, where there is probably little or no current influence.

Summary

The sedimentary strata recovered at Site 869 show stratigraphic variation caused by downhole changes in the amount, texture, and composition of volcaniclastic materials and composition of biogenic influx. In the lower portion of the hole, where recovery in the volcaniclastics is good, correlations among the cores and logs can be done on a section-by-section basis. The downhole measurements have been interpreted here with respect to the stratigraphic column as defined by the cores. Because the total recovery was only 20% in the upper, cherty units, such an interpretation is also valuable and necessary for defining unit thicknesses and boundaries with precision, and to check that no major lithologic event was missed as a result of partial recovery.

SEISMIC STRATIGRAPHY

The seismic stratigraphy at Site 869, at least down to the level of the last cores recovered, at 796.2 mbsf, is relatively straightforward, thanks to the good core recovery through much of the section, and to good-quality downhole logs. In many places, the logs, particularly the resistivity log, can be matched directly against lithologic contacts in the cores themselves.

The best seismic profile through Site 869 is the line run by the *Thomas Washington*, during the Tunes Expedition, Leg 8, a section of which is shown as Figure 56. The main reflectors in this profile are presented in Table 12.

Between the seafloor and the first prominent reflector (Reflector C1), the reflection patterns are irregular, suggesting broad channels. The seafloor itself, as seen in the 3.5-kHz record taken by the *JOIDES Resolution* during the approach to Site 869 (Fig. 10), shows an erosional surface that truncates beds at the seafloor.

One is tempted to place Reflector C1, at about 0.085 s two-way traveltime (twtt) below the seafloor (bsf) at the first porcellanite encountered in Hole 869A, at 97 cm in Section 2 of Core 143-869A-10X. This core was taken between 85.7 and 95.5 mbsf, and the "Geolograph" shows a marked slowing of penetration at about 90 mbsf. The downhole logs show a marked increase in velocity and resistivity between about 89 and 91 mbsf, just below the bottom of the BHA during logging Run 1. The interval velocity, from Reflector C1 to the seafloor, assuming the reflector is at 90 mbsf, would be about 2.1 km/s, which is much faster than velocities of about 1.6 km/s recorded in the sonic log from strata immediately below this reflector, from about 90 to 150 mbsf.

On the other hand, if we assume that 1.6 km/s is roughly the correct interval velocity for the strata above Reflector C1, then the calculated depth to the reflector would be at about 70 mbsf. Because of the interference of the BHA when logging the shallow subsurface section, we cannot know if another interval exists higher up in the stratigraphic column that shows an impedance contrast that could create Reflector C1. The only significant change in lithology was found in Cores 143-869A-7H and -8H (57.2–76.2 mbsf), where clayey nannofossil ooze occurs, in contrast to the nannofossil ooze above and the radiolarian nannofossil ooze below. It is possible that an impedance contrast at the base or top of this interval might account for Reflector C1. Reflector C1 shows up in the 3.5-kHz profile (see "Site Geophysics" section, this chapter); thus, it represents a marked, shallow change in acoustic impedance.

The reflector indicates an irregular, hummocky form in the seismic profile (Fig. 56), which suggests either an erosional unconformity near the Oligocene/Eocene boundary or preservation of a hummocky surface on large, dunelike bed forms, having a wavelength of about 1 km and a height of about 10 to 20 m.

Reflector C2, at about 0.165 s twtt bsf, has been placed at the top of the interval showing markedly higher resistivity and velocity, at 141 to 144 mbsf in the downhole log. In the cores, this is within

Table 9. Sonic velocity, anisotropy, and bulk density data for Holes 869A and 869B.

Core, section, interval (cm)	Depth (mbsf)	V_{pt} (cu) (km/s)	V_{pl} (cu) (km/s)	V_{pt} (mc) (km/s)	V_{pl} (mc) (km/s)	Anisotropy (cu) (%)	Anisotropy (mc) (%)	Bulk density (g/cm^3)
143-869A-								
10X-CC, 6–8	88.36	4.102	3.950			3.772		2.15
869B-								
2R-1, 3–6	140.07	3.415	5.193			−41.302		2.15
3R-CC, 10–13	149.18	4.763	4.846			−1.730		2.45
4R-1, 16–17	159.46	4.132	3.578			14.362		1.50
4R-1, 45–46	159.75	2.448	2.068			16.860		1.43
4R-1, 62–63	159.92	4.671	4.913			−5.052		2.43
5R-1, 10–12	169.01	5.053	4.243			17.422		2.54
6R-1, 5–7	178.12	3.232	3.279			−1.462		2.04
9R-CC, 3–5	207.64			2.944				
11R-4, 1–3	231.42	1.810	1.721			5.030		1.85
13R-4, 52–54	251.22	1.767	1.675			5.293		1.96
15R-1, 124–127	266.65				(1)			1.66
15R-2, 127–130	268.19	(2)	1.250					(1)
15R-4, 144–146	271.35	1.308	1.053			21.607		1.87
15R-CC, 13–16	272.03							1.95
16R-1, 66–68	275.77	1.686	1.431			16.362		2.01
16R-1, 90–92	276.01	2.245	2.062			8.507		1.52
16R-1, 92–94	276.03				2.142			
17R-2, 76–78	285.57	1.589	1.415			11.583		2.58
17R-CC, 3–5	286.78	2.240	2.194			2.052		1.99
19R-1, 28–30	304.39	2.854	2.750			3.700		1.55
19R-2, 9–11	305.70	1.743	1.665			4.624		2.32
19R-2, 23–26	305.85				1.702			
20R-1, 13–15	313.94	2.753	2.688			2.386		2.12
20R-2, 136–138	316.67	1.905	1.745			8.771		1.61
20R-3, 57–59	317.38	1.832	1.749			4.622		1.60
20R-CC, 12–14	318.43	2.403	2.404			−0.044		1.96
21R-1, 19–21	323.70							2.00
22R-2, 6–8	334.67	1.917	1.843			3.916		
22R-3, 0–4	335.62				2.667			
22R-3, 22–24	335.83	2.614	2.517			3.801		2.00
23R-1, 114–116	343.95	1.784	1.718			3.741		1.47
23R-2, 103–105	345.34	2.640	2.600			1.505		2.07
25R-2, 4–6	363.75	2.591	2.575			0.643		1.93
25R-2, 78–81	364.50				2.011			
25R-2, 104–106	364.75	1.804	1.695			6.175		1.83
25R-2, 109–112	364.81				(1)			
25R-3, 75–77	365.96	1.960	1.766			10.450		2.08
26R-1, 33–35	372.14	2.447	2.434			0.558		1.92
26R-1, 73–75	372.54	1.898	1.819			4.201		1.56
27R-1, 7–9	381.58	2.627	2.439			7.421		1.97
27R-1, 55–57	382.06	3.502	2.735			24.591		2.02
27R-1, 70–72	382.22	3.278	3.019			8.222		2.05
28R-CC, 12–14	391.23	3.359	2.559			27.041		2.08
29R-CC, 21–23	401.03	3.384	3.126		7.9		302.14	
30R-CC, 12–14	410.53	3.143	2.951			6.314		2.08
31R-1, 5–7	420.16	2.358	2.383			−1.038		2.01
31R-1, 82–84	420.93	1.889	1.870			0.992		1.92
31R-1, 97–99	421.08	2.262	2.208			2.406		1.87
32R-1, 65–67	430.46	1.956	1.880			3.928		1.81
32R-1, 86–88	430.67	2.296	2.013			13.140		1.86
32R-2, 87–89	432.18	2.278	2.078			9.202		1.95
33R-1, 16–18	439.57	2.443	2.346			4.037		1.93
33R-2, 17–18	440.93	2.330	2.166			7.291		1.83
34R-1, 87–89	449.98	3.309	3.199			3.383		2.15
34R-2, 107–110	451.68				2.075			
34R-2, 111–113	451.72	2.253	2.069			8.525		2.07
34R-2, 113–117	451.75			2.101			1.092	
34R-3, 31–33	452.42	2.373	2.222			6.568		2.07
35R-1, 13–14	458.94	2.374	2.286			3.763		1.92
35R-1, 24–26	459.05				2.642			
35R-1, 41–44	459.23	3.647	3.205			12.913		2.28
36R-1, 25–27	468.66	2.419	2.210			9.019		2.10
36R-2, 105–107	470.96	2.126	1.977			7.279		1.97
36R-3, 4–6	471.45	2.076	2.098			−1.021		2.07
36R-3, 115–118	472.55				(1)			
38R-1, 51–53	488.22	2.283	2.324			−1.768		2.01
38R-2, 25–27	488.60				(1)			
38R-2, 29–31	488.65			2.359				
38R-3, 34–36	490.19	2.897	2.914			−0.605		2.07
38R-CC, 2–4	491.29							2.11
39R-1, 126–128	498.67	2.576	2.730			−5.811		2.01

Table 9 (continued).

Core, section, interval (cm)	Depth (mbsf)	V_{pt} (cu) (km/s)	V_{pl} (cu) (km/s)	V_{pt} (mc) (km/s)	V_{pl} (mc) (km/s)	Anisotropy (cu) (%)	Anisotropy (mc) (%)	Bulk density (g/cm^3)
39R-CC, 7–9	500.20	3.233	3.028			6.540		2.16
40R-1, 101–102	508.12	3.282	3.336			−1.621		
40R-2, 36–38	508.97			3.232			−3.525	
40R-2, 40–42	509.01				3.348			
40R-3, 5–7	510.16	3.177	3.145			0.999		
41R-2, 114–118	517.96				3.794			
41R-2, 118–120	517.99	4.074	3.985			2.198		2.06
41R-4, 0–5	520.95				4.055			
41R-4, 5–7	520.98			4.262			4.978	
41R-4, 9–11	521.02	4.111	3.974			3.391		2.16
42R-1, 107–109	527.48			3.778				
42R-1, 110–112	527.51	4.044	3.773			6.927		2.12
42R-1, 112–116	527.54				3.962			
42R-4, 19–21	530.86	3.726	4.021			−7.609		2.19
43R-1, 83–85	536.94	2.710	2.568			5.408		2.12
43R-2, 38–40	537.99	2.658	2.557			3.889		2.08
44R-1, 94–96	546.55	4.630	4.733			−2.191		2.45
44R-2, 33–34	547.44	2.914	2.836			2.731		2.06
44R-CC, 26–28	551.87	2.682	2.756			−2.697		2.10
45R-1, 32–34	555.63	4.174	4.130			1.067		2.38
45R-2, 49–51	557.10			2.924				
45R-2, 62–65	557.24				(1)			
45R-CC, 19–21	561.96	2.758	2.748			0.358		2.13
46R-1, 76–79	565.38	2.765	2.579			6.957		2.01
48R-1, 40–44	584.32				2.455			
48R-1, 44–46	584.37	2.798	2.635			6.008		2.01
50R-1, 2–5	603.24	2.629	2.546			3.173		2.15
50R-3, 7–9	606.28			2.392				
50R-3, 10–13	606.32				(1)			
50R-5, 1–3	609.22	2.712	2.736			−0.881		2.14
50R-6, 126–128	611.97	2.610	2.338			10.975		2.03
51R-1, 55–57	613.26	2.874	2.554			11.797		2.22
51R-3, 104–106	616.75	2.395	2.135			11.444		2.04
51R-4, 33–34	617.54	2.431	2.298			5.653		1.96
52R-1, 146–148	623.87	2.813	2.810			0.124		2.13
52R-2, 113–115	625.04	2.742	2.542			7.588		2.13
52R-3, 2–5	625.44				(1)			
52R-3, 6–8	625.47			2.653				
52R-4, 2–4	626.93	2.654	2.494			6.224		2.08
53R-3, 53–55	635.44	2.533	2.198			14.162		2.05
54R-1, 91–93	642.72	3.647	3.794			−3.962		2.17
54R-1, 93–96	642.75				3.690			
54R-1, 97–99	642.78			3.376			−8.888	
54R-4, 32–36	646.32				4.182			
54R-4, 36–38	646.34	4.019	3.916			2.574		2.25
54R-4, 39–41	646.37			4.542			8.253	
54R-6, 108–110	650.06	4.780	5.498			−13.973		2.21
55R-2, 56–58	653.57	3.620	3.127			14.616		2.23
55R-3, 31–33	654.82	3.038	2.800			8.172		2.21
55R-3, 111–113	655.62	2.959	2.675			10.074		2.10
55R-5, 48–50	657.99	2.790	2.649			5.195		2.04
56R-1, 79–81	662.00	2.815	2.585			8.513		2.08
56R-2, 113–115	663.84				2.644			
56R-2, 115–117	663.86	4.053	3.648			10.536		2.03
56R-3, 68–70	664.89				2.703			
56R-3, 70–72	664.91	4.174	4.841			−14.779		1.89
57R1, 31–33	671.02	2.917	2.448			17.506		2.03
57R-2, 131–133	673.52	3.021	2.845			5.974		2.04
57R3, 56–57	674.27	2.871	2.511			13.397		2.00
57R-CC, 16–19	675.37	3.299	3.040			8.188		2.23
58R-1, 78–80	681.19	4.041	3.941			2.506		2.03
58R-5, 99–101	687.40	4.570	4.484			1.892		2.00
59R-1, 56–58	690.57	2.684	2.501			7.049		1.94
59R-3, 7–9	693.08	2.766	2.526			9.056		2.03
59R-4, 2–4	694.53	2.861	2.764			3.469		2.05
59R-5, 8–10	696.09	3.153	2.891			8.654		2.04
59R-6, 57–60	698.09				3.527			
59R-6, 61–63	698.12			3.362			−4.790	
60R-2, 84–86	700.85	4.074	4.218			−3.481		2.09
60R-5, 81–83	705.32	3.225	3.192			1.027		2.15
60R-7, 122–124	708.73	3.048	3.009			1.269		2.12
60R-8, 20–22	709.21	2.573	2.381			7.760		1.92
61R-1, 37–39	709.78			2.652				
61R-1, 39–44	709.81				(1)			
61R-1, 44–46	709.85	2.521	2.413			4.373		1.99
61R-2, 41–43	711.32			3.995				
61R-2, 45–48	711.36				4.083		−2.179	

Table 9 (continued).

Core, section, interval (cm)	Depth (mbsf)	V_{pt} (cu) (km/s)	V_{pl} (cu) (km/s)	V_{pt} (mc) (km/s)	V_{pl} (mc) (km/s)	Anisotropy (cu) (%)	Anisotropy (mc) (%)	Bulk density (g/cm^3)
61R-2, 48–50	711.39	4.254	3.947			7.491		2.09
63R-2, 48–50	730.69	3.025	2.503			18.890		2.10
63R-3, 28–31	732.00				2.563			
63R-3, 74–76	732.45	2.703	2.481			8.564		1.95
63R-4, 78–80	733.99	2.765	2.811			−1.664		2.04
63R-4, 81–85	734.04				(1)			
63R-6, 109–111	737.30	4.300	4.182			2.781		2.09
63R-CC, 2–4	738.34				4.412			
63R-CC, 6–8	738.38	4.355	4.511			−3.530		2.16
64R-1, 112–114	739.53	3.069	3.141			−2.318		2.12
64R-2, 38–40	740.29	2.615	2.355			10.460		1.99
64R-3, 46–48	741.87	2.442	2.420			0.894		1.96
64R-3, 113–116	742.55				2.639			
64R-4, 78–80	743.69	2.591	2.295			12.093		2.04
64R-5, 105–107	745.46	2.689	2.409			10.977		1.92
64R-6, 57–60	746.49				2.550			
64R-6, 125–127	747.16	2.773	2.537			8.891		2.00
65R-1, 14–17	748.05	2.696	2.382			12.363		1.99
65R-1, 70–73	748.62				2.426			
65R-2, 115–117	750.56	2.807	2.364			17.102		2.04
65R-2, 123–125	750.64	2.674	2.264			16.600		1.96
65R-3, 14–16	751.05	2.798	2.476			12.223		2.04
65R-4, 3–7	752.45				2.335			
65R-CC, 17–19	752.58	2.688	2.484			7.906		1.97
66R-1, 2–4	757.63	2.833	2.683			5.442		2.04
66R-2, 2–4	759.13	3.283	3.302			−0.579		2.06
66R-3, 59–61	761.20	2.785	2.702			2.999		2.09
67R-1, 74–76	768.05	2.778	2.587			7.094		2.04
67R-1, 146–149	768.78				2.375			
67R-2, 72–74	769.53	2.725	2.666			2.201		2.20
67R-2, 96–98	769.77	2.567	2.397			6.825		1.90
67R-4, 40–42	772.21	2.812	2.336			18.479		2.02
67R-5, 91–93	774.22	2.596	2.323			11.083		1.93
67R-6, 50–52	775.31	2.725	2.439			11.061		1.96
67R-CC, 2–5	775.68							
68R-1, 58–60	777.49	2.655	2.371			11.287		1.95
68R-1, 60–63	777.53				1.951			
68R-2, 44–47	778.88				2.575			
68R-2, 48–50	778.89	2.726	2.577			5.604		2.03
68R-3, 53–57	780.45				2.686			
68R-4, 57–59	781.98	3.463	3.161			9.113		2.36
68R-3, 67–69	780.58	2.751	2.422			12.738		2.02
68R-5, 58–60	783.49	3.009	2.478			19.343		2.06
69R-1, 7–9	786.68	4.196	4.009			4.547		2.35
69R-1, 144–146	788.05	2.768	2.353			16.201		2.04
69R-2, 21–23	787.94	2.693	2.365			12.986		2.09

Note: Measurements are labeled for direction and sample shape: V_{pt} (cu) is transverse (horizontal) from a cube; V_{pl} (cu) is longitudinal (parallel core-axis) from a cube; V_{pt} (mc) is transverse from a minicore; V_{pl} (mc) is longitudinal from a minicore. Samples that were too long for acoustic measurements (minicores) or collapsed during measurement have been labeled (1) and (2), respectively.

Core 143-869A-15X, from 135.5 to 145.5 mbsf, but in this core, only a trace of porcellanite is seen. Nonetheless, drilling rates slowed markedly in the last few meters of coring, and chert fragments were recovered in the following core (143-869A-16X). We suppose that the chert was present in the lowest few meters of the upper coring interval, but was not recovered. The interval velocity, to Reflector C1 (at 70 mbsf), is 1.78 km/s. The age of Reflector C2 is early Eocene.

Reflector C2 also has an irregular, hummocky surface with a relief of about 10 m, which may be caused by diagenetic effects that produce chert at variable stratigraphic levels.

Reflector C3, at about 0.190 s twtt bsf, was assigned to the major change in lithology at 165 mbsf, as shown in the downhole logs of hole diameter, resistivity, sonic velocity, and density. The lower Eocene and upper Paleocene radiolarian-nannofossil oozes below this level, to a depth of about 207 mbsf, contain chert nodules; in fact, the poorly recovered section in the interval from 165 to 207 mbsf consists of mainly chert fragments.

No prominent reflector marks the unconformable contact between Paleocene cherty radiolarian ooze above and late Campanian–early Maastrichtian volcaniclastic sandstone, siltstone, and claystone below, which is at a depth of about 207 mbsf in the cores, based on the depth to Sample 143-869B-8R-CC, where the first Cretaceous nannofossils were noted. A break occurs in the sonic, density, and resistivity logs at 207 mbsf, with generally smaller values below this depth, but the change is too small to generate a sufficient impedance contrast to produce a reflector, and nothing can be seen in the seismic profile at the appropriate two-way reflection time (about 0.23 s).

Reflector K1 is the top of a bundle of reflectors, from about 0.345 to 0.390 s twtt bsf. It most plausibly corresponds to the group of volcaniclastic sandstones in Cores 143-869B-19R to -21R, from about 303 to 331 mbsf, in the lower Campanian sequence.

Reflector K2 is the top of an interval of radiolarian claystone and siltstone of early Campanian age from 378 to 394 mbsf. The increases in velocity, density, and resistivity seen in the downhole logs probably

Table 10. Measurements from the digital sound velocimeter for Site 869.

Core, section, interval (cm)	Depth (mbsf)	Velocity (km/s)	Core, section, interval (cm)	Depth (mbsf)	Velocity (km/s)
143-869A-			8H-6, 84	73.59	1.545
			8H-7, 84	75.09	1.532
1H-1, 123	1.23	1.493	8H-8, 68	76.43	1.555
1H-1, 75	0.75	1.482	9H-1, 75	76.95	1.550
1H-2, 86	2.36	1.463	9H-2, 75	78.45	1.530
1H-3, 72	3.72	1.469	9H-3, 75	79.95	1.517
1H-4, 72	5.22	1.491	9H-4, 75	81.45	1.533
1H-5, 72	6.72	1.504	9H-5, 102	83.22	1.523
1H-6, 72	8.22	1.488	9H-6, 75	84.45	1.520
1H-7, 30	9.30	1.496	9H-7, 27	85.47	1.528
2H-1, 75	10.45	1.471	10X-1, 38	86.08	1.530
2H-2, 75	11.95	1.510	10X-2, 67	87.87	1.527
2H-3, 75	13.45	1.514	11X-1, 107	96.57	1.555
2H-4, 75	14.95	1.502	11X-2, 80	97.80	1.543
2H-5, 75	16.45	1.506	11X-3, 79	99.29	1.547
2H-6, 75	17.95	1.465	11X-4, 35	100.35	1.533
2H-7, 24	18.94	1.502	11X-5, 27	101.77	1.550
3H-1, 105	20.25	1.466	12X-1, 60	106.10	1.528
3H-2, 98	21.68	1.465	12X-2, 99	107.99	1.540
3H-3, 49	22.69	1.501	12X-2, 69	107.69	1.499
3H-4, 75	24.45	1.479	12X-3, 75	109.25	1.528
3H-4, 87	24.57	1.476	12X-4, 68	110.68	1.560
3H-6, 75	27.45	1.482	12X-4, 102	111.02	1.515
4H-1, 75	29.45	1.504	12X-5, 56	112.06	1.543
4H-2, 75	30.95	1.504	13X-2, 101	118.01	1.554
4H-3, 58	32.28	1.502	13X-2, 20	117.20	1.560
4H-3, 114	32.84	1.514	13X-3, 74	119.24	1.560
4H-4, 123	34.43	1.509	13X-3, 50	119.00	1.560
4H-5, 75	35.45	1.462	13X-4, 15	120.15	1.555
4H-6, 60	36.80	1.520	13X-4, 53	120.53	1.547
4H-7, 25	37.95	1.515	13X-5, 25	121.25	1.542
5H-1, 75	38.95	1.522	14X-2, 42	127.42	1.554
5H-2, 75	40.45	1.477	14X-3, 86	129.36	1.522
5H-3, 75	41.95	1.444	14X-3, 40	128.90	1.559
5H-4, 75	43.45	1.528	14X-4, 99	130.99	1.564
5H-5, 75	44.95	1.537	14X-5, 43	131.93	1.522
5H-6, 75	46.45	1.532	14X-5, 24	131.74	1.560
5H-7, 25	47.45	1.520	14X-6, 15	132.65	1.462
6H-1, 75	48.45	1.522	15X-1, 84	136.34	1.554
6H-2, 75	49.95	1.514	15X-1, 50	136.00	1.566
6H-3, 75	51.45	1.520	15X-2, 67	137.67	1.557
6H-4, 75	52.95	1.535	15X-2, 39	137.39	1.562
6H-5, 86	54.56	1.530	15X-3, 97	139.47	1.507
6H-6, 75	55.95	1.540	15X-3, 79	139.29	1.506
6H-7, 28	56.98	1.520	15X-3, 39	138.89	1.571
7H-2, 75	58.07	1.523	15X-4, 56	140.56	1.401
7H-2, 39	57.71	1.535	15X-4, 130	141.30	1.566
7H-3, 75	59.57	1.525	15X-5, 94	142.44	1.576
7H-4, 75	61.07	1.525	15X-6, 33	143.33	1.580
7H-5, 75	62.57	1.562			
7H-6, 75	64.07	1.559	143-869B-		
7H-7, 75	65.57	1.545			
7H-8, 42	66.74	1.567	10R-1, 95	218.15	1.639
8H-2, 75	67.50	1.566	10R-2, 44	219.14	1.376
8H-3, 75	69.00	1.535	11R-1, 89	227.79	1.576
8H-4, 84	70.59	1.562	11R-2, 76	229.16	0.641
8H-5, 84	72.09	1.554			

Table 11. Thermal conductivity data for Site 869.

Core, section, interval (cm)	Depth (mbsf)	Thermal conductivity (W/[m · K])	Core, section, interval (cm)	Depth (mbsf)	Thermal conductivity (W/[m · K])
143-869A-			9H-5, 75	82.95	1.197
			9H-6, 75	84.45	0.910
3H-1, 100	20.20	1.011	10X-2, 55	87.75	1.093
3H-2, 100	21.70	0.911	11X-3, 75	99.25	1.105
3H-3, 100	23.20	1.036	11X-1, 75	96.25	0.796
3H-4, 100	24.70	0.741	11X-5, 53	102.03	0.852
3H-5, 75	25.95	1.094	11X-4, 75	100.75	0.996
3H-6, 75	27.45	0.900	12X-1, 75	106.25	0.849
3H-1, 100	20.20	0.970	12X-2, 75	107.75	0.886
4H-1, 75	29.45	1.727	12X-3, 75	109.25	1.081
4H-2, 75	30.95	1.386	12X-4, 75	110.75	0.789
4H-3, 75	32.45	1.233	12X-5, 57	112.07	1.001
4H-4, 75	33.95	0.928	13X-1, 75	116.25	0.807
4H-5, 75	35.45	0.872	13X-2, 75	117.75	0.916
4H-6, 75	36.95	1.215	13X-3, 84	119.34	0.784
4H-7, 25	37.95	1.192	13X-4, 49	120.49	0.820
5H-1, 75	38.95	1.165	13X-5, 29	121.29	0.747
5H-2, 75	40.45	0.904	14X-2, 75	127.75	0.803
5H-3, 75	41.95	1.321	14X-3, 75	129.25	0.889
5H-4, 75	43.45	1.247	14X-4, 68	130.68	0.753
5H-5, 75	44.95	0.869	14X-5, 50	132.00	0.829
5H-6, 75	46.45	1.367	14X-6, 30	132.80	0.851
6H-1, 75	48.45	1.086	15X-1, 75	136.25	0.718
6H-2, 75	49.95	1.305	15X-2, 54	137.54	0.802
6H-3, 75	51.45	1.030	15X-3, 75	139.25	0.918
6H-4, 75	52.95	1.162	15X-4, 78	140.78	0.867
6H-5, 75	54.45	1.296	15X-5, 76	142.26	0.789
6H-6, 75	55.95	0.799	15X-6, 39	143.39	0.851
6H-7, 25	56.95	1.410			
7H-2, 75	58.07	1.347	143-869B-		
7H-3, 75	59.57	1.510			
7H-4, 75	61.07	0.937	16R-1, 50	275.60	1.235
7H-5, 75	62.57	1.331	15R-1, 73	266.13	0.955
7H-6, 75	64.07	1.225	15R-2, 62	267.52	1.077
7H-7, 75	65.57	1.136	15R-3, 72	269.12	0.994
7H-8, 25	66.57	1.213	15R-4, 75	270.65	1.150
8H-2, 75	67.50	1.494	15R-5, 26	271.66	1.020
8H-3, 75	69.00	1.415	10R-1, 60	217.80	1.230
8H-4, 75	70.50	1.307	10R-1, 122	218.42	1.151
8H-5, 75	72.00	1.435	10R-2, 40	219.10	1.305
8H-6, 75	73.50	1.459	11R-1, 75	227.65	0.918
8H-7, 75	75.00	1.363	11R-2, 75	229.15	1.034
8H-8, 40	76.15	1.164	11R-3, 70	230.60	1.288
9H-1, 75	76.95	1.404	11R-4, 82	232.22	1.334
9H-2, 75	78.45	1.406	13R-1, 44	246.64	1.016
9H-3, 75	79.95	1.276	13R-2, 76	248.46	1.272
9H-7, 40	85.60	1.074	13R-3, 70	249.90	1.232
9H-4, 75	81.45	0.953	13R-4, 56	251.26	1.340

were caused by extensive diagenesis of these relatively siliceous strata. The impedance change at the base of this interval, at 378 mbsf, has been selected as Reflector K2A, at 0.440 s twtt.

Reflector K3 is the top of a 25-m-thick set of massive coarse debris flows and turbidites from about 509 to 543 mbsf, in Cores 143-869B-40R to -43R in the upper Cenomanian. All the downhole sonic, resistivity, density, and caliper logs show this lithologic unit which has a moderately strong impedance contrast at the top (which is a somewhat gradational contact) and a very strong (negative) impedance contrast at the base (which is marked in the seismic profile by Reflector K4).

Reflector K5, at 0.620 s twtt, was selected at 617 mbsf, at the top of a series of upper Cenomanian debris flows and sandy turbidites that begins at 654 mbsf in the upper part of Section 2 of Core 143-869B-55R. The downhole logs show a typical "Christmas-tree" profile, with a very large negative impedance contrast at the base of the unit, marked by Reflector K6 (0.640 s twtt) at 654 mbsf, and a more gradational change in properties at the top of the interval. An extremely strong peak in the gamma-ray log, most plausibly associated with thin clayey turbidites in the top of Section 4 of Core 143-869B-51R, lies immediately above the upper debris flows in the sequence. The geochemical log shows this to be high in potassium and thorium and thus is most likely an ashy layer.

Between 654 mbsf and the total depth of Hole 869B, the strata consist of sandy turbidites, each with a "Christmas-tree" profile in the downhole logs, and these probably make up the series of closely spaced weak reflectors in the seismic profile, below 0.640 s twtt. No readily apparent base is seen for the reflectors, that is, no strong "acoustic basement." The last visible reflector in this profile (Reflector K7) is seen at about 0.89 s twtt. An even deeper, very faint reflector at 1.05 s twtt was noted in the *JOIDES Resolution* profile, which was shot with a larger acoustic source (Fig. 9). This suggests that the seismic reflection penetration at Site 869 was limited by the profiling equipment and that true volcanic basement may be very deep.

A plot of two-way reflection times vs. depth in Hole 869B is given in Table 12, and the values are plotted in Figure 57. In this figure, the extrapolated depth to Reflector K7 is shown as 1000 mbsf, if allowance were made for further increases downward in interval sonic velocity. A straight-line extrapolation, having the same velocity calculated for the interval between Reflectors K5 and K3, gives an estimated depth of about 950 mbsf for Reflector K7. Reflector K8, at 1.05 s twtt, has been estimated to be at about 1230 mbsf.

REFERENCES*

Berger, W.H., Vincent, E., and Thierstein, H.R., 1981. The deep-sea record: major steps in Cenozoic ocean evolution. *In* Warme, J.E., Douglas, R.G., and Winterer, E.L. (Eds.), *The Deep Sea Drilling Project: A Decade of Progress.* Spec. Publ.—Soc. Econ. Paleontol. Mineral., 32:489–504.

Berger, W.H., and Winterer, E.L., 1974. Plate stratigraphy and the fluctuating carbonate line. *In* Hsü, K.J., and Jenkyns, H.C. (Eds.), *Pelagic Sediments on Land and Under the Sea.* Spec. Publ. Int. Assoc. Sedimentol., 1:11–48.

Berggren, W.A., Kent, D.V., Flynn, J.J., and Van Couvering, J.A., 1985. Cenozoic geochronology. *Geol. Soc. Am. Bull.*, 96:1407–1418.

Cole, W.S., 1954. Larger foraminifera and smaller diagnostic foraminifera from Bikini drill holes. *U.S. Geol. Surv. Prof. Pap.*, 260-V: Washington (U.S. Govt. Printing Office), 743–784.

Davis, A.S., Pringle, M.S., Pickthorn, L.B.G., Clague, D.A., and Schwab, W.C., 1989. Petrology and age of alkalic lava from the Ratak chain of the Marshall Islands. *J. Geophys. Res.*, 94:5757–5774.

Duncan, R.A., and Clague, D.A., 1985. Pacific plate motions recorded by linear volcanic chains. *In* Nairn, A.E.M., Stehli, F.G., and Uyeda, S. (Eds.), *The Ocean Basins and Margins* (Vol. 7A): *The Pacific Ocean:* New York (Plenum), 89–121.

Emery, K.O., Tracey, J.I., Jr., and Ladd, H.S., 1954. *Geology of Bikini and Nearby Atolls.* U.S. Geol. Surv. Prof. Pap., 260-A:1–265.

Fischer, A.G., 1986. Climatic rhythms recorded in strata. *Annu. Rev. Earth Planet. Sci.*, 14:351–376.

Haggerty, J.A., and Premoli-Silva, I., 1986. Ooids and shallow-water debris in Aptian-Albian sediments from the East Mariana Basin, Deep Sea Drilling Project Site 585: implications for the environment of formation of ooids. *In* Moberly, R., Schlanger, S.O., et al., *Init. Repts DSDP,* 89: Washington (U.S. Govt. Printing Office), 399–412.

Hambach, U., and Krumsiek, K., 1989. A magnetostratigraphic subdivision of the upper Albian and lower Cenomanian on the basis of drill cores from wells in the Ruhr area. *Geol. Jahrb.*, A113:401–425.

Hamilton, E.L., and Rex, R.W., 1959. *Lower Eocene Phosphatized Globigerina Ooze from Sylvania Guyot.* U.S. Geol. Surv. Prof. Pap., 260-W:785–797.

Hancock, J.M., and Kauffman, E.G., 1979. The great trangressions of the Late Cretaceous. *J. Geol. Soc. London*, 136:175–186.

Jenkyns, H.C., 1972. Pelagic "oolites" from the Tethyan Jurassic. *J. Geol.*, 80:21–33.

Jenkyns, H.C., and Schlanger, S.O., 1981. Significance of plant remains in redeposited Aptian sediments, Hole 462A, Nauru Basin, to Cretaceous oceanic-oxygenation models. *In* Larson, R.L., and Schlanger, S.O., et al., *Init. Repts. DSDP,* 61: Washington (U.S. Govt. Printing Office), 557–562.

Kent, D.V., and Gradstein, F.M., 1985. A Cretaceous and Jurassic geochronology. *Geol. Soc. Am. Bull.*, 96:1419–1427.

Kulp, L.J., 1963. Potassium-argon dating of volcanic rocks. *Bull. Volcanol.*, 26:247–258.

Larson, R.L., 1976. Late Jurassic and Early Cretaceous evolution of the western Central Pacific Ocean. *J. Geomagn. Geoelectr.*, 28:219–236.

Larson, R.L., and Schlanger, S.O., 1981. Geological evolution of the Nauru Basin, and regional implications. *In* Larson, R.L., Schlanger, S.O., et al., *Init. Repts DSDP,* 61: Washington (U.S. Govt. Printing Office), 841–862.

Lincoln, J.M., Pringle, M.S., and Premoli Silva, I., in press. Early and Late Cretaceous volcanism and reef-building in the Marshall Islands. *In* Pringle, M.S., Sager, W.W., Sliter, W.V., and Stein, S. (Eds.), *The Mesozoic Pacific.* Am. Geophys. Union, Geophys. Monogr. Ser.

Lisitzin, A.P., 1971. Distribution of siliceous microfossils in suspension and bottom sediments. *In* Funnell, B. M., and Riedel, W. R. (Eds.), *The Micropalaeontology of the Oceans:* Cambridge (Cambridge Univ. Press), 173–195.

* Abbreviations for names of organizations and publication titles in ODP reference lists follow the style given in *Chemical Abstracts Service Source Index* (published by American Chemical Society).

Martini, E., 1971. Standard Tertiary and Quaternary calcareous nannoplankton zonation. *In* Farinacci, A. (Ed.), *Proc. 2nd Int. Conf. Planktonic Microfossils Roma:* Rome (Ed. Tecnosci.), 2:739–785.

McNutt, M.K., and Fischer, K.M., 1987. The South Pacific superswell. *In* Keating, B.H., Fryer, P., Batiza, R., and Boehlert, G.W. (Eds.), *Seamounts, Islands, and Atolls.* Am. Geophys. Union, Geophys. Monogr. Ser., 43:25–34.

Moberly, R., Schlanger, S.O., and Shipboard Scientific Party, 1986. Site 585. *In* Moberly, R., Schlanger, S.O., et al., *Init. Repts., DSDP,* 89: Washington (U.S. Govt. Printing Office), 29–156.

Mutti, E., and Ricci Lucchi, F., 1972. Le torbiditi del l'Appennino settentrional: introduzione all'analisi de facies. *Mem. Soc. Geol. Ital.*, 11:161–199.

Nakanishi, M., Tamaki, K., and Kobayashi, K., 1992. Magnetic anomaly lineations from Late Jurassic to Early Cretaceous in the west-central Pacific Ocean. *Geophys. J. Int.*, 109:701–719.

Normark, W.R., 1970. Growth patterns of deep-sea fans. *AAPG Bull.*, 54:2170–2195.

Perch-Nielsen, K., 1985. Mesozoic calcareous nannofossils. *In* Bolli, H.M., Saunders, J.B., and Perch-Nielsen, K. (Eds.), *Plankton Stratigraphy:* Cambridge (Cambridge Univ. Press), 329–426.

Petersen, L.D., Duennebier, F.K., and Shipley, T.H., 1986. Site surveys in the western Pacific conducted aboard the Kana Keoki, Cruise KK810626 Leg 4. *In* Moberly, R., Schlanger, S.O., et al., *Init. Repts. DSDP,* 89: Washington (U.S. Govt. Printing Office), 311–319.

Pickering, K.T., Hiscott, R.N., and Hein, F.J., 1989. *Deep Marine Environments: Clastic Sedimentation and Tectonics:* London (Unwin Hyman).

Premoli Silva, I., and Brusa, C. 1981. Shallow-water skeletal debris and larger foraminifers from Deep Sea Drilling Project Site 462, Nauru Basin, western equatorial Pacific. *In* Larson, R.L., Schlanger, S.O., et al., *Init. Repts. DSDP,* 61: Washington (U.S. Govt. Printing Office), 439–473.

Pringle, M.S., Jr., 1992. Geochronology and petrology of the Musicians Seamounts, and the search for hot spot volcanism in the Cretaceous Pacific [Ph.D. dissert.]. Univ. of Hawaii, Honolulu.

Rea, D.K., and Vallier, T.L., 1983. Two Cretaceous volcanic episodes in the western Pacific Ocean. *Geol. Soc. Am. Bull.*, 94:1430–1437.

Sager, W.W., 1986. Magnetic-susceptibility measurements of metal contaminants in ODP Leg 101 cores. *In* Austin, J.A., Jr., Schlager, W., et al., *Proc. ODP, Init. Repts.*, 101: College Station, TX (Ocean Drilling Program), 39–46.

————, 1988. Paleomagnetism of Ocean Drilling Program Leg 101 sediments: magnetostratigraphy, magnetic diagenesis, and paleolatitudes. *In* Austin, J.A., Jr., Schlager, W., et al., *Proc. ODP, Sci. Results,* 101: College Station, TX (Ocean Drilling Program), 327–360.

Schlager, W., 1980. Mesozoic calciturbidites in Deep Sea Drilling Project Hole 416A: recognition of a drowned carbonate platform. *In* Lancelot, Y., Winterer, E.L., et al., *Init. Repts. DSDP,* 50: Washington (U.S. Govt. Printing Office), 733–749.

Schlanger, S.O., 1963. Subsurface geology of Eniwetok Atoll. *U.S. Geol. Surv. Prof. Pap.*, 260-BB:991–1066.

————, 1986. High frequency sea-level fluctuations in Cretaceous time: an emerging geophysical problem. *In* Hsü, K.J. (Ed.), *Mesozoic and Cenozoic Oceans.* Am. Geophys. Union, 61–74.

Schlanger, S.O., Arthur, M.A., Jenkyns, H.C., and Scholle, P.A., 1987. The Cenomanian-Turonian Oceanic Anoxic Event, I. Stratigraphy and distribution of organic carbon-rich beds and the marine $\delta^{13}C$ excursion. *In* Brooks, J., and Fleet, A.J., *Marine Petroleum Source Rocks.* Geol. Soc. London Spec. Publ., 26:371–399.

Schlanger, S.O., Jenkyns, H.C., and Premoli Silva, I., 1981. Volcanism and vertical tectonics in the Pacific Basin related to global Cretaceous transgressions. *Earth Planet. Sci. Lett.*, 52:435–449.

Schlanger, S.O., and Premoli Silva, I., 1981. Tectonic, volcanic, and paleogeographic implications of redeposited reef faunas of Late Cretaceous and Tertiary age from the Nauru Basin and the Line Islands. *In* Larson, R.L., Schlanger, S.O., et al., *Init. Repts. DSDP,* 61: Washington (U.S. Govt. Printing Office), 817–827.

————, 1986. Oligocene sea-level fall recorded in mid-Pacific atoll and archipelagic apron settings. *Geology,* 14:392–395.

Sissingh, W., 1977. Biostratigraphy of Cretaceous calcareous nannoplankton. *Geol. Mijnbouw,* 56:37–65.

Tarduno, J.A., Lowrie, W., Sliter, W.V., Bralower, T.J., and Heller, F., 1992. Reversed polarity characteristic magnetizations in the Albian Contessa section, Umbrian Apennines, Italy: implications for the existence of a mid-Cretaceous mixed polarity interval. *J. Geophys. Res.*, 97:241–271.

Tarduno, J.A., Mayer, L.A., Musgrave, R., and Shipboard Scientific Party, 1991. High-resolution, whole-core magnetic susceptibility data from Leg 130, Ontong Java Plateau. *In* Kroenke, L.W., Berger, W.H., Janecek, T.R., et al., *Proc. ODP, Init. Repts.*, 130: College Station, TX (Ocean Drilling Program), 541–548.

Tarduno, J.A., Sliter, W.V., Bralower, T.J., McWilliams, M., Premoli Silva, I., and Ogg, J.G., 1989. M-sequence reversals recorded in DSDP sediment cores from the western Mid-Pacific Mountains and Magellan Rise. *Geol. Soc. Am. Bull.*, 101:1306–1316.

van Andel, T.H., 1975. Mesozoic-Cenozoic calcite compensation depth and the global distribution of calcareous sediments. *Earth Planet. Sci. Lett.*, 26:187–194.

Warme, J.E., Kennedy, W.J., and Schneidermann, N., 1973. Biogenic sedimentary structures (trace fossils) in Leg 15 cores. *In* Edgar, N.T., Saunders, J.B., et al., *Init. Repts. DSDP*, 15: Washington (U.S. Govt. Printing Office), 813–831.

Wetzel, A., 1991. Ecologic interpretation of deep-sea trace fossil communities. *Palaeogeogr., Palaeoclimatol., Palaeoecol.*, 85:47–69.

Ms 143IR-109

NOTE: For all sites drilled, core-description forms ("barrel sheets") and core photographs have been reproduced on coated paper and can be found in Section 3, beginning on page 381. Forms containing smear-slide data can be found in Section 4, beginning on page 691. Conventional and geochemical-log, FMS, and dipmeter data can be found in CD-ROM form (back pocket).

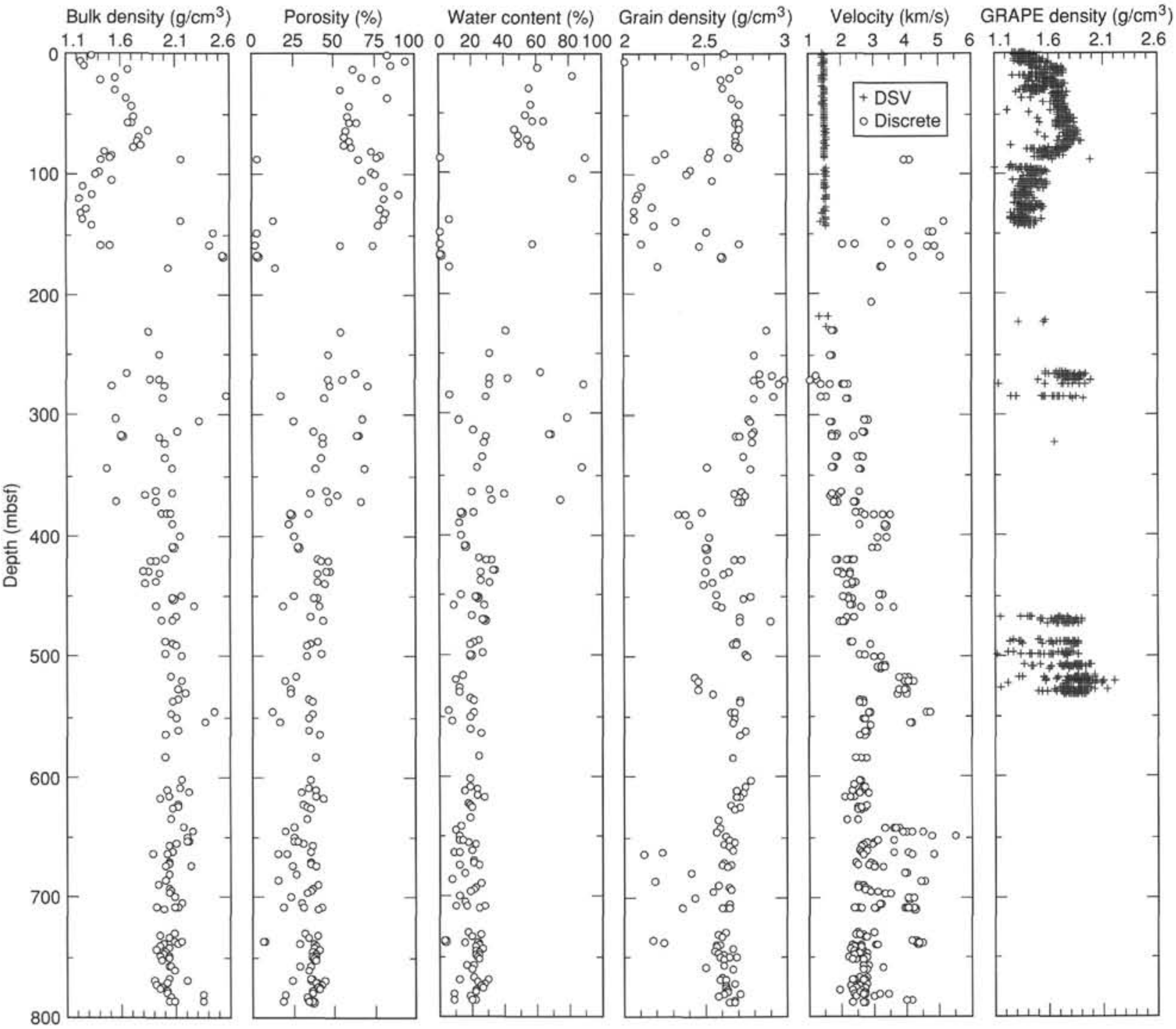

Figure 44. Index properties, sonic velocity, and GRAPE-density data for Holes 869A and 869B.

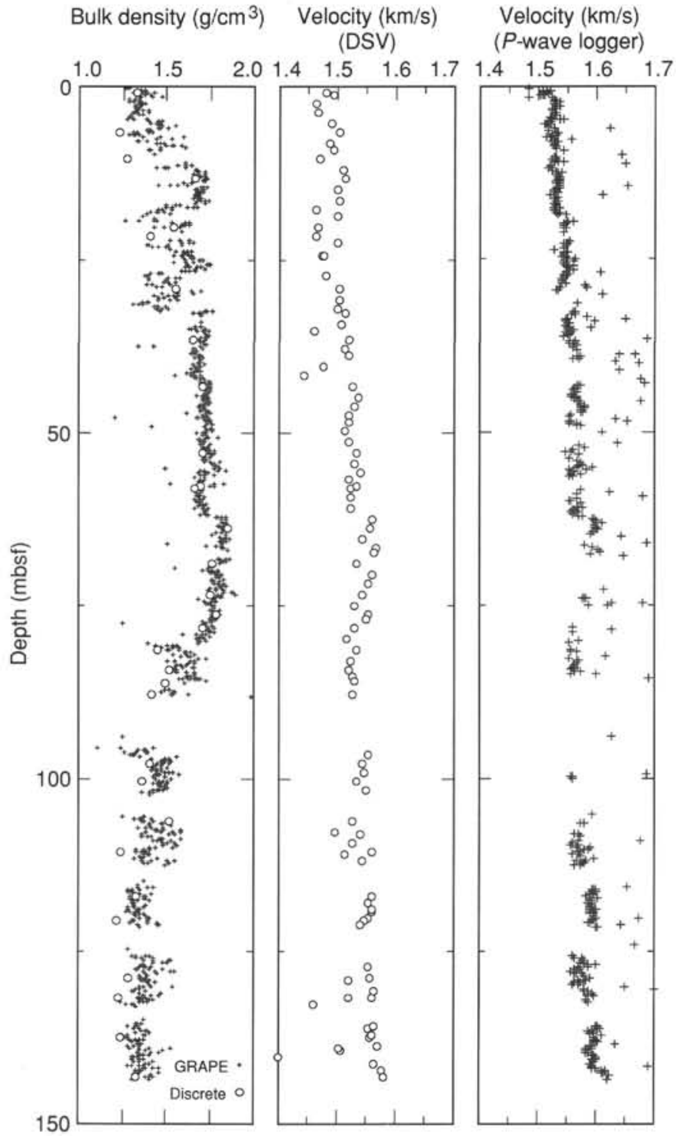

Figure 45. Bulk density from discrete measurements and GRAPE-density logger, and *P*-wave velocity from the DSV and MST *P*-wave logger, vs. depth, Hole 869A.

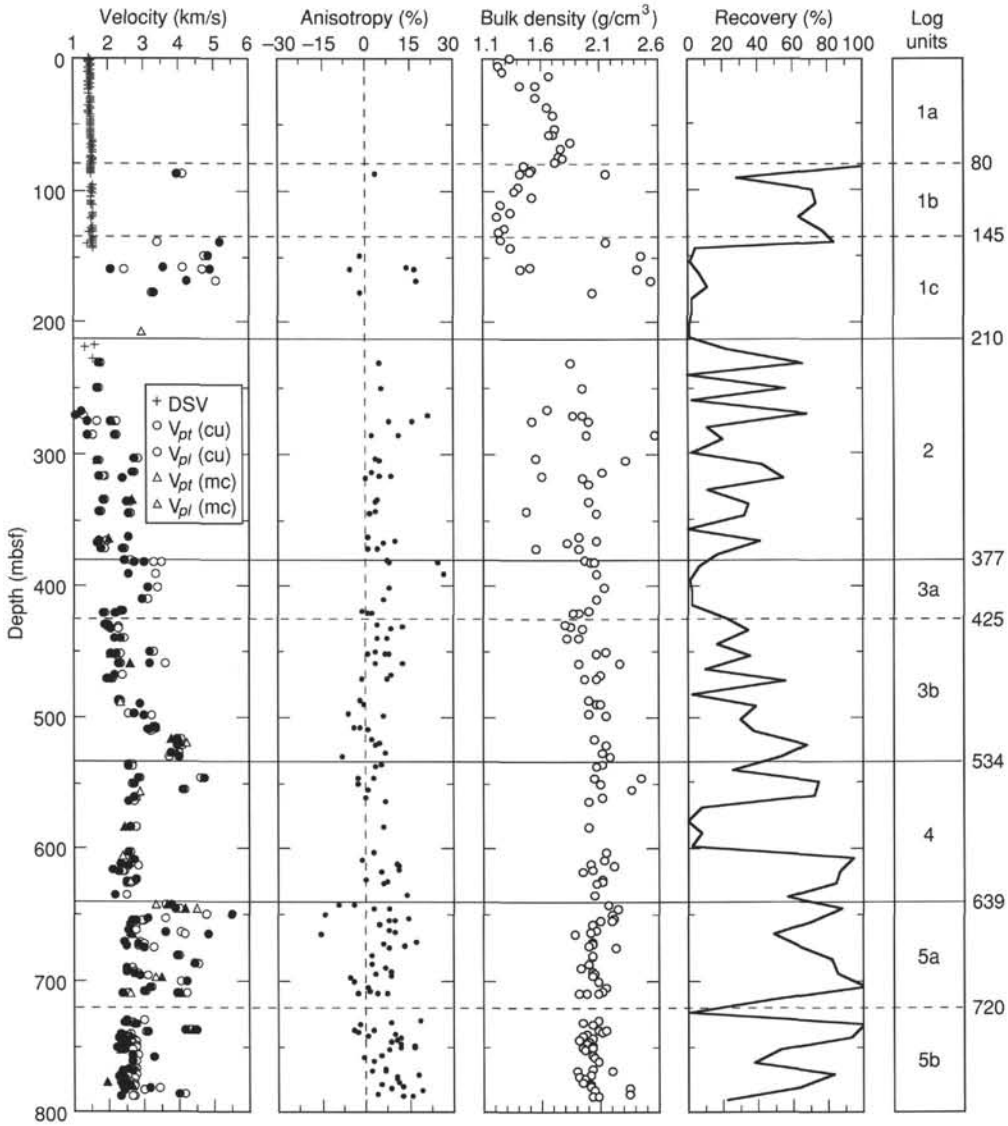

Figure 46. Plot of sonic velocity, anisotropy, bulk density, and recovery for Site 869. Indicated on the left are the physical property units (depth in mbsf). DSV = digital sound velocimeter; V_{pt} is transverse; V_{pl} is longitudinal (parallel core-axis); letters in parentheses in legend indicate measurements from cubes, "cu," or measurements from minicores, "mc."

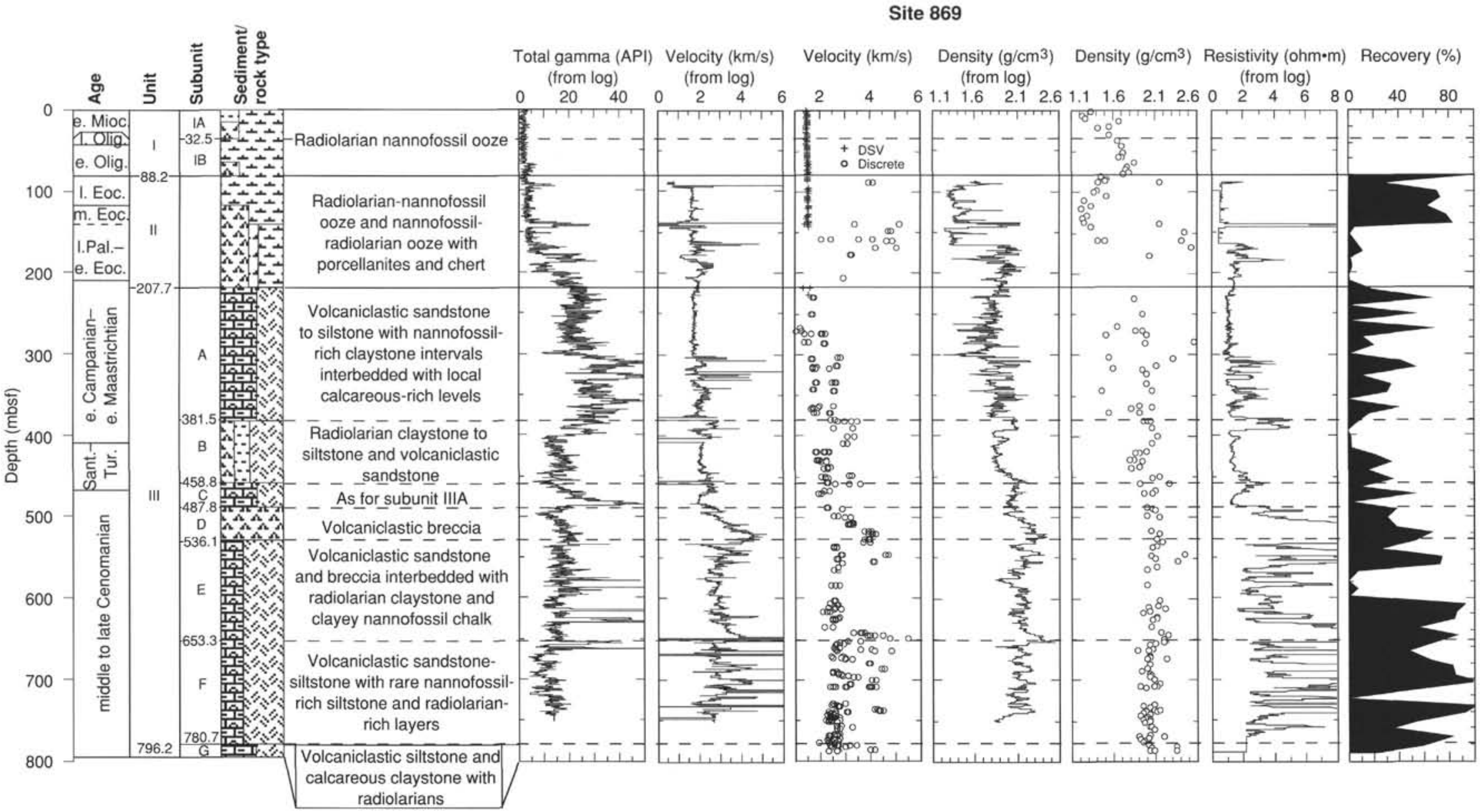

Figure 47. Comparison of lithostratigraphy with index physical properties, sonic velocity and density, and wireline log measurements (gamma, sonic velocity, density, and resistivity) for Site 869.

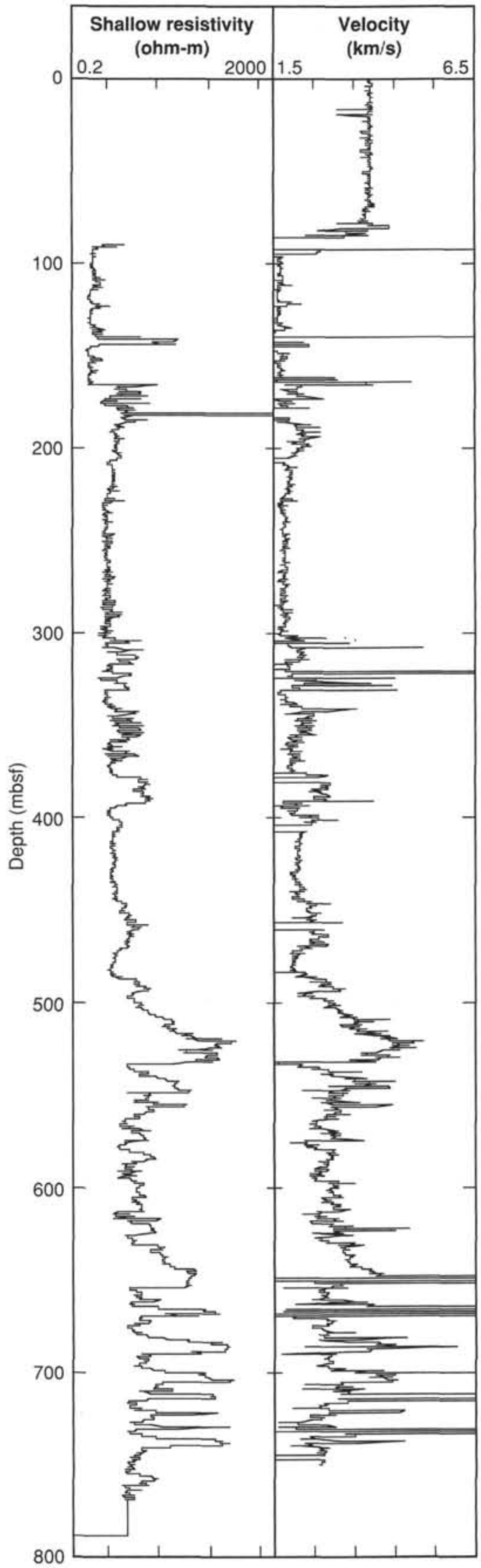

Figure 48. Summary of logs used to define logging units, Hole 869B. Unit boundaries are shown within the SGR (total gamma) and SFLU (shallow-resistivity) data columns. RHOB is density and NPHI is porosity. The mechanical caliper log is on the right.

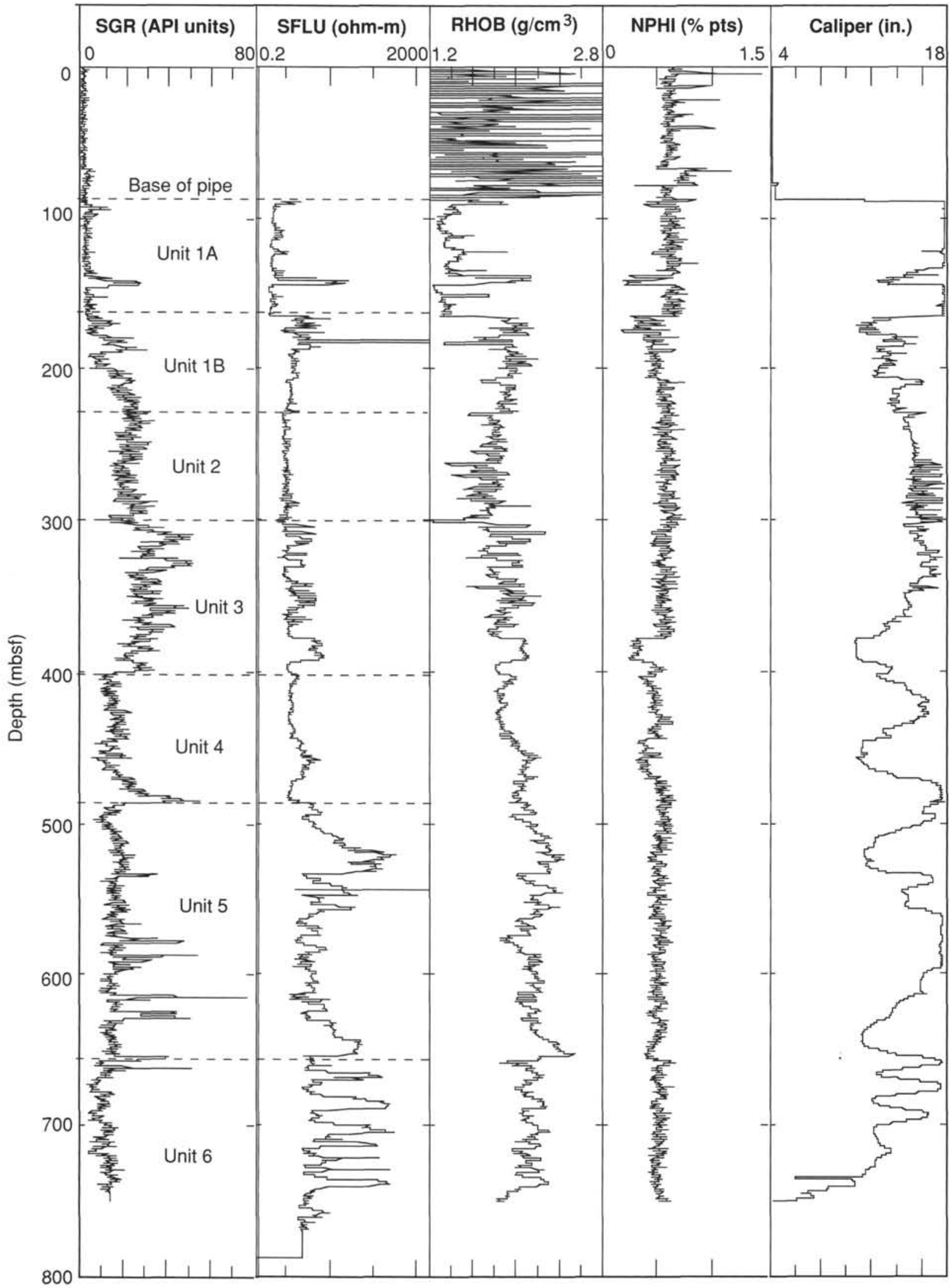

Figure 49. Comparison of velocity and resistivity logs, Hole 869B.

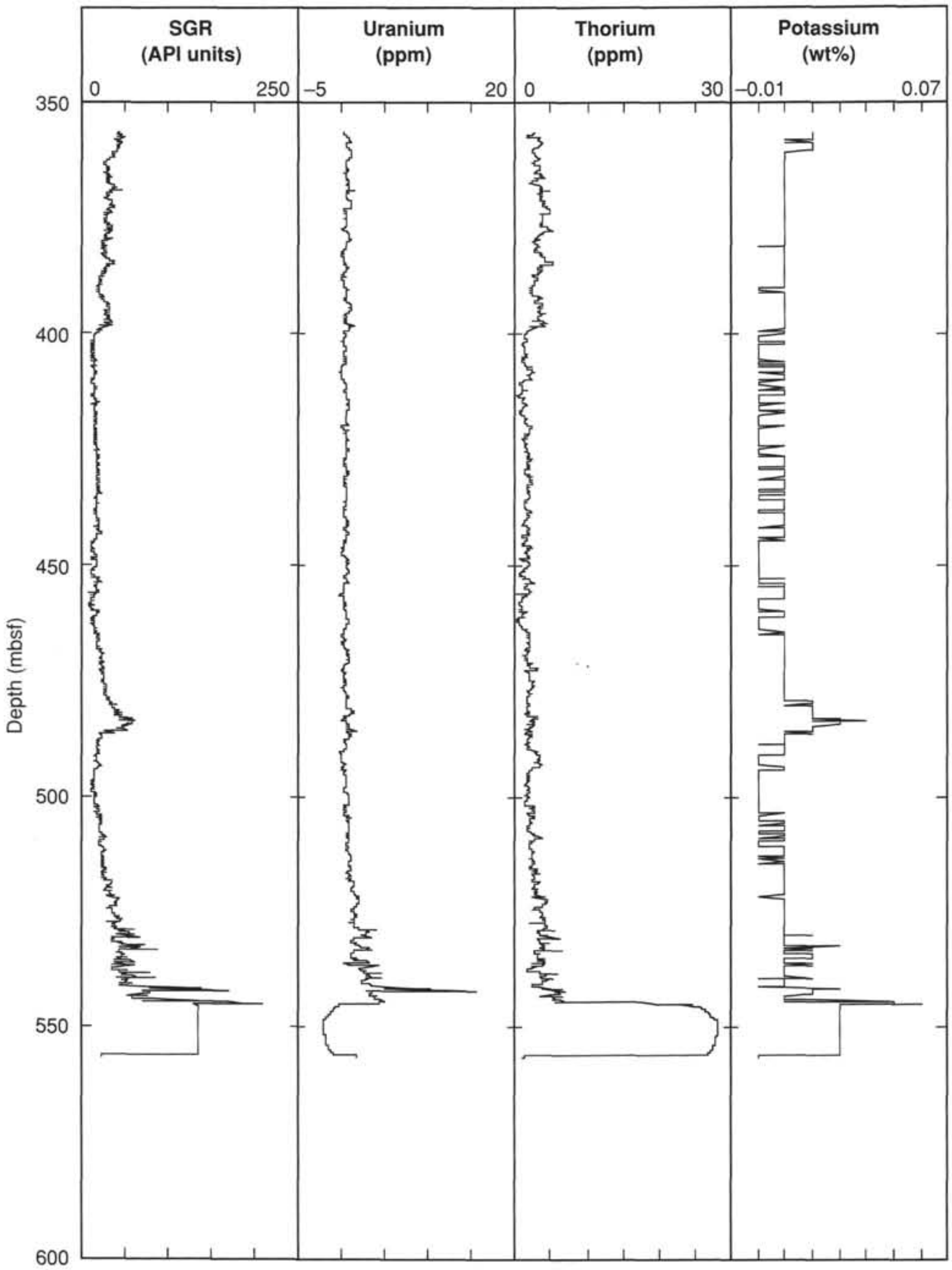

Figure 50. Spectral gamma-ray log compared with uranium, thorium, and potassium logs, Hole 869B.

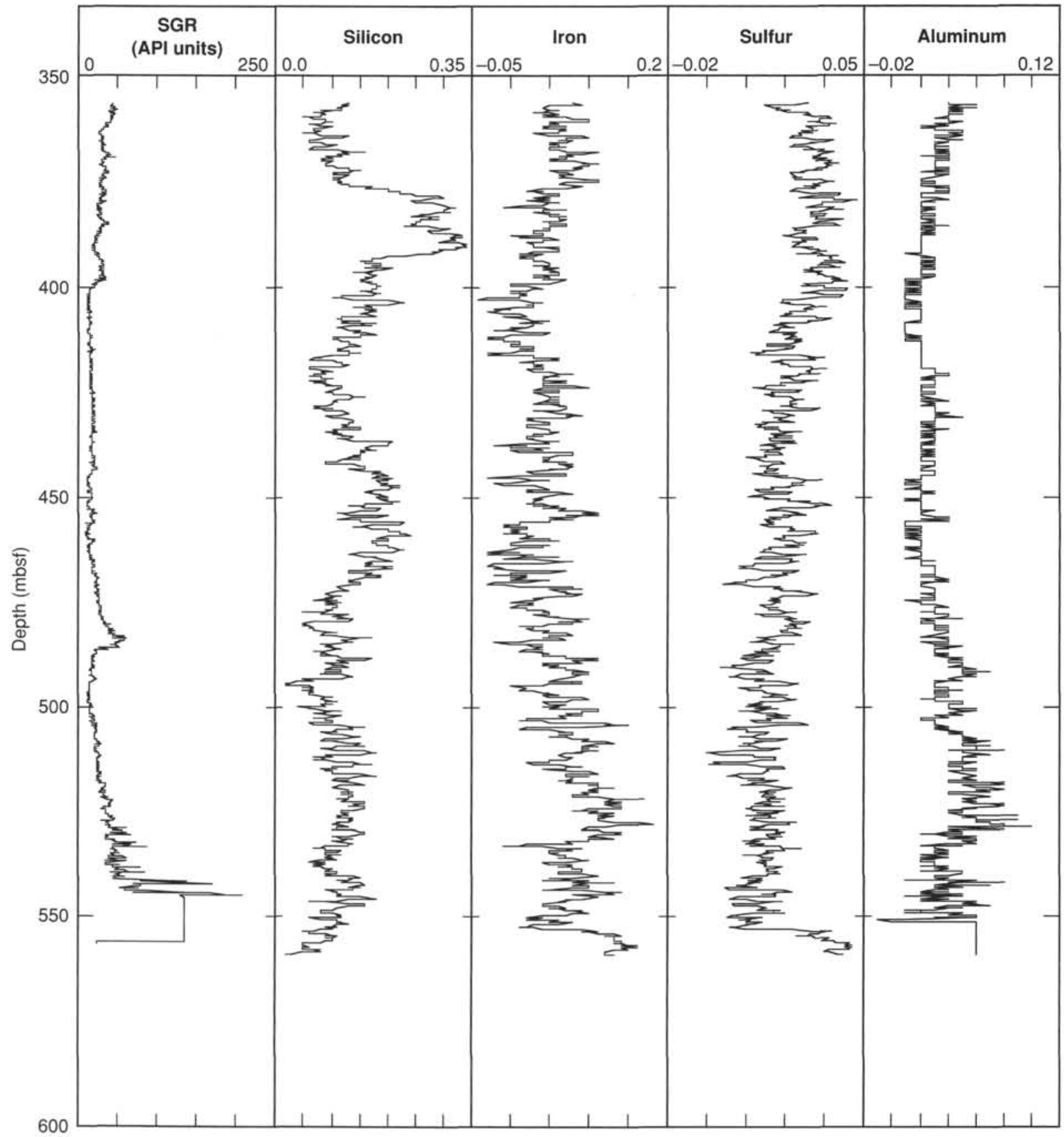

Figure 51. Spectral gamma-ray log compared with relative yield of silicon, iron, sulfur, and aluminum, expressed as decimal fractions. Calcium was uniformly zero for the entire logged interval.

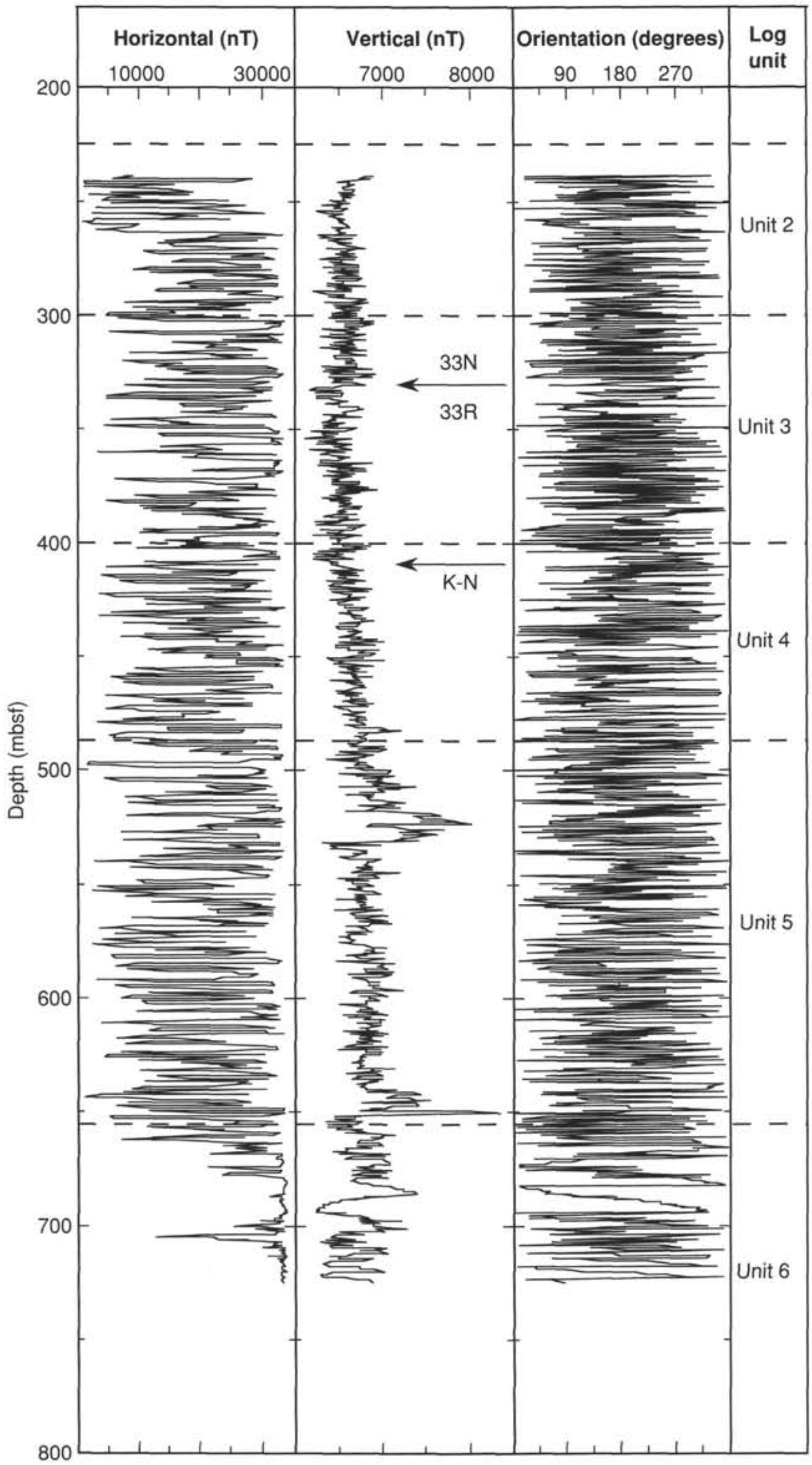

Figure 52. Variations of horizontal and vertical components of the geomagnetic field, and the orientation of the tool with respect to the present geomagnetic field within Hole 869B from 239 to 725 mbsf. Dashed lines indicate the boundaries of the log-based units. Arrows show the normal-reverse polarity boundaries inferred from vertical magnetic field variations and shipboard paleomagnetic results. K-N indicates the Cretaceous normal super chron.

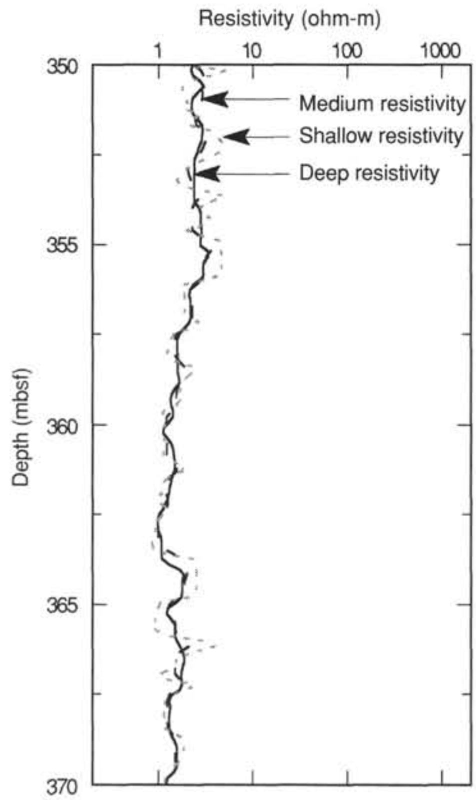

Figure 53. Comparison of deep-, medium-, and shallow-focused resistivity measurements, Hole 869B.

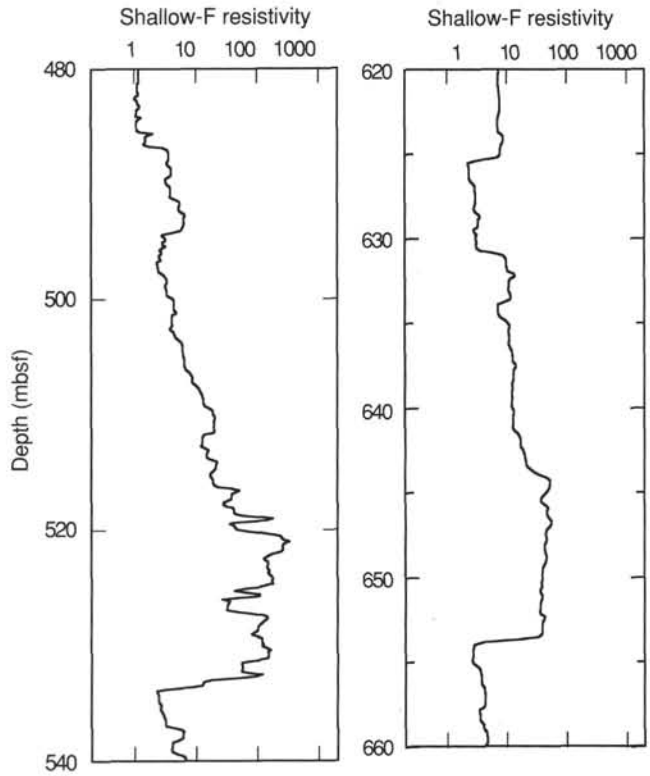

Figure 54. Shallow resistivity profiles of large fining-upward sequences bounding logging Unit 5 (left) 487.2 to 534.0 mbsf (Cores 143-869B-38R through -42R), (right) 625.8 to 654.2 mbsf (Cores 143-869B-52R through Section 143-869B-55R-2).

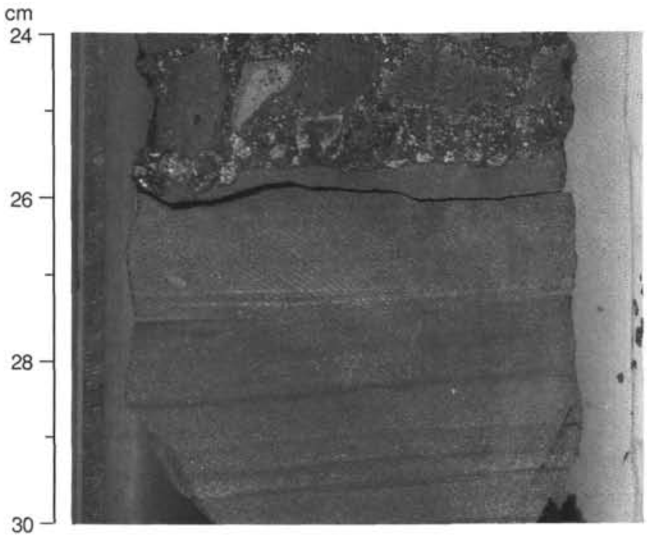

Figure 55. Interval 143-869B-55R-2, 24–30 cm, close-up photo showing contact between the breccias of the second fining-upward sequence and the underlying siltstones. (Same close-up photo as Figure 25.)

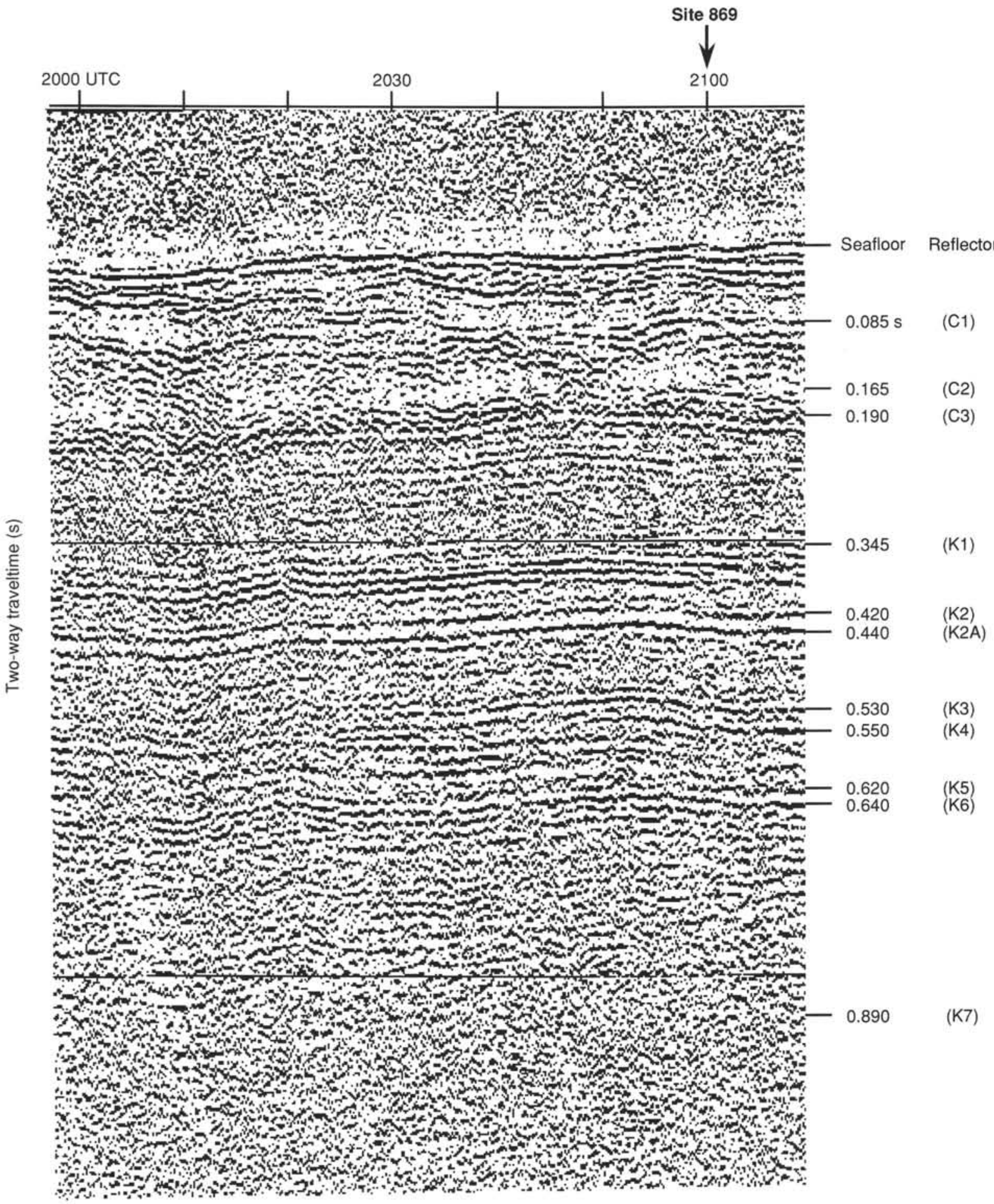

Figure 56. Seismic reflection profile at Site 869, showing two-way reflection time to most prominent reflectors. Profile taken by the *Thomas Washington* of the Scripps Institution of Oceanography, during Leg 8 of the Tunes Expedition.

Table 12. Prominent reflectors seen in Figure 56, showing their corresponding depths in Holes 869A and 869B.

Reflector no.	Twtt (bsf) (s)	Depth (mbsf)	Int. vel. (km/s)	Ave. vel. to seafloor (km/s)
C1	0.085	70	1.65	1.65
C2	0.165	141	1.78	1.71
C3	0.19	165	1.92	1.74
K1	0.345	303	1.78	1.76
K2	0.42	378	2.00	1.80
K2A	0.44	394		1.79
K3	0.53	509	2.38	1.92
K4	0.55	534		1.94
K5	0.62	617	2.40	1.98
K6	0.64	654		2.04
K7	0.89	*1000*	*2.77*	2.24
K8	1.05	*1230*	*2.86*	2.34

Interval velocities between reflectors and average velocities to the seafloor are shown in the last two columns of the table. Figures in italics are estimated values from extrapolation of the curve in Figure 57.

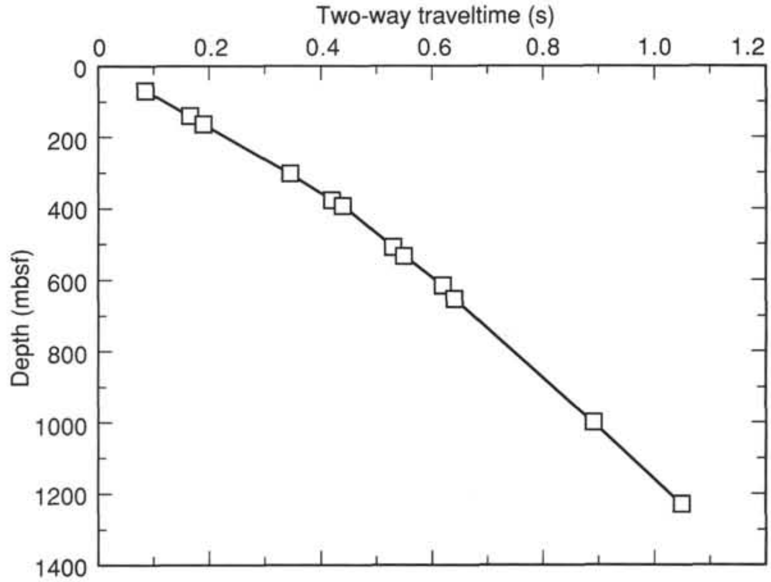

Figure 57. Plot of depth in Hole 869B vs. reflection time of the most prominent reflectors shown in Figure 56. The final two points, at 1000 and 1230 mbsf, have been extrapolated from the curve where control is good.

Hole 869B: Resistivity-Sonic-Natural Gamma Ray Log Summary

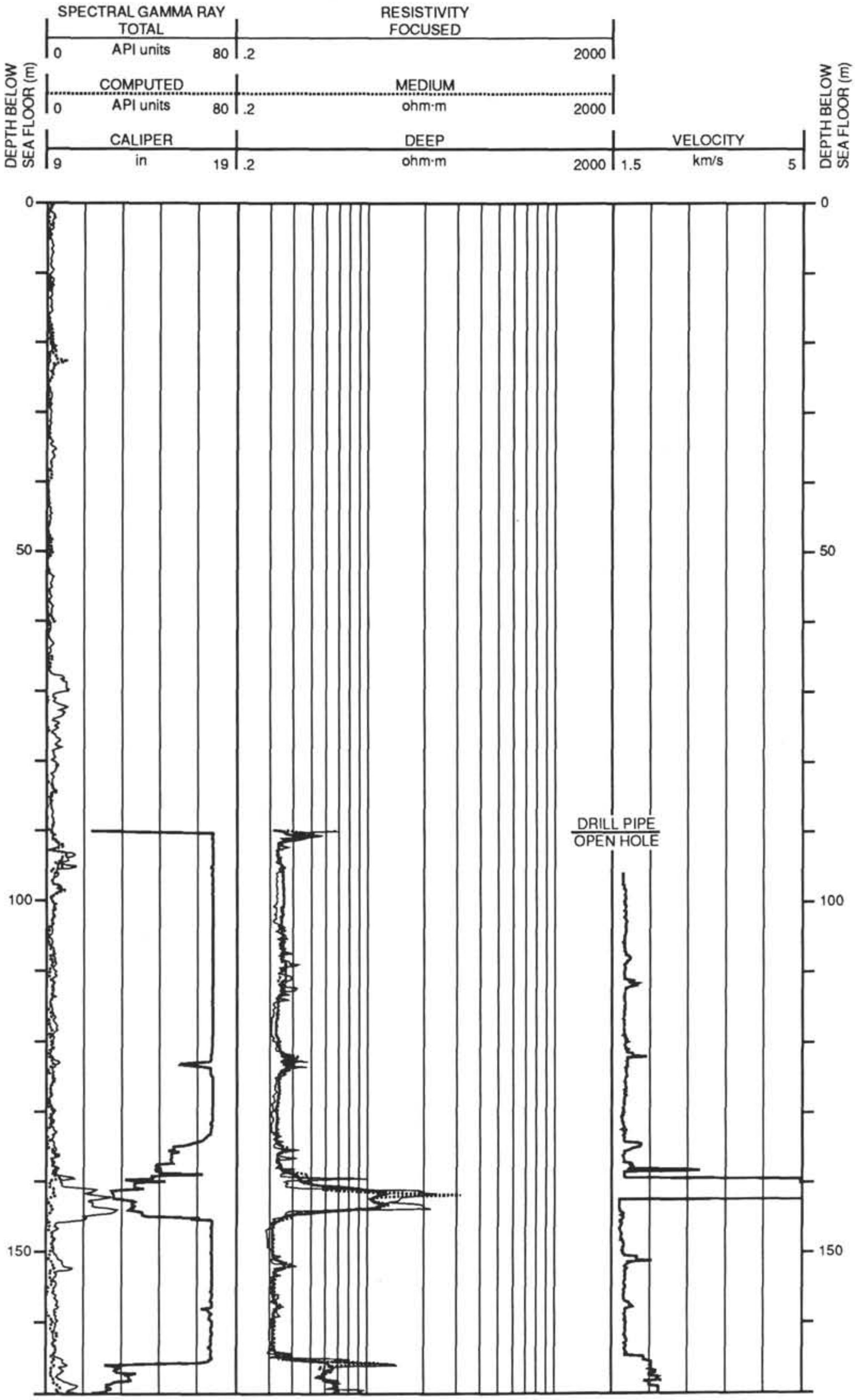

Hole 869B: Resistivity-Sonic-Natural Gamma Ray Log Summary (continued)

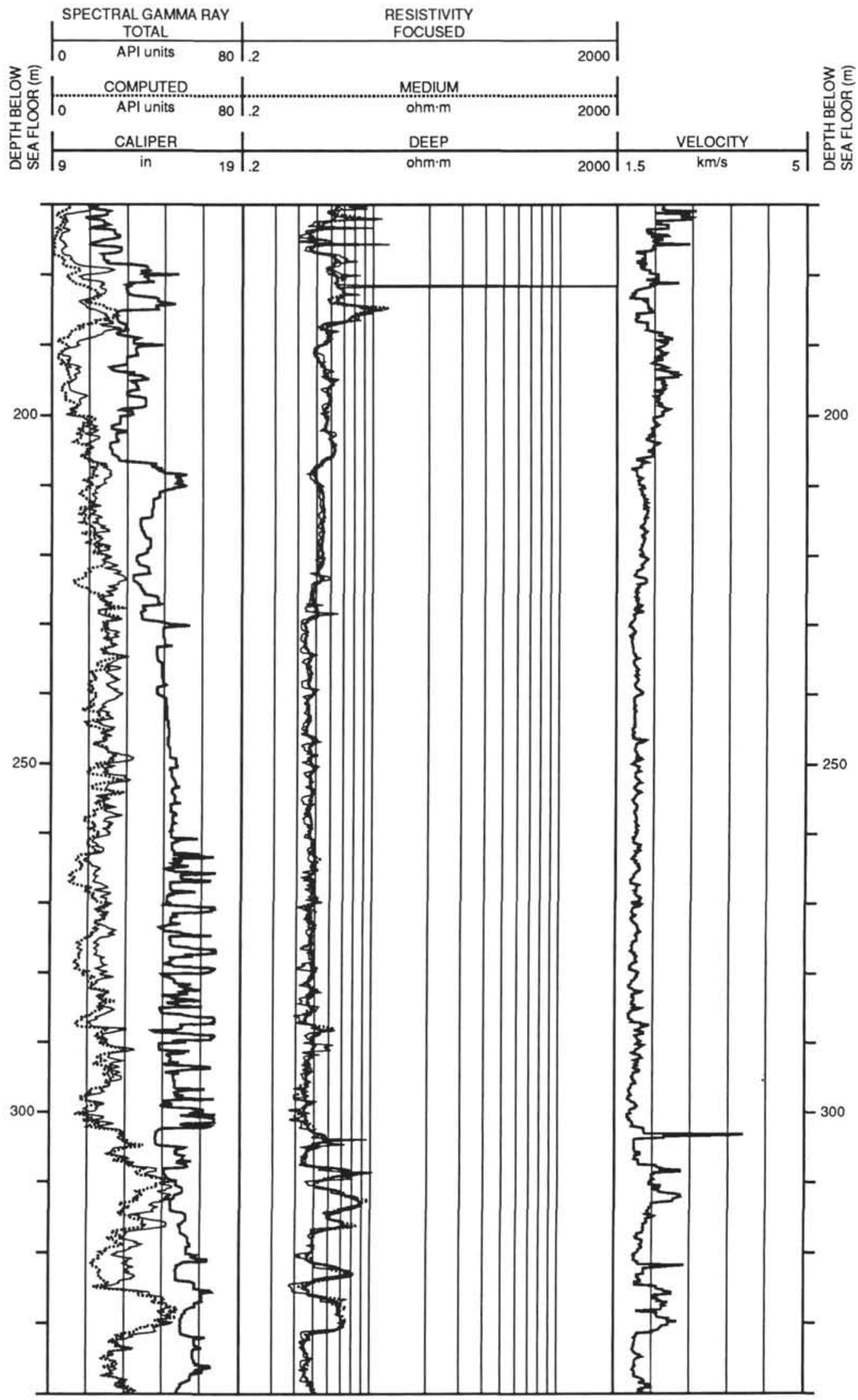

Hole 869B: Resistivity-Sonic-Natural Gamma Ray Log Summary (continued)

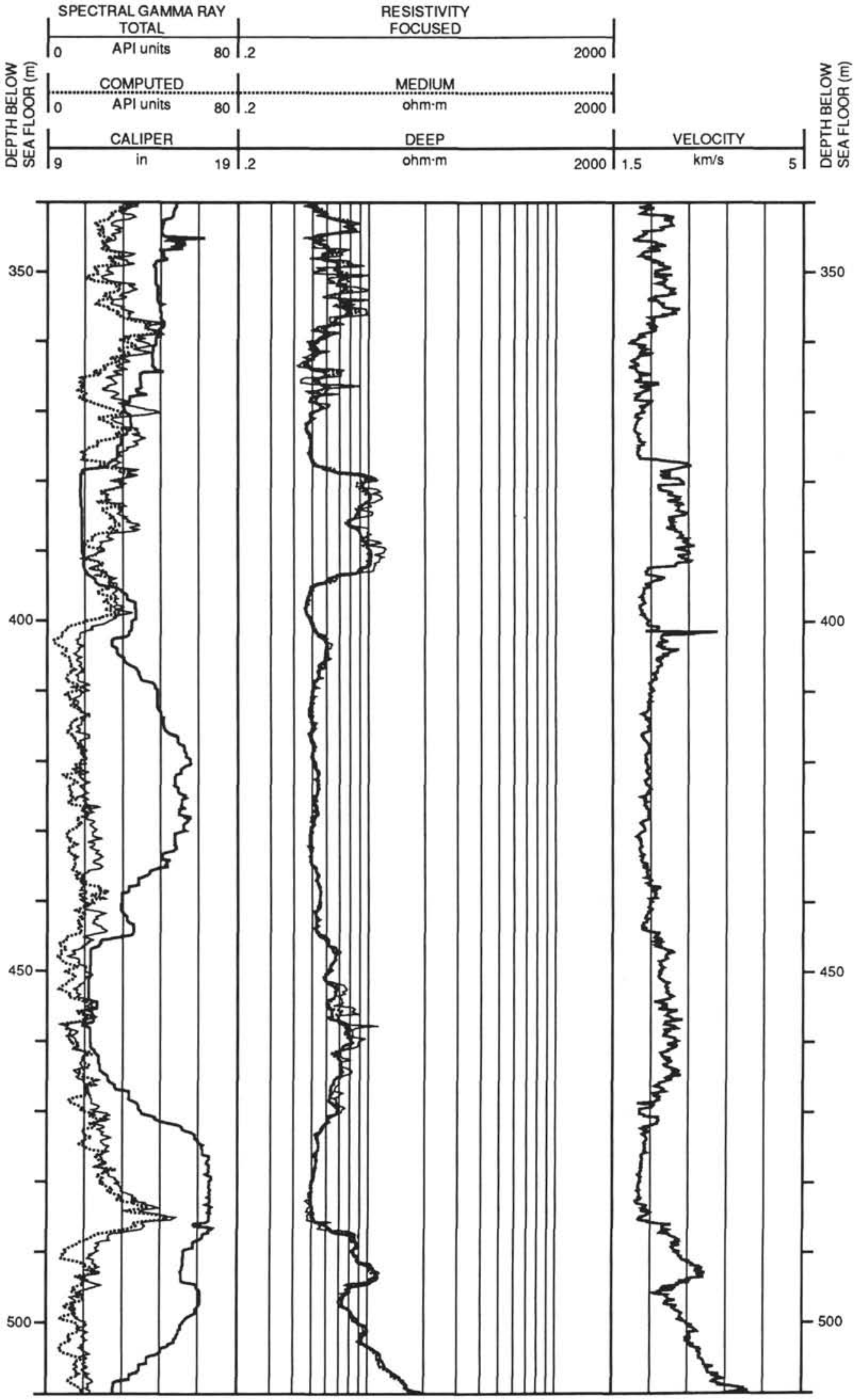

Hole 869B: Resistivity-Sonic-Natural Gamma Ray Log Summary (continued)

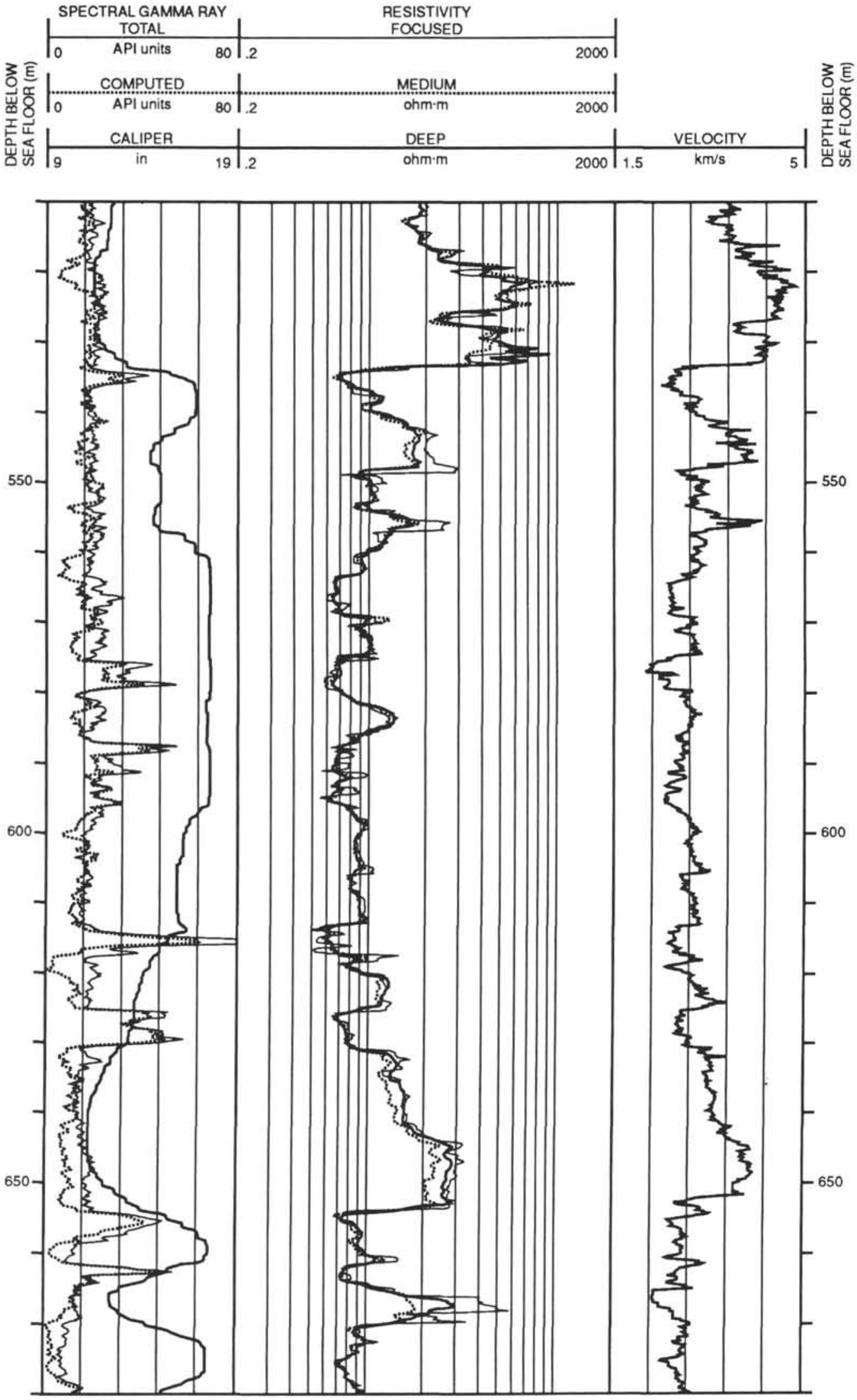

Hole 869B: Resistivity-Sonic-Natural Gamma Ray Log Summary (continued)

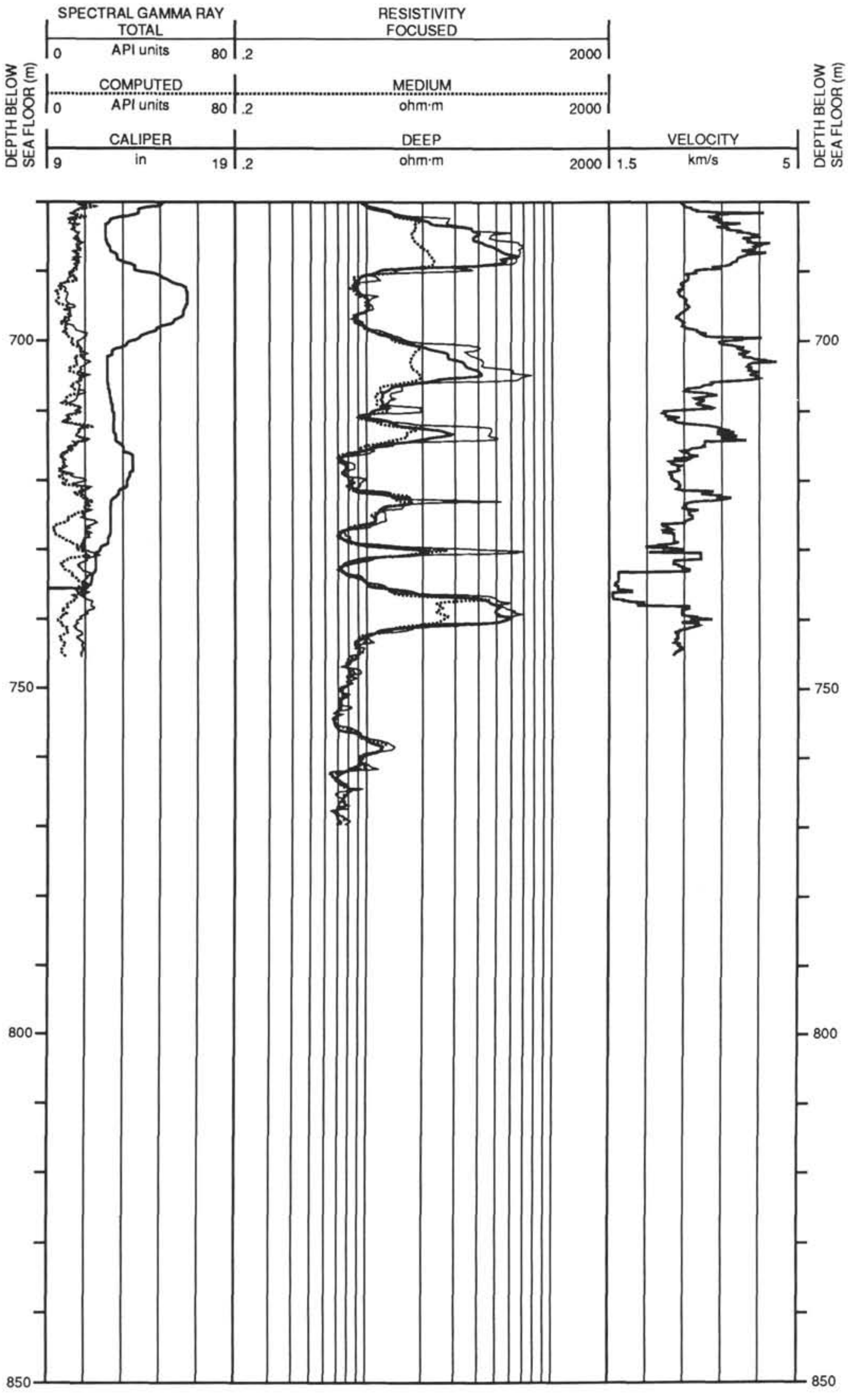

Hole 869B: Density-Porosity-Natural Gamma Ray Log Summary

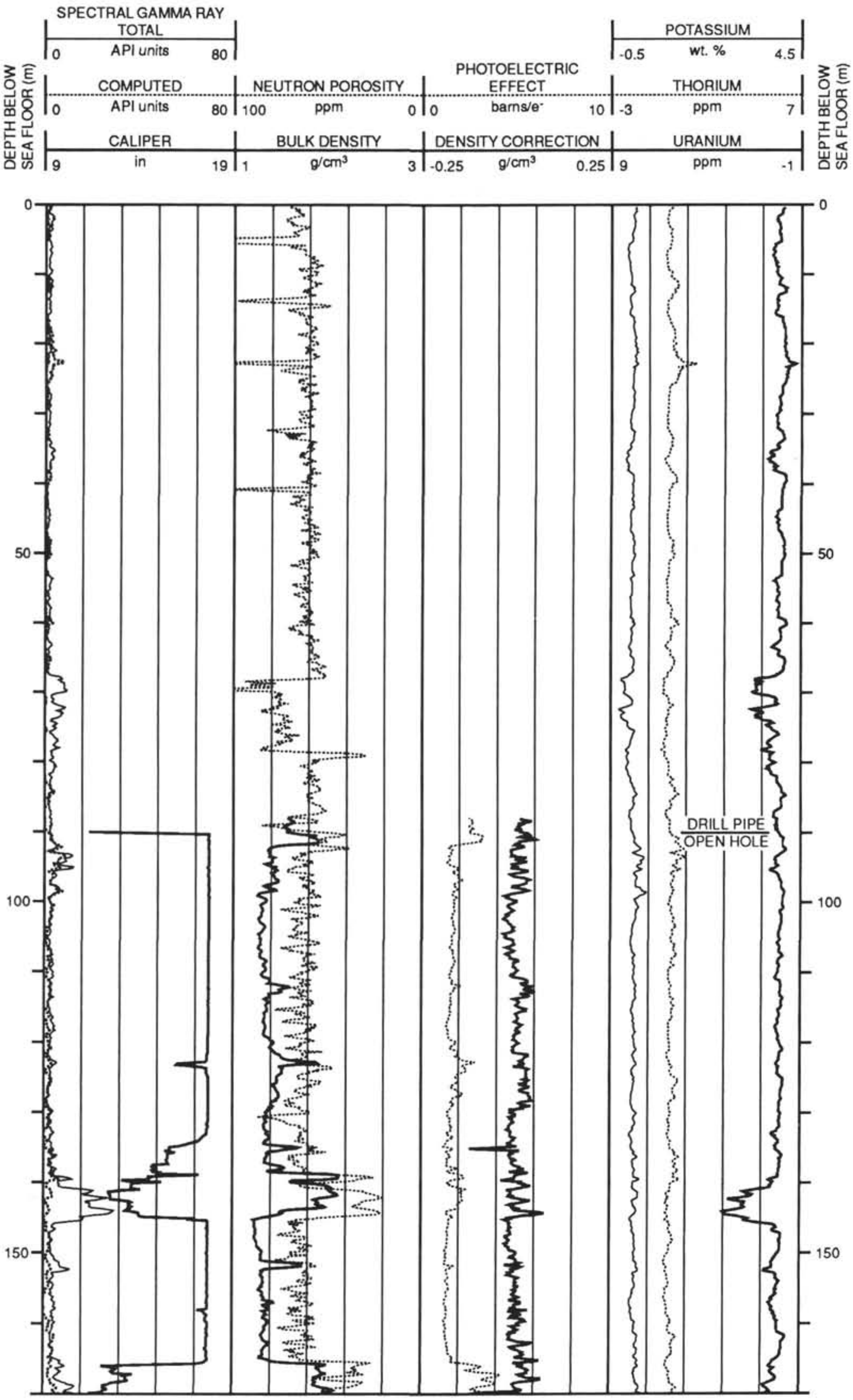

Hole 869B: Density-Porosity-Natural Gamma Ray Log Summary (continued)

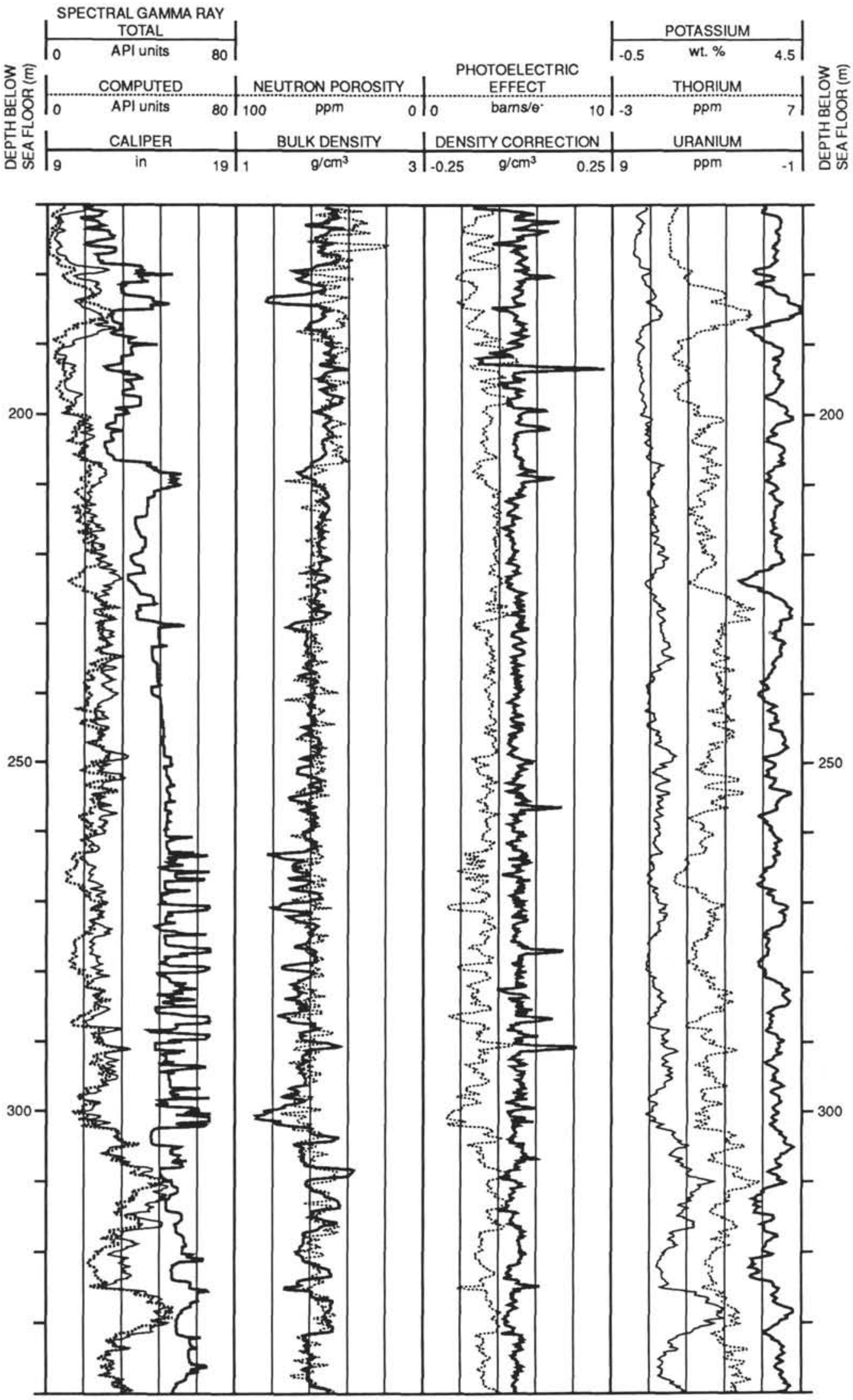

Hole 869B: Density-Porosity-Natural Gamma Ray Log Summary (continued)

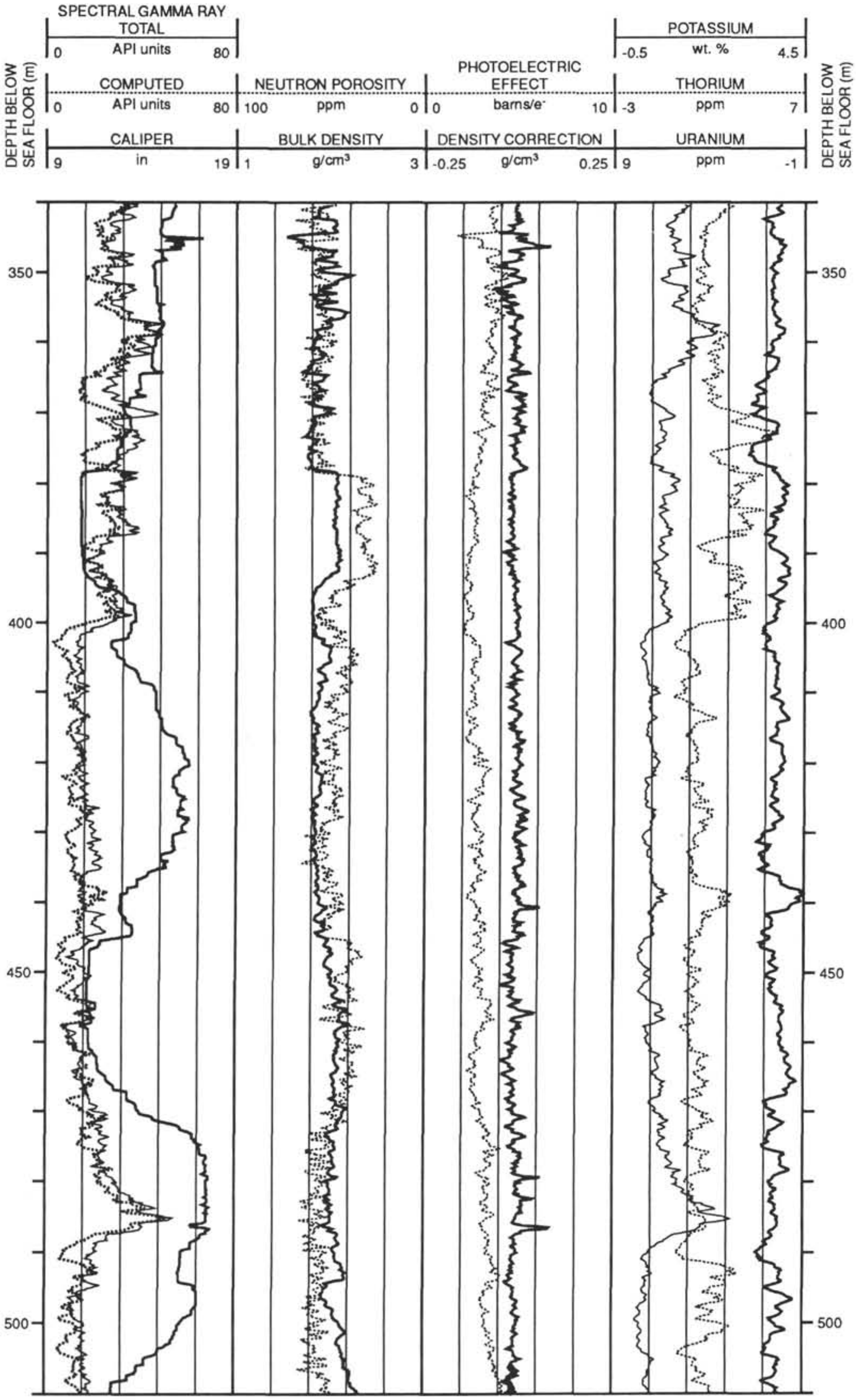

Hole 869B: Density-Porosity-Natural Gamma Ray Log Summary (continued)

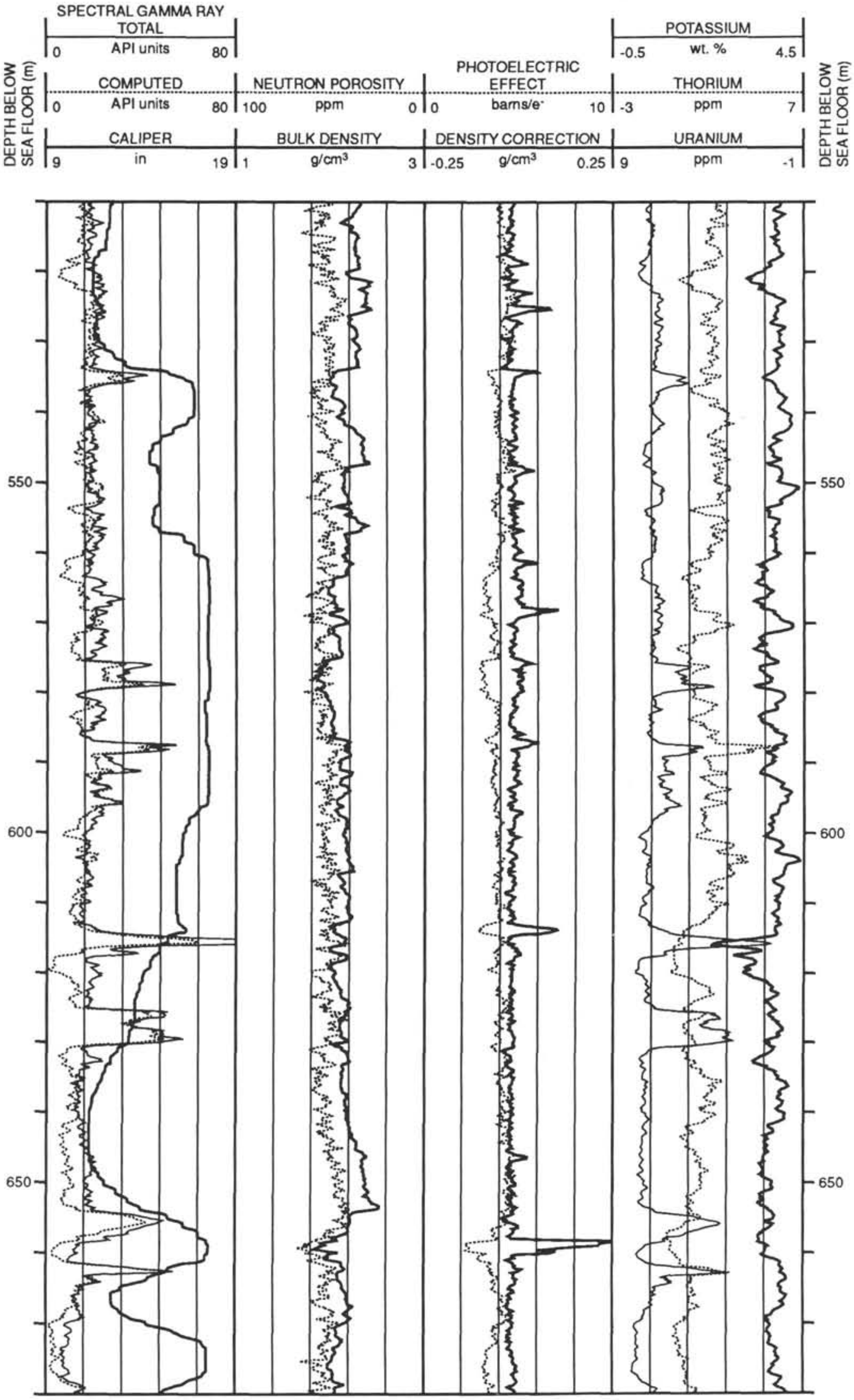

Hole 869B: Density-Porosity-Natural Gamma Ray Log Summary (continued)

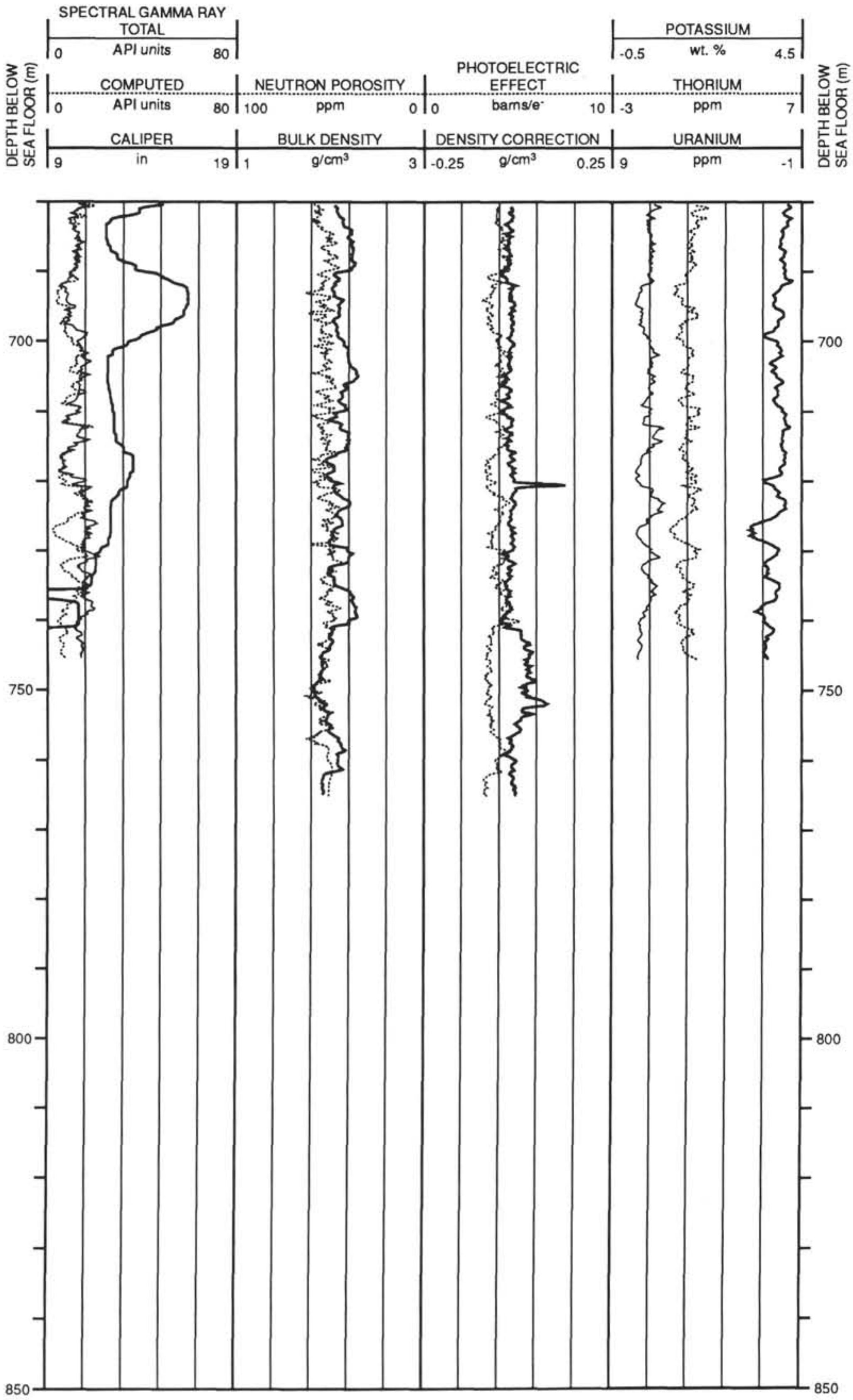

Hole 869B: Geochemical Log Summary

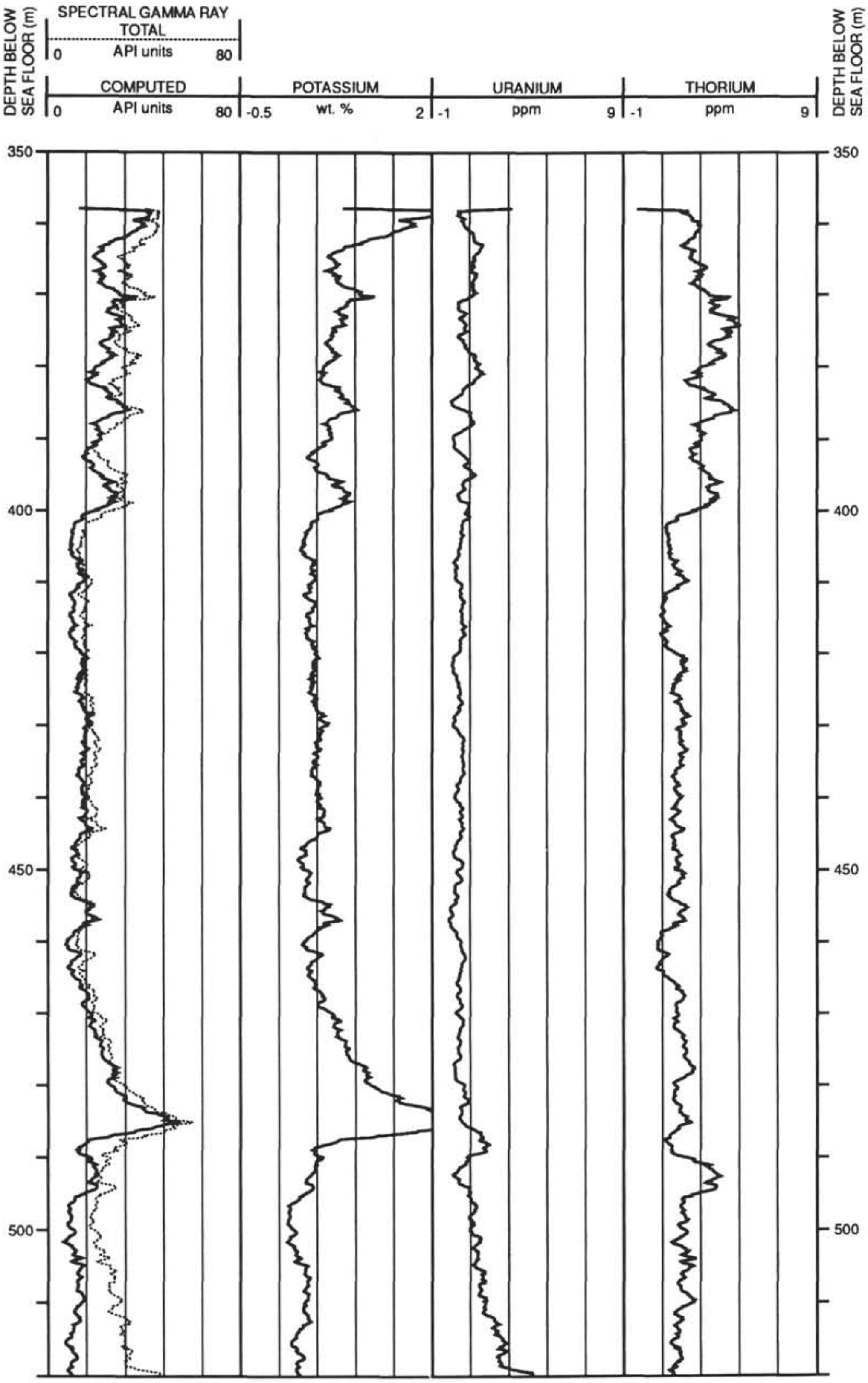

Hole 869B: Geochemical Log Summary (continued)

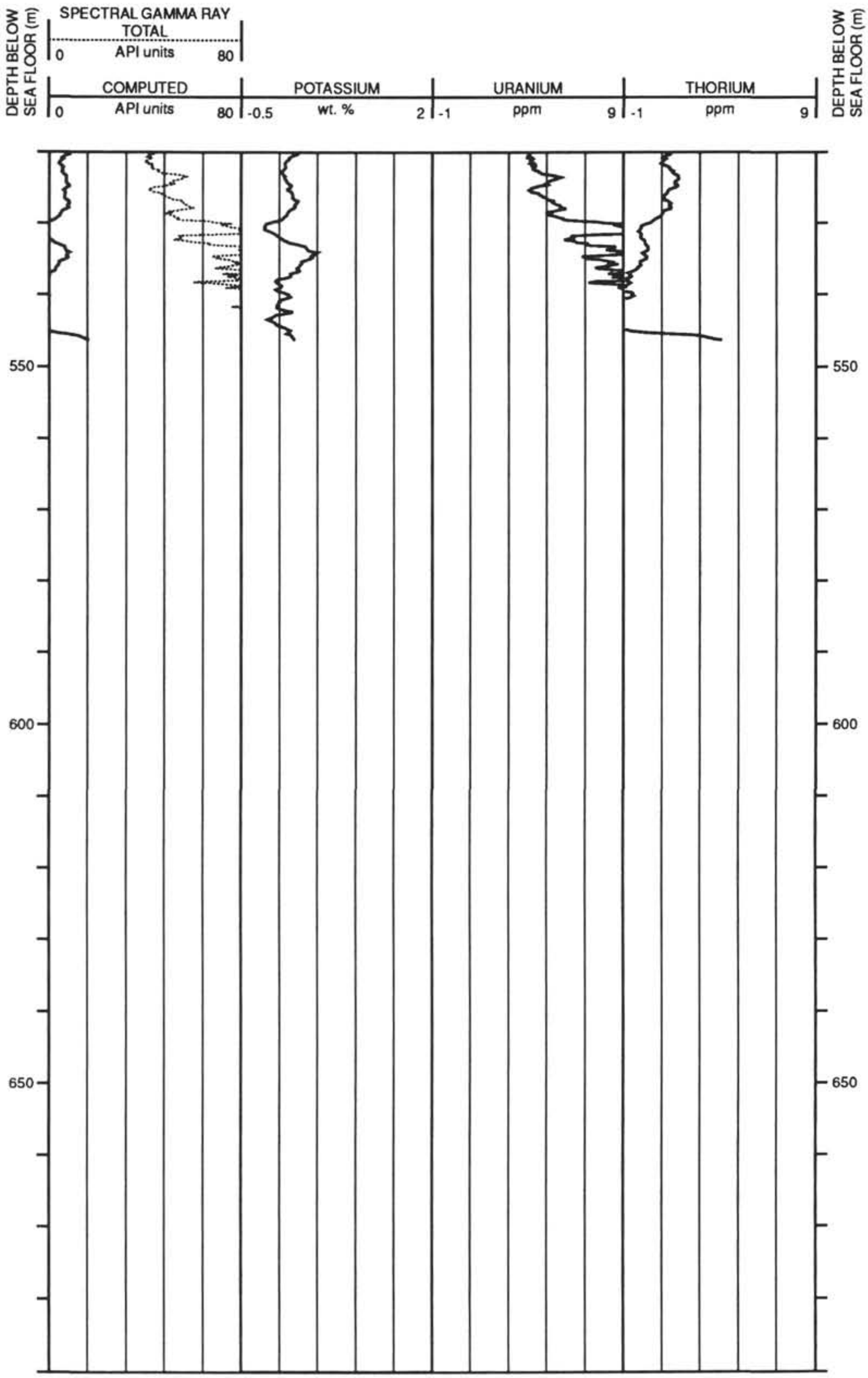

Hole 869B: Processed Geochemical Log Summary

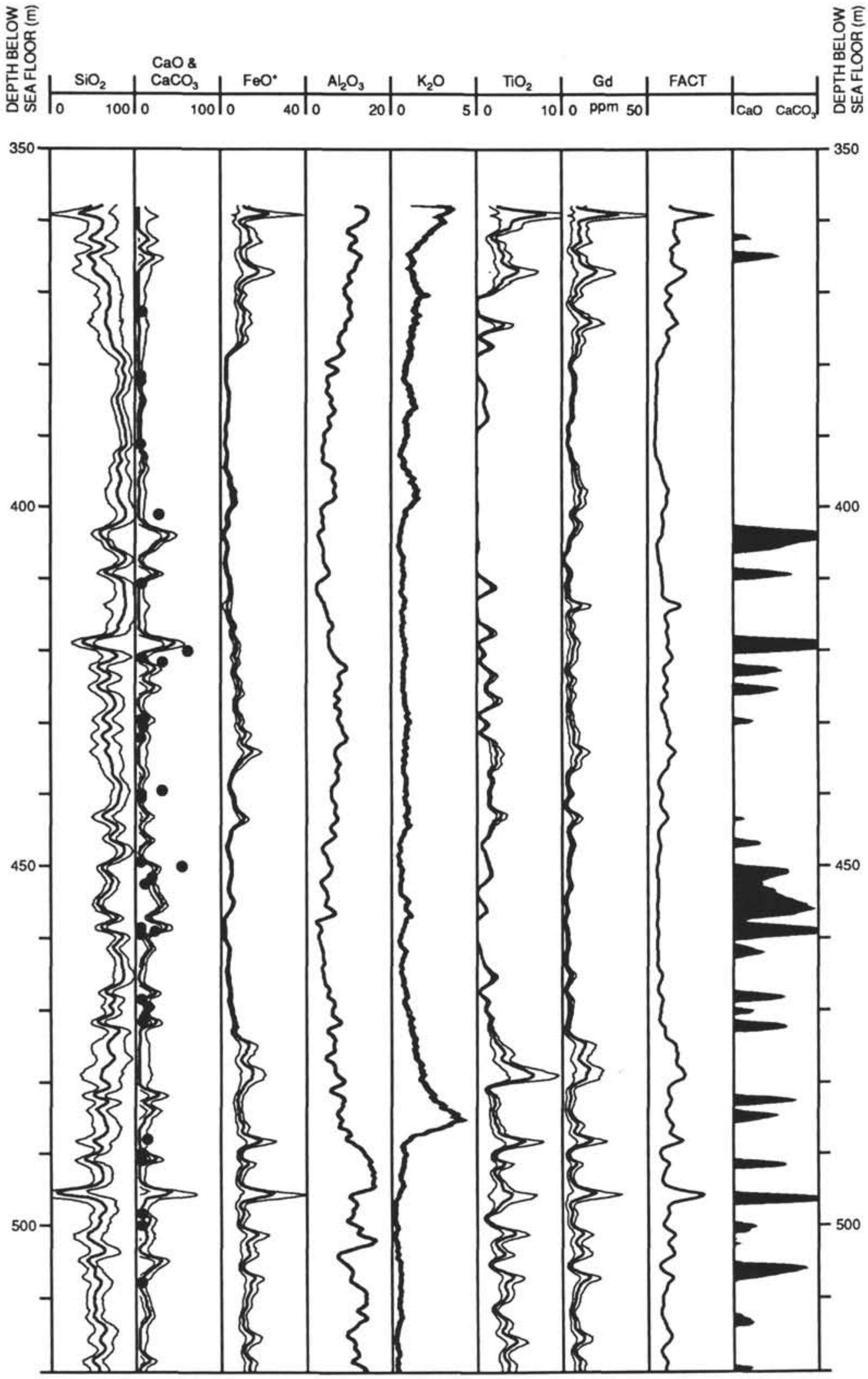

Hole 869B: Processed Geochemical Log Summary (continued)